Universidade do Minho
Escola de Engenharia

Chandan Chinnagiri Gowda

Use of NSM FRP for torsional strengthening on thin walled tubular RC structures

FCT Fundação para a Ciência e a Tecnologia
MINISTÉRIO DA CIÊNCIA, TECNOLOGIA E ENSINO SUPERIOR

POPH QUALIFICAR É CRESCER.
QREN QUADRO DE REFERÊNCIA ESTRATÉGICO NACIONAL
GOVERNO DA REPÚBLICA PORTUGUESA
UNIÃO EUROPEIA Fundo Social Europeu

Use of NSM FRP for torsional strengthening on thin walled tubular RC structures
Chandan Chinnagiri Gowda

UMinho | 2019

março de 2019

Universidade do Minho
Escola de Engenharia

Chandan Chinnagiri Gowda

Use of NSM FRP for torsional strengthening on thin walled tubular RC structures

Tese de Doutoramento
Engenharia Civil

Trabalho efetuado sob a orientação de
Professor Doutor Joaquim Antonio Oliveira de Barros
Doutor Maurizio Guadagnini

março de 2019

STATEMENT OF INTEGRITY

I hereby declare having conducted my thesis with integrity. I confirm that I have not used plagiarism or any form of falsification of results in the process of the thesis elaboration.

I further declare that I have fully acknowledged the Code of Ethical Conduct of the University of Minho.

University of Minho, 14/30/2019

Full name: Chandan Chinnagiri Gowda

Signature: 

To my
mom, sister and dad.

ACKNOWLEDGEMENTS

The present research was carried out mainly in the department of Civil engineering at University of Minho, Portugal and a short period in department of Civil Engineering at The University of Sheffield, U.K. The experimental work was performed in LEST, structural laboratory of UMinho and at Casais group, Portugal.

The research was supervised by Prof. Joaquim Barros and co-supervised by Dr. Maurizio Guadagnini. I would like to express my sincere gratitude to Prof Barros, for the interesting conversations and discussions regarding work and life, upgrading the quality overall. I would like to thank Dr. Maurizio Guadagnini for his suggestions and supporting my way through at roadblocks. I would like to thank Marie-Curie Initial training Network (ITN): ENDURE, for financially supporting my research for the first half and providing me with many opportunities to attend different COST action and MC-ITN meetings. The grant from Foundation for Science and Technology (FCT) is equally appreciated, without which the research would not have been completed.

The support by the technicians at the structural laboratory of UMinho (Sr. Matos, Marco, Cesar, Sr. Gonsalves and Sr. Manuel), colleagues from UMinho (Ton, Marcin, Joao and Alberto), colleagues from CiviTest (Ines and Delfina) and, colleagues and technicians at Casais group (Eng. Miguel Pires and Sr. Joao) is greatly appreciated in executing the experimental work.

More importantly I would like to thank my friends who have supported me for long or short periods, listening to my complaints, almost experiencing my troubles and prolonging my agonies, and finally helping me achieve the doctorate degree (at least soon to be). I would like to personally thank Szymon, Alberto, Luis, Maria, Telma, Laura, Marilu, Mariana, Mafalda, Gianpaolo, Jaime, Marcin, Ankit, Anjana, Divya, Joao, Matteo, Leonardo, Carlos, Michal, Basia and many other well-wishers or not, for enduring most of me and have definitely encouraged me.

Finally, my gratitude to my sister, mom and dad for their unlimited love, encouragement and support all the way, by tolerating my twists and turns.

ABSTRACT

The use of near surface mounted (NSM) FRP reinforcement has been proven to be a very promising technique for the strengthening of reinforced concrete (RC) structures in both flexure and shear. The application of NSM FRP to improve the torsional performance of RC structures is limited, however, and despite the many potential advantages this technique has never been applied to thin walled tubular RC members. This research study focuses on the development of strengthening strategies for torsional deficient elements using NSM straight and L-shaped CFRP laminates. The proposed strengthening solutions offer substantial advantages over other available conventional and innovative (externally bonded techniques) strengthening methods. The research includes an extensive experimental programme followed by the development of a design model, complemented by a numerical study.

A nonlinear analysis based on the finite element method is performed to assist in the preparation of the experimental work and the development of the test setup. A parametric study is carried out to assess the influence of longitudinal and transverse steel reinforcement ratios, concrete strength, strengthening configurations and longitudinal and transverse NSM FRP reinforcement ratios. The main objective of the experimental work is to derive reliable data to assess the performance of the NSM technique for the strengthening of thin walled RC elements, and for the development of design formulations. For this purpose, three series of tests with RC tubular prototypes are experimentally tested by determining the torsional moment versus torsional angle of rotation, strains in the reinforcements and in the CFRP laminates, and the crack patterns and failure modes. Digital image correlation is also used in an attempt of enriching the knowledge provided by conventional sensors. The strengthening configurations are categorized into three series (i) four face strengthening with straight CFRP laminates (ii) three face strengthening with straight CFRP laminates and (ii) four face strengthening with L-CFRP laminates. All the strengthening proposals show improved performance in torsional moment carrying capacity (18% - 46%), torsional angle of rotation (20% - 76%) and decrease in crack spacing (16% - 56%).

Based on the obtained results, analytical equations are developed using space truss analogy for thin walled tubular reinforced concrete members strengthened with NSM CFRP laminates. The equations are presented for ultimate torsional moment carrying capacity, effective strain of

CFRP laminates and diagonal compressive strut angle. The proposed analytical equations predict the experimental results well with a 7% error.

Keywords: Torsional strengthening, thin-walled tubular structures, L-CFRP laminates.

RESUMO

A técnica de reforço baseada na introdução de finos laminados de fibra de carbono (CFRP) em entalhes executados no betão de recobrimento do elemento a reforçar, designada pelo acrónimo NSM, tem sido aplicada no reforço à flexão e corte de estruturas de betão armado (RC) ao longo das últimas duas décadas. No entanto, a aplicação da técnica NSM no reforço à torção das estruturas de betão armado é praticamente inexistente, em especial em elementos de secção tubular de paredes finas. Assim, a presente tese foca-se no reforço desses elementos com comportamento deficiente à torção, usando a técnica de NSM com utilização de laminados de CFRP retos e em forma de L. A técnica oferece vantagens substanciais em relação às técnicas tradicionais suportadas na utilização de materiais de reforço convencionais, e mesmo em relação à técnica baseada na colagem externa de CFRP (EBR). A investigação envolve trabalho experimental e analítico, sendo complementado com simulações numéricas.

A análise não linear material baseada no método dos elementos finitos é realizada para auxiliar a preparação do programa experimental e no projeto do sistema de ensaio. Um estudo paramétrico é efetuado para avaliar a influência que os seguintes parâmetros têm na eficácia da técnica NSM com laminados de CFRP: variação longitudinal e transversal da armadura de aço; variação da classe de resistência do betão; percentagem do reforço longitudinal e transversal em CFRP. O principal objetivo do trabalho experimental é determinar resultados confiáveis para avaliar as potencialidades e as debilidades da técnica NSM no reforço de elementos tubulares de paredes finas em betão armado, e contribuir para o desenvolvimento de formulações que permitam o dimensionamento destes sistemas de reforço. Para o efeito, três séries de testes com protótipos tubulares de betão armado são testadas experimentalmente, determinando-se: a relação entre o momento torsional e o ângulo de rotação por torsão; deformações nas armaduras e nos laminados CFRP; e os padrões de fendilhação e modos de rotura. A técnica baseada na correlação de imagens digitais (DIC) também é usada na tentativa de enriquecer o conhecimento fornecido por esses testes, em especial o relativo à formação e propagação de fissuras, e ao campo de extensões na superfície dos protótipos. As configurações de reforço são categorizadas em três séries: (i) reforço com laminados retilíneos de CFRP nas quatro faces dos protótipos (ii) reforço com laminados retilíneos de CFRP em três das quatro faces dos protótipos e (iii) reforço das quatro faces dos protótipos com laminados de CFRP de geometria L. Todas as propostas de reforço aumentaram o máximo momento de torção (18% -

46%), o correspondente ângulo de rotação torsional (20% - 76%), e promoveram uma diminuição no espaçamento entre fendas (16% - 56%).

Com base nos resultados obtidos, equações analíticas são desenvolvidas usando o método de escoras e tirantes para elementos tubular de paredes finas de betão armado reforçados com laminados de CFRP aplicados segundo a técnica NSM. As equações apresentadas servem para determinar o momento de torção último, a extensão efetiva em laminados CFRP e o ângulo diagonal de compressão. As equações analíticas propostas preveem os resultados experimentais com um erro médio de 7%.

Palavras-chave: Reforço à torção, estruturas tubulares de paredes finas, laminados de CFRP.

TABLE OF CONTENTS

LIST OF SYMBOLS

a_f	Thickness of FRP laminate
a_g	Maximum coarse aggregate size
A	Outer cross sectional area
A_c	Area of concrete section
A_c	Cross sectional area of prism surrounding the concrete
A_f	Area of FRP laminates
A_{fl}	Area of FRP laminates in longitudinal direction
A_{fw}	Area of FRP laminates in transverse direction
A_k	Area enclosed by center line of connecting walls
A_l	Area of longitudinal steel reinforcement
A_o	Gross area enclosed by shear flow path
A_{of}	Area enclosed inside the critical shear flow path due to strengthening
A_{pt}	Cross sectional area of pre-stressing tendons
A_{sl}	Area of longitudinal steel reinforcement
A_{sw}	Area of transverse steel reinforcement
A_t	Area of one leg of closed stirrup
b	Breadth of beam
b_f	Width of the FRP laminate
b_h	Breadth of hollow section
b_v	Effective web width
C_3	Integration constant
D_2	Diagonal force
d_g	Maximum nominal aggregate size
d_h	Depth of hollow section
d_f	Internal arm of FRP reinforcement
d_s	Internal arm of steel reinforcement
d_v	Effective shear depth
E_c	Modulus of elasticity of concrete
E_{cm}	Average modulus of elasticity of concrete
E_f	Modulus of elasticity of FRP laminates

E_{fm}	Average elasticity modulus of FRP laminates
E_{fw}	Modulus of elasticity of FRP laminates in transverse direction
E_p	Modulus of elasticity of pre-stressing tendons
E_s	Modulus of elasticity of steel reinforcement
E_{sm}	Average modulus of elasticity of steel reinforcement
$f_c^{'}$	Compressive strength of concrete
f_{cd}	Desgin compressive strength
f_{cm}	Average concrete compressive strength
f_{ctd}	Concrete desgin tensile strength
f_{ctm}	Concrete mean tensile strength
f_{fu}	Tensile strength of FRP laminates
f_{um}	Tensile strength of steel reinforcement
f_y	Yield strength of longitudinal reinforcement
f_{yd}	Design yield strength of transverse/ longitudinal steel reinforcement
f_{yl}	Yield stress of steel reinforcement in the longitudinal direction
f_{ym}	Yield stress of steel reinforcement
f_{yt}	Yield strength of transverse steel reinforcement
J_1	Bond modelling constant
$k_{t,lin}$	Torsional stiffness in linear stage
$k_{t,Mcr}$	Torsional stiffness in macro cracking stage
$k_{t,syi}$	Torsional stiffness at initial stage of steel yielding
L_d	Critical diagonal crack length
L_e	Effective bond length
L_{fi}	Effective bond length
L_p	Perimeter of FRP laminate
L_{Rfe}	Effective resisting bond length
$\overline{L}_{Rfi}$	Average avaible bond length
$\overline{L}_{Rfi}^{eq}$	Equivalent average resisting bond length
M^*	Design bending moment
M_t	Torsional moment

$M_{t,cr}$	Torsional cracking moment
$M_{t,f}$	Torisonal capacity due to transverse FRP laminates
$M_{t,fl}$	Torsional capacity due to longitudinal FRP laminates
$M_{t,Mcr}$	Torsional macro cracking moment
$M_{t,syi}$	Torsional cracking moment at steel yielding
$M_{t,p}$	Peak torsional cracking moment
$M_{t,Rd}$	Desgin resistance of concrete in torsion
$M_{t,Rd,\max}$	Design maximum torsional resistance
$M_{t,s}$	Design resistance of transverse steel reinforcement
$M_{t,sl}$	Design resistance of longitudinal steel reinforcement
$M_{t,syi}$	Torsional moment at steel yielding
N^*	Axial compressive or tensile force
N_2	Axial force
$N^l_{f,\text{int}}$	Integer number of FRP laminates crossing the CDC
P_u	Ultimate load
P_v	Vertical component of pre-stressing force
p_h	Perimeter of closed stirrups
q	Shear flow
s	Spacing of transverse steel reinforcement
s_{fl}	Spacing of longitudinal FRP laminates
s_{fw}	Spacing of transverse FRP laminates
s_{rm}	Average crack spacing
s_x	Vertical distance between longitudinal steel reinforcements
s_w	Spacing of transverse reinforcement
T^*	Torional moment
t	Thickness of hollow section
t_n	Load step
$t_{ef,i}$	Effective wall thickness
u	Outer perimeter
u_h	Perimeter of closed transverse reinforcement
u_k	Perimeter of area A_k
u_m	Perimeter of the resistant core
V^*	Design shear force

V_{Ed}	Design transverse shear force
V_f	Shear force contribution by FRP laminates in transverse direction
V_{f1}^{bd}	Maximum bond force
V_f^{tr}	FRP laminate tensile strength
$V_{fi,eff}^{\max}$	Maximum effective shear force capacity of NSM FRP laminate
$V_{Rd,\max}$	Maximum design shear resistance
V_2	Vertical shear force
w_f	Width of FRP
z	Lever arm length
z_i	Length of wall “i”
α	Angle of semi-pyramid cone of concrete
α_{crm}	Average crack orientation
α_{cw}	Coefficient considering the state of stress in compression chord
α_f	Constant considering the difference in stress between the continuous and strip FRP’s
β	Angle of FRP laminates
β_f	Angle of orientation of fibre to the longitudinal axis of the beam
β_s	Angle of inclination of steel reinforcement
γ_{Rd}	Saftey factor
Δ_u	Midspan deflection
$\Delta M_{t,Mcr}$	Torsional moment increase in macro cracking
$\Delta M_{t,syp}$	Torsional moment increase from steel yielding upto peak torsional moment
$\Delta M_{t,\mu cr}$	Torsional moment increase in micro cracking
$\Delta\theta_{t,Mcr}$	Increment of torsional angle of rotation in macro cracking
$\Delta\theta_{t,syp}$	Increment of torsional anlge of rotation from steel yielding upto peak torsional moment
$\Delta\theta_{t,\mu cr}$	Increment in torsional angle of rotation in micro cracking

δ	Displacement
δ_{Lu}	Imposed end slip
ε_{fe}	Effective strain of FRP laminates
$\varepsilon_{fe,w}$	Effective strain of FRP laminates in transverse direction
$\varepsilon_{fu,w}$	Ultimate tensile strain of the FRP laminate
ε_{syl}	Yield strain of longitudinal steel
ε_{t}	Strain in stirrups
ε_{x}	Longitudinal strain of concrete
ε_{um}	Strain at tensile strength of steel reinforcement
ε_{ym}	Yield stress of steel reinforcement
η	Reduction factor
θ	Angle of compressive struts
$\theta_{t,cr}$	Angle at torsional cracking moment
$\theta_{t,syi}$	Angle of rotation at steel yielding
$\theta_{t,u}$	Torsional angle of rotation at ultimate moment
θ_{v}	Inclination of diagonal concrete compressive struts
λ	Modification factor
λ	Differential equation constant
ν	Poisson's ratio
ν	Strength reduction factor for cracked concrete in shear
ν	Shear strength of the RC section
ν_{c}	Shear strength contribution of concrete
ν_{s}	Shear strength contribution of steel
ν_{fw}	Shear strength contribution of FRP laminates
ρ_{fl}	Longitudinal FRP reinforcement ratio
ρ_{fw}	Transverse FRP reinforcement ratio
$\rho_{l,eq}$	Equivalent longitudinal reinforcement ratio
ρ_{sl}	Longitudinal steel reinforcement ratio
ρ_{sw}	Transverse steel reinforcement ratio
$\rho_{w,eq}$	Equivalent transverse reinforcement ratio
σ_{cp}	Pre-stress
τ	Bond stress
$\tau_{t,i}$	Torsional shear stress in wall "i"

ϕ	Stress reduction factor
ψ_{cr}	Angle of twist at cracking
ψ_{u}	Angle of twist at ultimate cracking

CHAPTER:

1. INTRODUCTION

The need for structural strengthening arises when a building, an element or the whole structure, no longer fulfils its intended purpose. This may be due to changes in existing standards or the need to implement new codes, changes in building usage (building conversions), increase in service loads, damage induced by earthquakes, poor construction quality or use of poor materials, and deterioration. According to the European Construction Industry Federation (2014), about 320bn euros were invested on rehabilitation and maintenance in 2013 and 342bn euros in 2017, thus showing the importance of this sector and demonstrating the large potential impact of research in the field.

The engineering community is always striving to improve current practice to preserve existing structures by using new materials, methods and technologies. The introduction of Fibre Reinforced Polymer (FRP) reinforcement in the construction industry is one of the latest advancements in the field and it has already enabled significant developments in strengthening and rehabilitation methods. Though several innovative solutions already exist to enhance the flexural and shear capacity of existing reinforced concrete (RC) elements, less attention has been paid to address torsional performance, which is critical in key structural elements of large structures and infrastructure.

1.1. RESEARCH SIGNIFICANCE

Thin walled reinforced concrete (RC) elements are extensively used as main structural elements in bridge construction and larger infrastructure. With a large proportion of the existing infrastructure in Europe and across the world now reaching their service life or requiring rehabilitation and strengthening, reliable and durable ways to increase their torsional capacity are required.

Fibre reinforced polymer (FRP) systems have proven to be a valid alternative to conventional materials, such as RC and steel plates and profiles, in strengthening applications and their use has resulted in the development of several innovative solutions. FRP offer superior corrosion resistance, higher stiffness & strength to weight ratio, and can be easily applied to existing structural elements as either externally bonded (EBR) or near surface mounted (NSM)

reinforcement. NSM FRP has been shown to offer improved performance over an equivalent EBR solution and promises excellent advantages for the torsional strengthening of thin walled tubular structures. However, no comprehensive research has been carried out to develop an efficient torsional strengthening solution for tubular type thin walled RC elements and the lack of refined design guidelines often results in conservative applications and inefficient use of materials. For example, a conservatively high amount of FRP (about 42 km of 'thick and thin' laminates) was used for the strengthening of Westgate bridge (2.58 km), in Australia, where lower FRP strain was considered for torsional design, resulting in higher cost of rehabilitation (Gosbell and Meggs 2002). More advanced design guidelines and efficient application strategies are therefore needed for the successful rehabilitation of torsionally-critical elements. The work presented in this thesis develops an innovative and efficient torsional strengthening solution using NSM CFRP laminates.

1.2. OBJECTIVES

This research study aims to gain a deep understanding of the torsional behaviour of thin walled tubular reinforced concrete structures and develop efficient strengthening solutions, as well as analysis and design methods. The main objectives can be summarised as follows:

- Carry out a thorough background investigation on available innovative strengthening methods for reinforced concrete members subjected to torsion;
- Perform a numerical finite element study to prepare and to examine the performance of different strengthening configurations for torsion and develop efficient and practical solutions using NSM CFRP for experimental tests;
- Examine experimentally the performance of different strengthening configurations using straight CFRP laminates and special L-CFRP laminates;
- Develop design guidelines for the torsional strengthening of RC members using NSM CFRP reinforcement;
- Develop an analytical model to predict the torsional moment carrying capacity of thin walled tubular reinforced concrete beams strengthened using NSM CFRP laminates.

1.3. OUTLINE OF THE THESIS

The current thesis is divided into six chapters. Chapter one serves as an introduction to the research work and summarises the research significance as well as the main aims and objectives. Chapter two presents a detailed review of the state of the art, including an overview

of traditional and innovative strengthening materials and techniques for reinforced concrete structures. Existing strengthening methods for flexure, shear and torsion are reviewed so as to examine and understand their benefits and limitations.

Chapter three presents a preliminary numerical finite element analysis, which was carried out in preparation for the experimental work. The chapter describes the strategy adopted for the numerical analysis and includes the validation of the proposed models, a parametric study to assess the performance of different strengthening schemes, and the final strengthening proposals based on the obtained results. The possibility of pre-stressing the NSM CFRP to further enhance the performance of the proposed strengthening method is also discussed and explored numerically.

Chapter four discusses the experimental work performed as part of this research study. Three series of beams were tested with different strengthening configurations, including four face strengthening, three face strengthening with straight CFRP laminates and four face strengthening with special L-laminate strengthening. The chapter presents a detail account of all tasks carried out for the preparation of the specimens, test setup and execution of the tests and summarises all results and conclusions.

Chapter five presents the proposed analytical model for thin walled tubular reinforced concrete structures to predict the torsional moment carrying capacity, compressive strut angle and effective strain prediction of CFRP laminates for different cases. A brief introduction of the available torsional mechanisms is also included. Finally, the main conclusions of this comprehensive study are presented in chapter six, along with some suggestions for future work.

CHAPTER:

2. STATE OF THE ART

The current chapter is subdivided into three parts: (i) primarily describing the torsional mechanisms (section 2.1) (ii) description of few available standard codes (2.2) (iii) review of traditional and innovative strengthening techniques, where the innovative strengthening techniques is sub divided into (a) externally bonded reinforcement (section 2.4.1) and (b) near surface mounted reinforcement (section 2.4.2).

Although limited in both number and scope, the latest research efforts on strengthening methods for thin walled tubular structures in torsion are reviewed in detail in this chapter, so as to inform the remainder of the work and assist with the development of a new strengthening methodology.

2.1. TORSIONAL MECHANISMS

The torsional resistance of reinforced concrete structures has been described through the implementations of two basic models: (i) the skew bending theory and (ii) the space truss analogy. In addition, torsional moments can be classified as: (i) primary or equilibrium torsion, where torque is necessary for equilibrium and (ii) secondary or compatibility torsion, which arises solely due to the relative rotation of neighbouring structural members. Secondary torsional moments can generally be neglected as long as sufficient transverse reinforcement is provided in the design. Further, some authors also categorize torsion into (i) circulatory torsion, which is resisted by a closed shear flow (thin walled tube analogy: used in space truss theory) and (ii) warping torsion (used in skew bending theory) caused by the presence of restraints along the longitudinal direction of an element. In the following sections the main concepts underlying the skew bending theory and the space truss analogy are briefly discussed.

2.1.1 SKEW BENDING THEORY

The skew bending theory was first proposed by Lessig in 1959 (Lessig. 1959). According to this theory, the behaviour of a reinforced concrete structure is governed by the development of a stress flow that can result into crushing of the concrete strut at three different locations depending on the geometry of the cross-section of the beam, amount and distribution of reinforcement, and the interaction of shear and bending and torsional moments (Figure 2.1).

Assuming a beam subjected to a bending moment resulting into compression stresses at the top of the cross-section, if failure takes place on the top face of the element, failure is classified as mode I failure. If failure takes place on the sides (vertical faces), this is categorized as mode II, while mode III is used to describe failure on the bottom face. In cases where the torsional moment to bending moment ratios are high, with similar longitudinal reinforcements in the top and bottom, the failure is governed by mode I. If the tensile reinforcement (bottom) is higher than in the top face of the beam, which is generally the case, the compression zone is formed in the bottom due to the yielding of the top longitudinal reinforcements, resulting in mode III failure. In cases where the shear loading is dominant, failure takes place on the right or left faces leading to mode II failure. The cracking is initiated on the face where torsion and shear are dominant, with cracks spiralling on three faces which is then intercepted on the fourth face forming a skew bending failure.

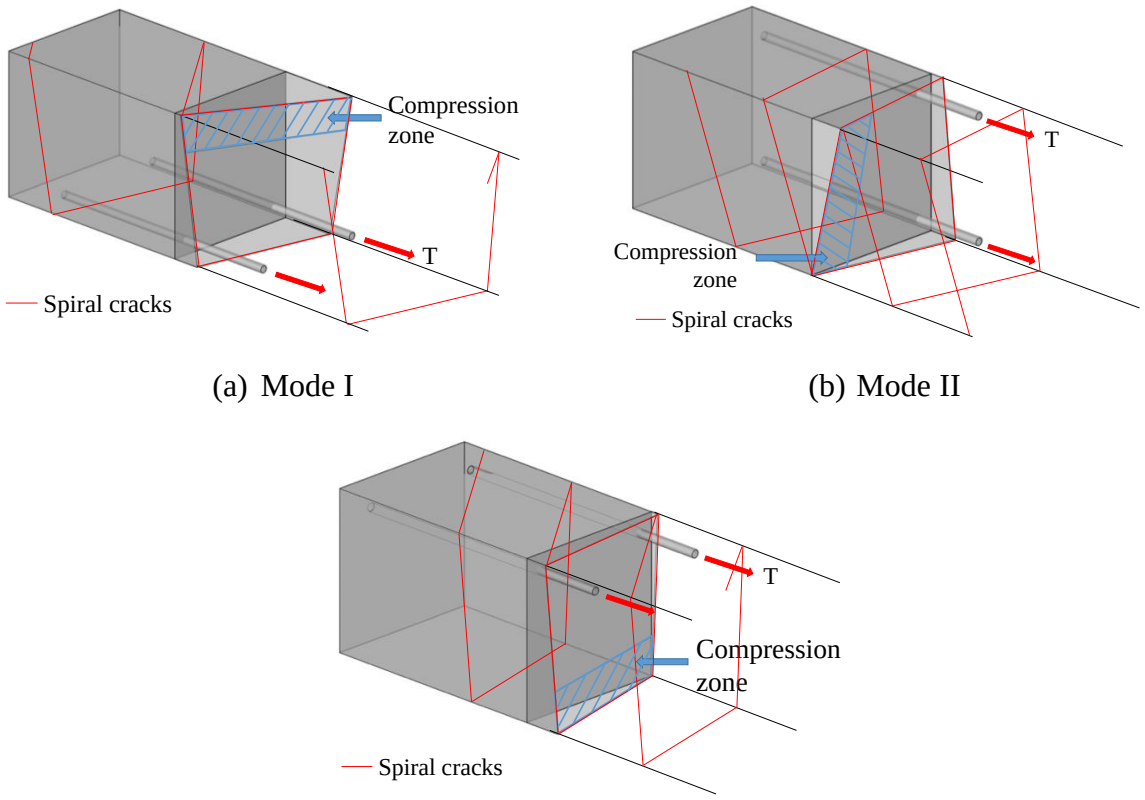

Figure 2.1 Different failure modes according to skew bending theory (i) Mode I, (ii) Mode II and (iii) Mode III

The torsional resistance in skew bending theory is assumed to be offered by axial force in the stirrups, shear-compression in concrete and dowel action of longitudinal bars as shown in Figure 2.2 (Csikós and Hegedûs 1998, Akhtaruzzaman (1990)).

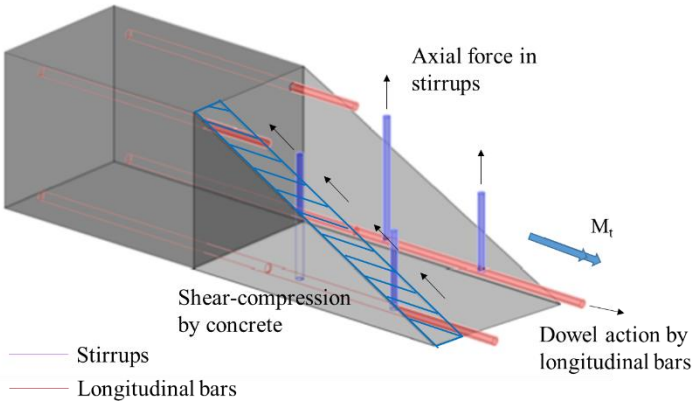

Figure 2.2 Torsional resistance by skew bending theory

2.1.2 SPACE TRUSS THEORY

The space truss theory was the first theoretical concept to be developed to determine the resistance of elements subjected to torsion. The concept was developed by Rausch (1929) in his PhD thesis, and then improved by many researchers like Anderson (1935), Cowan (1950), Hsu and Mo (1985), Hsu and Mo (1985b), MacGregor and Ghoneim (1995). The ACI 318 (2011), ModelCode (1990), Eurocode 2 (2004) and NTC-CNR (2018) implement the space truss theory for torsional design and torsional moment evaluation, albeit with some variations.

Rausch's (1938) theoretical approach is based on the elastic theory and idealises a reinforced concrete member as a space truss (Figure 2.3b). The torsional moment is assumed to be resisted by the closed shear flow (q) acting on the walls of the thin walled tube. This assumption was proven to be appropriate through a series of experimental tests that confirmed that hollow- and solid-section beams have similar torsional capacity (MacGregor and Ghoneim (1995)). As a result, solid beams can be considered as tubular thin-walled elements (Figure 2.3a). However, after cracking, the section is assumed to act as a space truss, with concrete in the centre having little to no contribution in resisting torsion. The transverse and longitudinal reinforcement act as tension chords, while the concrete between the cracks acts as diagonal struts inclined at 45 degrees to the longitudinal axis of the member. However, Rausch's (1938) theory was shown to significantly over estimate torsional capacity and modifications were introduced by

Anderson (1935) and Cowan (1950), mainly to account for the type of cross section (circular, square or rectangle) through a coefficient .

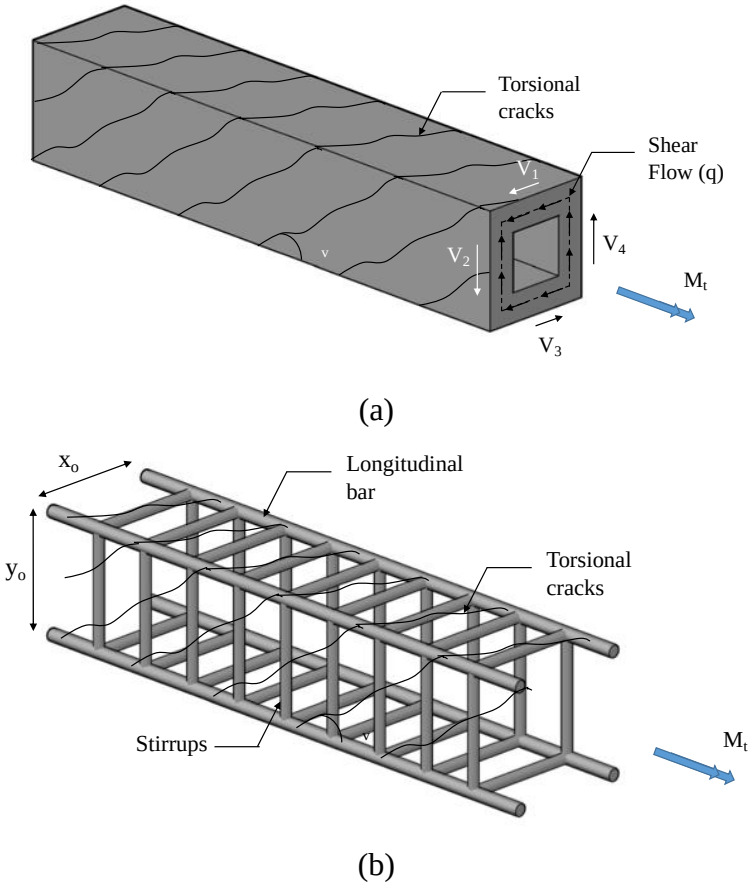

Figure 2.3 (a) Thin-walled tube analogy and (b) Space-truss analogy

A space truss model adopting a softened stress-strain model for the behaviour of concrete strut in pure torsion was presented by Hsu and Mo (1985, 1985b). This modified approach was capable to predict the torsional angle, strains in the reinforcements and strains in the concrete throughout the loading process. Based on this rather complex approach, simplified design models were also developed by the authors (Hsu and Mo (1985b)). The design provisions recommended by ACI 318 (2011) are based on the space truss model proposed by MacGregor and Ghoneim (1995). The details for calculating the contributions of the transverse and longitudinal reinforcement are presented in Chapter 5.

2.2. EXISTING STANDARDS ON TORSION

Different codes follow different theories to evaluate the torsional capacity of reinforced concrete (RC) beams, such as the truss model, space truss analogy, skew bending theory etc. Few codes include the contribution of concrete to resist the applied torsional moment, while the rest only account for the contribution of the longitudinal and transverse steel

reinforcements. A few standard codes are discussed in the following subsections giving a wider perspective and direction for the proposal of torsional strength prediction using NSM CFRP technique (Chapter 5). The symbols used in the following have been modified in some occasions in order to maintain uniformity throughout the thesis and to avoid ambiguity. The original terms used in the respective codes are also included in parenthesis for reference. All safety factors or load factors have been taken as equal to 1 to enable a more accurate comparison between the various design models.

2.2.1. EUROCODE 2 (2004)

EuroCode 2 (2004) follows the design procedure originally implemented in ModelCode (1990), where the torsional design is taken into consideration only for equilibrium conditions. The resistance of the section is calculated as that of a thin-walled closed section, where the closed shear flow satisfies the equilibrium as shown in Figure 2.4. The shear stress on a wall of a section is calculated using equation 2.1 and the shear force using equation 2.2. To evaluate the torsional cracking moment, the shear stress is replaced by the concrete tensile strength (f_{ctd}) in equation 2.1.

$$\tau_{t,i} t_{ef,i} = \frac{M_t}{2A_k} \qquad 2.1$$

$$V_{Ed,i} = \tau_{t,i} t_{ef,i} z_i \qquad 2.2$$

M_t = applied torsional moment (notation T_{Ed} is used in EuroCode 2); A_k = area enclosed by centre-lines of connecting walls; $\tau_{t,i}$ = torsional shear stress in wall "i"; $t_{ef,i} = \frac{A}{u}$ = effective wall thickness; A cross section with outer circumference including inner hollow area; u = perimeter/outer circumference of cross section; z_i = length of wall "i".

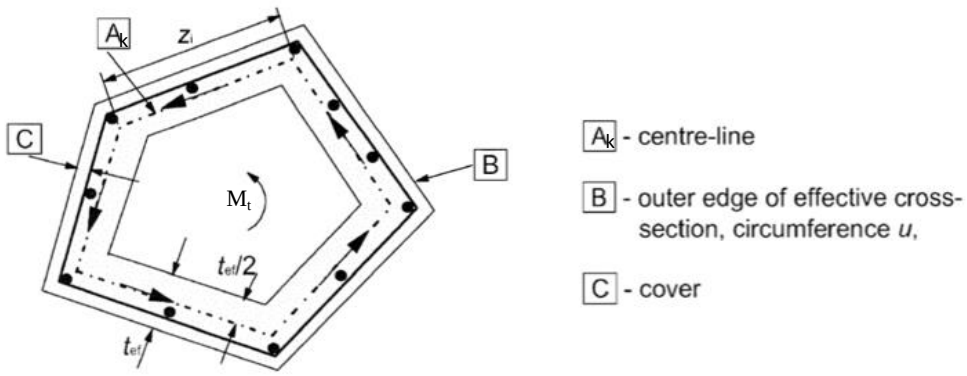

Figure 2.4 Notations and definitions according to EuroCode 2 (2004)

Even though the code does not specify an equation to estimate the required area of transverse reinforcement to resist torsion, equation 2.3 can be used, since the equation provides the necessary shear reinforcement with vertical reinforcement (stirrups). Where A_{sw} is the area of the steel shear reinforcement; s is the spacing of the reinforcement; f_{yd} is the yield strength of the shear reinforcement and z is the inner lever arm.

$$V_{Rd,s} = \frac{A_{sw}}{s} z f_{yd} \cot\theta \qquad 2.3$$

The longitudinal cross sectional area of steel reinforcement necessary to resist torsion is calculated using equation 2.4. In this equation $\sum A_{sl}$ is the area of longitudinal reinforcement in the cross section, f_{yd} is the design yield stress of longitudinal reinforcement; u_k is the perimeter of the cross section of area A_k; θ is the angle of compression strut and $M_{t,sl}$ is the torsional contribution by longitudinal reinforcement.

$$\frac{\sum A_{sl} f_{yd}}{u_k} = \frac{M_{t,sl}}{2A_k} \cot\theta \qquad 2.4$$

The maximum resistance of a reinforced concrete member subjected to torsion and shear is limited by the capacity of the concrete struts, calculated using equation 2.5, while the strength envelop is defined by the equation 2.6.

$$M_{t,Rd,\max} = 2\nu\alpha_{cw} f_{cd} A_k t_{ef,i} \sin\theta\cos\theta \qquad 2.5$$

$$\frac{M_t}{M_{t,Rd,\max}} + \frac{V_{Ed}}{V_{Rd,\max}} \leq 1.0 \qquad 2.6$$

Where $M_{t,Rd,\max}$ is the design torsional resistance (notation $T_{Rd,\max}$ is used in the code), ν is strength reduction factor for cracked concrete in shear, $\nu = 0.6\left[1 - \frac{f_{ck}}{250}\right]$, f_{ck} is the charateristic compressive strength of the cylinder, α_{cw} is the coefficient taking into account the state of the stress in the compression chord (taken as "1" for non-prestressed structures), f_{cd} is the design compressive strength, V_{Ed} is the design transverse force and $V_{Rd,\max}$ is the maximum design shear resistance calculated according to 2.11. (For more details the reader is referred to section 6.2 and 6.3 in EuroCode 2 (2004)).

$$V_{Rd,\max} = \frac{\alpha_{cw} b_w z \nu f_{cd}}{(\cot\theta + \tan\theta)} \qquad 2.7$$

2.2.2. NTC-CNR (2018): ITALIAN CODE

The Italian code NTC-CNR (2018) follows the space truss analogy as EuroCode 2 (2004). However, in this case the contribution of concrete, longitudinal steel reinforcement and transverse steel reinforcement are calculated separately, and the minimum value of the three terms is taken as the torsional resistance of the section, as shown in equation 2.8.

$$M_t = \min(M_{t,Rd}, M_{t,s}, M_{t,sl}) \qquad 2.8$$

Where $M_{t,Rd}$ is the design resistance of concrete for torsion (notation T_{Rcd} is used in code NTC-CNR), $M_{t,s}$ is the design resistance of transverse steel reinforcement (T_{Rsd}), and $M_{t,sl}$ is the design resistance of longitudinal steel reinforcement (T_{Rld}). The design resistance of the concrete is calculated using equation 2.9.

$$M_{t,Rd} = \frac{2At_{ef,i} f'_{cd} \cot\theta}{\left(1 + \cot^2\theta\right)} \qquad 2.9$$

Where $t_{ef,i}$ is the thickness of hollow section calculated as described in section 2.2.1. The design resistance of the transverse steel reinforcement is calculated by equation 2.10, while the design resistance of the longitudinal reinforcement is computed using equation 2.11. In these last two equations, A_{sw} is the area of transverse steel reinforcement (A_s used in code); s is the spacing of the transverse reinforcement; f_{yd} is the design yield stress; θ is the angle of the compressive struts, $\sum A_{sl}$ is the overall area of longitudinal reinforcement; and u_m perimeter of the resistant core.

$$M_{t,s} = 2A \frac{A_{sw}}{s} f_{yd} ctg\theta \qquad 2.10$$

$$M_{t,sl} = 2A \frac{\sum A_{sl}}{u_m} \frac{f_{yd}}{ctg\theta} \qquad 2.11$$

The maximum resistance of the section is limited by the concrete, similar to equation 2.5 of EuroCode 2 (2004).

2.2.3. ACI 318 (2011): AMERICAN CONCRETE INSTITUTE

The torsional design according to ACI 318 (2011) is based on thin-walled tube, space truss analogy. In this theory, the torsional resistance is assumed to be provided by the outer portion of the cross section (solid hatch shown in Figure 2.5). Both the solid and thin-walled sections are idealised as thin-walled tubes for design as shown in Figure 2.5. In case of solid sections, the thickness of wall is calculated as $\left(0.75A/u\right)$. Once the reinforced concrete cracks, the resistance is assumed to be provided by closed stirrups and longitudinal bars near the surface.

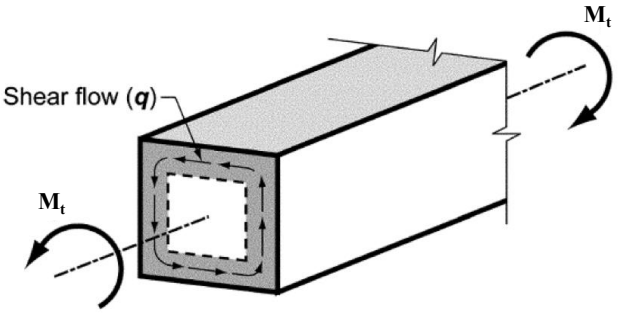

Figure 2.5 Thin-walled tube according to ACI 318 (2011)

The design for torsion is considered only if the applied torsional moment exceeds the threshold torsion, calculated according to equation 2.12 for non-prestressed reinforced concrete members.

$$\phi 0.083\lambda\sqrt{f_c^{'}}\left(\frac{A^2}{u}\right) \qquad 2.12$$

where ϕ is the stress reduction factor; λ is the modification factor; $f_c^{'}$ is the concrete compressive strength ; A is the area enclosed by outside perimeter of concrete cross section (notation A_{cp} is used in the code), u is the outside perimeter of concrete cross section (notation p_{cp} is used in the code). The torsional cracking moment $(M_{t,cr})$ is calculated according to equation 2.13.

$$M_{t,cr} = 0.33\lambda\sqrt{f_c^{'}}\left(\frac{A^2}{u}\right) \qquad 2.13$$

The nominal torsional strength $M_{t,s}$ (notation T_n is used in the ACI 318 code) for the element is calculated using equation 2.14, where A_o is the gross area enclosed by shear flow path; A_t is the area of closed stirrup resisting torsion (area of one leg) with spacing ' s '; f_{yt} is the yield strength of transverse reinforcement; θ is the compression diagonal angle; p_h is the perimeter

of closed stirrups and f_y is the yield strength of longitudinal reinforcement. The area of longitudinal reinforcement (A_l) to resist torsion is given by equation 2.15.

$$M_{t,s} = \frac{2A_o A_t f_{yt}}{s}\cot\theta \qquad 2.14$$

$$A_l = \frac{A_t}{s} p_h \left(\frac{f_{yt}}{f_y}\right)\cot^2\theta \qquad 2.15$$

2.2.4. DR_AS-3600 (2017): AUSTRALIAN CODE

The Australian code for concrete structures follows the ACI 318 (2011) with some modifications. It includes the application of modified compressive field theory (MCFT) to calculate k_v and θ_v, using general and simplified approaches. The MCFT is used to determine the shear force contribution of concrete, shown from equation 2.16 to 2.19, according to the general method.

$$V_u = k_v b_v d_v \sqrt{f_c'} \qquad 2.16$$

$$k_v = \left[\frac{0.4}{1+1500\varepsilon_x}\right]\left[\frac{1300}{1000+k_{gd}d_v}\right] \qquad 2.17$$

$$k_{gd} = \frac{32}{\left(16+d_g\right)} \qquad 2.18$$

$$\theta_v = \left(29+7000\varepsilon_x\right) \qquad 2.19$$

Where θ_v is the angle of inclination of the concrete compressive struts to the longitudinal axis of the member; ε_x is the longitudinal strain in concrete; d_g is the maximum nominal aggregate size; b_v is the effective web width and d_v is the effective shear depth. In the case of combined shear and torsion, the longitudinal strain (ε_x) of concrete is evaluated according to equation 2.20 or equation 2.21, where the longitudinal strain is dependent on the bending moment, shear force, torsion and prestressing force. The code also specifies the longitudinal strain evaluation for the case of only shear. The reader is referred to DR_AS-3600 (2017) for more details regarding, minimum torsional reinforcement, spacing of the reinforcements and detailing of the torsional reinforcement.

$$\varepsilon_x = \frac{\left| \frac{M^*}{d_v} + \sqrt{\left(V^* - P_v\right)^2 + \left[\frac{0.9T^* u_h}{2A_0}\right]^2} \right| + 0.5N^* - A_{pt} f_{po}}{2(E_s A_{sl} + E_p A_{pt})} \leq 3.0 \times 10^{-3} \qquad 2.20$$

Where M^* is the design bending moment, V^* is design shear force, P_v is the vertical component of the prestressing force, T^* is the torsional moment, u_h is the perimeter of center-line of closed transverse torsion reinforcement, A_o is the area enclosed by shear flow path including hollow area, N^* is the axial compressive or tensile force, A_{pt} is the cross sectional area of prestressing tendons, E_s is the modulus of elasticity of steel reinforcement, A_{sl} is the cross sectional area of the longitudinal reinforcement, E_p is the modulus of elasticity of the pre-stressing tendons, and E_c is the modulus of elasticity of concrete. If the longitudinal strain calculated from above equation is less than zero, it is assumed zero or recalculated according to the following equation 2.21. The values of k_v and θ_v are determined using a value of ε_x, however the strain should not exceed 3×10^{-3}.

$$\varepsilon_x = \frac{\left| \frac{M^*}{d_v} + \sqrt{\left(V^* - P_v\right)^2 + \left[\frac{0.9T^* u_h}{2A_0}\right]^2} \right| + 0.5N^* - A_{pt} f_{po}}{2(E_s A_{sl} + E_p A_{pt} + E_c A_{ct})} \qquad 2.21$$

Within limits $0.2\times10^{-3} \leq \varepsilon_x \leq 0$

The algorithm to evaluate the shear force according to the current code is as follows:

1. Assume value of ε_x
2. Calculate k_{dg} using equation 2.18
3. Evaluate k_v and θ_v using equations 2.17 and 2.19
4. Calculate value of ε_x using equation 2.20 or 2.21 (depending on the condition)
5. The difference of ε_x in step 4 and step 1 is evaluated. If the difference is less than the assumed tolerance level, the value of ε_x is used to calculate the shear force according to equation 2.16. If not the value of ε_x obtained in step 4 is assumed as new ε_x in step 2 and the calculations are repeated. The iterations are continued until the assumed tolerance level is reached.

The torsional cracking moment $(M_{t,cr})$ is calculated using equation 2.22, where A is the total area enclosed by outside perimeter of concrete section (A_{cp}); u is the length of the outside perimeter of concrete cross-section (notation p_c used in the code); σ_{cp} is the prestress, if any.

$$M_{t,cr} = 0.33\sqrt{f_c^{'}}\frac{A^2}{u}\sqrt{1+\frac{\sigma_{cp}}{0.33\sqrt{f_c^{'}}}} \qquad 2.22$$

The torsional resistance $(M_{t,s})$ is calculated using equation 2.23, in which the capacity is determined by the amount of transverse reinforcement. In equation 2.23, $A_o = 0.85A_{oh}$, where A_{oh} is the area enclosed by centre-line of exterior closed transverse torsion reinforcement, including hollow area, f_y = yield strength of transverse reinforcement (used as $f_{sy.f}$ in the code).

$$M_{t,s} = 2A_o\frac{A_{sw}f_y}{s}\cot\theta_v \qquad 2.23$$

The summary of all the above referred codes are tabulated in Table 2.1. As seen, the codes define torsional cracking moment, torsional moment limited by concrete crushing, contribution of transverse steel and longitudinal steel with the respective theories.

Table 2.1 Summary of equations according to existing codes

Codes	Torsional cracking moment	Maximum resistance limited by concrete compressive strut failure	Contribution of transverse bars	Contribution of longitudinal bars
EuroCode 2 (2004)	$M_{t,cr} = 2A_k f_{ctd} t_{ef,i}$	$M_{t,Rd,\max} = 2\nu\alpha_{cw} f_{cd} A_k t_{ef,i} \sin\theta\cos\theta$	-	$M_{t,sl} = \frac{\sum A_{sl} f_{yd}}{u_k} \frac{2A_k}{\cot\theta}$
NTC-CNR (2018)	-	$M_{t,Rd} = \frac{2Atf_{cd}^{'} ctg\theta}{\left(1+ctg^2\theta\right)}$	$M_{t,s} = 2A\frac{A_{sw}}{s} f_{yd} ctg\theta$	$M_{t,sl} = 2A\frac{\sum A_l}{u_m} \frac{f_{yd}}{ctg\theta}$
ACI 318 (2011)	$M_{t,cr} = 0.33\sqrt{f_c^{'}}\left(\frac{A^2}{u}\right)$	-	$M_{t,s} = \frac{2A_o A_t f_{yt}}{s}\cot\theta$	$A_l = \frac{A_t}{s} p_h \left(\frac{f_{yt}}{f_y}\right)\cot^2\theta$
DR_AS-3600 (2017)	$M_{t,cr} = 0.33\sqrt{f_c^{'}}\frac{A^2}{u}\sqrt{1+\frac{s_{cp}}{0.33\sqrt{f_c^{'}}}}$	-	$M_{t,s} = 2A_o \frac{A_{sw} f_y}{s}\cot\theta_v$	-

2.3. TRADITIONAL STRENGTHENING TECHNIQUES

Traditional strengthening methods involve two types of materials, i.e. concrete and steel. The different techniques under this category involve (i) member enlargement, (ii) span shortening, (iii) stress reduction, (iv) post tensioning, (v) applying shotcrete, (vi) external plate bonding, (vii) steel encasement, etc. (Emmons et al. 1998, Rodriguez & Park 1991, Schladitz & Curbach 2009, Alkhrdaji & Thomas 2002).

In member enlargement, an additional layer of concrete, with thickness usually in the range of few centimetres, is applied over existing concrete. New steel reinforcement bars can also be sometime added to the new concrete layer. Before enlarging the structure, the surface of the existing concrete needs to be treated in order to have proper bonding between the new and the old concrete for assuring a monolithic behaviour (Figure 2.6). This method results in increased stiffness, size and self-weight of the structure. Member enlargement can be performed using the shotcrete method, which involves spraying concrete at high velocity on the surface to be repaired/strengthened. Usually a layer of reinforcement bars or mesh wires are provided for additional strength. Shotcrete develops a better bond with the original surface than conventionally cast concrete (Beaupré 1999).

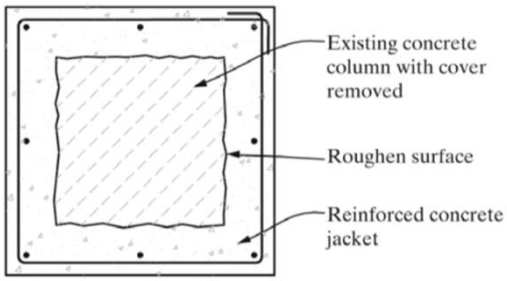

Figure 2.6 Member enlargement

Post-tensioning is a widely used method to reduce excessive deflections and to increase load carrying capacity of structures. It is very effective in increasing both flexural and shear capacity, since the strengthening material, i.e. the prestressed steel, is already active at the time of application. Tension is applied to the strengthening material, which is anchored in the exterior of the strengthening element. The anchoring system is usually covered by concrete, shotcrete or other materials to increase the effectiveness of the system, as well as to avoid possible problems due to vandalism and corrosion.

Steel plate bonding is a relatively simple method of providing additional stiffness and load carrying capacity to the structure. A steel plate of specified thickness is attached to the external surface of the member using epoxy as bonding adhesive. Adequate bond between the plate and the original surface is key in transferring the stresses from the member to the steel plate. One of the major drawbacks of this strengthening technique is the difficulty of handling the steel plates due to their high self-weight, which restrict the plates to be of smaller length, thus requiring the use of multiple lengths. In addition, exposure of the steel plates to harsh environments can compromise the long-term performance of the strengthening application.

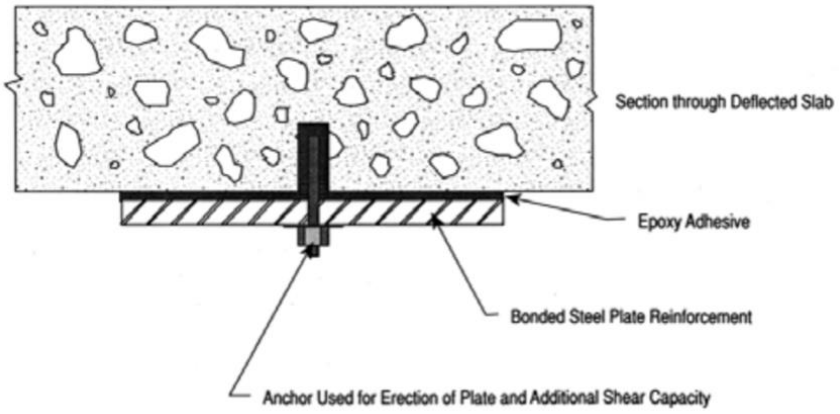

Figure 2.7 Bonded steel plates (Emmons et al. 1998)

In span shortening, additional supports, generally made of concrete and/or steel, are introduced along the existing spans, thus reducing the overall effective span and reducing the magnitude of internal stresses. However, this method can result in limited clear spacing between the supports, as well as clear height when additional beams are introduced between the supports.

2.4. INNOVATIVE STRENGTHENING TECHNIQUES

Innovative materials and solutions have been developed over the last few decades to overcome some of the drawbacks of traditional strengthening methods, such as increase in self-weight, complex preparation of the substrate, undesired changes to dimensions and clear distances, additional protection and maintenance of the strengthening systems from environmental conditions. Innovative strengthening systems involve the use of novel materials such as fibre reinforced polymers (FRP) made of carbon, glass, aramid or basalt fibres immersed in a polymeric matrix. Strengthening with FRP can be carried out adopting two main techniques (i) externally bonding the reinforcement (EBR) to the original structure; or (ii) installing the FRP

reinforcement in small grooves executed in the concrete cover (near surface mounted - NSM). These techniques are discussed in turn in the following sections.

2.4.1. EXTERNALLY BONDED REINFORCEMENT

In this technique, the fibre reinforced polymers are applied on the surface of the element to be strengthened in the form of sheets, which are impregnated with resin via the wet-layup method, or pre-cured laminates. In both cases, the substrate needs to be prepared prior to application of the FRP.

The different steps involved in the procedure using the wet-layup method are as follows:

i. Application of a layer of putty;
ii. Application of first saturate layer (adhesive);
iii. Installation of the FRP sheet;
iv. Application of a second saturate layer;
v. Impregnation of the FRP sheet and removal of excess resin by passing a roller on the FRP;
vi. Application of a protective topcoat.

Similarly, the application of FRP laminates using the pre-cured system is as follows

i. Application of a layer of putty (optional);
ii. Application of adhesive to the FRP laminates;
iii. Bonding of the FRP laminate to the concrete surface;
iv. Removal of excessive adhesive and trapped air by pressing the laminate with a roller.

Limited research has been carried out on the torsional strengthening of concrete structures using the EBR method. The available experimental and numerical research studies are presented in the following:

Panchacharam and Abdeldjelil (2002) performed experimental and numerical investigation on pure torsional behaviour of reinforced concrete beams, strengthened with glass fibre reinforced polymer composites. Eight beams, including a reference specimen, were tested to study the effect of different parameters, such as: number of plies; fibre orientation; number of sides of strengthening; and addition of U-wrap anchors. The cross-sectional dimensions of the beams were 279.4 mm × 279.4 mm. The specimens were reinforced with four 12.7 mm and

four 9.53 mm diameter steel bars in the longitudinal direction, and 9.53 mm diameter steel shear links in the transverse direction spaced at 152.4 mm in the central section and 38.1 mm spacing at the extremities. The total length of each tested beam was 3.96 m.

The reinforcement details and the experimental test setup are shown in Figure 2.8. Load was applied at one end, and the reaction end was allowed to rotate freely. The reaction end was supported on rollers to accommodate the longitudinal elongation.

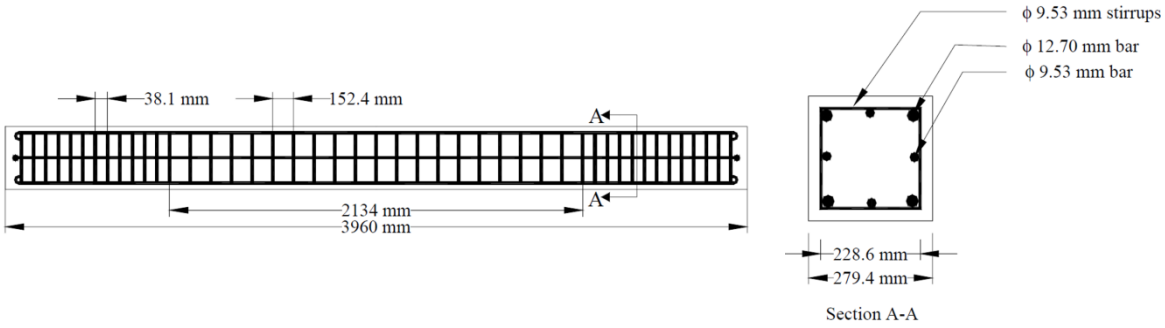

(a)

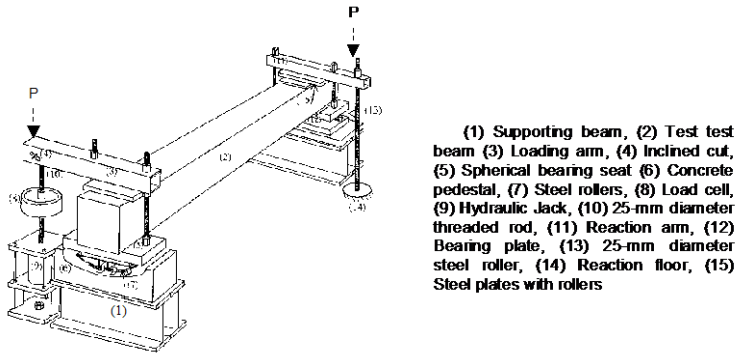

(b)

Figure 2.8 (a) Reinforcement and beam details (b) Experimental setup, Panchacharam and Abdeldjelil (2002)

As shown in Figure 2.9, the different types of strengthening methods involved: continuous wrapping with fibres oriented at 90-degree (4 sides); discrete strips with fibres oriented at 90-degree (4 sides); continuous U-wrapping (3 sides); continuous U-wrapping with anchors (3 sides); continuous wrapping with fibres at 0-degree (4 sides); continuous U-wrapping with fibres at 0-degree (3 sides); continuous wrapping with fibres at 0-degree together with strips with fibres at 90-degree (4 sides). The properties of the concrete and steel reinforcement are shown in Table 2.2. The GFRP had a design tensile strength of 1,520 MPa and an elastic modulus of 72 GPa.

Table 2.2 Mechanical properties of reinforcement and concrete, Panchacharam and Abdeldjelil (2002)

Batch	Steel reinforcement				Concrete
	9.53 mm diameter bars		12.7 mm diameter bars		
	f_y (MPa)	f_u (MPa)	f_y (MPa)	f_u (MPa)	f_c (MPa)
A	420	700	460	700	34
B	450	620	320	510	26
C	450	620	320	510	31

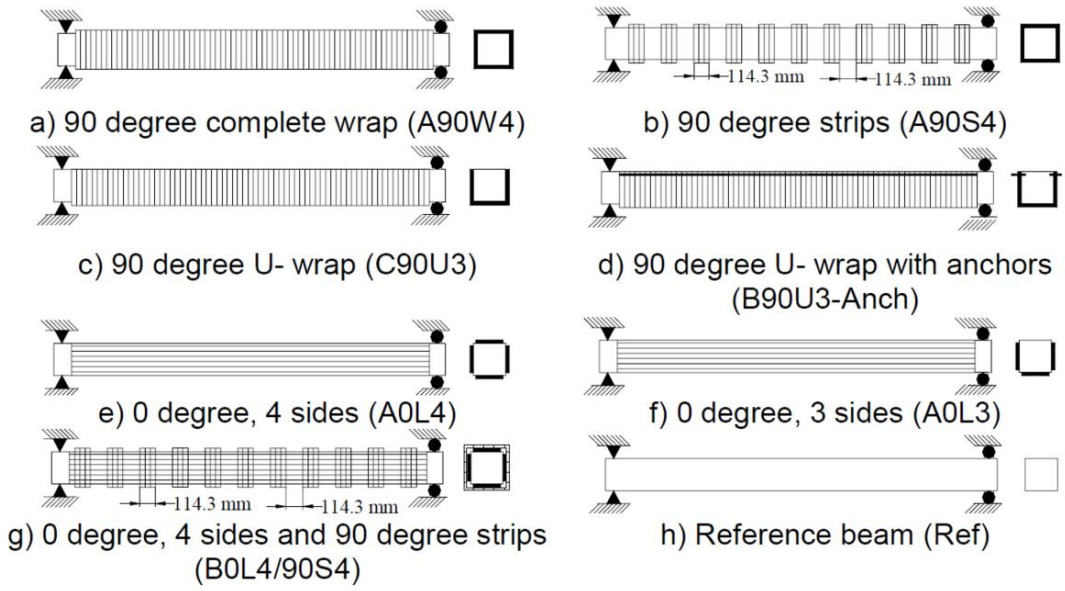

Figure 2.9 Different types of strengthening, Panchacharam and Abdeldjelil (2002)

Figure 2.10, shows the torque-twist behaviour of the reference and strengthened beams. The cracking strength of the beams was increased when 0-degree orientated fibres were used for strengthening. The energy absorption capacity and ductility of the beams strengthened with 0-degree fibres were also better than for those strengthened with 90-degree orientated fibres. The use of 90-degree oriented fibres, however, provided better confinement and resulted in an increase in ultimate strength. Continuous wrapping provided higher ultimate strength and post cracking stiffness in comparison with strip strengthening. The use of a three-side strengthening and four-side strengthening schemes with FRP sheets in the longitudinal direction led to an almost similar increase in ultimate and cracking strength. In case of continuous wrapping and U-wrapping, the beams with continuous wrapping had much better ultimate strength (149% increase with respect to reference beam) than U-wrapping with (39%) or without anchors (35%). The beam with longitudinal and transverse reinforcement provided the best

strengthening with respect to all other strengthening methods. In terms of failure modes, the following modes were observed: FRP rupture in beam A90W4; tearing off of the GFRP sheet along the fibre direction in beam A0L4; premature failure (peeling of GFRP sheets) in C90U3; crushing of concrete and lateral separation of anchor bars with GFRP sheets in beam B900U3-Anch.

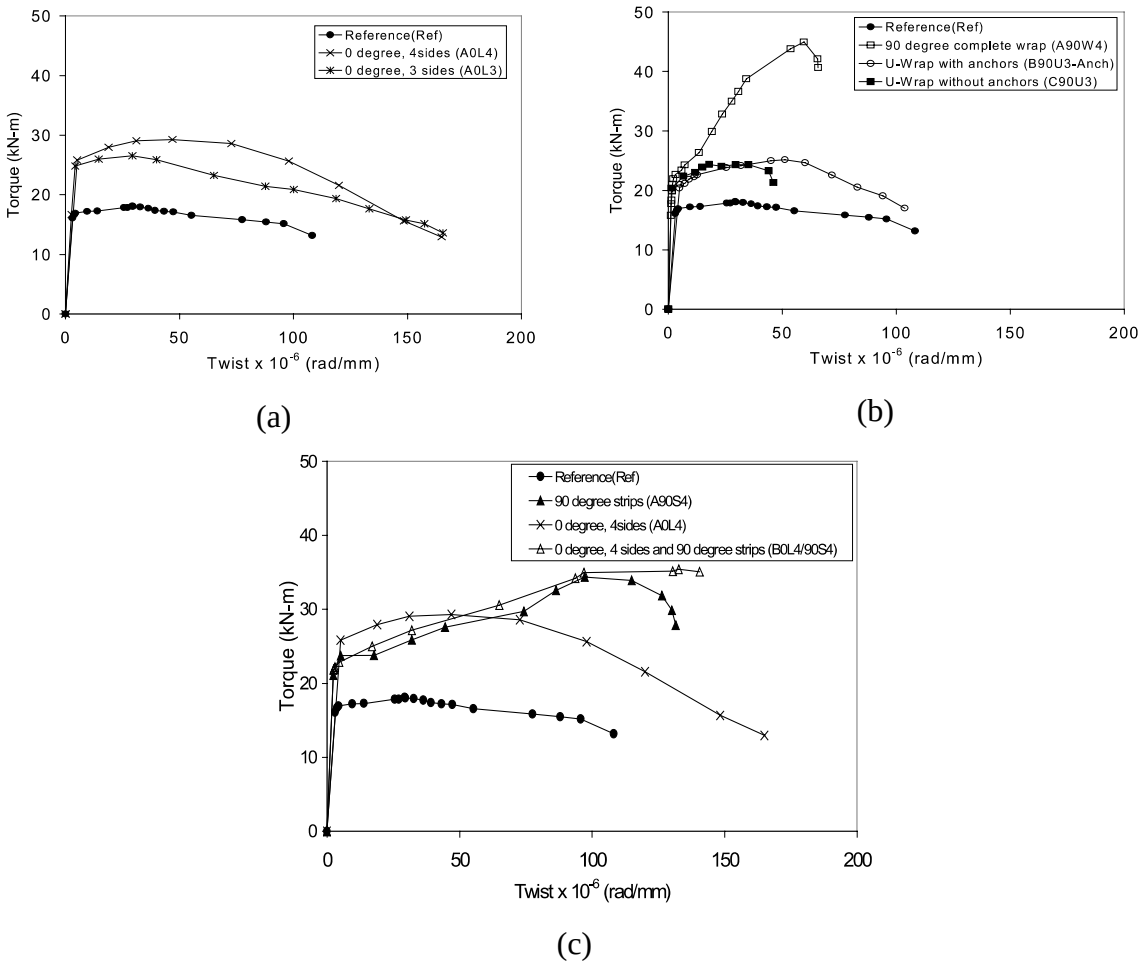

Figure 2.10 Torque-twist results (a) Based on number of strengthened sides, (b) Complete wrap and U-wrap beams & (c) Strengthening on both sides, Panchacharam and Abdeldjelil (2002)

The authors performed analytical calculations to verify the experimental results by considering, the strengthened reinforced concrete beams as subjected to a prestress action. The FRP resistance for the tensile stresses and strain variation on the surface of the beam was considered as applying a passive prestressing force along the direction of the fibres. The results of the experimental and numerical model are shown in Table 2.3. The values of cracking and ultimate torsional moment predicted by the proposed analytical design equations are very close to the experimental results.

Table 2.3 Experimental and numerical results, Panchacharam and Abdeldjelil (2002)

Test Beams	Cracking torque (kN·m)			Ultimate torque (kN·m)		
	Exp.	Ana.	Exp./Ana.	Exp.	Ana.	Exp./Ana.
Reference	17.1	15.7	1.09	18.2	16.9	1.07
A90W4	22.9	20.8	1.10	47.1	45.4	1.04
A90S4	22.1	17.7	1.25	36.0	36.4	0.99
A0L4	27.0	29.9	0.90	30.7	29.9	1.03
A0L3	26.3	28.8	0.91	27.8	28.8	0.97
B0L4/90S4	20.1	24.4	0.82	32.6	35.9	0.91
B90U3-Anch	22.0	18.2	1.20	26.3	28.1	0.94
C90U3	20.6	19.1	1.08	24.6	26.4	0.93
Mean			1.04			0.98

Deifalla and Ghobarah (2005) carried out analytical modelling using a simplified model for strengthening reinforced concrete beams subjected to torsion. The proposed model was compared with the results obtained according to the FIB design procedure (FIB 2001), and validated against experimental data. The developed analytical model takes into account various parameters such as number of FRP layers, spacing of the FRP strips, use of anchors, different types of strengthening technique, thickness of each FRP layer, orientation of FRP and the non-uniform distribution of the FRP strain along the crack. The model provides good accuracy and reliable predictions when compared to the available literature. A brief summary of the proposed model is given below.

The total torsional resistance (T) of a RC beam (equation 2.3) is the summation of the steel reinforcement contribution (T_s) and FRP contribution (T_f) calculated using equation 2.24 and equation 2.25, respectively.

$$T_s = \frac{2A_o f_y A_t \left[\cot(\beta_s) + \cot(\theta)\right]\sin(\beta_s)}{s_s} \qquad 2.24$$

$$T_f = \frac{2A_{of} E_f \varepsilon_f A_f \left[\cot(\beta) + \cot(\theta)\right]\sin(\beta)}{s_f} \qquad 2.25$$

$$T = T_s + T_f \qquad 2.26$$

Where A_o is the area enclosed inside the centreline of the shear flow path, f_y is the yield stress of the reinforcement, A_t is the area of the reinforcement resisting torsion, θ is the angle of inclination of the principal cracks, β_s is the angle of inclination of the steel reinforcement, A_{of} is the area enclosed inside the critical shear flow path due to the strengthening, E_f is Young's modulus of the FRP sheets, ε_f is the effective average FRP strain, β_f is the angle of orientation of the fibre direction to the longitudinal axis of the beam, s_f is the spacing between the centreline of the FRP strips and A_f is the effective area of the FRP resisting torsion, calculated according to equation 2.27, where n_f is the number of FRP layers and w_f is the width of FRP strip.

$$A_f = n_f t_f w_f \qquad 2.27$$

A limit on the shear stress transfer through the bond joint between the FRP and the concrete is introduced in the model. The effective FRP strain for the failure due to debonding of FRP is taken as the minimum of equation 2.28 and equation 2.29, limited by concrete fracture and bond slip.

$$\varepsilon_f = \min \begin{cases} \dfrac{0.33}{L_e}\dfrac{w}{s_f} & 2.28 \\ \dfrac{0.02\alpha_f}{L_e} & 2.29 \end{cases}$$

$$L_e = \sqrt{\frac{E_f t_f}{\sqrt{f_c}}} \qquad 2.30$$

$$\alpha_f = \sqrt{\frac{\left(2 - \dfrac{w_f}{s_f \sin\beta_s}\right)}{\left(1 + \dfrac{w_f}{s_f \sin\beta_s}\right)}} \qquad 2.31$$

Where L_e is the effective bond length, w_f is the width of FRP, s_f is the spacing of the strips, α_f is a constant to take into account the difference in stress between the continuous and strip FRP's. The effective strain in case of FRP rupture is calculated using equation 2.32.

$$\varepsilon_f = 0.1\left(E_{fu}\rho_{ft}\right)^{-0.86} \qquad 2.32$$

$$\rho_{ft} = \frac{A_f}{t_c s_f} \qquad 2.33$$

E_{fu} is the modulus of ealsticity at ultimate, ρ_{ft} is the reinforcement ratio of the FRP and t_c is the thickness of the eequivalent hollow tube section.

FIB procedure:

According to the FIB design procedure (FIB 2001) the torsional capacity of a RC beam for complete wrapping and U-wrapping is calculated using equation 2.34 and equation 2.35, respectively. The effective strain for CFRP and GFRP is calculated using equations 2.36 and 2.37.

$$T_f = \frac{2E_f \varepsilon_f t_f w_f bh \cot\theta}{s_f} \qquad 2.34$$

$$T_f = \frac{E_f \varepsilon_f t_f w_f bh \cot\theta}{s_f} \qquad 2.35$$

$$\varepsilon_f = 0.17\left(\frac{f_{cm}^{2/3}}{E_{fu}\rho_f}\right)^{0.30} \varepsilon_{fu} \qquad 2.36$$

$$\varepsilon_f = 0.048\left(\frac{f_{cm}^{2/3}}{E_{fu}\rho_f}\right)^{0.47} \varepsilon_{fu} \qquad 2.37$$

where E_f is the modulus of elasticity of FRP, t_f is the thickness of the FRP, b and h are respectively the width and depth of concrete beam's cross section, w_f is the width of FRP, s_f is the spacing of the strips, θ is the angle of inclination of the diagonal cracks to the longitudinal axis of the beam.

Table 2.4 presents the results of comparison, between FIB (2001) and the developed analytical model (Deifalla and Ghobarah (2005)). As seen, the proposed analytical model has good prediction with respect to the experimental results than the FIB formulations with standard deviation of 23.09% with coefficient of variation of 21.15% of the presented results.

Table 2.4 Comparison of results, Deifalla and Ghobarah (2005)

Beam	FRP		Measured	FIB (2001)	Proposed
	w_f (mm)	s_f (mm)	T_f (kN·m)	Calculated/ measured	Calculated/ measured
A90W4	Continuous		27.00	0.039	0.740
A90S4	114.3	228.6	16.00	0.045	1.133
C90U3	Continuous		6.00	0.170	1.384
B90U2-anchor	Continuous		7.00	0.14	1.135
B0L4/90S4	114.3	228.6	17.00	0.039	1.067

Hii and Al-Mahaidi (2006) investigated experimentally, as well as numerically, the torsional strengthening of solid reinforced concrete (RC) beams and box-section RC beams using CFRP laminates. The investigation involved six beams with one solid reference beam (CS1), one solid strengthened beam (FS050D2), one box-section as reference beam (CH1) and three strengthened box-section beams (FH075D1, FH050D1 and FH050D2). Beams FS050D2 represents solid beam with CFRP strip spacing at 0.50D and two layers of CFRP, FH075D1 represents hollow beam with one layer of 0.75D strip spacing, FH050D1 and FH050D2 consists of hollow beams with one and two layers of CFRP strip spacing at 0.50D, D presenting the full depth of the beam.

Each beam had a cross section of 500 mm × 350 mm each, with a total length of 2500 mm. The cross sectional and reinforcement details of the beams are shown in Figure 2.11. The reinforcements consist of 12 bars of 10 mm in the longitudinal direction and 6 mm diameter bars as stirrups. The stirrups were placed at 125 mm in the testing region. The strengthening consisted of applying CFRP strips placed at 0.50D and 0.75D. The number of layers of CFRP was also varied.

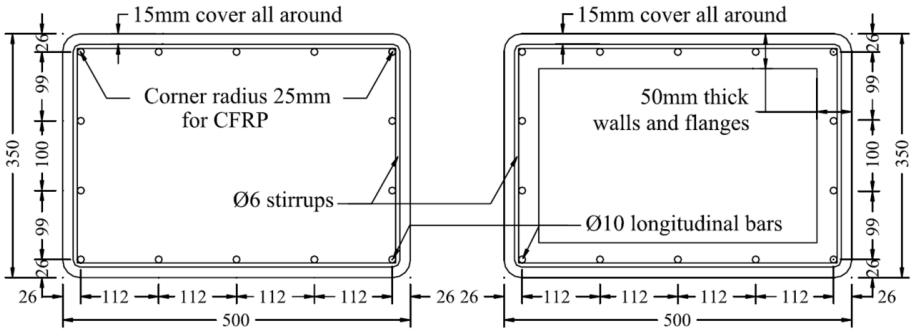

Figure 2.11 Cross sectional details of (a) Solid beam (b) Box-section beam (dimensions in mm), Hii and Al-Mahaidi (2006)

The concrete compressive strength varied from 48.9 MPa to 56.4 MPa. The modulus of elasticity of the CFRP strips was 240 GPa and the fabric had a thickness of 0.176 mm. The steel reinforcement properties are shown in Table 2.5.

Table 2.5 Reinforcement details, Hii and Al-Mahaidi (2006)

Reinforcement properties	Stirrups, 6 mm diameter bars	Longitudinal, 10 mm diameter bars
Area, A_s (mm^2)	28.27	78.54
Young's modulus, E_s (MPa)	213444	207046
Yield strength, f_y (MPa)	426.50	398.2
Poisson's ratio, ν	0.30	0.3

The experimental set up of the box-section beam is shown in Figure 2.12, where one end of the beam is fixed to a steel collar restricting longitudinal and transverse (horizontal and vertical) movements and rotations. The other end was allowed to rotate freely, and to elongate or shorten on a spherical seat. A steel lever arm was fixed to apply the load at this end.

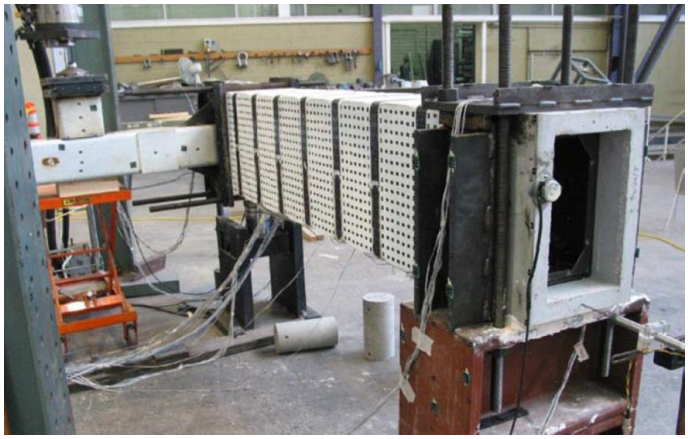

Figure 2.12 Experimental set up, Hii and Al-Mahaidi (2006)

The experimental results in terms of torque-twist relationships are shown in Figure 2.13. The solid beams have higher cracking and ultimate strength than the box-section beam. The strengthened solid beams had 8% and 49% increase in cracking and ultimate strength, whereas the box-section beams had 40% and 78% increment, respectively. The CFRP strips reduced the crack propagation and widening. The damage initiated by the rupture of the CFRP in the corner of the beams, followed by peeling of a thin layer of concrete underneath. The strain distribution between and across the strip varied widely. According to the authors, this large variation was due to the non-ductility of the CFRP composites and torsional cracking action.

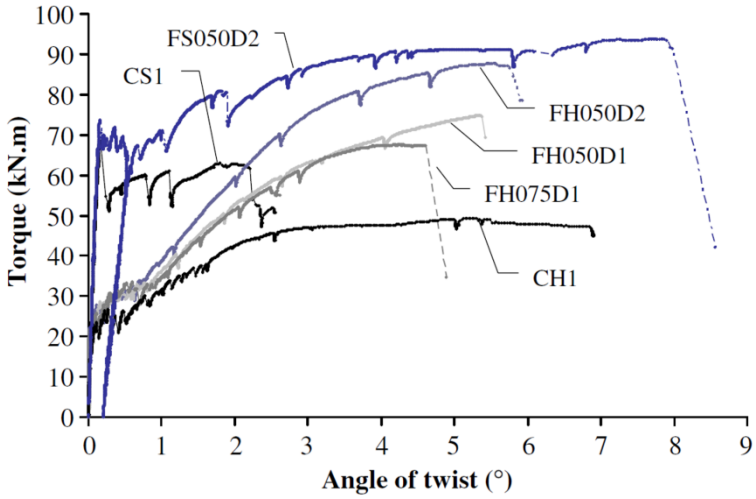

Figure 2.13 Torque - twist curves, Hii and Al-Mahaidi (2006)

Jing et al. (2007) conducted an experimental investigation on the torsional strengthening of reinforced concrete box beams using carbon fibre reinforced polymers. Four beams were tested: (i) three strengthened using CFS (Carbon fibre reinforced polymer sheet) and (ii) a reference beam without strengthening. The main parameters studied in this experimental

program were the amount of CFS and different type of wrapping schemes under combined bending, shear and cyclic torques.

The test setup, geometry and the reinforcement details of the beam are shown in Figure 2.14. Each beam has a cross section of 600 mm × 400 mm, with a wall thickness of 50 mm. The total length of the beam was 3400 mm. The longitudinal reinforcement consisted of three 20 mm diameter bars at the bottom and three 12 mm diameter bars ($f_y = 310MPa$) at the top. Bars of 6.5 mm diameter ($f_y = 210MPa$) were used for the transverse reinforcement spaced at 100 mm centre to centre in the central region (2300 mm). In the initial 200 mm and final 900 mm regions, the stirrups were spaced at 50 mm.

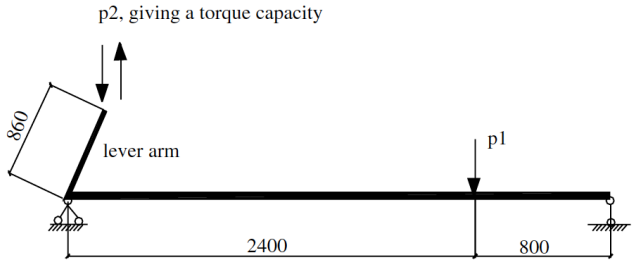

Fig. 2. Schematic of test setup.

(a)

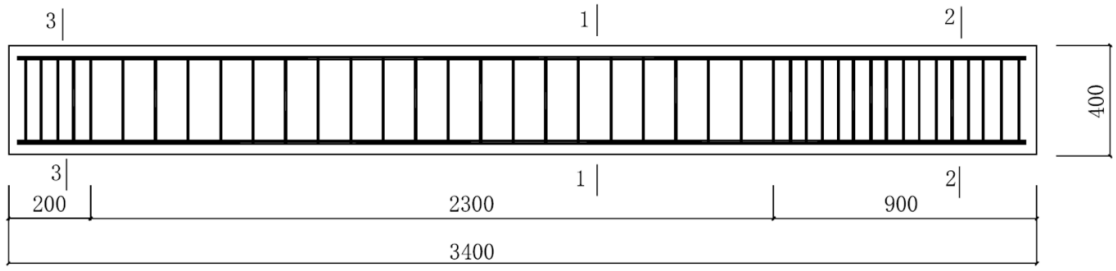

(b)

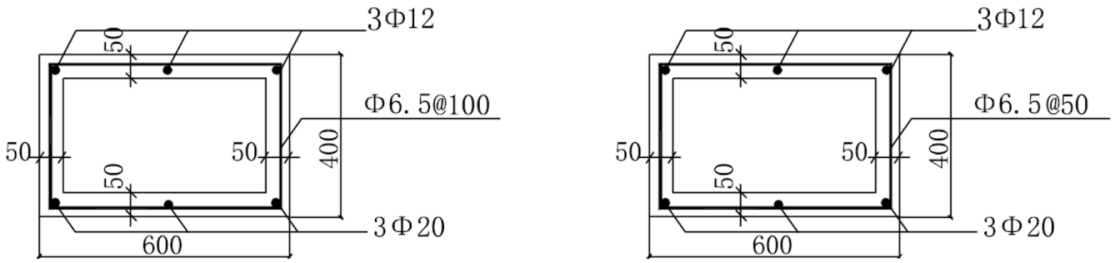

(c) (d)

Figure 2.14 (a) Test setup (b) Longitudinal section (c) & (d) Cross section at 1-1 & 2-2 (dimensions in mm), Jing et al. (2007)

The tensile strength of one ply, which was 0.111 mm thick, was 4100 MPa and its modulus of elasticity was 233 GPa. The concrete compressive strength was assessed to be 40 MPa. Specimen B5 was the reference beam, while the rest of the beams were strengthened with 100 mm wide carbon fibre strips in transverse direction with spacing of 200 mm with an anchorage length (overlapping) of 150 mm on the top surface. It was also strengthened with 150 mm wide carbon fibre strips in the longitudinal direction on the bottom face with 250 mm spacing. In addition to these: beam B6 was wrapped with one layer of CFRP in the transverse direction; beam B7 was wrapped with one layer of CFRP in both transverse and longitudinal direction; and beam B8 was wrapped with 2 layers of CFRP in the transverse direction and one layer of CFRP in the longitudinal direction.

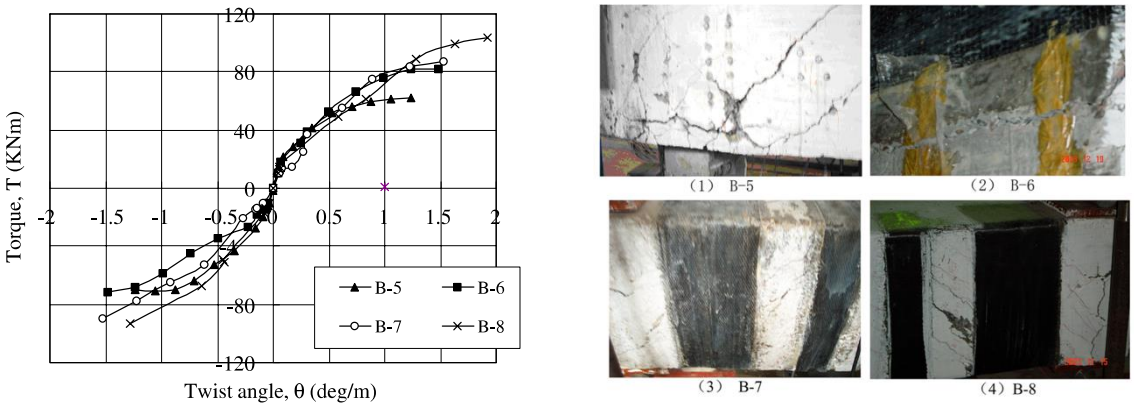

(a) (b)

Figure 2.15 (a) Results of torque - twist angle and (b) Failure patterns, Jing et al. (2007)

The results with the values of maximum crack torque, crack twist angle, yielding torque and yield twisting angle are shown in Table 2.6, while the torque-angle of twist is shown in Figure 2.15. The strengthened beams had cracks more evenly distributed with small width and developed more slowly. The deformation capacity improved with the amount of CFS, and the transversal CFS strips had a greater retrofitting effect than the longitudinal CFS on the bottom surface of the beam. All four beams developed a bending torsional failure pattern, with netlike cracks formed on the beam surfaces after yielding.

Table 2.6 Results of the experimental program, Jing et al. (2007)

Specimen	Crack torque (kN·m)	Crack twist angle (deg./m)	Yielding torque (kN·m)	Yielding twist angle (deg./m)	Ultimate torque (kN·m)	Ultimate twist angle (deg./m)
B5	12.01	0.084	42.14	0.308	62.36	1.23
					-71.05	-1.23
B6	14.31	0.079	43.89	0.494	82.21	1.48
					-71.52	-1.48
B7	14.00	0.076	52.27	0.510	86.82	1.53
					-89.40	-1.53
B8	14.95	0.074	51.69	0.640	103.99	1.92
					-93.18	-1.92

The application of CFS increased the torsional capacity and deformation capacity of the beam. A higher number of layers provided more torsional resistance, which also resulted in decreased ductility.

Al-Mahaidi & Hii (2007) analysed experimentally and numerically the bond behaviour of CFRP reinforcement for torsional strengthening of solid and box-section RC beams. This paper is an extension of Hii and Al-Mahaidi (2006) where six beams were tested, with two solid sections and four box-sections. The strengthening schemes examined in this study included different number of CFRP strips and spacing of the strips. The cross-sectional details are shown in Figure 2.11 and the experimental set up in Figure 2.12. The material properties of concrete, steel reinforcements and FRP are as already described in Hii and Al-Mahaidi (2006).

The main focus of this study was to measure the slip behaviour and the strain development of the CFRP reinforcement. Photogrammetry was used to determine the slip between concrete and FRP material. Before cracking, the slip was in the negligible range. As the cracks initiated, significant slip was observed and propagated from the crack location. The bond-slip development of the critical CFRP strip with torque is shown in Figure 2.16. An average slip of 0.05 mm is defined as the initiation of macro-debonding.

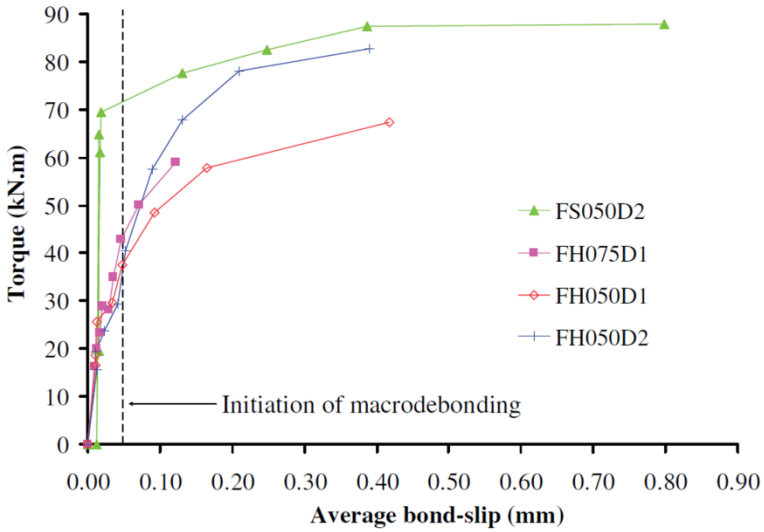

Figure 2.16 Average bond - slip with torque, Al-Mahaidi & Hii (2007)

The strain development in the CFRP were registered through strain gauge measurements and photogrammetry. The average strains were very small in the pre-cracking stage. At higher loads the strain measurements increased with the formation of torsional cracks, which proves that part of the load was carried by the CFRP strips. The strain variation along the beam depth is shown in Figure 2.17. Numerical simulations were performed in the finite element programme DIANA version 8.1. A bond-slip model between the CFRP and the concrete was implemented in the analysis, while concrete cracking was based on a smeared crack approach and the yielding of the reinforcement by Von Mises yield criterion with strain hardening. The bond-slip model adopted for the analysis was derived from shear lap tests by Pham and Al-Mahaidi (2005). The numerical results are in good agreement with the experimental results. Similar failure modes of the experiments were also observed in the numerical analysis, with crack propagation at higher loads followed by debonding of the CFRP strips.

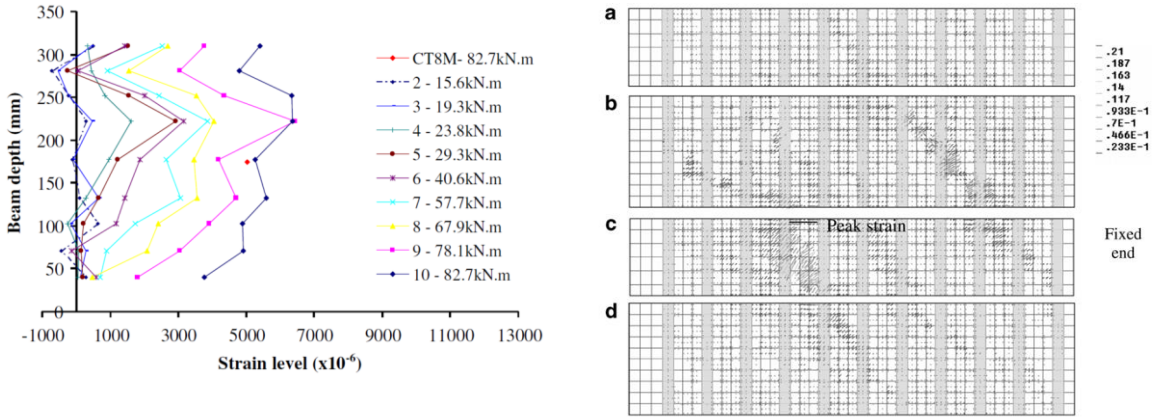

Figure 2.17 (a) Strain variation of CFRP along the depth of the beam and (b) Vector plots of tensile strains for fully open cracks (FH050D2-Bslip), Al-Mahaidi & Hii (2007)

Chalioris (2007) developed a model for simulating the behaviour of FRP strengthened reinforced concrete beams in torsion. In order to validate the developed model, an experimental program was also performed. The experimental study involved testing 12 reinforced concrete beams with and without strengthening, including four reference beams and 8 beams strengthened with different type of strengthening systems along with different steel reinforcements ratios (with and without stirrups). The cross sections of the beams were 200 mm × 100 mm and 300 mm × 150 mm, while their span measured 1000 mm. The details of the tests are shown in Figure 2.18. The CFRP used in this study had an elastic modulus of 230 GPa, an ultimate tensile strength of 3900 MPa and an elongation at failure of 15 mm/m.

Beams Ra, Rb, RaS and RbS are control beams with and without stirrups. Beam Ra-FC(1) is strengthened with one layer of CFRP sheet and beam Ra-FC(2) with two layers for a length of 1000 m. Beam Ra-FS150(2) with two layers of FRP at 150 mm spacing for a width of 150 mm. Beam Rb-FC(1) is similar to Ra-FC(1), beam Rb-FS200(1) is with 200 mm strips at 200 mm spacing, Rb-FS300(1) is with 300 mm strips at 300 mm spacing. Beam RaS-FS150(2) is strengthened with CFRP sheets with two layers spaced at 150 mm with 150 mm wide strips. Beam RbS-FS200(1) is with single layer of FRP sheets of 200 mm width spaced at 200 mm.

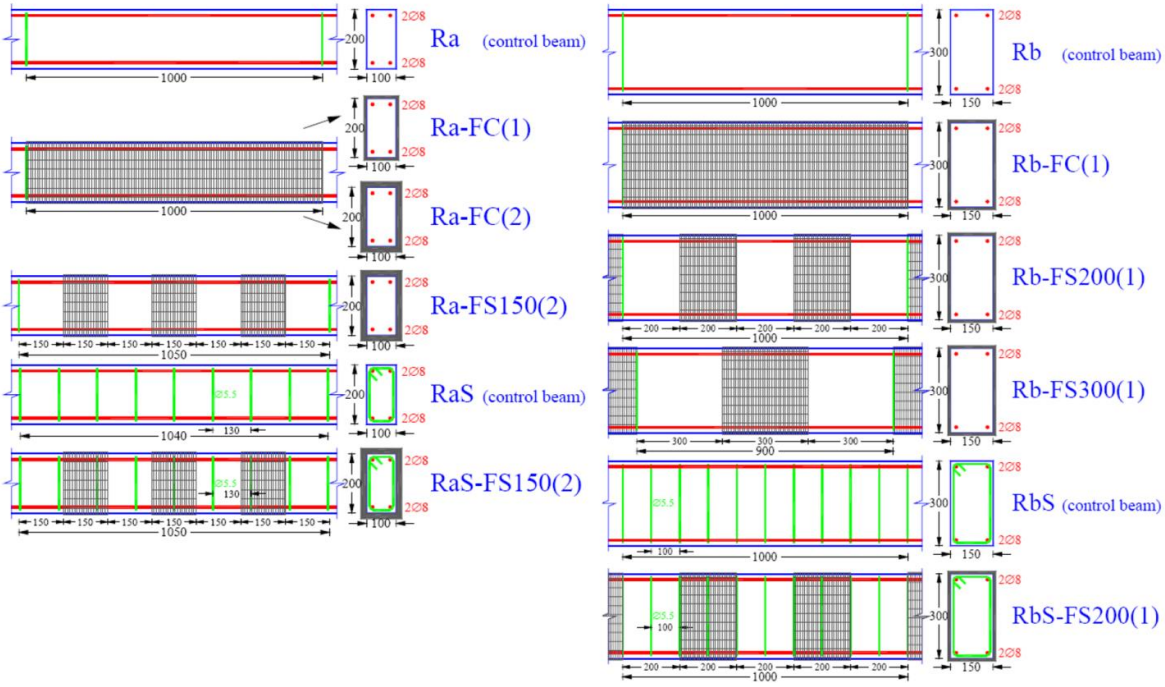

Figure 2.18 Geometry and reinforcement arrangement of the tested beams, Chalioris (2007)

The analytical model was developed by combining two well established theories of torsional behaviour of (a) Plain concrete members ((Karayannis 2000), (Karayannis and Chalioris 2000))

and (b) Reinforced concrete members ((T. C. Hsu and Mo 1985), (T. C. Hsu and Mo 1985)). These methodologies were extended to involve the effect of FRP materials on the torsional behaviour as externally bonded reinforcement. To calculate the post-elastic torsional behaviour and the ultimate torque strength, the basic equations and considerations of softened truss model was adopted and modified to include the contribution of FRP materials. The results of the experimental and numerical analyses is shown in Figure 2.19.

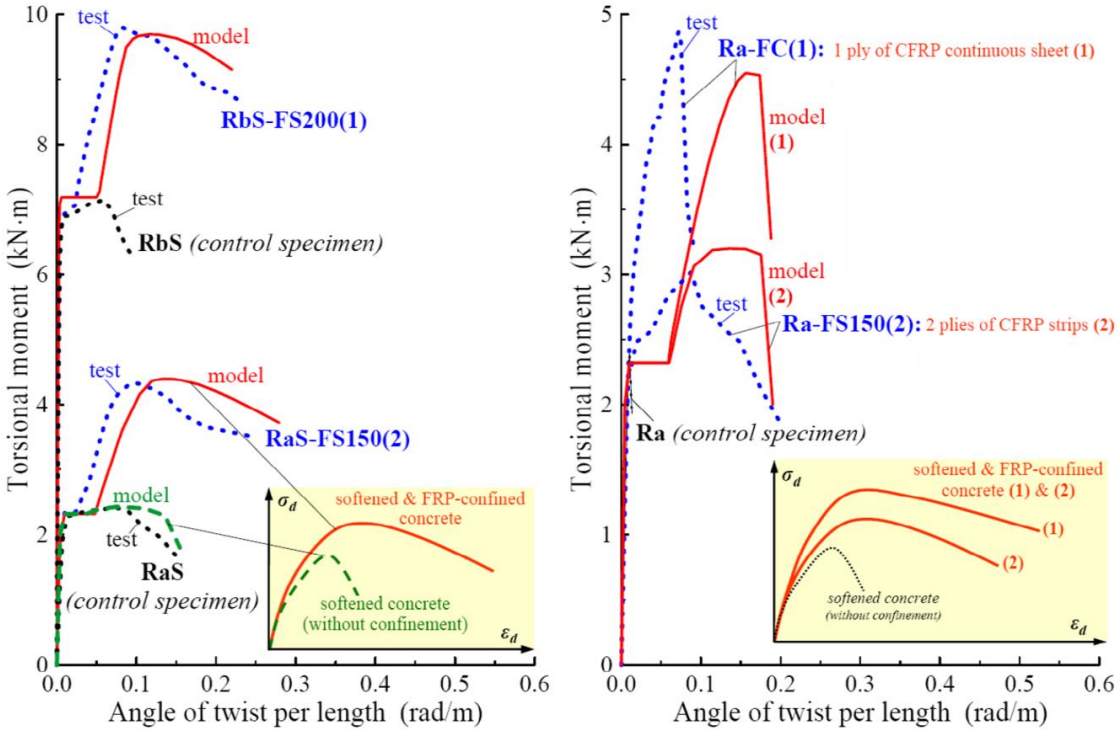

Figure 2.19 Experimental and analytical comparison (a) Beams with stirrups (b) Beams without stirrups, Chalioris (2007)

The developed analytical model predicted well the experimental results. The cracking load (T_{cr}) and ultimate load (T_u) of each beam are shown in Table 2.7.

Table 2.7 Analytical and experimental results, Chalioris (2007)

Beam	$T_{cr,\exp}$	$T_{cr,cal}$	$\frac{T_{cr,\exp}}{T_{cr,cal}}$	$T_{u,\exp}$	$T_{u,cal}$	$\frac{T_{u,\exp}}{T_{u,cal}}$
Ra-FC(1)	2.80	2.32	1.21	4.87	4.55	1.07
Ra-FC(2)	2.83	2.32	1.22	6.65	5.54	1.20

Ra-FS150(2)	2.22	2.32	0.96	3.02	3.20	0.94
RaS-FS150(2)	2.35	2.32	1.01	4.33	4.40	0.98
Rb-FC(1)	8.79	7.19	1.22	10.05	10.49	0.96
Rb-FS200(1)	6.73	7.19	0.94	9.32	8.84	1.05
Rb-FS300(1)	6.96	7.19	0.97	7.52	8.84	0.85
RcS-FS200(1)	6.93	7.19	0.96	9.80	9.69	1.01

Chalioris (2008) studied experimentally torsional strengthening of rectangular and flanged beams using carbon fibre reinforced polymers. The main objective was to evaluate the use of epoxy bonded CFRP as external transverse reinforcement on under-reinforced RC beams in torsion. A total of 14 beams were tested including some control beams. The testing involved 3 categories of beams: Ra, Rb and T. Ra comprised 200 mm × 100 mm cross sectioned beams, Rb 300 mm × 150 mm beams, while T specimens were T-section beams. The cross-sectional and the reinforcement details, and the strengthening techniques of each category of beams are shown in Figure 2.20. The numbers in the parentheses of the beam designation indicate the FRP strengthening layers applied on each beam.

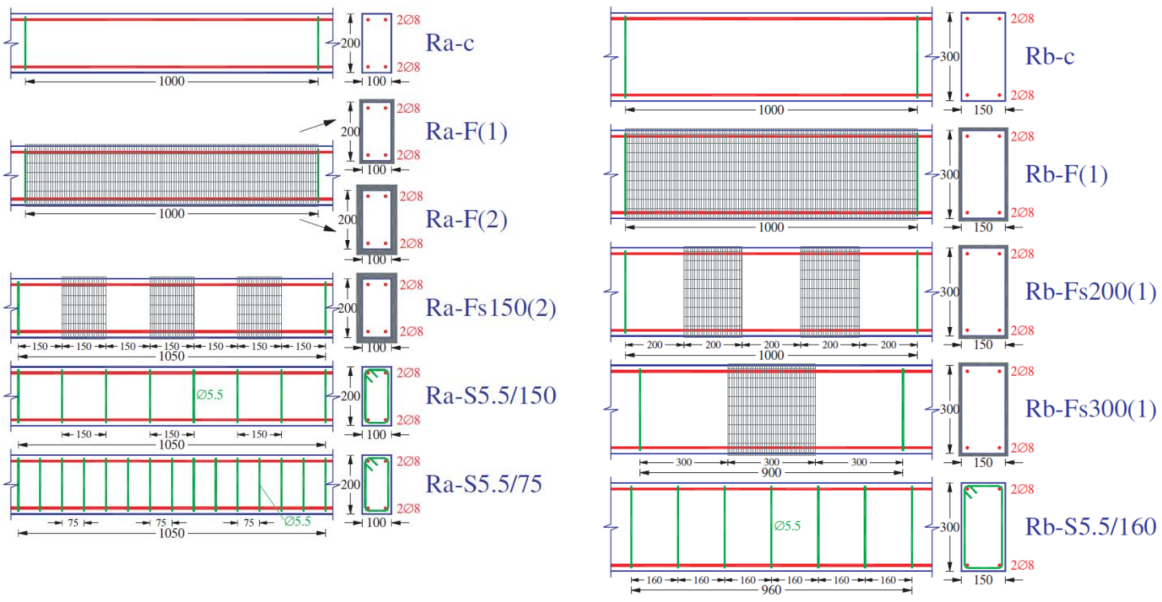

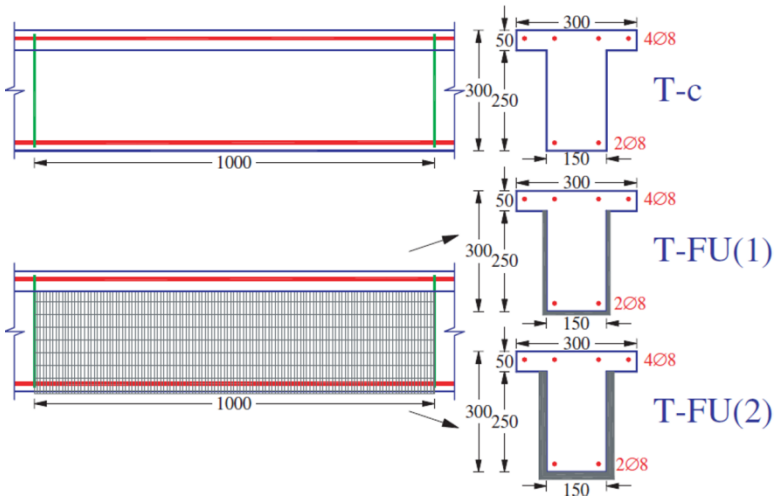

Figure 2.20 Geometry, cross section, reinforcement and strengthening details of all the beams, Chalioris (2008) (dimensions in mm)

The compressive strength and tensile strength of concrete was evaluated to be 27.5 MPa and 2.8 MPa, respectively. The yield strength of the steel longitudinal reinforcing bars were 560 MPa and in the case of transverse bars was 350 MPa. The FRP strips had a modulus of elasticity of 230 GPa, a tensile strength of 3900 MPa, an elongation at failure of 1.5 mm/m, and a thickness of 0.11 mm. The torque vs. angle of twist curves for all the tested beams are shown in Figure 2.21.

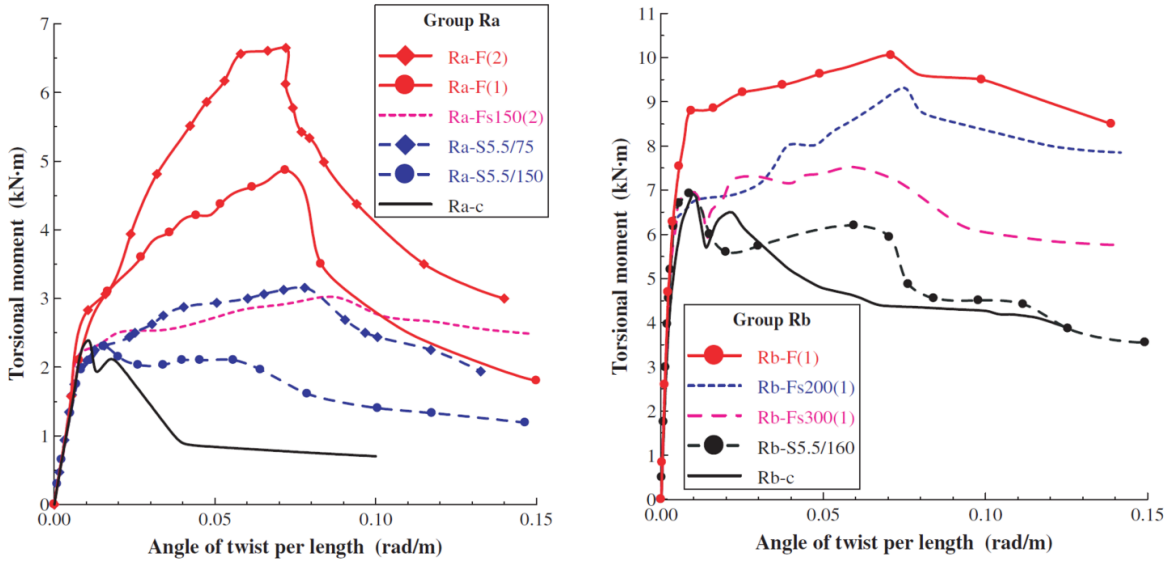

(a) (b)

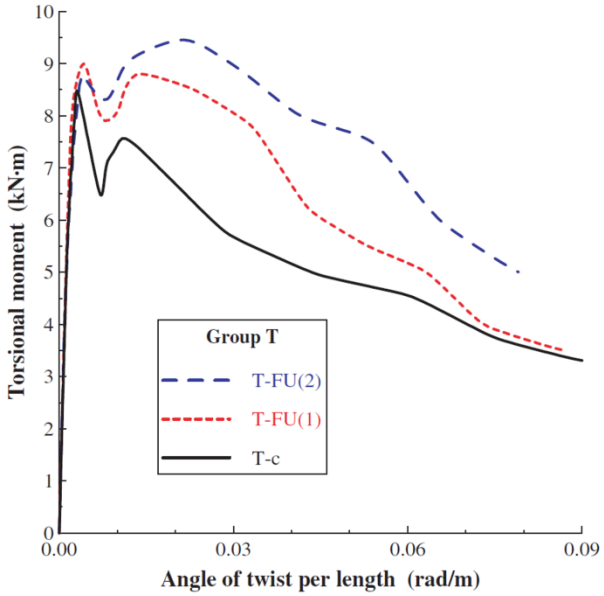

(c)

Figure 2.21 Torque - Angle of twist for all the beams (a) Ra (b) Rb & (c) T,Chalioris (2008)

Except Ra-S5.5/150, Rb-S5.5/160 and T-FU (1) all other configurations showed significant improvement in the post cracking behaviour along with the torsional capacity of the beams. Fully wrapped beams had higher torsional capacity than the beams strengthened with strips. The width and spacing of the FRP strips influenced the torsional capacity of the strengthened beams. U-jacketed beams had premature debonding failure at the concrete and FRP sheet adhesive interface. All the beams strengthened with FRP composites resulted in higher torsional capacity and higher angle of rotation with respect to the reference beams.

A Deifalla & Ghobarah (2010) investigated experimentally the behaviour of RC T-beams subjected to combined torsion and shear and strengthened using CFRP. Six half-scale beams were tested with two reference beams and four strengthened beams with different types. The beams were strengthened under two categories considering torque to shear ratios of 0.5 and 0.1. The experimental setup, geometry and reinforcement details of the beams are shown in Figure 2.22. Each beam had a total length of 3400 mm. For more details on the loading configuration the reader is referred to A Deifalla & Ghobarah (2010).

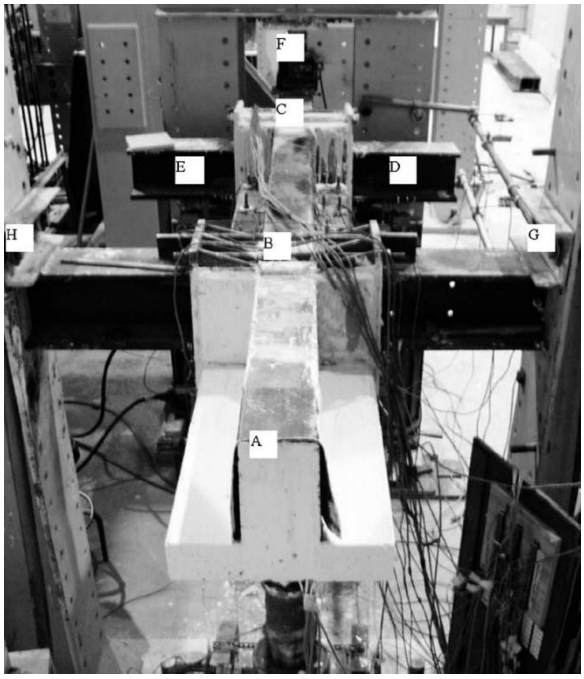

(a)

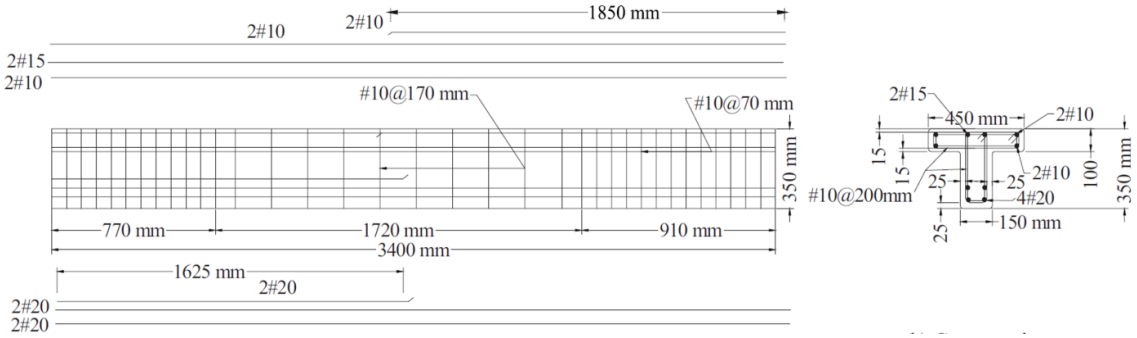

(b)

Figure 2.22 (a) Experimental set up (b) Longitudinal and cross section reinforcement details, A Deifalla & Ghobarah (2010)

The concrete had a compressive strength of 25.6 MPa, the average yield stress of the longitudinal reinforcement was tested to be 496 MPa. The CFRP sheets were ± 45 bidirectional fabrics (Tyfo BCC composite, is a combination of Tyfo BCC reinforcing fabric and Tyfo S epoxy) with tensile strength of 609 MPa, modulus of elasticity of 63.3 GPa, maximum elongation of 9.6 mm/m and thickness of 0.86 mm. The different type of strengthening schemes are shown in Figure 2.23. Beam TB1S1 comprised U-jacket strengthening, TB1S2 was strengthened with extended U-jacket and anchors, TB1S3 involves full wrapping with anchors and TB3S4 involves full wrapping and U-jacket along with the anchors.

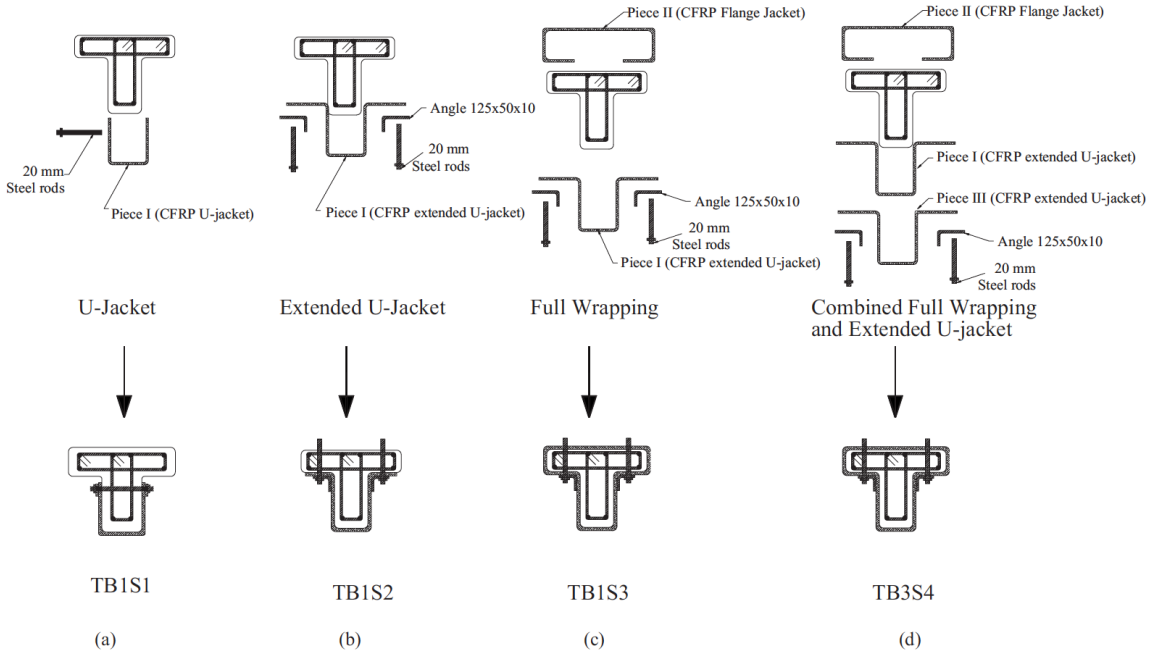

(a) TB1S1 (b) TB1S2 (c) TB1S3 (d) TB3S4

Figure 2.23 Strengthening schemes (a) TB1S1 (b) TB1S2 (c) TB1S3 (d) TB3S4, A Deifalla & Ghobarah (2010)

The results of the torque *vs.* angle of twist is shown in Figure 2.24, while the values of maximum torsional resistance and maximum angle of twist for all the tested beams are shown in Table 2.8. The beam strengthened with full wrapping (TB1S3) had the maximum torsional resistance as well as the maximum angle of twist. TB1S2 (strengthened with U-jacket along with anchors) had torsional resistance close to TB1S3.

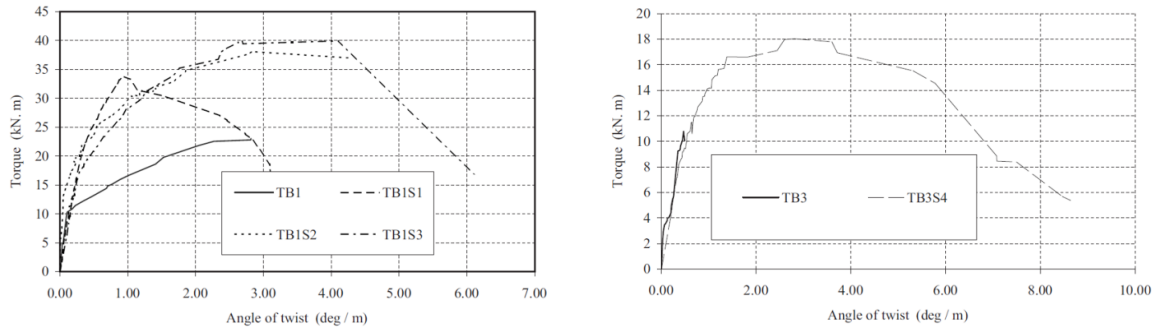

(a) T/V = 0.5 (b) T/V = 0.1

Figure 2.24 Torque - angle of twist (a) T/V = 0.5 (b) T/V = 0.1, A Deifalla & Ghobarah (2010)

The failure mode of beam TB1 (reference beam) was brittle and lacked adequate ductility; in beam TB1S1 failure was observed to be FRP debonding in spiral form originating from the corner. Beam TB1S2 (debonding with diagonal cracking of the concrete underneath), TB1S3

and TB1S4 had debonding of FRP as well. Externally bonded CFRP reinforcement improved the performance of beams subjected to combined shear and torsion. The anchorage system with steel angle delayed the premature end anchorage failure.

Table 2.8 Results of the experimental tests, A Deifalla & Ghobarah (2010)

Beam	Max. torsional resistance (kN·m)	Max. angle of twist (deg./m)	FRP strain (mm/m)
TB1	23.39	2.82	-
TB3	11.00	1.00	-
TB1S1	33.85	3.11	4.26
TB1S2	38.09	4.29	4.70
TB1S3	40.01	6.10	7.69
TB3S4	18.00	8.50	7.59

Deifalla et al. (2013) performed an experimental investigation to study the behaviour of flanged beams externally strengthened with fibre reinforced polymers (FRP) subjected to torsion. Eleven beams were tested with different types of strengthening using U-jacket strips, extended U-jacket strips and fully wrapped strips. The results were analysed in terms of torsional strength, ductility and stiffness.

The cross-sectional details of the beam are shown in Figure 2.25, along with the reinforcement details and the location of strain gauges used to measure the strain variation in the reinforcement. All beams were 1600 mm long. The concrete had a compressive strength of 25 MPa. The yield strength of the longitudinal and transverse reinforcement was 360 MPa and 240 MPa, respectively.

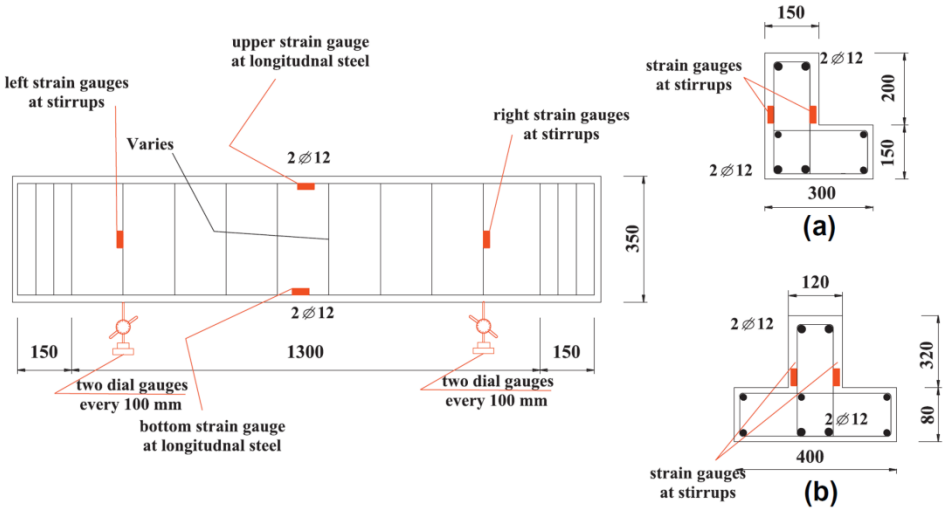

Figure 2.25 Details of the beam (a) L-shaped beams & (b) T-shaped beams, Deifalla et al. (2013)

Three types of beams with rectangular, L-shaped and T-shaped cross-section were strengthened and tested. RB1 is the rectangular reference beam, RB1ER6-50 and RB1ER6-100 are strengthened rectangular beams where ER6 indicates vertical fully wrapped strips. TB1 is the T-shaped reference beam, TB1ER1 and TB1ER5 are T-shaped strengthened beams, ER1 indicates vertical U-jacket strips and ER5 indicates extended vertical U-jacket strips. LB1 is L-shaped reference beam, LB1ER2, LB1ER3, LB1ER4 and LB1ER7 are the strengthened beams, where ER2 indicates vertical anchored U-jacket strips, ER3 indicates inclined U-jacket strips, ER4 indicates anchored inclined U-jacket strips and ER7 indicates inclined fully wrapped strips. The continuous wrapping, vertical strips, inclined strips, U-jacket, extended U-jacket and fully wrapped are shown in Figure 2.26.

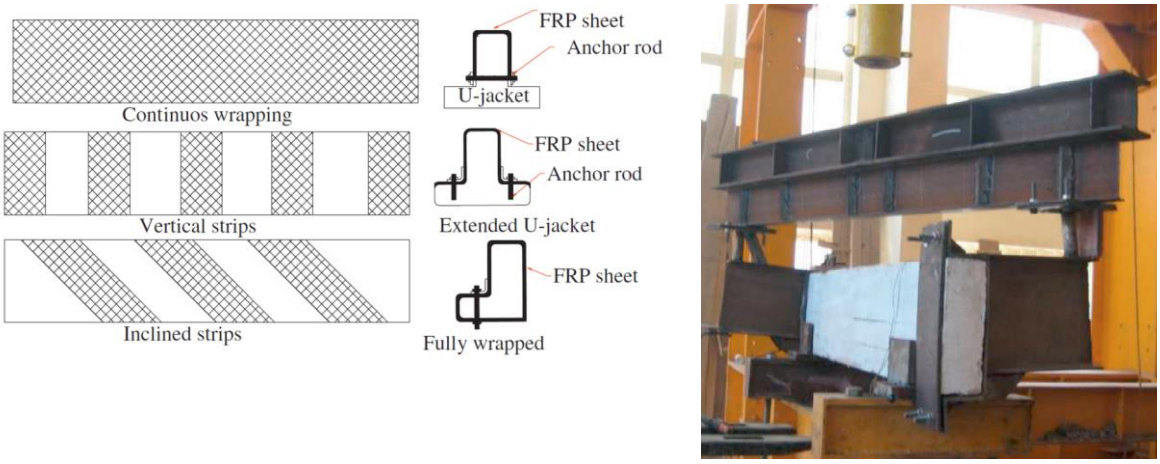

(a) (b)

(c) (d) (e) (f)

Figure 2.26 (a) External reinforcement techniques (b) Test setup, Deifalla et al. (2013) and (c)-(f) Failure images of RB1, RB1ER6-50, RB1ER6-100

The summary of the results of all experiments for all the beams are presented in Table 2.9, GK represents the initial torsional stiffness, GK_{cr} is the post cracking torsional stiffness, T_{cr} is the cracking torsional strength, ψ_{cr} is the angle of twist at cracking, T_u is the ultimate torsional strength, ψ_u is the angle of twist at ultimate torsional strength and ε_t is the stirrup strain. All the beams exhibited diagonal spiral cracking combined with steel yielding before failure. The observed modes of failure are indicated in Table 2.9, where mode I was characterized by steel stirrup yielding followed by diagonal failure (either by concrete strut crushing due to compression or excessive cracking due to diagonal tension), mode II by steel stirrup yielding followed by FRP end debonding and diagonal failure and mode III by steel yielding followed by FRP peeling.

Table 2.9 Results of all beams, Deifalla et al. (2013)

Beam	GK kNm^2	GK_{cr} kNm^2	T_{cr} kN.m	ψ_{cr} deg./m	T_u kN.m	ψ_u deg./m	θ deg.	ε_t (%)	Failure mode
RB1	417	134	1.60	0.22	6.7	2.81	44	0.23	I
RB1ER6-50	400	175	1,75	0.25	7.84	3.55	49	0.27	III
RB1ER6-100	441	175	2.89	0.38	8.98	3.7	53	0.30	
LB1	520	168	2.10	0.24	8.16	3.13	29	0.20	I
LB1ER2	640	304	2.72	0.32	11.56	4.09	39	0.36	I
LB1ER3	530	170	3.40	0.38	10.20	3.91	36	0.39	II
LB1ER4	650	170	4.08	0.50	12.92	4.38	44	0.42	I
LB1ER7	692	190	4.76	0.78	14.96	5.09	52	0.48	I

TB1	470	233	3.10	0.38	11.7	3.44	43	0.30	I
TB1ER1	554	228	5.25	0.53	15.23	4.69	47	0.29	II
TB1ER5	575	197	6.71	0.75	19.2	5.10	52	0.31	II

Comparing the performance of different strengthening solutions with the same FRP reinforcement ratio, fully wrapped U-jacket (64%) and inclined fully wrapped (83%) led to the highest increment. The anchored inclined FRP U-jacket strengthening (LB1ER4) had higher strength and ductility with respect to regular inclined U-jacket strip (LB1ER3). The performance of beams strengthened with inclined U-jacket strips (LB1ER4) was comparable with that of fully wrapped beams (LB1ER7). The use of extended U-jacket vertical strips (TB1ER5) led to an increment of 213% and 133% in ultimate strength and ductility in comparison with vertical U-jacket strips (TB1ER1).

2.4.2. NEAR SURFACE MOUNTED TECHNIQUE

The NSM technique was developed to overcome the drawbacks of using externally bonded reinforcement (EBR), such as surface preparation, premature delamination, susceptibility to fire, external acts of vandalism etc. In this strengthening technique the fibre reinforced polymer laminates/bars are installed into thin grooves created within the concrete cover of the element to be strengthened, which generally ensures a better bond than that developed between EBR laminates and the concrete surface, leading to a more effective strengthening solution. The amount of surface preparation necessary for the application is minimal in NSM technique and does not result into significant alterations of the original appearance of the structural elements. The main steps involved in applying the NSM reinforcement are:

i. Opening grooves on the surface of concrete cover;
ii. Filling the grooves with a bonding agent, typically an epoxy adhesive;
iii. Cleaning the FRP material and applying a layer of adhesive;
iv. Placing the FRP laminate/bars inside the groove;
v. Removing the excess epoxy.

Applications using NSM reinforcement to strengthen members in torsion are very limited. When this research project was initiated, no research studies were available on torsional strengthening with NSM, and only two publications have been published since and are

discussed at the end of this section. The current section is subdivided into (i) flexural strengthening (ii) shear strengthening and (iii) torsional strengthening and few research studies are described to highlight the technique as well as its efficiency.

2.2.2.1 Flexural strengthening

El-Hacha & Rizkalla (2004) performed experimental tests by strengthening T-beams to increase the flexural strength using near surface mounted FRP reinforcement. Eight simply supported specimens were tested under monotonic loading. The experimental test set up and the cross section of the T-beam are shown in Figure 2.27.

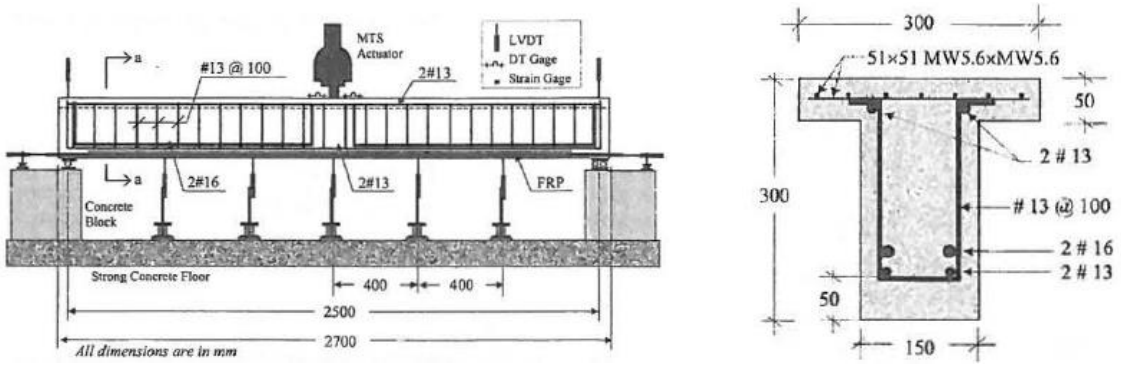

(a) (b)

Figure 2.27 (a) Experimental set up (b) Cross section of T-beam, El-Hacha & Rizkalla (2004)

The concrete compressive strength at 28-day was 45 MPa. The bottom tensile reinforcement consisted of two 12.7 mm diameter and two 15.9 mm diameter rods. The top compressive reinforcement consisted of two 12.7 mm diameter bars, and double legged stirrups of 12.7 mm diameter were spaced at 100 mm throughout the beam. CFRP bars and strips, and GFRP strips were used for strengthening. The details of the FRP reinforcement is shown in Table 2.10.

Table 2.10 Mechanical properties of CFRP and GFRP, El-Hacha & Rizkalla (2004)

FRP Product	Dimensions (mm)	Elastic Modulus, E (GPa)	Ultimate tensile strength (MPa)	Ultimate strain (%)
CFRP bars (Manf-1)	9.5	122.5	1408	1.14
CFRP strips (Manf-2)	2 x 16	140	1525	1.08
CFRP strips (Manf-2)	1.2 x 25	150	2000	1.33
GFRP strips (Manf-3)	2 x 20	45	1000	2.22

Beam B0 was the control specimen, beam B1 had one NSM CFRP reinforcing bar, beam B2 with two type 1 NSM CFRP strips, beam B3 with two type 2 NSM CFRP strips, beam B4 had five NSM GFRP thermoplastic strips, beam B2a had two type 1 externally bonded CFRP strips, beam B2b had two type 2 externally bonded strips and beam B4a had five externally bonded GFRP thermoplastic strips. The outcome of the experimental results is shown in Table 2.11.

Table 2.11 Experimental results, El-Hacha & Rizkalla (2004)

Strengthening system	Beam No.	Ultimate load P_u (kN)	Max. mid span deflection, Δ_u	Max. tensile strain ε_u (%)	Failure mode	% increase in P_u
-	B0	55.4	64.4	-	C	-
NSM FRP reinforcement	B1	93.8	29.2	0.88	D	69.3
	B2	99.3	30.5	1.34	R	79.2
	B3	110.2	50.8	1.38	R	98.9
	B4	102.7	44.3	1.34	D	85.4
EBR FRP	B2a	64.6	43.7	0.48	D	16.6
	B2b	64.3	21.7	0.44	D	16.1
	B4a	71.1	22.2	0.62	D	28.3

C = Crushing of concrete, D = Debonding of FRP, R = Rupture of FRP

According to the results obtained, the authors concluded that strengthening with NSM FRP bars and strips increased both flexural stiffness and ultimate load carrying capacity. The main difference is the improvement in the behaviour of the beams after crack initiation. The different strengthening schemes also limited the deflection as well as the crack widths. The main mode of failure in FRP were due to tensile rupture of the strips and in the case of CFRP bars were due to CFRP-epoxy-split failure. GFRP strips failed due to splitting of concrete and in externally bonded reinforcement failure was due to debonding between the strips and the concrete. The NSM reinforcement technique also provided a significant improvement in the overall ductility of the member. Finally, the NSM method results in higher performance and efficient utilization of the FRP with respect to the EBR technique. This may also be due to the higher bond area in NSM over EBR method.

Barros & Fortes (2004) carried out experimental work on 8 beams, including 4 control beams and 4 beams strengthened in flexure with NSM CFRP. The main purpose of the research was to double the load carrying capacity of the control beams with NSM technique. The experimental setup and the adopted strengthening schemes are shown in Figure 2.28.

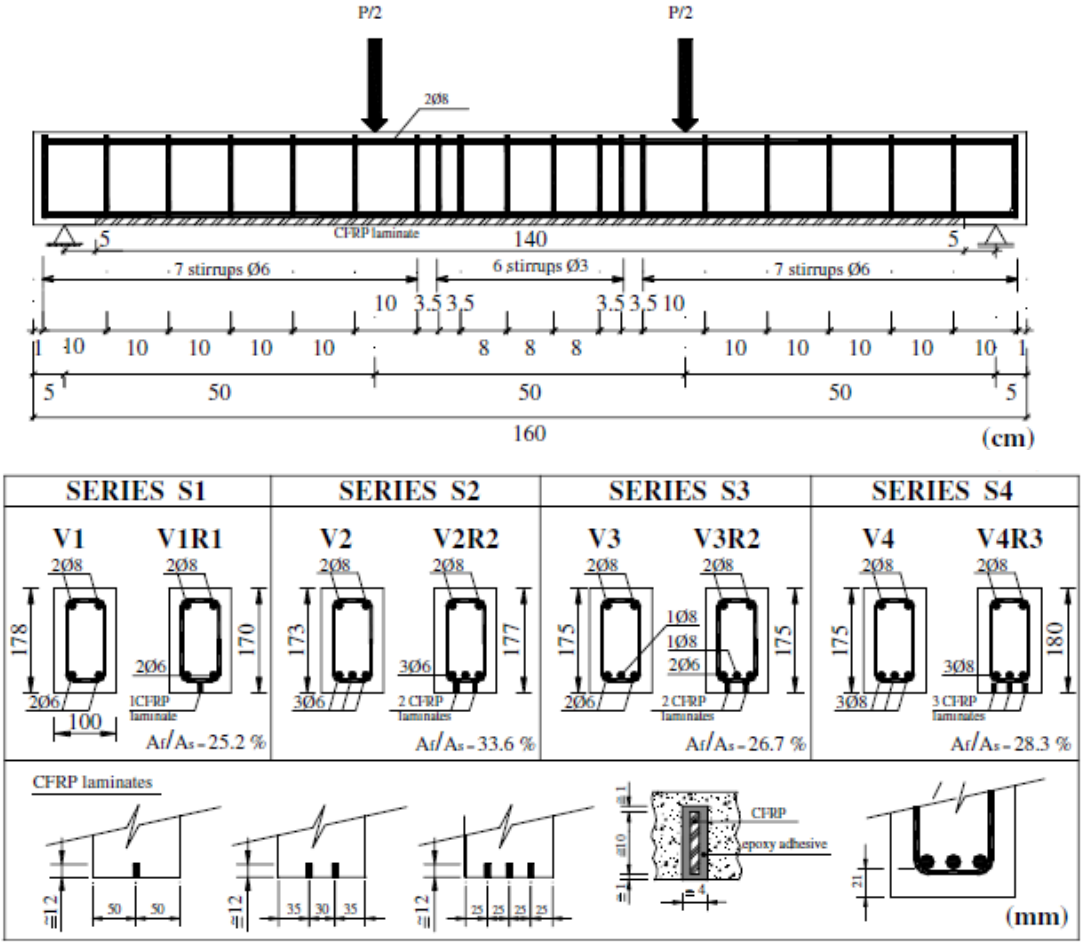

Figure 2.28 Experimental setup and strengthening techniques, Barros & Fortes (2004)

The compressive strength of concrete at 90 days was 46.1 MPa. The reinforcement consisted of 6 mm and 8 mm diameter bars, 6 mm and 3 mm diameter stirrups were used for shear reinforcement. The CFRP strips were 9.59 mm ($\pm$0.09 mm) wide × 1.45 mm ($\pm$0.005 mm) thick and were characterized by a modulus of elasticity of 158.8 GPa ($\pm$2.60 GPa), a tensile strength of 2739.5 MPa ($\pm$85.7 MPa) and an ultimate strain of 1.70% 9 ($\pm$0.4% %). The beams were 1.60 m long and their cross section was about 175 mm ($\pm$5 mm) high and 100 mm wide. The slits were 4.0 mm wide and 12 mm deep. The experimental results are shown in Table 2.12.

Beam V1R1 was strengthened with one CFRP laminate with respect to its control beam. Similarly beam V2R2 had two CFRP laminates, beam V3R2 had two CFRP and beam V4R3 had three CFRP laminates. The control beams (V1, V2, V3 and V4) differed with the internal bottom steel reinforcements.

Table 2.12 Experimental results, Barros & Fortes (2004)

Series	Beam	Ultimate load P_u (kN)	$\frac{P_u(VR)}{P_u(V)}$	Max. Strains ε_u (%)
S1	V1	28.2		
	V1R1	50.3	1.78	15.5
S2	V2	41.0		
	V2R2	78.5	1.91	12.8
S3	V3	41.3		
	V3R2	81.9	1.98	12.8
S4	V4	48.5		
	V4R3	94.9	1.96	10.6

According to the results obtained, the load carrying capacity almost doubled. The strengthened beams had higher stiffness than their reference beams. The maximum strains in the CFRP ranged from 62% to 91% of their ultimate strain. Failure of all the strengthened beams except V1R1 was characterized by detachment of a layer of concrete at the bottom of the beam (the test on beam V1R1 was interrupted when the deflection reached 27 mm). A numerical approach was developed to predict the experimental results involving a cross section layer model and matrix stiffness method. According to the results obtained from the numerical modelling, the FEM results match the experimental results with high accuracy. As an example, a comparison between the load-displacement behaviour of beam V3 and V3R2 and their simulated response is shown in Figure 2.29.

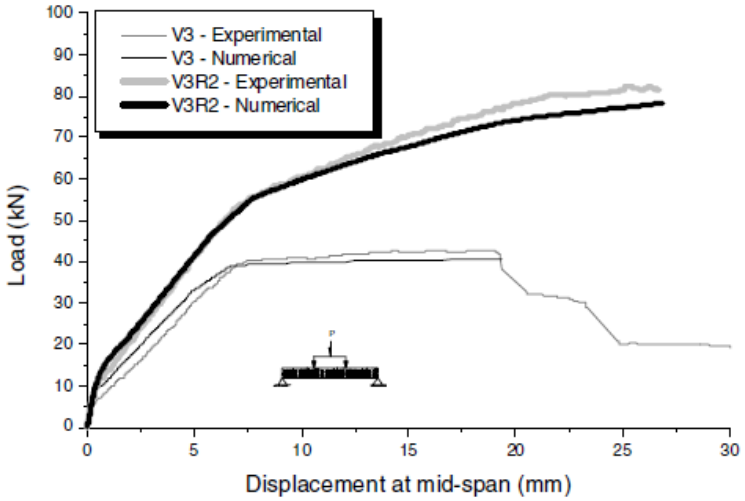

Figure 2.29 Comparison of experimental and numerical results for beams V3 and V3R2, Barros & Fortes (2004)

2.2.2.2 Shear strengthening

Many research works are available in NSM FRP application for shear deficient structures. Few of the investigations are De Lorenzis & Nanni (2001), Lorenzis et al. (2000), Khalifa & Nanni (2000), Nanni et al. (2004), Barros & Dias (2006), Dias & Barros (2008), Bianco et al. (2014), Baghi & Barros (2017) and more. The current section describes a few papers briefly to project the importance of NSM FRP application in increasing the shear capacity of the structural elements.

De Lorenzis & Nanni (2001) investigated shear strengthening using NSM FRP on reinforced concrete beams. Eight beams were tested, including two reference (control) beams and six strengthened beams. Spacing of the rods, strengthening pattern, end anchorage of rods and presence of internal steel reinforcement were examined in this study.

The average concrete compressive strength was equal to 31 MPa. The first six beams were cast without steel stirrups and the last two beams with shear reinforcement. The details of the beam with and without stirrups along with the reinforcement details are shown in the Figure 2.30. The tensile strength of CFRP was assessed to be 1875 MPa and the modulus of elasticity of 104.8 GPa.

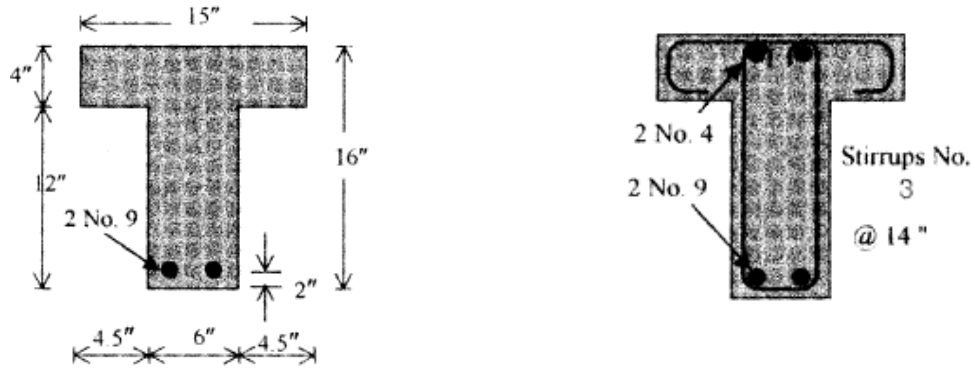

(a) (b)

Figure 2.30 Cross sectional details of the tested beams (a) Beam without stirrups (b) Beams with stirrups, Lorenzis & Nanni (2001)

The beams were designated BV, the reference beam, B90-7 where the beam had steel reinforcement with spacing of 177.8 mm (7 inches) and CFRP placed at 90 degrees, beam B90-5 with steel reinforcement spaced at 127 mm (5 inches), B90-5A similar to B90-5 with additional end anchorage in flange, B45-7 with steel reinforcement spaced at 177.8 mm (7 inches) and NSM CFRP rods placed at 45 degrees, B45-5 spacing of steel reinforcement at 127 mm (5 inches). In beam BSV the steel stirrups were placed at 355.6 mm (14 inches) spacing while beam BS90-7A had steel stirrups and steel reinforcement along with end anchorage. The beams were tested in four-point loading. The results of force *vs.* mid span deflection are shown in Figure 2.31.

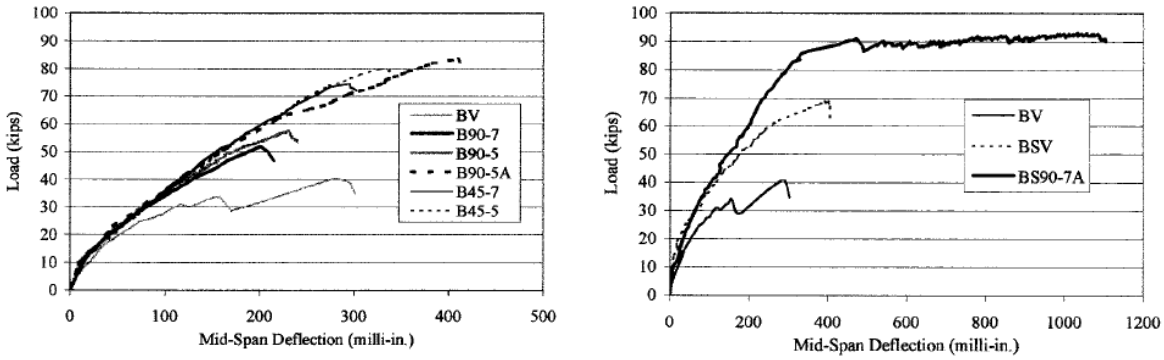

(a) (b)

Figure 2.31 Force - mid span deflection (a) Without steel stirrups (b) With steel stirrups, Lorenzis & Nanni (2001)

Table 2.13 Experimental results, Lorenzis & Nanni (2001)

Beam	Ultimate load (kN)	Failure mode
BV	180.58	Shear compression
B90-7	230.41	Bond failure
B90-5	255.32	Bond failure
B45-5A	377.41	Splitting of concrete cover
B45-7	330.93	Bond failure
B45-5	355.84	Splitting of concrete cover
BSV	306.47	Shear compression
BS90-7A	413.66	Shear compression + Flexural failure

Ultimate loads and failure modes for the tested beams are presented in Table 2.13. According to the investigation performed, three types of conclusions can be obtained. First, decreasing the spacing between the rods (177.8 mm to 127 mm) corresponded to an increase of shear strengthening by 40%, secondly changing the angle of NSM rods from vertical (90 degree) to inclined (45 degree) increased the load carrying capacity by 41.4%, and finally anchoring the rods in the flange region, increased the load carrying capacity by 45.5%.

The proposed strengthening methods resulted in an increased load carrying capacity. Numerical modelling was also performed by the authors, who were able to predict the performance of the tested beams with reasonable accuracy.

Nanni et al. (2004) performed experimental investigation on two damaged double T-girders from a bridge. The beams were cut in half in the longitudinal direction to have four single T-specimens. Each specimen had a length of 12.2 m, 915 mm wide, 585 mm depth with 125 mm flange thickness. The details of the specimen is shown in Figure 2.32.

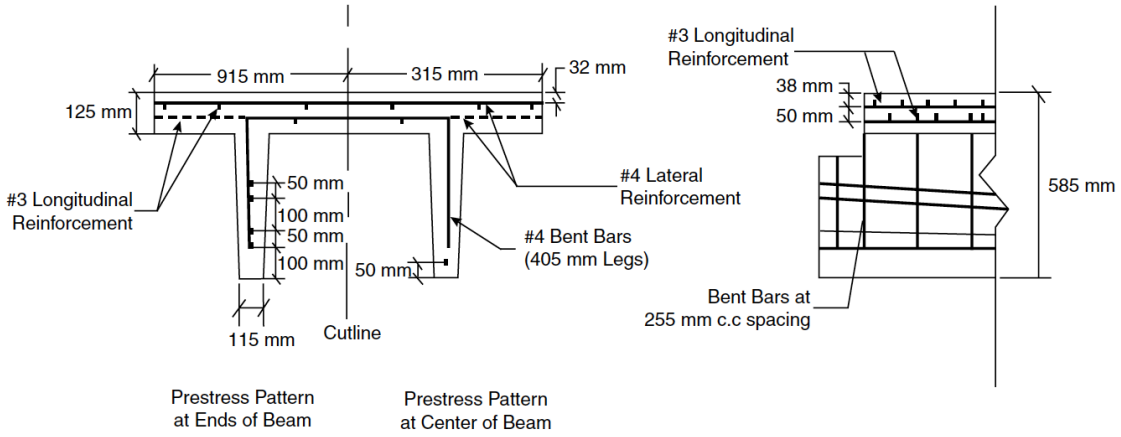

Figure 2.32 Details of the specimens, Nanni et al. (2004)

The experimental tests were performed in two phases: (i) first phase with three specimens under three point bending configuration, where the first specimen was used as the reference (S1), the second specimen (S2) was strengthened in flexure with two FRP plies on the bottom of the web, extending 95 mm on the sides of the web. A U-wrap was also installed in the ends of flexural strengthening to avoid peeling of laminates. The third specimen (S3) was with flexural and shear strengthening consisting of double ply FRP U-wraps of 150 mm wide at 455 mm on centres. (ii) the second phase consisted of one specimen (S4) with CFRP bars installed for shear combined with externally bonded flexural strengthening.

The specimens had four layers of pre-stressing steel tendons and two layers of steel reinforcement in the longitudinal and transverse direction as shown in Figure 2.32. Concrete had a compressive strength of 46.2 MPa, yield strength of steel 420 MPa, prestressing steel 1860 MPa and modulus of elasticity of the prestressing steel was 196.5 GPa. The FRP ply flexural strengthening had thickness of 1.4 mm with 100 mm width and the properties of FRP system in S4 is presented in Table 2.14.

Table 2.14 Details of FRP system in S4, Nanni et al. (2004)

Property	Pre-cured laminate	U-wrap anchor	Rectangular bar
Modulus of elasticity (MPa)	205,000	227535	131000
Ultimate tensile strength (MPa)	2,400	3,800	2070
Ultimate strain	0.0116	0.0167	0.0157

The results of the specimens are presented in Table 2.15. Specimen S1 failed by flexure, S2 failed by shear as it was strengthened in flexural region. As a result of which specimen S3 was strengthened both in flexure and shear, resulting in flexural failure effectively utilizing the FRP material in flexure and specimen S4 failed by flexure. The CFRP strains reached a maximum of 12000 $\mu\varepsilon$ in flexure and 6500 $\mu\varepsilon$ in FRP laminates.

Table 2.15 Experimental results, Nanni et al. (2004)

Beam	Failure load (kN)	Max. Moment (kN.m)	Moment increase (%)	Max. shear (kN)	Shear increment (%)	Failure mode
S1	130	384.0	-	66.7	-	Flexure
S2	160	458.2	19.3	81.8	-	Shear
S3	162	463.6	20.7	83.2	1.7	Flexure (FRP rupture)
S4	210	437.0	13.8	125.5	53.4	Flexure (FRP delamination)

The authors also proposed analytical model to evaluate the shear capacity of beams strengthened with NSM FRP bars in shear, according to ACI 440 (2002), where the shear capacity is a combination of concrete, steel and FRP (equation 2.38). The contribution of NSM FRP laminate is limited by two strain conditions i.e., strain controlled by bond and threshold strain of 0.004 (to maintain shear integrity) of the laminates. The shear capacity is calculated according to equation 2.39, where a and b are the cross sectional dimensions of the bar, τ_b is the average bond stress of bars crossing the shear crack and $L_{tot}(=\sum_i L_i)$ is the summation lengths of bars intercepted by shear crack.

$$V_n = V_c + V_s + V_f \qquad 2.38$$

$$V_f = 4(a+b)\tau_b L_{tot} \qquad 2.39$$

$$L_i = \begin{cases} \dfrac{s}{\cos\alpha + \sin\alpha} \; i \le l_{0.004} & i = 1....\dfrac{n}{2} \\ l_{net} - \dfrac{s}{\cos\alpha + \sin\alpha} \; i \le l_{0.004} & i = \dfrac{n}{2} + 1...n \end{cases} \qquad 2.40$$

$$l_{net} = l_b - \frac{2c}{\sin\alpha} \qquad 2.41$$

L_i is evaluated using equation 2.40, where α is the inclination of bar with respect to the longitudinal axis, s is the horizontal FRP bar spacing and l_{net} is calculated according to equation 2.41, where l_b is the length of FRP bar and c is the concrete cover. Few of the notations are presented in Figure 2.33.

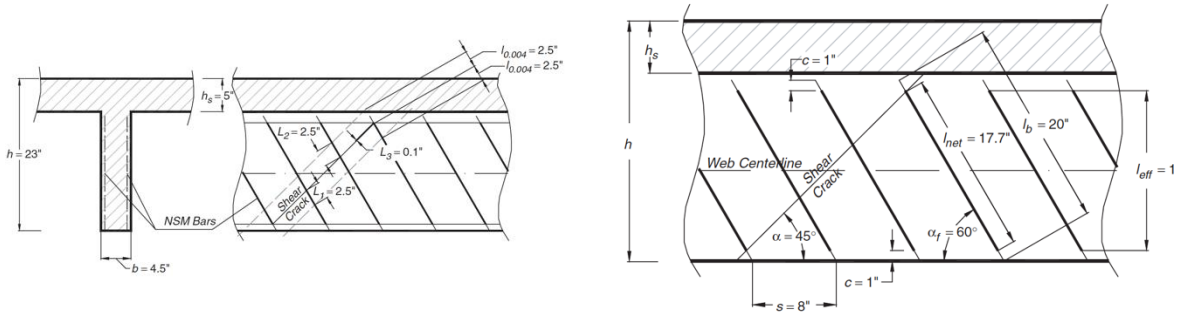

(a) (b)

Figure 2.33 Representation of the terms used in the analytical model, Nanni et al. (2004)

The bond failure is taken into consideration as the first limit in equation 2.40, with minimum effective length of bar intercepted by shear crack n (equation 2.42) and shear integrity is taken into account by the second limitation, where $l_{0.004}$ is evaluated according to equation 2.44.

$$n = \frac{l_{eff}(1+\cot\alpha)}{s} \qquad 2.42$$

$$l_{eff} = l_b \sin\alpha - 2c \qquad 2.43$$

$$l_{0.004} = 0.002\frac{a.b}{a+b}\frac{E_f}{\tau_b} \qquad 2.44$$

The proposed analytical model was used to evaluate specimens S2 and S4 from the experimental work. The V_n/V_u yielded results of 0.80 and 1.04, where V_n is the experimental result and V_u, the analytical result.

Barros & Dias (2006) carried out experimental tests on four series of beams (A10 series, A12 series, B10 series and B12 series), with two different cross sections to increase the shear capacity. The research also analysed the influences of laminate inclination, depth of beam and variation of longitudinal steel reinforcement ratio. Each series had five beams: (i) without stirrups (C) (ii) with stirrups (S) (iii) with CFRP U-shaped strips (M) (iv) NSM vertical

laminate (90 degree, VL) and (v) NSM inclined laminate (45 degrees, IL) strengthening's. The two series 'A' and 'B' had cross sections of 150 mm × 300 mm and 150 mm × 150 mm. All beams with and without strengthening configurations are presented in Figure 2.34 with beam description of each beam. Four point bending tests were performed on each beam. The compressive strength of concrete at 28 days were 37.6 MPa (A) and 49.5 MPa (B). Series A10 and B10 consisted of four bars of 10 mm diameter in the bottom tensile longitudinal reinforcement ($f_y = 464$ MPa), series A12 and B12 had four bars of 12 mm diameter ($f_y =$ 574 MPa). In case of top longitudinal bars, all beams were made up of two bars of 6 mm. Series A, longitudinal bar had yield strength, $f_y = 622$ MPa and transverse bar, $f_y = 464$ MPa and series B, longitudinal bar with $f_y = 618$ MPa and transverse bar, $f_y = 540$ MPa. The tensile strength, Young's modulus and ultimate strain of the CFRP sheets were 3000 MPa, 390000 MPa and 0.8% and the CFRP laminates had 2200 MPa, 150000 MPa and 1.4%.

The results of load *vs.* mid span deflection of each series of beams are presented in Figure 2.35. The maximum deflection is considered at 95% of the peak load for comparison, the results presented are all in comparison with the beam without strengthening and steel stirrups in the respective series. In series A10, beam A10_S with steel stirrups had the maximum increase in load carrying capacity (169%), followed by beams A10_VL (158%) and A10_IL (157%). Maximum deflection was obtained in beam A10_IL (1106%), with inclined NSM FRP strips. In series A12, both NSM FRP strengthened beams had the maximum increase in load carrying capacity by 202% (A12_VL) and 225% (A12_IL) and also maximum deflection in A12_IL (429%). In series B10 and B12, beam B10_VL and B12_S had maximum increase in load carrying capacity (177% and (210%).

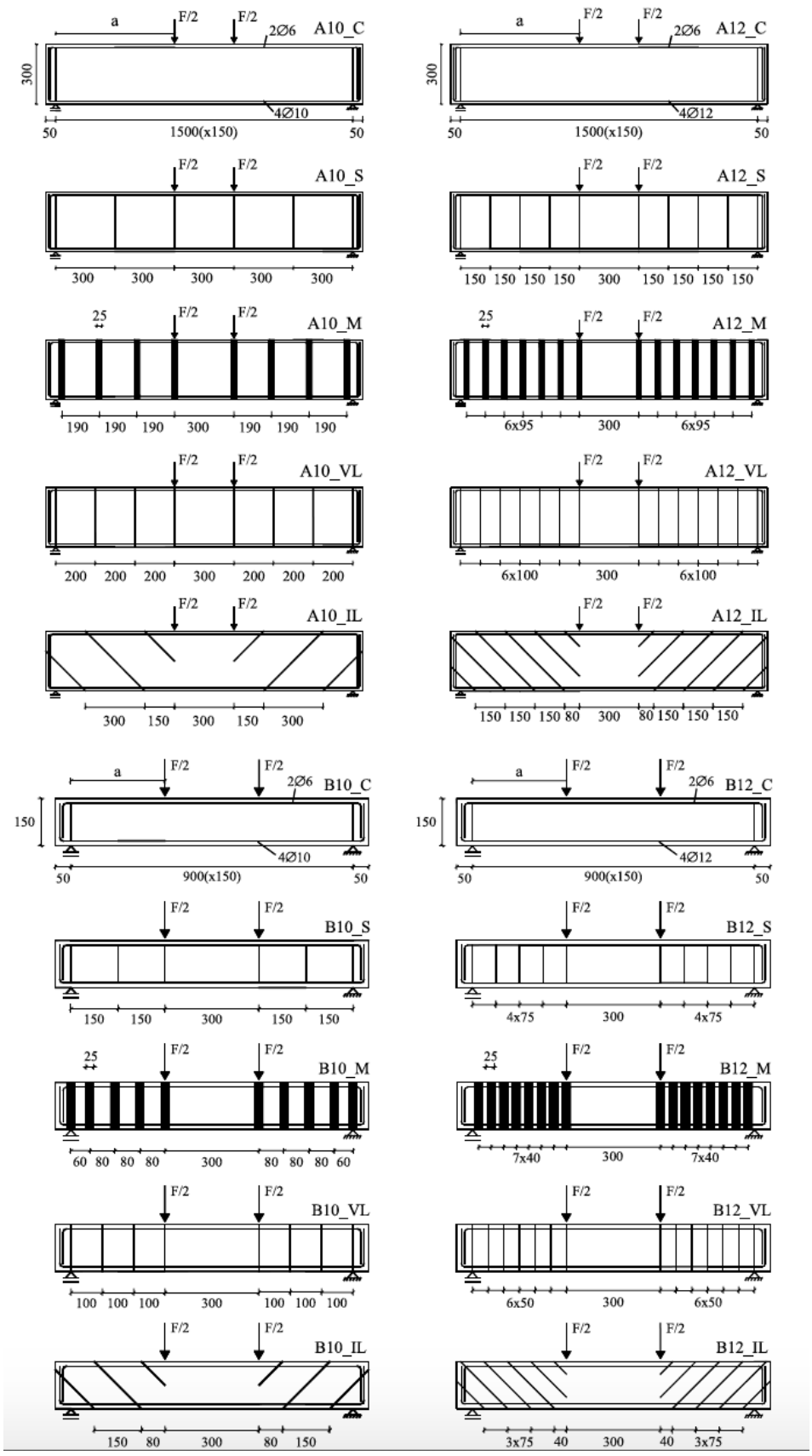

Figure 2.34 Beams with and without strengthening configurations, Barros & Dias (2006)

The unreinforced shear beams failed by single shear failure crack without yielding of longitudinal reinforcement. Beam A10_S and A12_S failed in shear by yielding of longitudinal reinforcement. Beam B10_S and B12_S failed in shear without yielding of longitudinal reinforcement. Beams strengthened with U-strip CFRP failed in shear, with peeling of laminates at locations of critical crack crossing. A distinct failure mode of lateral concrete wall detachment from the core is observed in beams B12_M, B10_IL, B12_VL and B12_IL. Beam A12_VL failed in shear along the shorter bond length. Beams A10_IL and A12_IL failed by rupture in flexural crack.

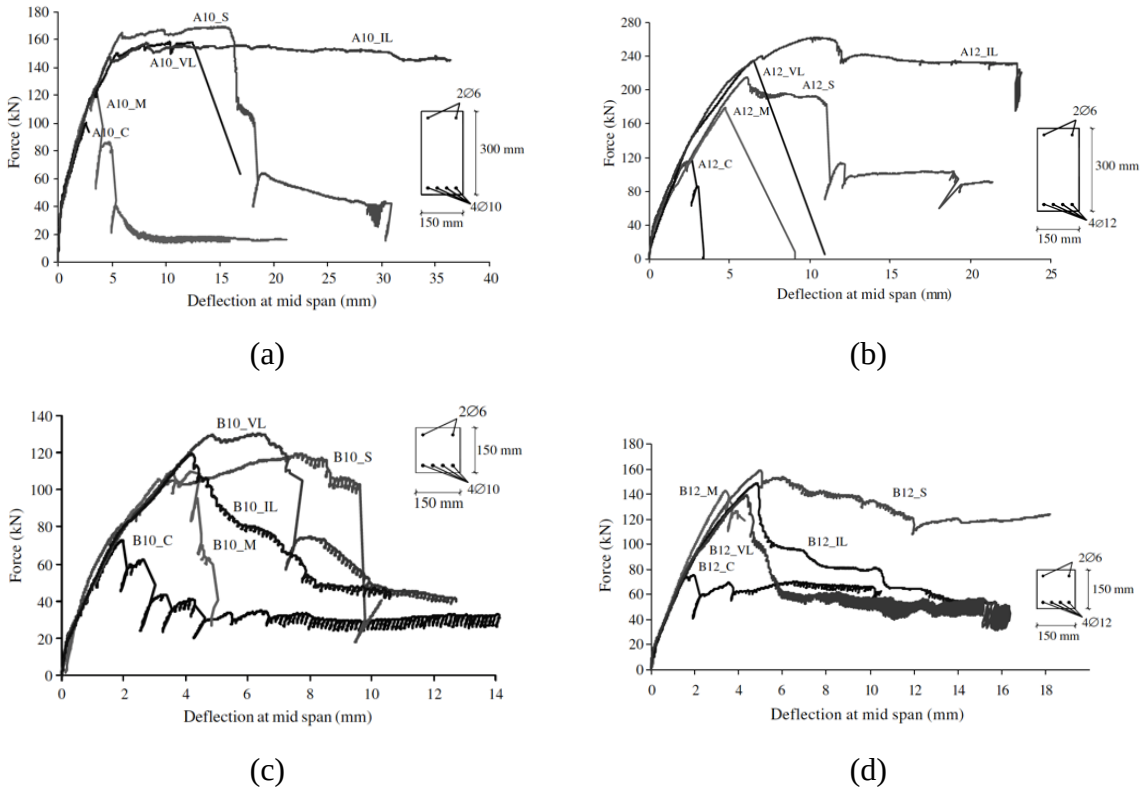

Figure 2.35 Load *vs.* mid-span deflection (a) A10 series, (b) A12 series, (c) B10 series and (d) B12 series, Barros & Dias (2006)

The authors also assessed the analytical predictions of the experimental work by using ACI recommendation for EBR, fib recommendations for EBR and Nanni et al. (2004) for NSM techniques. By updating the bond stress value and the effective strain for NSM calculations, good conservative results were obtained.

An analytical model to evaluate the shear strength contribution of an RC beam by NSM FRP application is described in Bianco et al. (2014). The model is described in chapter 0, as it is used to evaluate the shear force for the present experimental research presented in chapter 0.

2.2.2.3 Torsional strengthening

Al-Bayati et al. (2017) tested 8 reinforced concrete beams in torsion using different strengthening configurations of NSM FRP with epoxy resin and cement-based adhesives. The experimental work is comprised of two reference beams and six strengthened beams, with full wrapping (two beams on all four faces) and U-wrapping (four beams with three face strengthening). Each beam was 2000 mm long with a cross section of 260 mm x 140 mm, and the central 1200 mm length was designed to be torsionally deficient. The longitudinal reinforcement consists of five 12 mm steel bars with two in the top and three in the bottom faces, the stirrups are made up of 6 mm steel reinforcement bars spaced at 60 mm (end zones) and 120 mm (study zone of central 1200 mm). The 28-day concrete compressive strength was 48 MPa, with tensile strength of 3.54 MPa and modulus of elasticity of 38520 MPa. The yield strength of the longitudinal bars was $f_y = 540.50$ MPa and their modulus of elasticity was $E_s = 207700$ MPa. Similarly for the transverse bars the yield stress was $f_y = 352$ MPa and $E_s = 232000$ MPa.

Figure 2.36, presents the cross sectional details of the beam and the strengthening details of U-wrapping and four face strengthening. The strengthening reinforcement ratios are maintained same as in Hii and Al-Mahaidi (2006) with EBR strengthening, in order to compare EBR and NSM strengthening techniques. Groove details are shown in Figure 2.36b, where an offset of 5 mm is provided on alternative faces, with 10 mm overlapping in the corners. The reference beams are labelled C1 and C2, beams EU1 and EU2 are strengthened with epoxy adhesive on three faces. Beams MU1 and MU2 are beams strengthened with mortar on three faces. Finally beams EF and MF are beams strengthened on four faces with epoxy and mortar based adhesives using NSM CFRP laminates.

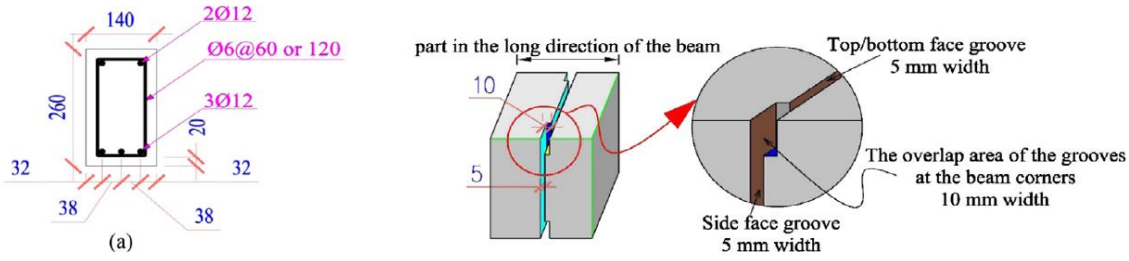

(a) (b)

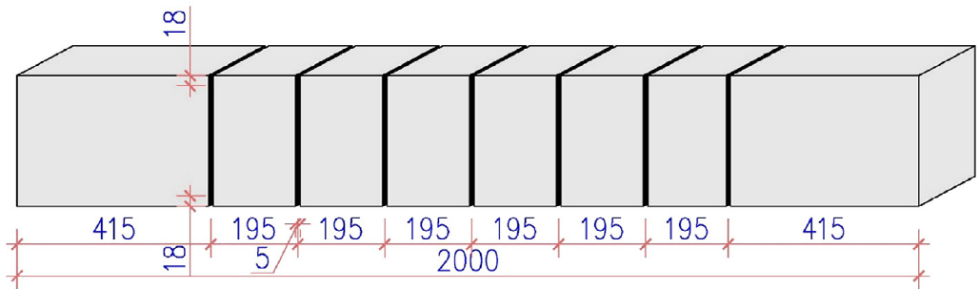

(c)

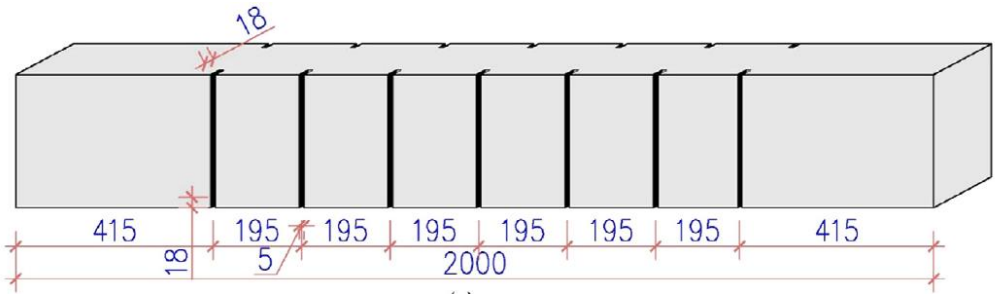

(d)

Figure 2.36 (a) Cross sectional details (b) Groove details (c) Strengthening details of beams on four face and (d) Strengthening details of the beams on three faces

The rig used for testing is shown in Figure 2.37, which consisted of fixing the beam in one end and applying load in the other end using a hydraulic actuator. The test was performed under displacement control at a loading rate of 1mm/minute. The results of the experimental work are presented in Table 2.16 in terms of ultimate torque and twist at ultimate torque. The torque *vs.* twist results of all the beams are shown in Figure 2.38.

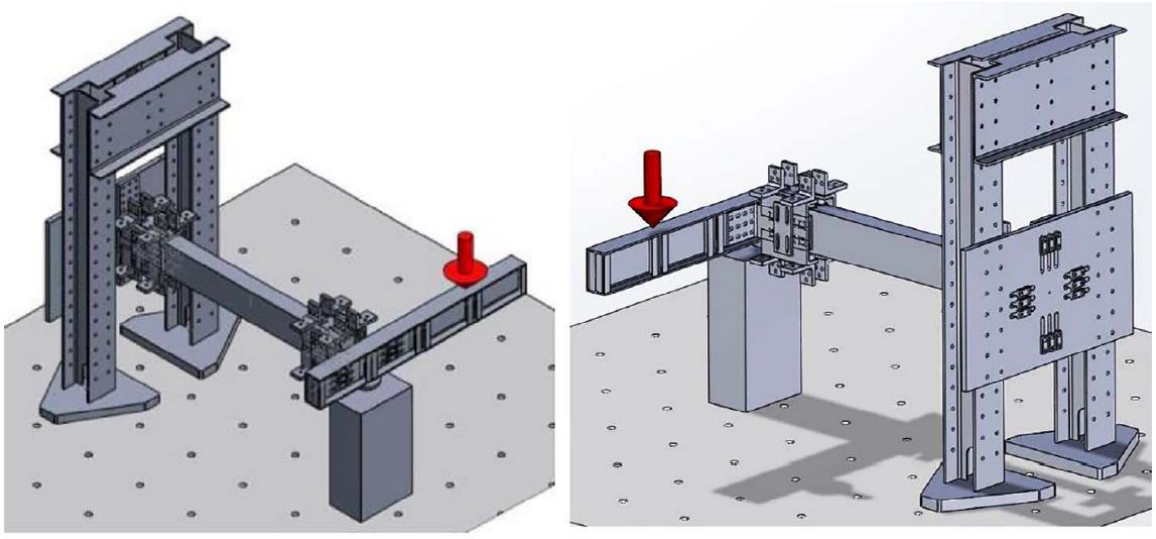

Figure 2.37 Test setup, Al-Bayati et al. (2017)

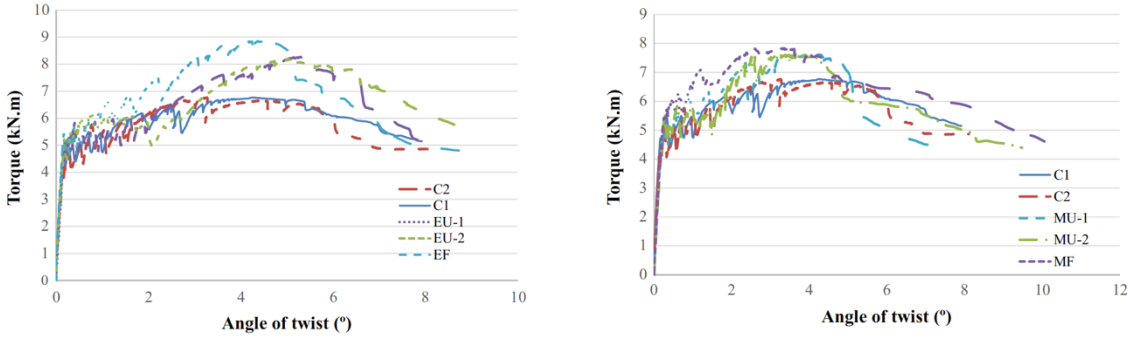

(a) (b)

Figure 2.38 Torque *vs.* twist results (a) Beams strengthened with epoxy and (b) Beams strengthened with cement based adhesive

Table 2.16 Experimental results, Al-Bayati et al. (2017)

Beam description	Ultimate torque (kN·m)	Average (kN·m)	Twist at ultimate torque (degrees)	Average (degrees)
C1	6.77	6.77	4.255	3.761
C2	6.77		3.267	
EU-1	8.27	8.23	5.384	5.265
EU-2	8.18	(+21.6)	5.146	(40%)
MU-1	7.63	7.62	3.645	3.918
MU-2	7.62	(+12.7%)	4.191	(+4.1%)
EF	8.85	(+30.7%)	4.629	(+23.1%)
MF	7.83	(+15.7%)	3,358	(-10.7%)

As seen in the table, the ultimate torsional capacity increased by 21.6% and 30.7% when using epoxy as adhesive for U-wrapping and full wrapping. Similarly, 12.7% and 15.7% increment was obtained using cement based adhesive for U-wrapped and fully wrapped beams. The three face strengthening provided an acceptable improvement in the torsional capacity, even though it is lower than fully wrapped beams. Beams with epoxy adhesive performed better than beams strengthened with cement based adhesives. However, the cement based adhesives can be adopted when application of epoxy is unfavourable, such as in case of fires. In case of beams strengthened on all faces, the critical cracks originated from the corners leading to concrete cover delamination. Since mortar is less adhesive than epoxy, beams with mortar strengthening developed interface cracks between concrete and mortar.

Al-Bayati et al. (2018) investigated experimentally the torsional performance of solid beams strengthened using NSM reinforcement with CFRP ropes and CFRP laminates, using epoxy and cement based adhesives. The experimental work included testing 10 beams with 2 control beams and 8 CFRP strengthened beams. Four beams were strengthened with CFRP laminates, which included two beams with epoxy adhesive (EL1 and EL2) and two beams with cement based adhesive (ML1 and ML2). Similarly, four beams were strengthened with CFRP ropes, with two of them using epoxy (ER1 and ER2) while cement adhesive (MR1 and MR2) was used for the remaining two.

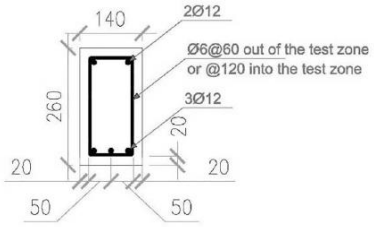

(a)

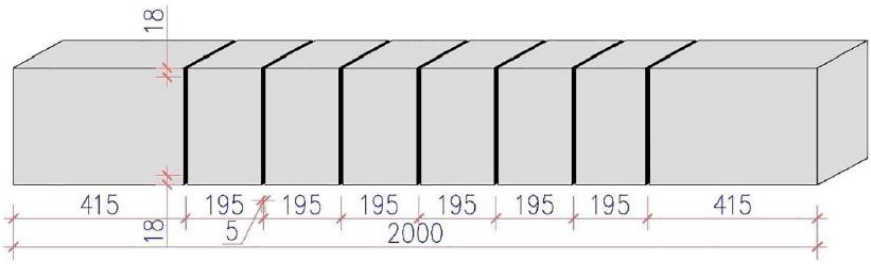

(b)

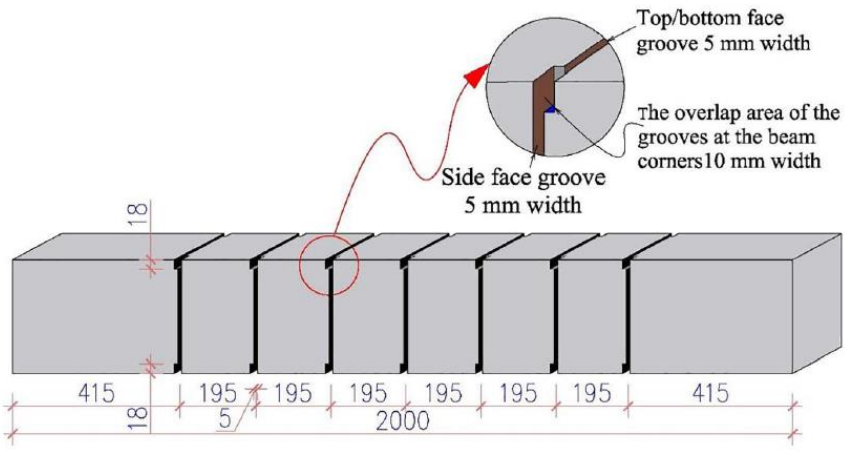

(c)

Figure 2.39 (a) Cross sectional details (b) Strengthening details of beams with CFRP ropes and (c) Strengthening detail of beams with CFRP laminates, Al-Bayati et al. (2018)

The details of the cross section and strengthening schemes are presented in Figure 2.39. Each beam had a length of 2000 mm, with cross sectional dimensions of 260 mm × 140 mm. Beams

with CFRP laminate strengthening, have an offset of 5 mm in executing grooves on parallel faces as shown in Figure 2.39. The laminates were spaced at 195 mm in order to have comparison of torsional capacity in Hii and Al-Mahaidi (2006) with EBR strengthening. The 28-day compressive strength of concrete was evaluated to be 54.39 MPa, the tensile strength was 3.84 MPa and the modulus of elasticity was 40040 MPa. The yield strength of the longitudinal bars was $f_y = 545$ MPa and the modulus of elasticity was $E_s = 195000$ MPa. Similarly for the transverse bars, the yield strength was $f_y = 506$ MPa and $E_s = 224300$ MPa. The CFRP laminates had a tensile strength of 3600 MPa and modulus of elasticity of 212400 MPa, whereas CFRP ropes had tensile strength of 4050 MPa and modulus of elasticity of 233000 MPa.

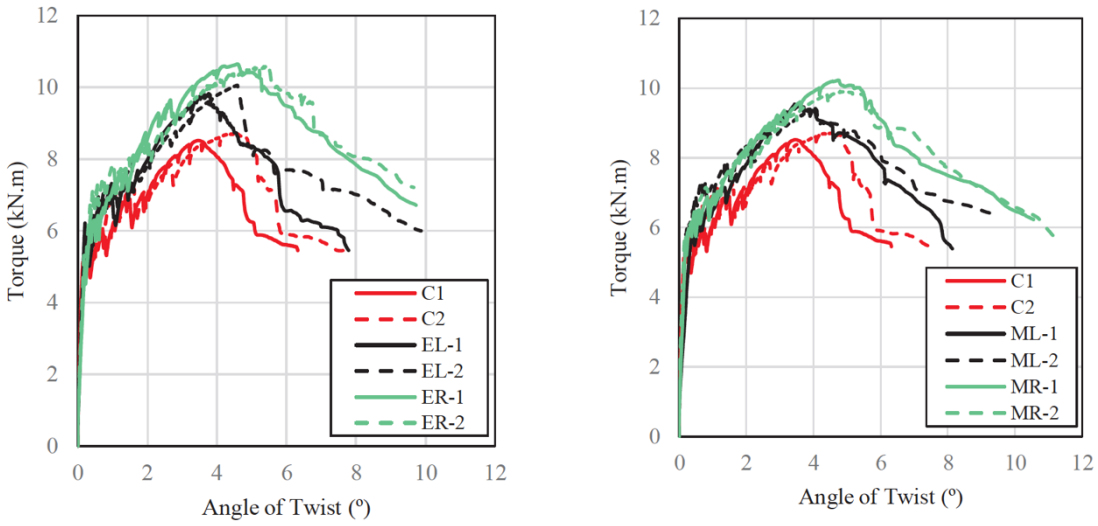

(a) (b)

Figure 2.40 Torque *vs.* angle of twist of beams (a) with epoxy strengthening and (b) with mortar strengthening

Table 2.17 Experimental results of Al-Bayati et al. (2018)

Beam	Ultimate torque (kN·m)	Average (kN·m)	Twist at ultimate load (degrees)	Average
C1	8.52	8.61	3.453	4.011
C2	8.71		4.569	
EL-1	9.83	9.94	3.766	4.177
EL-2	10.06	(+15.4%)	4.588	(+4.1%)

ML-1	9.54	9.48	3.439	3.749
ML-2	9.41	(+10%)	4.059	(-6.5%)
ER-1	10.65	10.62	4.593	5.009
ER-2	10.59	(+23.3%)	5.424	(+24.9%)
MR-1	10.23	10.07	4.728	4.762
MR-2	9.91	(+16.9%)	4.796	(+18.7%)

The experimental results are presented in terms of torque *vs.* angle of twist plots in Figure 2.40 and in Table 2.17. The control beams failed by yielding of the closed ties followed by local concrete spalling and concrete crushing. The strengthened beams with epoxy failed mainly by concrete cover delamination, and the beams with mortar strengthening by yielding of the closed steel ties followed by local concrete cover spalling. All beams failed by yielding of steel transverse reinforcement followed by concrete spalling, however, the higher the FRP strengthening ratios, lower is the strain developed in the steel reinforcement. Comparing the torsional moment carrying capacity of the beams strengthened with EBR in Hii and Al-Mahaidi (2006) and NSM reinforcement of the present research, the increase obtained in EBR technique is 25.2% and that in NSM is 15.4% for epoxy and 10% for mortar with ropes, and 23.3% for epoxy and 16.9% for mortar using laminates. However, high ductility and ultimate torques were obtained using the NSM technique.

2.5. CONCLUSIONS

The current chapter summarises the available strengthening techniques for reinforced concrete structures, with a greater focus on torsional strengthening, as well as the approaches adopted by different standard codes to evaluate torsional capacity. As briefly presented, different traditional and innovative methods are available for the strengthening of concrete structures. In general, NSM reinforcement has many advantages over all the other available strengthening methods, such as minimal disturbance to appearance, addition of minimal weight to the element to be strengthened, ease of application, simpler surface preparation, higher efficiency of the strengthening material owing to its superior bond with concrete, protection against vandalism and fire.

A few investigations of NSM FRP application for shear strengthening is presented above in section 2.2.2.2. As seen from the experimental and numerical research, the method offers

significant improvement in enhancing the shear capacity of shear deficient structures. The strengthening method is considerably easy and quick in installing with minimal interference on the concrete structures. Many factors like application of straight laminates, inclined laminates, depth of the laminates, effect of existing longitudinal steel reinforcement, spacing of the rods, strengthening patterns, end anchorage rods are explored experimentally, giving a wider perspective of different areas to be explored in torsional strengthening.

Few standard codes are described in section 2.2, giving an overview to determine the torsional capacity of the element. As seen, all the four codes use space truss analogy as the basis for evaluation. In EuroCode 2 (2004), the compressive strut angle is varied between 21.8 – 45 degrees, in NTC-CNR (2018) and ACI 318 (2011) it is assumed to be 45 degrees. However, in case of DR_AS-3600 (2017) the angle is evaluated based on modified compressive field theory (MCFT) which is dependent on the strain at mid-depth. The evaluation of shear force is dependent on a factor considering the tensile stress in cracked concrete and the longitudinal strain at mid-depth.

Based on the available research data, the following results can be summarized for the NSM FRP strengthening application in shear, flexure and torsion:

- The stiffness of the element is improved, mainly after crack initiation;
- The use of inclined strengthening reinforcement improves the shear and torsional capacity of the beam;
- Anchoring the FRP material can positively affect performance;
- Improved ductility performance of the member and higher strains of the FRP material is attained;
- Higher FRP strengthening ratio reduces the rate of steel yielding.

All of these aspects make the use of NSM very attractive for strengthening and worth of exploring its applicability to increase the torsional performance of thin-walled tubular sections. The current investigation includes a series of complementary experimental, analytical and numerical studies, which are discussed in turn in the following chapters.

CHAPTER:

3. PRELIMINARY NUMERICAL ANALYSIS

This chapter discusses the numerical methodology that was adopted to assist the development and design of the planned experimental programme. A finite element analysis was performed to examine the behaviour of an un-strengthened reference beam as well as that of a series of beams strengthened in torsion. The numerical analysis was also used to design the test set-up and examine all possible issues before the bespoke testing rig was finalised and manufactured. The chapter describes in detail the following aspects: model verification; analysis of the beams; mesh refinement; parametric analysis; strengthening proposals; and finally the analysis of the whole experimental test setup.

3.1. VERIFICATION OF NUMERICAL MODEL

The predictive performance of the constitutive models adopted for the material nonlinear analysis of the beams of the experimental program is first assessed by comparing the FE results of Hii & Al-Mahaidi (2006) with those recreated in FEMIX (J. A. Barros 2016). The geometrical details of the beam and the parameters adopted in the analysis are shown in Figure 2.11 (see section 2.4.1) and Table 2.5. Taking advantage of symmetry, only half the beam is analysed, as modelled by the authors, with the respective boundary conditions. One end of the beam is fixed in all three directions (X, Y and Z direction) and the other end is supported on a pivot (restriction in vertical direction) allowing free rotation along X-axis and elongation/shortening of the beam. The load is applied at the end of a cantilever beam to produce torsion as shown in Figure 3.1.

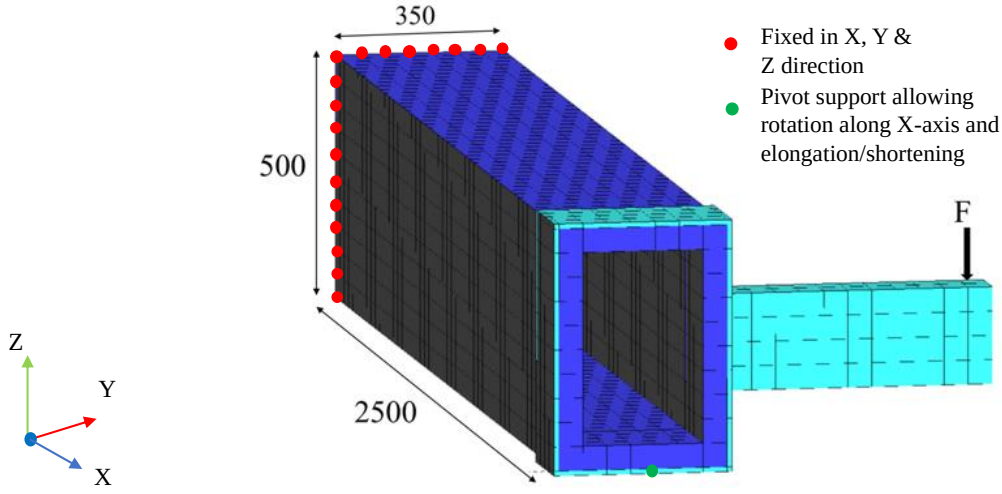

Figure 3.1 FEM model of Hii & Al-Mahaidi (2006) recreated in FEMIX (dimensions in mm)

The comparison of torsional moment *vs.* torsional angle of rotation obtained with FEMIX and the experimental results by Hii & Al-Mahaidi (2006) is presented in Figure 3.2. A very good agreement between the results are obtained, thus validating the adopted model, which will be used in the following sections to carry out a parametric analysis and the analysis of a strengthened beams. However, the current analysis stops at an angle of 1.92 degrees, due to problems in convergence viz., caused by the formation of multiple cracks at different integration points in the concrete elements and resulting in a highly non-linear behaviour.

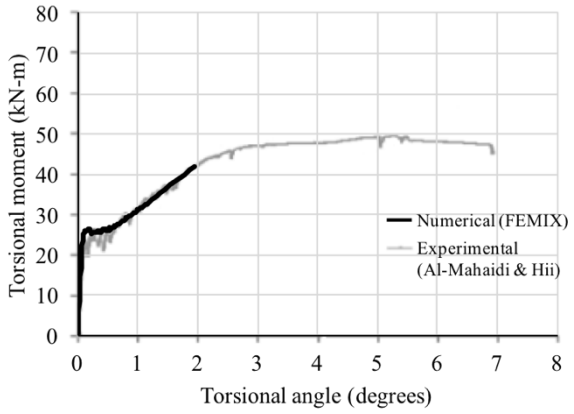

Figure 3.2 Comparison of $M_t - \theta_t$, FEMIX numerical results with Hii & Al-Mahaidi (2006)

3.2. BEAMS

3.2.1. DATA AND ANALYSIS

A thin walled tubular beam of 1900 mm length is considered for the analysis. The outer dimensions measure 400 mm × 400 mm, while the inner hollow section measures 200 mm × 200 mm with a wall thickness of 100 mm. The reinforcement configuration consists of eight 10 mm diameter bars in the longitudinal direction with 25 mm cover. Bars of 8 mm diameter are provided as four legged stirrups with two legs at 25 mm and two legs at 75 mm from the outer section. The transverse reinforcements are spaced at 100 mm centre to centre in the end zones of 450 mm length. In the central 1000 mm (study zone) the stirrups are spaced at 200 mm as shown in Figure 3.3. The reduced spacing of the stirrups in the ends are to transfer the applied load to the central region without causing any failure at the loading end, and the other end is to restrict the damage when firmly fixed.

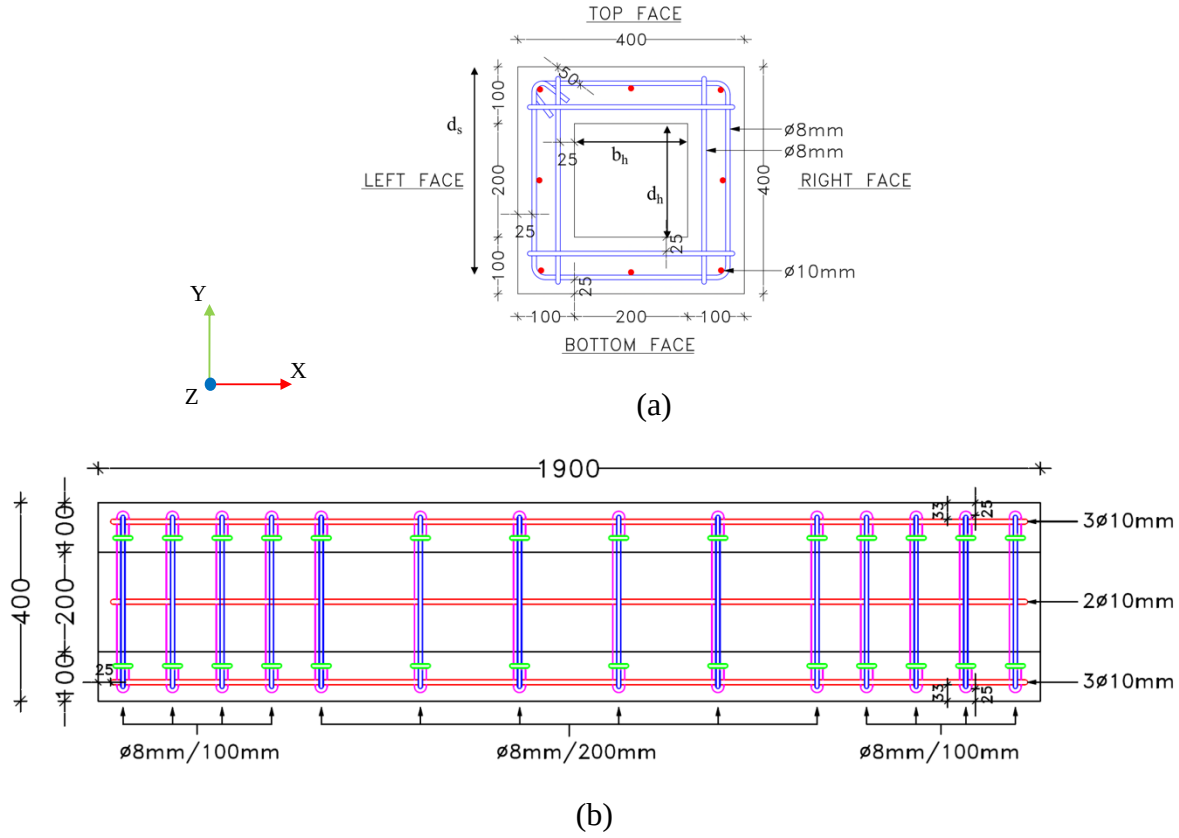

Figure 3.3 Beam geometric details (a) Cross section (b) Longitudinal section (dimensions in mm)

The torsional moment is applied through a steel section specifically designed for the purpose. One end of the section is inserted inside the hollow section of the beam up to a length of 300 mm and the other end is connected to the load cell. The details of the steel section and its position on the beam is shown in Figure 3.4.

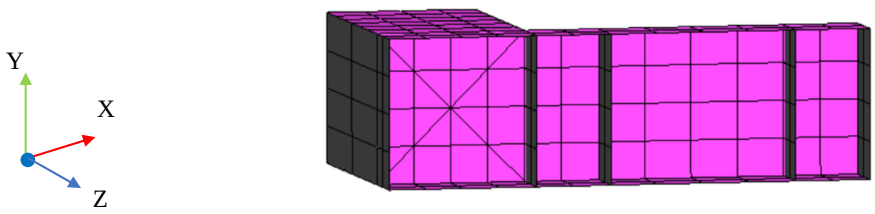

(a)

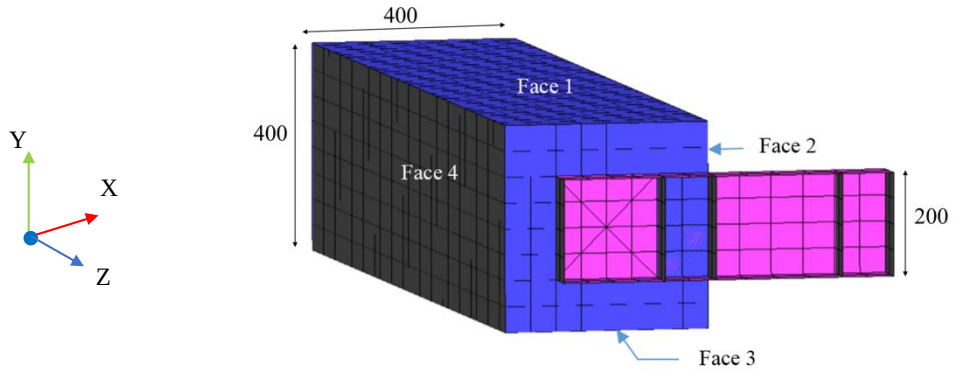

(b)

Figure 3.4 (a) Steel section (b) Steel section with beam (all dimensions are in mm)

GiD software is used as a pre- and post-processor using FEMIX computer code as the processor for the finite element analysis. Three finite element analysis are performed, each with a different mesh size, including: 25 mm (L10S8_25); 50 mm (L10S8_50); and 100 mm (L10S8_100). The results of these models are discussed in Section 3.2.3. Primarily, model L10S8_50 (50 mm mesh size) is used to assess the calculation method and examine the results. The beam labels are of the format "L*i*S*j*_*k*", where L indicates the longitudinal reinforcement and "i" indicates the diameter of the longitudinal reinforcement, S represents the stirrups and "j" represents the diameter of the stirrups (transverse reinforcements) and "k" indicates the mesh size of the model (concrete and reinforcements).

The mesh is generated with 50 mm × 50 mm × 50 mm hexahedra FEs for modelling the concrete, and 3D embedded cables of 50 mm dimension for simulating the longitudinal and transverse reinforcements. A total of 4239 nodes are created with 1632 hexahedra elements of concrete, 1616 linear elements of reinforcements and 232 quadrilateral elements according to the Reissner-Mindlin shell theory to model the steel sections used to apply the external load. The details of the model presenting the mesh, loading points and roller supports are shown in Figure 3.5. The beam is fixed in one end and loaded in the other. In order to simulate these conditions, the fixed end of the beam is restricted in all directions (x, y and z). The loading end of the beam is restricted only in Y-direction up to a length of 300 mm along the central nodes simulating the vertical pinned support.

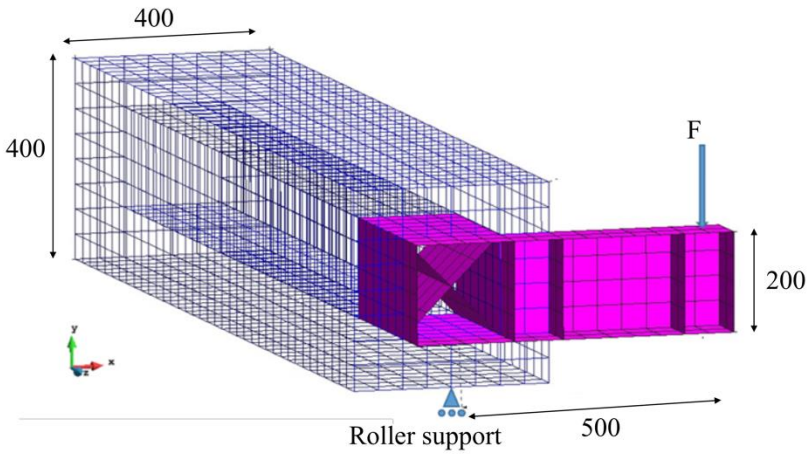

Figure 3.5 Details of the model (mesh, loading point & support)

The beam is also supported on rollers (shown in the figure) allowing the elongation/ shortening of the beam. Load is applied on the centre of the steel section at a distance of 500 mm from the centroid of the beam creating a torsional moment of $M_t = 0.5F$ kN·m.

A 3D multidirectional smeared crack model (Ventura-Gouveia et al. 2008) available in FEMIX is used for the numerical simulations. The Gauss-Legendre 2×2×2 integration scheme allowing the formation of a maximum of two cracks at each integration point is adopted. A modified Newton-Raphson iterative algorithm is applied, and the stiffness matrix is updated at each increment. An independent path behaviour (dependent on the previous converged step) is used with the tolerance of $1x10^{-3}$ in terms of energy for convergence criterion. The analysis is performed in displacement control under arc-length method. 8-noded solid hexahedra elements are used to model the reinforced concrete, while 2-noded 3D embedded cables are used for longitudinal and transverse reinforcements as shown in Figure 3.6. The reinforcement is assumed to be perfectly bonded to concrete elements.

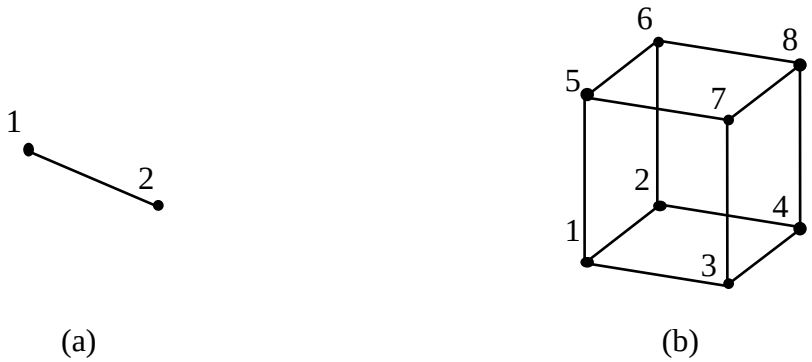

Figure 3.6 Element types (a) 2-node 3D embedded cable (b) 8-node hexahedron

A compressive strength of 25 MPa is assigned for concrete, along with a modulus of elasticity of 29000 MPa and a tensile strength of 2 MPa. Fe 400 steel with a characteristic tensile strength of 400 MPa for both the longitudinal and transversal reinforcements is used. The final model of the beam for the finite element analysis is as shown in Figure 3.5. The tri-linear tensile softening diagram (J. A. O. Barros et al. 2013) shown in Figure 3.7(a) is selected for the reinforced concrete to simulate crack opening propagation. The non-linear material behaviour for the reinforcements is shown in Figure 3.7(b). Further details on the material models can be found in Barros et al. (2013) and Ventura-Gouveia et al. (2008).

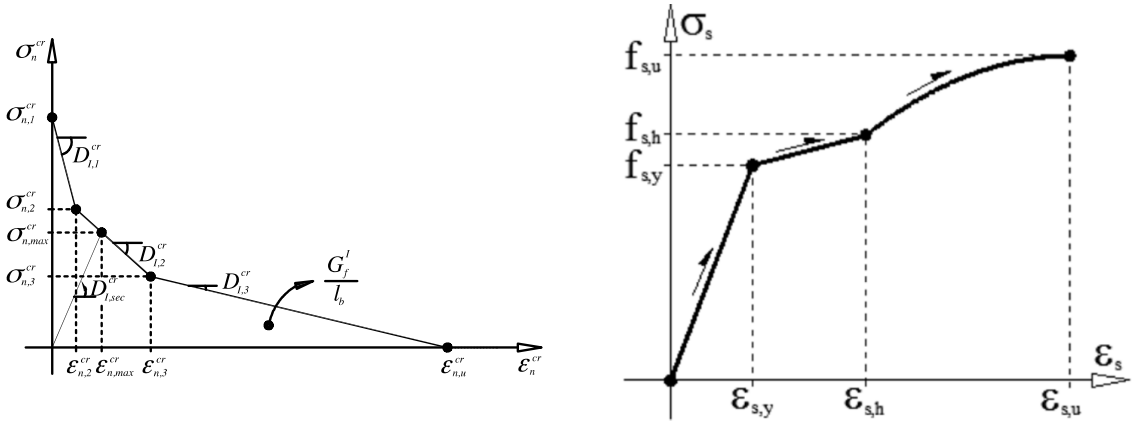

(a) (b)

Figure 3.7 Numerical models (a) Tri-linear softening diagram (concrete) (b) Non-linear material property of steel

The transverse section and the longitudinal section of beam L10S8_50 after mesh generation (50 mm × 50 mm × 50 mm) is shown in Figure 3.8.

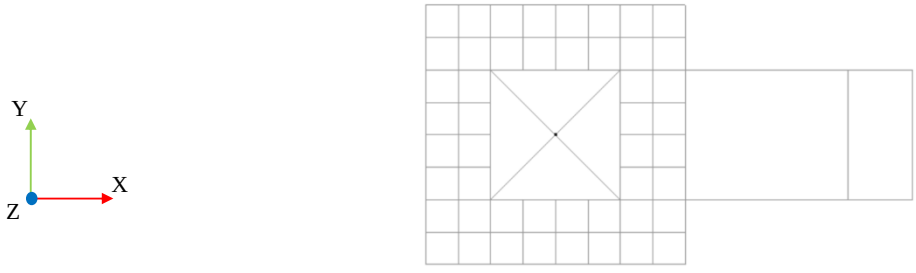

(a)

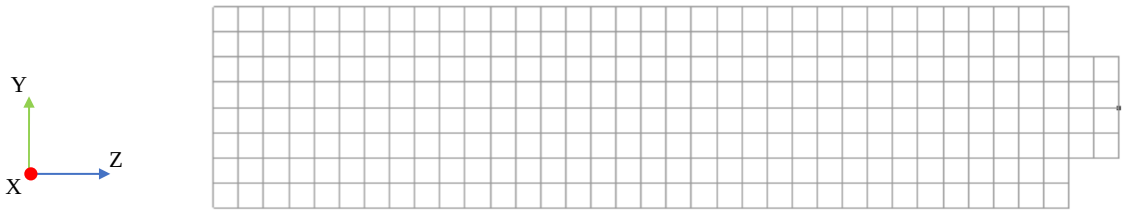

(b)

Figure 3.8 Mesh details of L10S8_50 (a) Transverse section (b) Longitudinal section

3.2.2. RESULTS

The results of FE model L10S8_50 is presented first to explain the calculation method and then, the results of L10S8_25 and L10S8_100 are presented (mesh sensitivity analysis) for opting 50 mm mesh size for the rest of the analysis (parametric and strengthening analysis).

MODEL L10S8_50

The main aim of these analyses is to determine the torsional angle of rotation for the applied torque. The torsional moment *vs.* torsional angle of rotation is measured at a distance of 550 mm from the loading end in XY section (along the length, Z-axis). The selected section is 100 mm inside the study zone.

In order to determine the torsional angle of rotation, the displacements of each node in the section for every load increment is extracted from the results. The tangent inverse of this displacement with respect to its distance (d) from the centre of the section gives the angle of rotation of that specific node. For part I and part III the displacements in x-direction (δ_x) are taken, and for part II and part IV the displacements in y-direction (δ_y) are read. An average tangent inverse from all nodes for each load step is calculated and plotted against the torsional increment. Equation 3.1 is used to measure the angle of rotation and the calculation method is shown in Figure 3.9.

$$\theta = \frac{\sum_{i=1}^{n}\left(\tan^{-1}\left(\frac{\delta_x}{d_y}\right)+\tan^{-1}\left(\frac{\delta_y}{d_x}\right)\right)_i}{n} \qquad 3.1$$

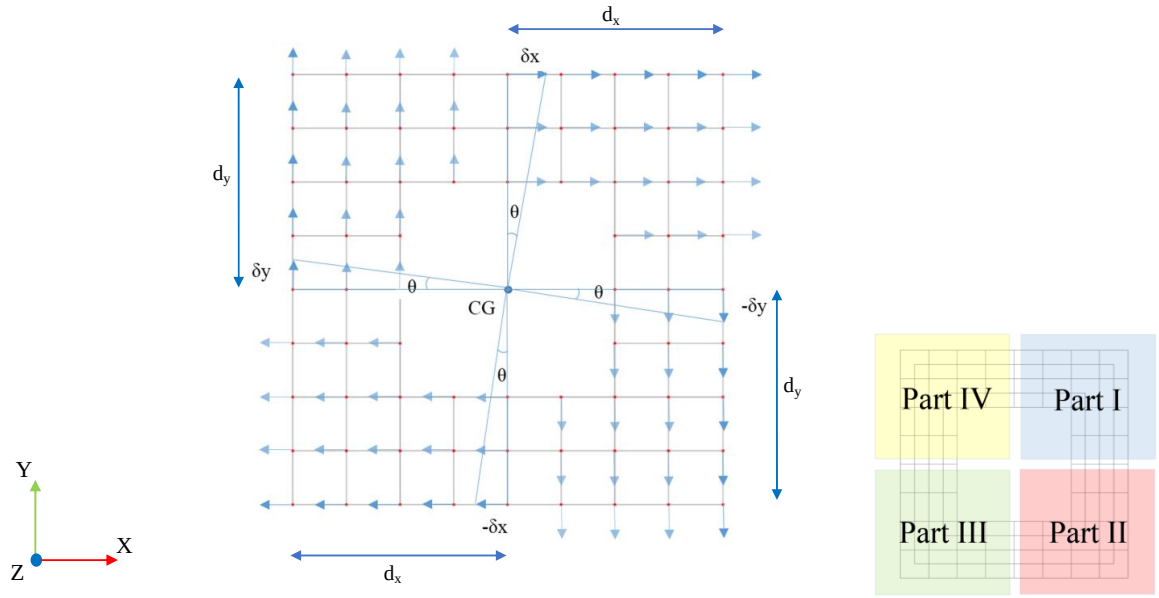

Figure 3.9 Presentation of nodal displacements to determine torsional angle of rotation

The result of torsional moment *vs.* torsional angle of rotation according to the method described above is shown in Figure 3.10. Point 'A' is the torsional crack occurrence (27.35 kN·m and 0.038 degrees), and the corresponding crack pattern is shown in Figure 3.12(a). The cracking initiates in the central top (face 1) and central bottom (face 3), in the loading end section of the beam.

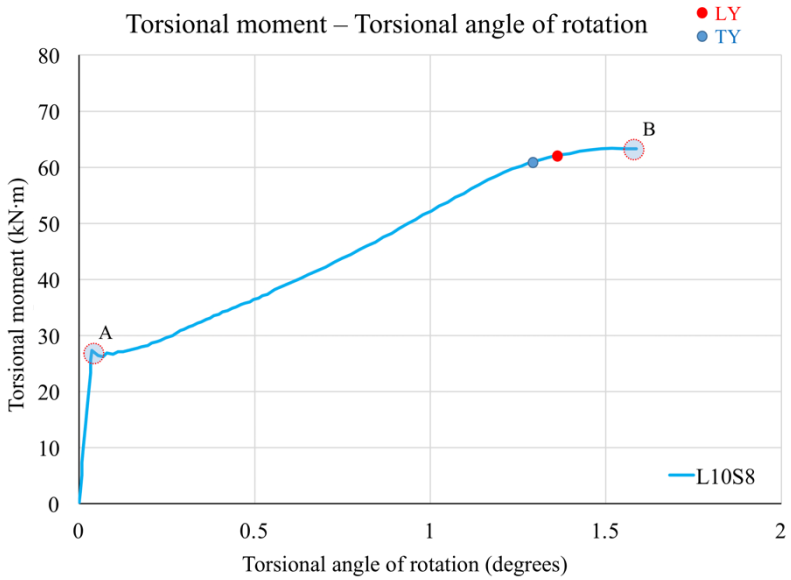

Figure 3.10 Torsional moment *vs.* torsional angle of rotation of L10S8_50

The reinforcement starts to actively contribute only after the torsional cracking moment is exceeded (point A: 27.35 kN·m), which is evident from the evolution of steel strain graph in Figure 3.11(a) and from torsional moment *vs.* torsional angle of rotation in Figure 3.10, due to

the ductile response and lower stiffness of the beam. The torsional moment and the angle of rotation increases up to point 'B' (Figure 3.10) reaching the maximum moment of 63.34 kN·m. The yielding of the transverse reinforcement is indicated by a blue dot, while the red dot indicates yielding of the longitudinal reinforcement. Yielding is considered when the reinforcement reaches a strain of 0.002 $\left(\varepsilon_u = \frac{f_y}{E} = \frac{400}{200000} = 0.002\right)$, as shown in Figure 3.11(a) and (b), evaluated at a section 550 mm from the loading end. Similarly, yielding of the reinforcement is also recorded for the internal stirrups.

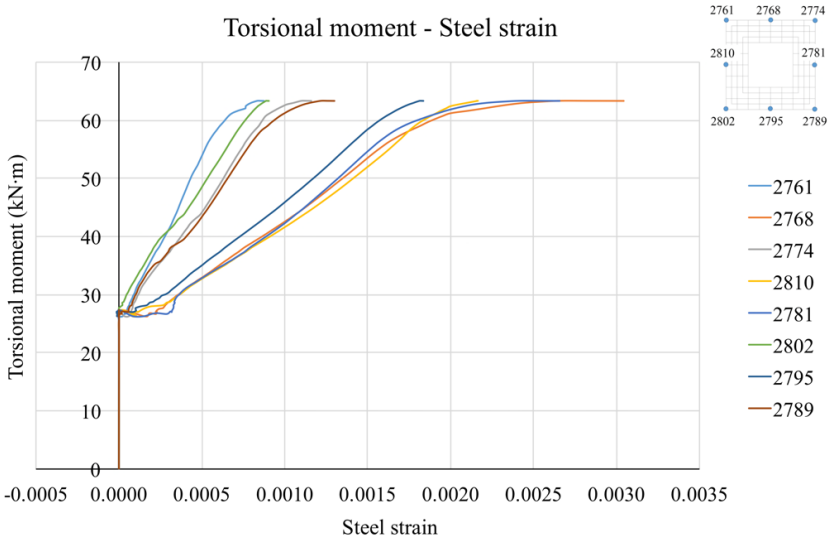

(a)

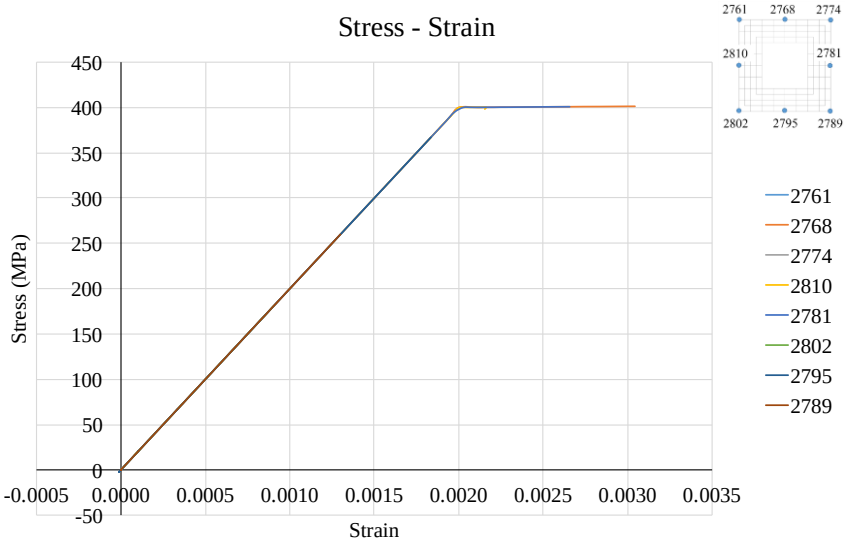

(b)

Figure 3.11 (a) Torsional moment *vs.* steel strain graph (b) Stress *vs.* strain graph of external stirrups with the position of nodes

As soon as yielding initiates at few locations, the beam attains its torsional carrying capacity (Figure 3.10) reaching a plateau response of $M_t - \theta_t$. The central bar on face 2 and on face 4 are the first bars to start yielding, followed by the central bars in face 1 and face 3. Figure 3.12(b) shows the crack pattern of the beam (all crack statuses: opening, closing, reopening and fully open, Figure 3.7a) at maximum torque of 63.34 kN·m (1.587 degrees). Figure 3.12(c), shows the same but with only completely opened cracks. The maximum crack width of 0.298 mm is obtained in a concrete element closer to the central yielded reinforcement bar on face 2. Crack opening is obtained by multiplying the crack normal tensile strain to the crack bandwidth ($l_{cb} = \sqrt[3]{V_{IP}}$, where V_{IP} is the volume of the integration point). Due to problems of convergence, the analysis stops at the maximum torque (point B). At maximum torque, several integration points are changing the crack statuses, resulting in overall lack of convergence.

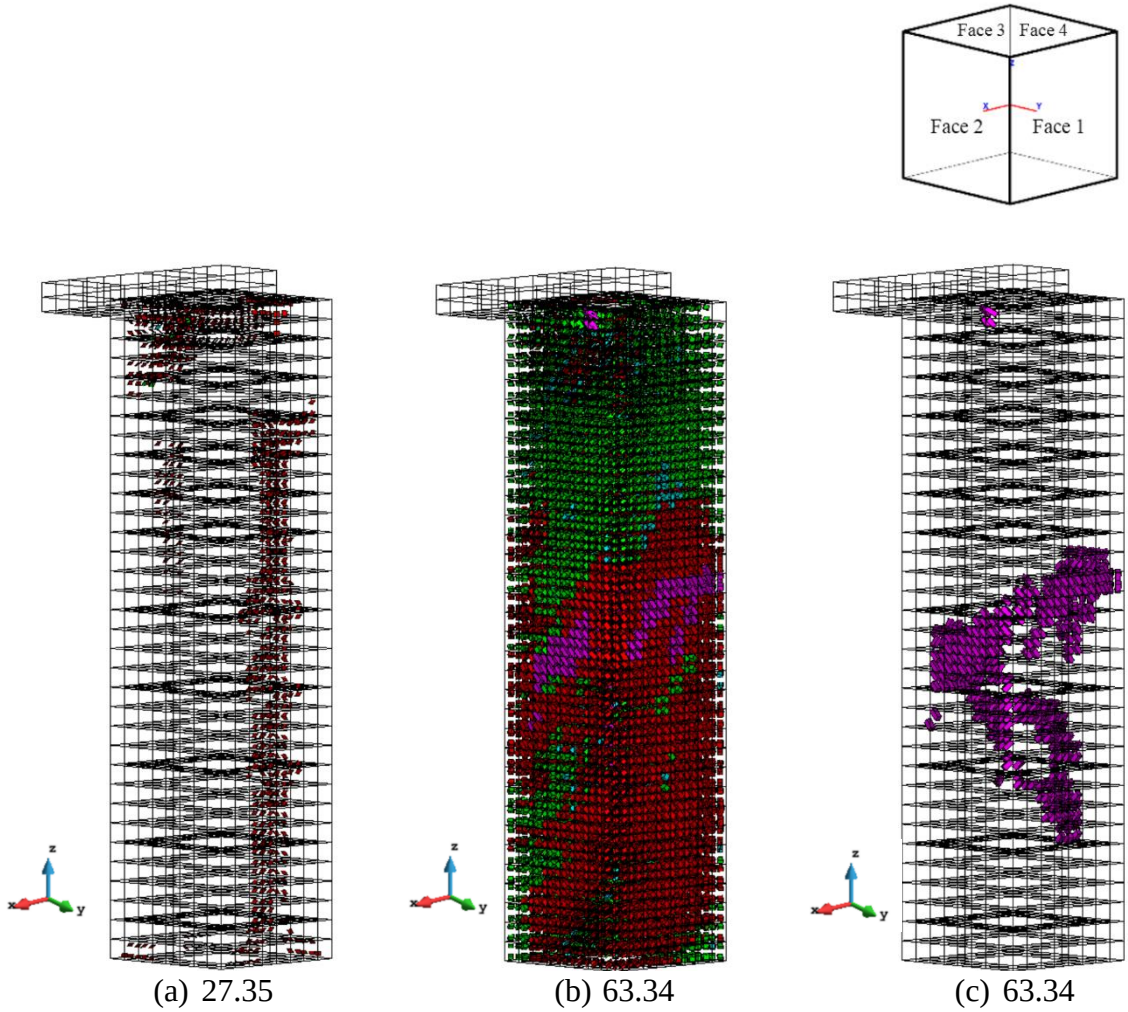

Crack status: Red: Crack opening, Green: Crack closing, Blue: Closed crack, Cyan: Crack reopening, Pink: Fully open.

Figure 3.12 Crack pattern of L10S8_50 (a) Concrete crack initiation (b) Peak moment with all crack status (c) Peak moment with fully opened cracks

3.2.3. MESH REFINEMENT

In a finite element analysis, the mesh size plays an important role to assure accuracy of results. This is mainly relevant in the material nonlinear analysis of brittle materials, like concrete, and when using smeared crack approaches, where a characteristic length needs to be used for bridging the concept of tensile strain to crack width. In order to set the mesh size necessary for the analysis and to capture the important variations and changes in the model, a sensitivity analysis is performed. Each analysis has different mesh size, namely 25 mm (L10S8_25), 50 mm (L10S8_50) and 100 mm (L10S8_100) for concrete (solid elements of cubic geometry) and reinforcement elements. The number of elements, nodes and crack bandwidth (evaluated as the cube root of the volume of the integration point) in the respective models are presented in Table 3.1, and the cross section of the beams with the different meshes are shown in Figure 3.13. The number of hexahedron elements are increased 8 times when the mesh size is decreased from 100 mm to 50 mm and 64 times when decreased from 100 mm to 25 mm, in each element.

Table 3.1 Details of the model for mesh refinement

	25 mm	50 mm	100 mm
Model name	L10S8_25	L10S8_50	L10S8_100
Total nodes	18905	4239	1719
Hexahedron elements (concrete)	13056	1632	204
Linear elements (reinforcements)	1888	1616	1288
Quadrilateral elements (steel loading section)	592	232	118
Crack bandwidth (mm)	12.5	25	50

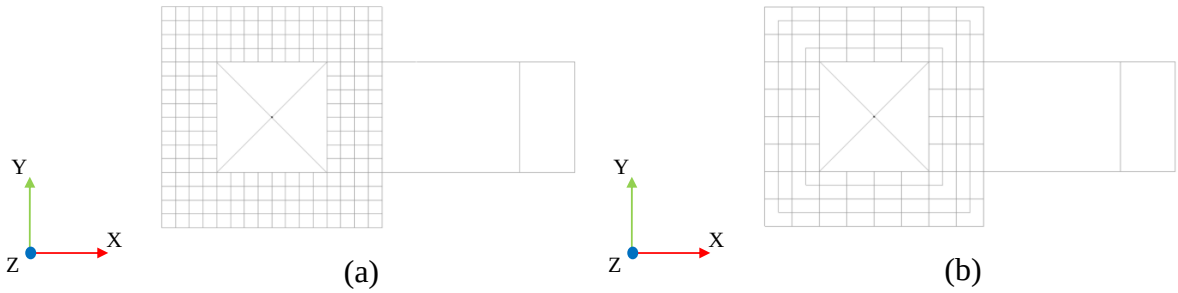

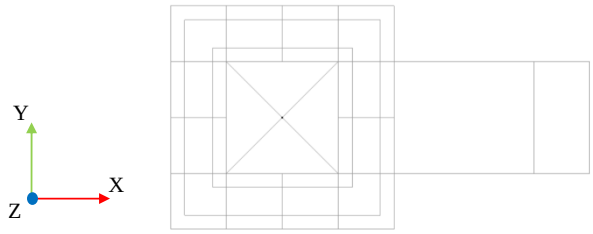

(c)

Figure 3.13 Finite element cross section: (a) L10S8_25 (b) L10S8_50 & (c) L10S8_100

The maximum moment and maximum angle of rotation for each model obtained from the analysis is shown in Figure 3.14. Model L10S8_25 (with 25 mm mesh size) predicts the maximum moment and maximum angle of rotation with respect to all the three models. Model L10S8_100 with maximum mesh size (100 mm) is not able to yield similar results to those obtained with L10S8_50 or L10S8_25 because of the bigger size of the mesh elements which fail to capture the non-linear local behaviour of the beam. However, in case of L10S8_25 (25 mm mesh size) the elements are 4 times smaller than model L10S8_100, providing more local predictions. The results of model L10S8_50 are much closer to those of L10S8_25, suggesting convergence of the results already at these mesh sizes. Based on these results, it is practical and convenient to use the model with 50 mm mesh size than 25 mm resulting in reduced calculation time and data accumulation.

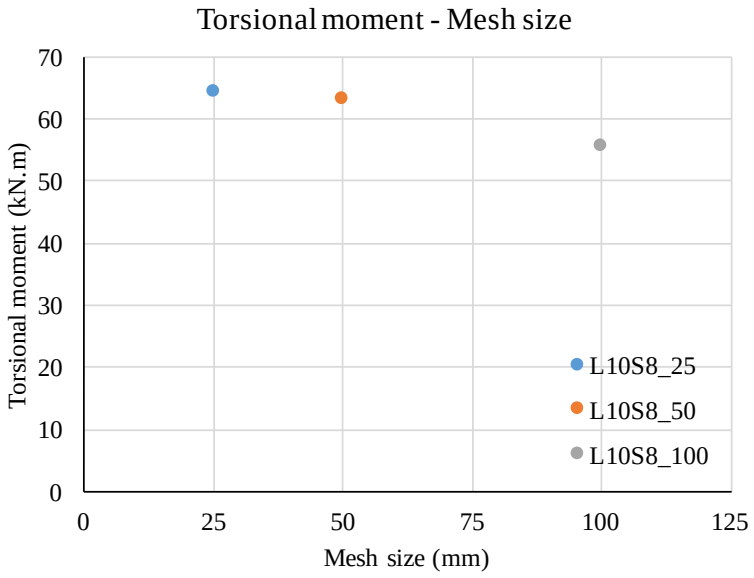

(a)

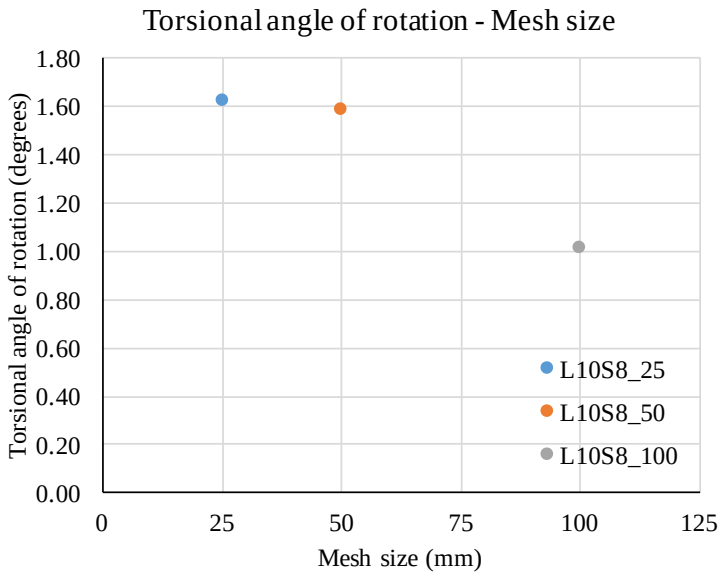

(b)

Figure 3.14 (a) Torsional moment *vs.* mesh refinement (b) Torsional angle of rotation *vs.* mesh refinement

Model L10S8_25 predicts 2.11% higher angle of rotation, 1.73% higher moment and 10.50% higher crack width with respect to L10S8_50 and model L10S8_100 predicts 56.72% lower angle of rotation, 14.06% lower maximum moment and 16.02% lower crack width in comparison with model L10S8_50. The maximum crack width, maximum moment and maximum angle of rotation of all the models are shown in Table 3.2.

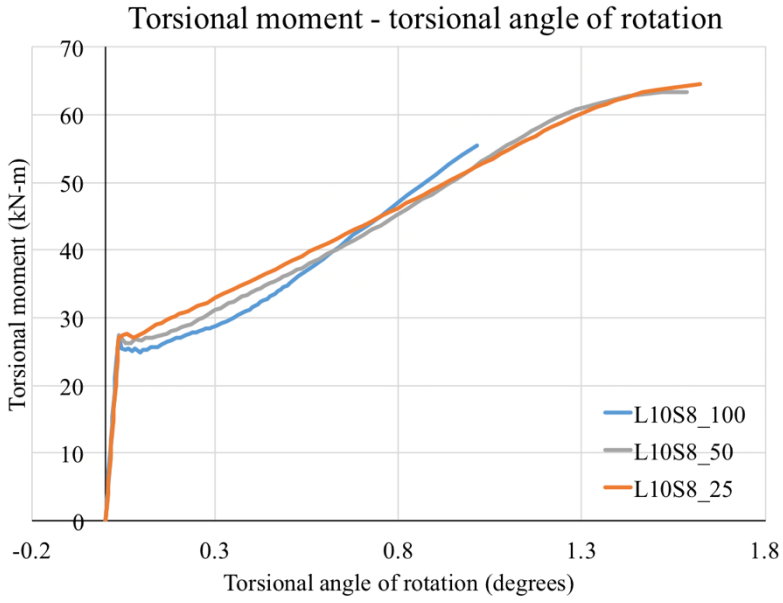

Figure 3.15 Comparison of torsional moment-angle of rotation for L10S8_25, L10S8_50 & L10S8_100

Table 3.2 Maximum crack width & maximum moment for L10S8_25, L10S8_50 & L10S8_100

Sl. No.	Model name	Mesh size (mm)	Maximum crack width (mm)	Maximum torsional moment (kN·m)	Maximum angle of rotation (deg.)
1	L10S8_100	100	0.257	55.548	1.013
2	L10S8_50	50	0.298	63.357	1.587
3	L10S8_25	25	0.333	64.473	1.621

3.2.4. PARAMETRIC ANALYSIS

In order to study the effect of transverse reinforcement, longitudinal reinforcement and the concrete strength class on the torsional behaviour of thin walled tubular reinforced concrete beams, a parametric analysis is carried out. The transverse reinforcement is varied with diameters of 6 mm, 8 mm and 10 mm, while diameters of 8, 10 and 12 mm were considered for the longitudinal reinforcement. The resulting torsional moment *vs.* torsional angle of rotation graph for the variation of the diameters of the transverse and longitudinal reinforcement is shown in Figure 3.16a and Figure 3.16b. The torsional stiffness and moment capacity of the beam have increased with the diameter of both types of reinforcements after torsional cracking moment, while the steel yielding initiation of the reinforcement has been postponed for larger torsional angle. The maximum angle of rotation, maximum torsional moment, longitudinal reinforcement ratio and transverse reinforcement ratio for all the beams are summarized in Table 3.3.

Table 3.3 Maximum angle of rotation and maximum torsional moment for variation of longitudinal and transverse reinforcements

Sl. No.	Beam	Max. torsional Angle (degrees)	Max. torsional moment (kN.m)	Increase in torsional moment	ρ_{sl}	ρ_{sw}
	Transverse variation					
1	L10S6	1.316	52.855	-19.87%	0.571	0.283
2	L10S8	1.587	63.357	0.00%	0.571	0.502
3	L10S10	1.602	72.297	12.37%	0.571	0.785

	Longitudinal variation					
1	L8S8	1.358	51.916	-22.04%	0.365	0.502
2	L10S8	1.587	63.357	0.00%	0.571	0.502
3	L12S8	1.495	74.533	14.99%	0.822	0.502

ρ_{sl} = *longitudinal reinforcement variation &* ρ_{sw} = *transverse reinforcement ratio*

$$\rho_{sl} = \left(\frac{A_{sl}}{(b_w d_s) - (b_h d_h)}\right)100 \, , \rho_{sw} = \left(\frac{A_{sw}}{b_w s_w}\right)100$$

Where A_{sl} is the area of longitudinal reinforcement, b_w is breadth of the section, d_s is internal lever arm, b_h is breath of hollow section, d_h is depth of hollow section, A_{sw} is area of transverse reinforcement and s_w is spacing of stirrups.

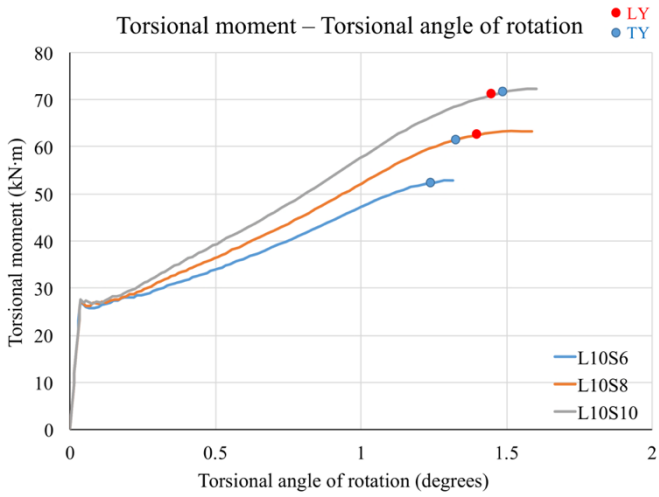

(a)

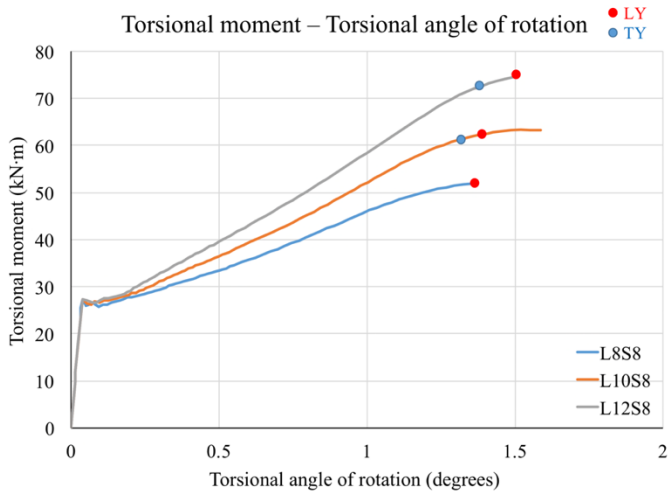

(b)

Red dot: longitudinal reinforcement yielding, blue dot: transverse reinforcement yielding

Figure 3.16 Torsional moment *vs.* torsional angle of rotation (a) Transverse reinforcement variation & (b) Longitudinal reinforcement variation

The increase in transverse reinforcement ratio by 36% in model L10S10 increases the maximum torsional moment carrying capacity by 12.37% (comparing with beam L10S8). Similarly, the increase in longitudinal reinforcement ratio by 30% increases the maximum torque by 15%. The stiffness of the beam in the elasto-plastic region, after torsional cracking moment up to the yielding of the reinforcement, increases with the increase in longitudinal as well as transverse reinforcement ratio, i.e., higher the reinforcement ratio, stiffer is the beam behaviour and vice versa. The blue dots indicate the yielding of the transverse reinforcement and the red dots indicate the yielding of the longitudinal reinforcement. The increase in the torsional moment capacity of the beams takes place up to a certain maximum value limited by concrete crushing (compressive struts). As a result, both the variation of longitudinal and transverse reinforcement ratio increases the torsional moment.

The torsional moment *vs.* torsional angle of rotation for the variation of concrete compressive strength for different strength classes according to Eurocode 2 (2004) is also analysed and presented in Figure 3.17. The analysis for beam L10S8 is investigated with strength classes of C12/15, C20/25, C25/30 and C40/50, and their corresponding modulus of elasticity, tensile strength, compressive strength for concrete, fracture energy and the tensile softening diagram is updated for respective analysis from the code.

The torsional cracking moment of each beam increases with the increase in concrete tensile strength, according to the respective strength class. However, after torsional cracking moment, the beam capacity is governed by the reinforcements. Hence a sudden drop in the response is obtained, where the load carrying capacity is shifted from concrete to reinforcements. Irrespective of the concrete strength class, the ultimate torsional resistance of all the beams should be in the same range, since all the beams have the same reinforcement configuration, observed only in C12/15 & C20/25, since the rest of the analysis have convergence problems.

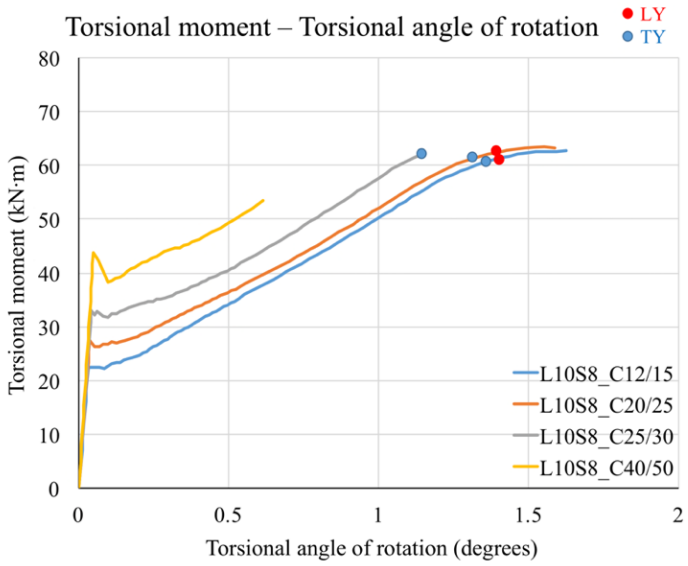

Red dot: longitudinal reinforcement yielding, blue dot: transverse reinforcement yielding

Figure 3.17 Torsional moment *vs.* torsional angle of rotation for concrete compressive strength variation

3.3. STRENGTHENING PROPOSALS AND RESULTS

According to the results obtained in the previous sections, four types of strengthening configurations are analysed numerically. The strengthening system consists of CFRP laminates in the longitudinal and in the transverse directions, with different reinforcement ratios. The transverse laminates are spaced at 65 mm $\left(s = \left(\frac{1}{3}\right)200 = 65 \right)$ and 40 mm $\left(s = \left(\frac{1}{5}\right)200 = 40 \right)$, while the longitudinal laminates are spaced at 135 mm $\left(s = \left(\frac{1}{3}\right)400 = 135 \right)$ and 80 mm $\left(s = \left(\frac{1}{5}\right)400 = 80 \right)$. The cross section and the isometric section of each strengthening system is shown in Figure 3.18. The transverse laminates are applied only in the central study area of 1000 mm, whereas the longitudinal laminates are applied throughout the beam length. The description of the configurations are as follows:

i. S_L2S5 (Strengthening 1): one transverse CFRP laminate is placed in the central 1000 mm region between two steel stirrups on each wall at a distance of 65 mm. Two longitudinal laminates are spaced at 135 mm on each wall;

ii. S_L2S10 (Strengthening 2): two transverse CFRP laminates are placed in the central 1000 mm region between two steel stirrups on each wall at a distance of 40 mm. Two longitudinal laminates are spaced at 135 mm on each wall;

iii. S_L4S5 (Strengthening 3): one transverse CFRP laminate is placed in the central 1000 mm region between two steel stirrups on each wall at a distance of 65 mm. Four longitudinal laminates are spaced at 80 mm on each wall;

iv. S_L4S10 (Strengthening 4): two transverse CFRP laminates are placed in the central 1000 mm region between two steel stirrups on each wall at a distance of 40 mm. Four longitudinal laminates are spaced at 80 mm on each wall.

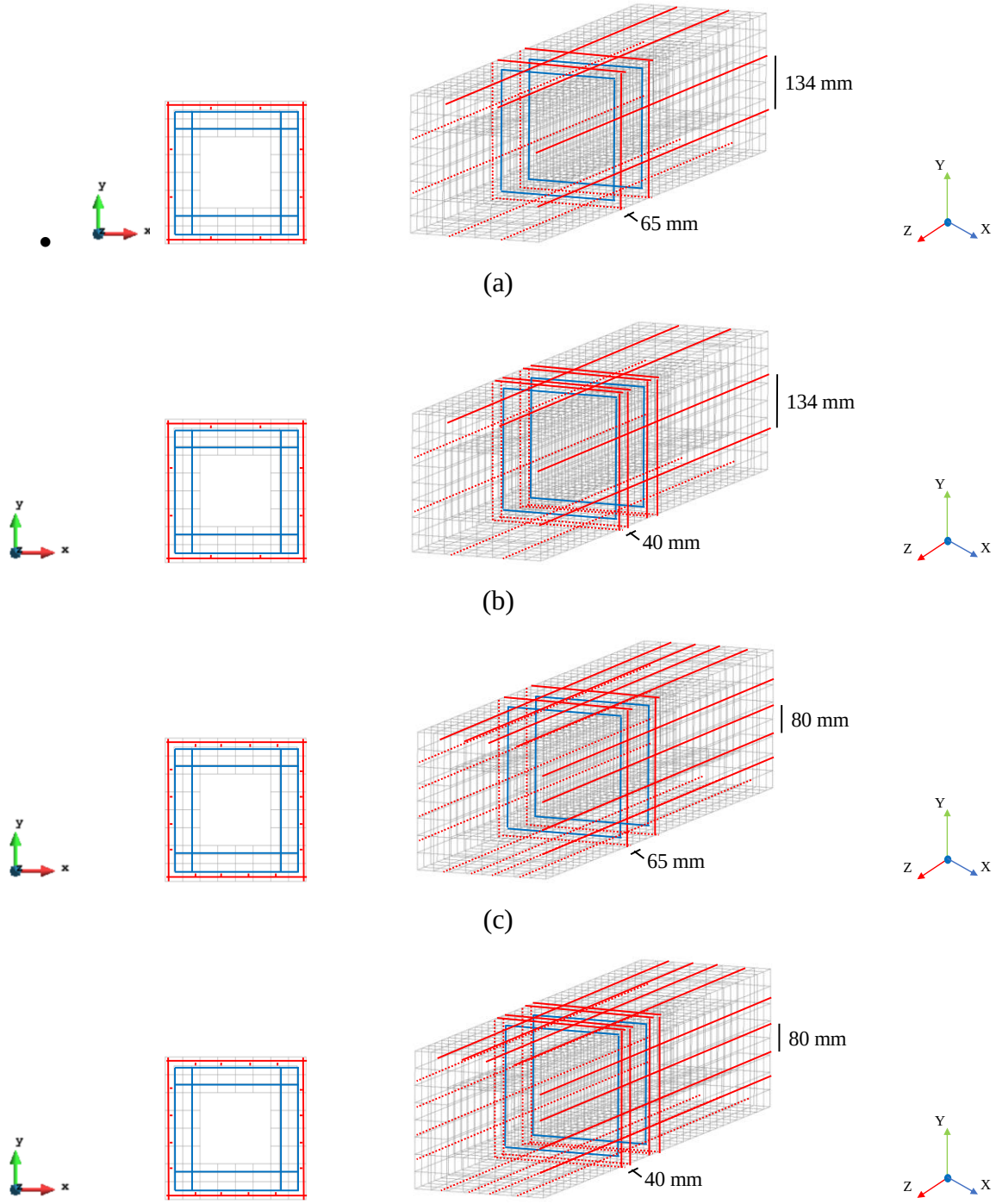

Figure 3.18 Strengthening proposals (a) S_L2S5 (b) S_L2S10 (c) S_L4S5 & (d) S_L4S10

The cross-section of the CFRP laminates measures 10 mm × 1.4 mm, with a tensile strength of 2500 MPa and modulus of elasticity of 160 GPa. The longitudinal CFRP laminates are placed deeper, close to the transverse steel reinforcements at a depth of 15 mm (centre of the laminate), and the transverse laminates are placed close to the outer surface at a depth of 5 mm.

3.3.1. RESULTS

Figure 3.19 shows the torsional moment *vs.* torsional angle of rotation of all the beams calculated according to the method described in section 3.2.2 and the results are presented in Table 3.4. All the strengthened beams have increased torsional moment carrying capacity and stiffness in the elasto-plastic stage of the response. The increase is directly proportional to the amount of CFRP reinforcement ratios: the higher the strengthening ratios, the higher the increase in the moment capacity and vice versa. The yielding of the longitudinal steel reinforcement and the transverse steel reinforcement in each beam are indicated by red and blue dots.

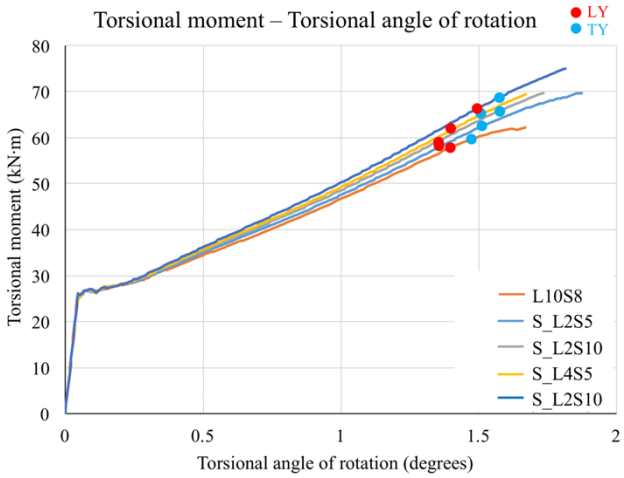

Red dot: longitudinal reinforcement yielding, blue dot: transverse reinforcement yielding

Figure 3.19 Torsional moment *vs.* torsional angle of rotation for strengthened beams

Table 3.4 Results of strengthened models

Model beam	Max. Torsional moment (kN·m)	Max. Angle of rotation (degrees)	Moment at rotation of 1.67 degrees (kN·m)	Increase in torsional moment (%)
Ref_4S	62.18	1.67	62.18	-
S_L2S5	69.64	1.87	66.25	6.55
S_L2S10	69.65	1.73	68.50	10.17

S_L4S5	69.44	1.67	69.44	11.68
S_L4S10	74.97	1.81	71.39	14.81

The crack patterns of all the strengthened beams (S_L2S5, S_L2S10, S_L4S5 and S_L4S10) and the reference beam are shown in Figure 3.20, at a rotational angle of 1.66°. Only fully opened cracks are presented in the figures. The control in crack propagation is clearly visible in Figure 3.20, where the number of cracks have drastically reduced in the beam with the highest degree of strengthening in comparison to that with the minimum level of NSM strengthening. This is due to the higher reinforcement ratios and effectiveness of the CFRP laminates in increasing torsional moment and controlling crack growth.

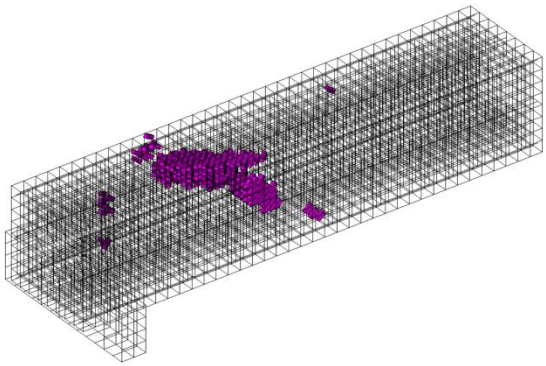

(a) Ref_4S

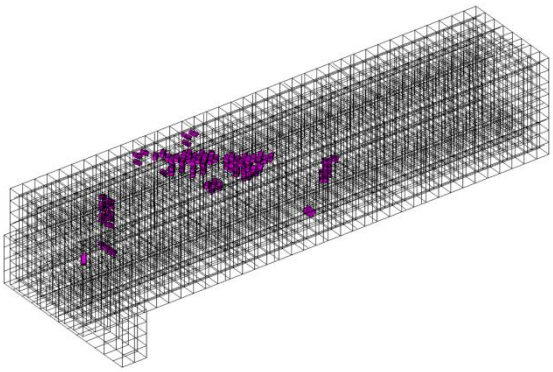

(b) S_L2S5

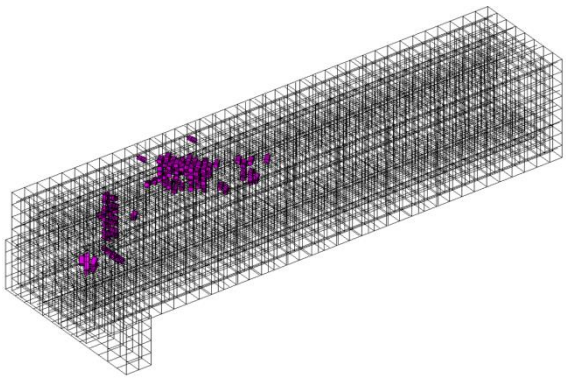

(c) S_L2S10

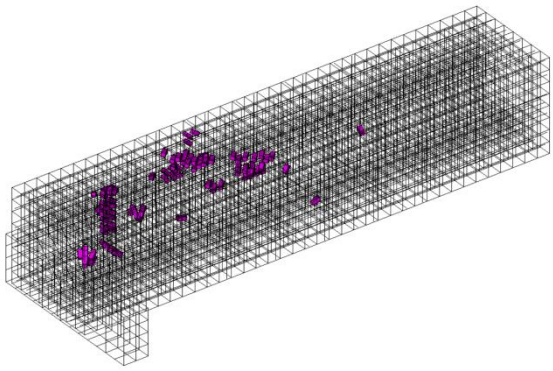

(d) S_L4S5

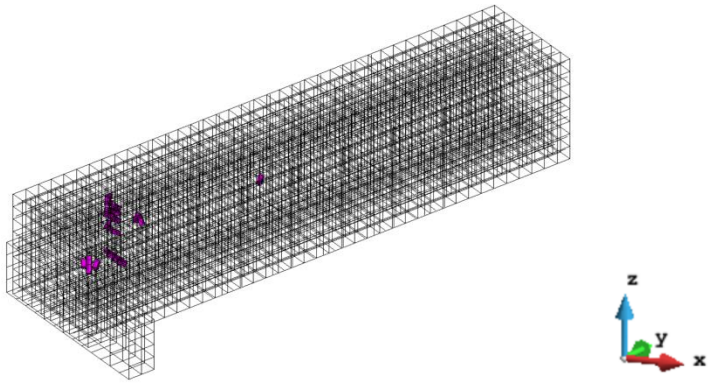

(d) S_L4S10

Figure 3.20 Crack pattern (a) S_L2S5 (b) S_L2S10 (c) S_L4S5 & (d) S_L4S10

In order to study the effectiveness of fibre reinforced polymer laminates, a FE analysis is performed by varying the modulus of elasticity with values of 60 GPa, 160 GPa and 240 GPa. The corresponding results of torsional moment *vs.* torsional angle of rotation for E_f variation are presented in Figure 3.21a. The graph is split into four parts:

i. The linear phase of the $M_t - \theta_t$ response, where neither the CFRP nor the steel reinforcements have any contribution, the load is purely resisted by the concrete alone (observed in the graph);

ii. After torsional cracking moment, it is followed by crack propagation phase, where there is an abrupt activation of the reinforcement contribution (both steel and CFRP);

iii. Elasto-plastic stage where concrete contribution is minimal and most of the torsional resistance is ensured by reinforcements;

iv. Yielding of steel reinforcements where the increment of the torsional capacity is mainly provided by the CFRP laminates, observed by the change in stiffness in the last stage.

The modulus of elasticity of the FRP material has a major influence on the stiffness response of the overall behaviour of the beam: the higher the E_f of the FRP material, the stiffer the response and the earlier the FRP material starts resisting the torsional moment. Comparing the tensile stresses in fibre reinforced polymers at an angle of 1.72° in beam S_L2S5 (E_f = 60 GPa) and S_L2S5 (E_f = 160 GPa), the stress is 1.41 times higher in S_L2S5 (E_f = 160 GPa). Similarly, between S_L2S5 (E_f = 60 GPa) and S_L2S5 (E_f = 240 GPa), beam S_L2S5 (E_f = 240 GPa) the stress is 2.16 times higher.

Figure 3.21(b), shows the maximum crack width in each of the three analyses with varying E_f The crack width (w) is calculated as a product of crack normal strain $(\varepsilon_{n,\max}^{cr})$ to the crack bandwidth (l_b), as shown in equation 3.2, where $l_b = \sqrt[3]{V_{IP}}$, V_{IP} being the volume of the integration point. As expected, the beam with lower modulus of elasticity had the maximum crack width causing an early failure.

$$w = \varepsilon_{n,\max}^{cr} l_b \qquad 3.2$$

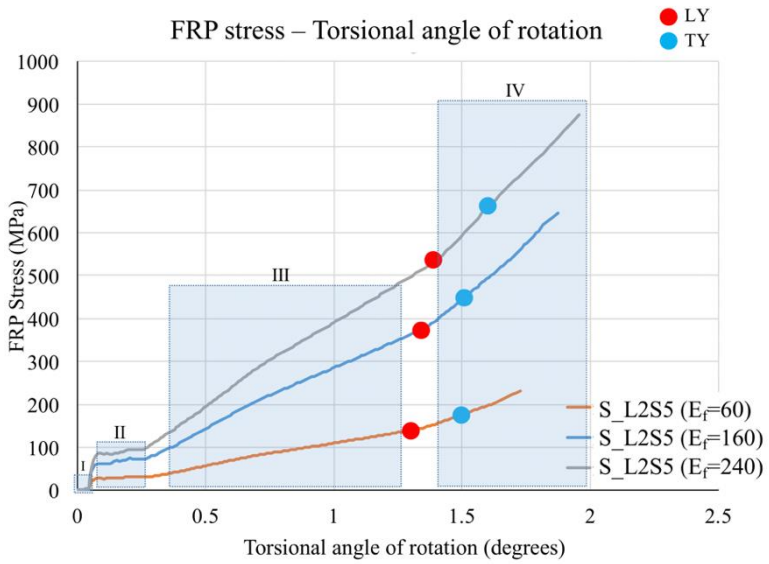

(a)

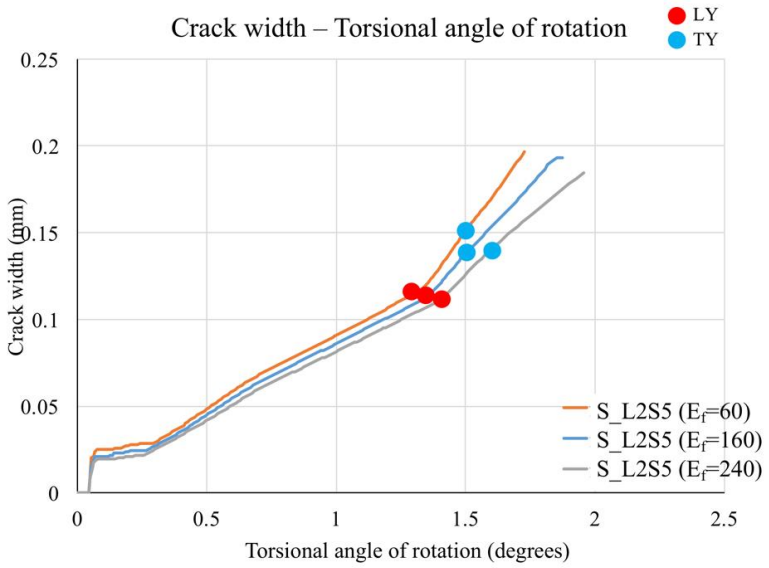

(b)

Red dot: longitudinal reinforcement yielding, blue dot: transverse reinforcement yielding

Figure 3.21 (a) Evolution of stress in FRP laminates & (b) Crack width opening *vs.* torsional angle of rotation

3.3.2. APPLICATION OF PRESTRESS:

The application of NSM FRP systems seems to assure relatively small increase of torsional capacity for loading conditions corresponding to the SLS conditions. As a result, beam S_L2S5 is analysed by applying both the longitudinal and transverse CFRP laminates with a prestress level equal to 50% of the ultimate tensile capacity, since according to Rezazadeh, Ramezansefat, and Barros (2016) this is the maximum prestress level in terms of strengthening effectiveness and ductility performance. The $M_t - \theta_t$ relationship for the passive and prestress situations are compared in Figure 3.22a. The benefits of applying the FRP with a certain prestress level is quite evident as this increases significantly the torsional capacity for SLS conditions, delaying yield initiation of the reinforcements and decreasing the maximum crack width. The relationship between the crack width and θ_t is shown in Figure 3.22b. As seen, the FRP laminates are effective in restricting the crack width after yield initiation, observed by the change in FRP stiffness. By taking advantage of the prestress that can be applied to FRP's and adopting an innovative type of NSM CFRP laminate (Barros et al. 2017), a new strengthening NSM-based active technique can be developed for the shear and torsional strengthening of tubular type bridge sections (Figure 3.22c).

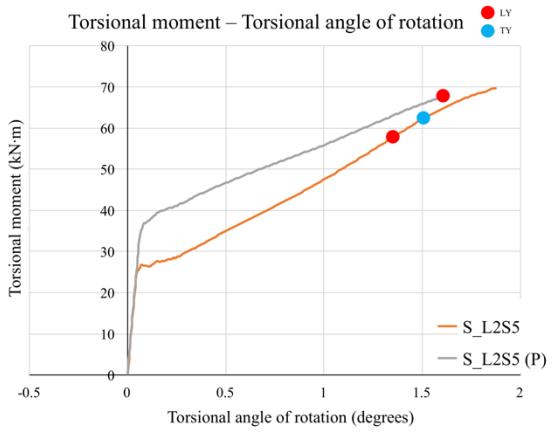

(a)

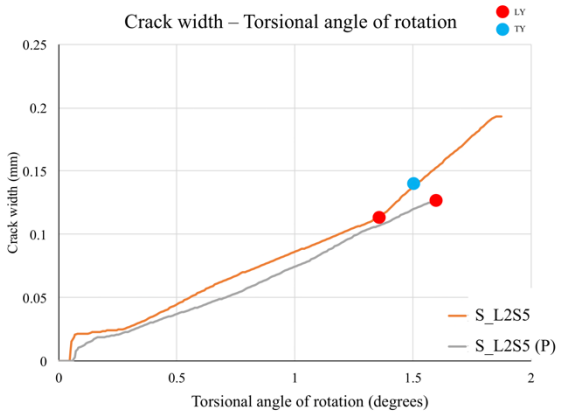

(b)

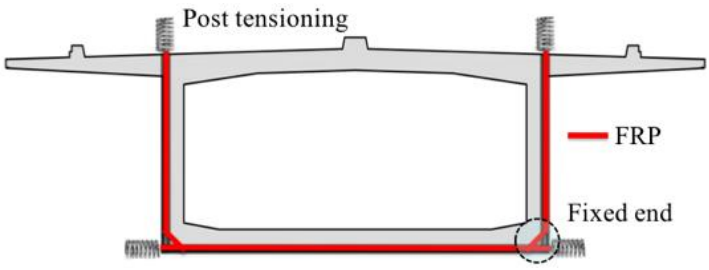

(c)

Figure 3.22 (a) Torsional moment *vs.* torsional angle of rotation of beam S_L2S5 with and without prestress (b) Crack width *vs.* torsional angle of rotation and (c) Future proposal of pre-stress application

3.4. EXPERIMENTAL TEST SETUP

As the proposed experimental test setup for the torsional beam testing is new, there is a need to analyse the behaviour of the frames and all components of the test setup in order to ensure that all issues are resolved before manufacturing the testing rig. For achieving this, a linear finite element analysis is carried out by simulating the whole experimental test setup. It includes beams, supports in the fixed end and the loading end (partial), all connections including bolts and steel plates. The final model of the FE test setup is as shown in Figure 3.23. The setup consists of a loading end and a fixed end, the former to apply the load, by introducing a torsional moment, while the latter for clamping the other extremity of the beam. The loading end in this model consists of a steel section as shown in Figure 3.23, the beam and a pinned support on which the beam rests. Below the pinned support, a circular arc bearing is placed, made of steel creating pure rotation of the plane as well as the beam. In order to simulate this plane, the nodes are restricted in y-direction by describing special co-ordinate system to the auxiliary nodes. Two rollers will be placed below the circular arc bearing, allowing the elongation or shortening of the beam. The rollers are supported on a steel section, fixed to the reaction floor slab.

In the fixed end, the beam rests on a steel section fixed to the concrete block by four metallic bolts of 32 mm. To analyse the complete fixity, a hydraulic jack is also placed in the centre of the steel support to adjust the height of the beam during testing. To restrict any movement or rotation at this end, a steel I-section forming a frame is placed on top of the beam. The base of the frame consists of a system of steel plates and C-sections.

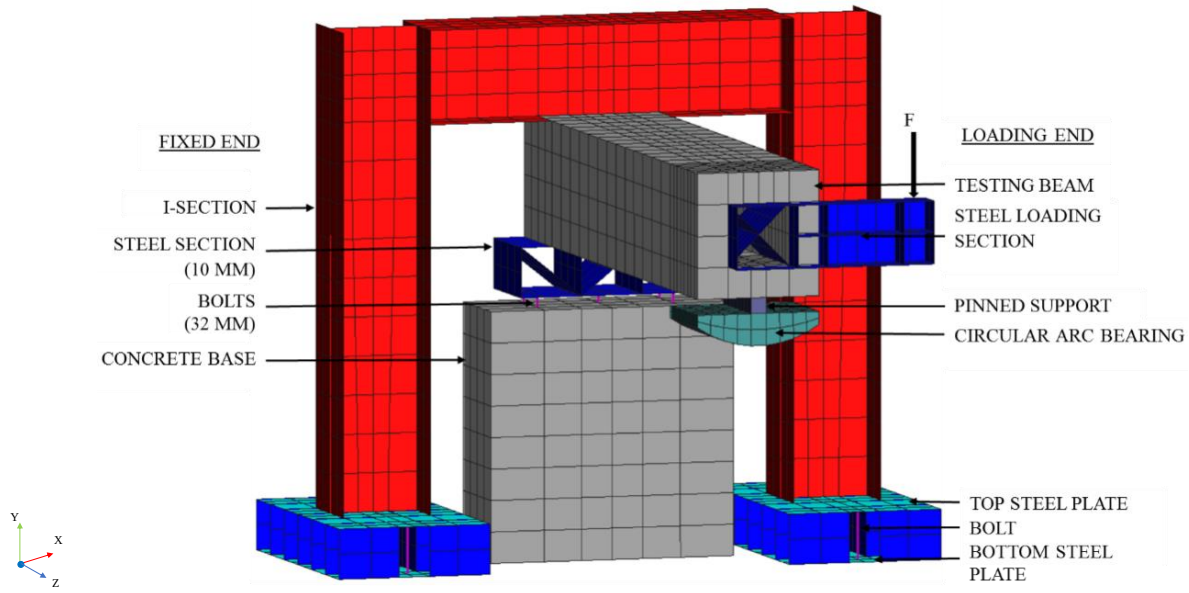

Figure 3.23 Finite element model of the proposed experimental test rig

The beam is simulated by 8-node solid hexahedra elements (Figure 3.6), reinforcements by 2-node 3D embedded cable, steel plates and I-sections by quadrilateral shell elements and bolts by 3D truss elements. Four bolts of 32 mm diameter connect the setup to the reaction floor, to simulate this the bolts are fixed in all co-ordinate directions and all the nodes of the bottom steel plate are restricted in Y-direction. The model consists of 391 hexahedra elements, 1381 linear elements (reinforcements and bolts) and 1177 quadrilateral shell elements (I-section, steel plates and steel loading section) with a total of 2949 nodes. Concrete and steel are assigned linear material property with the values presented in Section 3.2.1 as well as the other conditions described for the analysis.

A 3D multidirectional smeared crack model (Ventura-Gouveia et al. 2008) available in FEMIX is used for the numerical simulations. The Gauss-Legendre 2×2×2 integration scheme allowing the formation of a maximum of two cracks at each integration point is adopted. A modified Newton-Raphson iterative algorithm is applied, and the stiffness matrix is updated at each increment. An independent path behaviour (dependent on the previous converged step) is used with the tolerance of $1x10^{-3}$ in terms of energy for convergence criterion. The analysis is performed in displacement control under arc-length method. The reinforcement is assumed to be perfectly bonded to concrete elements.

The maximum load (150 kN), considering a safety factor of 2 from the results of the strengthened beam analysis (Section 3.3), is applied on the steel loading section of the beam to

study the behaviour of the experimental test set up. The boundary conditions adopted in the model are as follows:

i. The bottom steel plate is fixed in the z-direction;
ii. Four bolts (2 shown in the front and 2 in the back are not seen) in between the C-sections are fixed in all directions to simulate the fixity to the floor of the laboratory (0.80 m thick).

Figure 3.24 shows the deformation and displacements of the model in all directions. The overall deformation of the experimental setup for the load (150 kN·m) is presented in Figure 3.24a with a magnification factor of 1.5. The displacement of the model in X-direction is shown in Figure 3.24b where the maximum positive displacement is 0.67 mm (red colour) and a minimum of 1.30 mm (maximum negative presented in blue colour) is obtained. Similarly, the displacement in Y-direction has a maximum of 0.88 mm and a minimum of 0.76 mm, and the displacement in Z-direction with a maximum of 0.65 mm and a minimum of 3.92 mm are obtained, shown in Figure 3.24c & d.

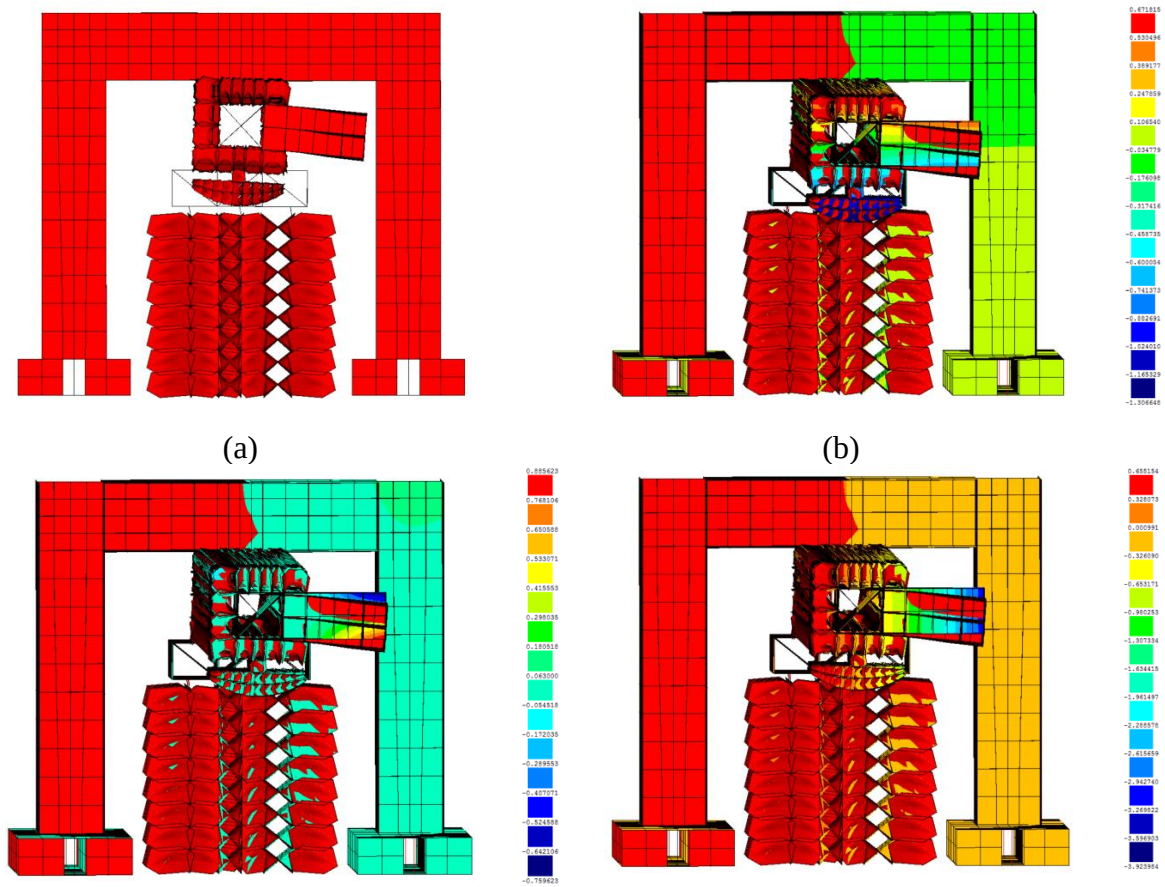

(a) (b)

(c) (d)

Figure 3.24 FE results of experimental setup (a) Deformed mesh (b) Displacement in x (c) Displacement in y (d) Displacement in z

According to the results obtained, it is observed that the proposed experimental test setup is viable to be executed in the laboratory. The concrete base, steel box-sections, bolts, steel plates, C-sections and I-sections are within the permissible linear limits of the corresponding elements. The stresses and strains developed near the fixed end, especially in the contact surfaces of the beam with the I-section (top) and the steel section (bottom) is able to provide the complete fixity of the beam during testing, for maximum torsion considering the safety factor.

3.5. CONCLUSIONS

The following conclusions are obtained based on the finite element analysis described above:

- The adopted numerical model is capable of predicting the torsional behaviour of thin-walled tubular reinforced concrete beams;
- The proposed strengthening configurations can effectively improve performance in terms of torsional moment carrying capacity (7%-15%) and stiffness after torsional cracking;
- All strengthening configurations with varied transverse and longitudinal CFRP laminates arrest the crack propagation;
- The variation of E_f corresponds to its contribution to the torsional capacity;
- The pre-stressed CFRP laminates increases the torsional capacity at serviceability limit state, delaying the yield initiation and reducing crack width;
- The idealized experimental test setup can be adopted in the laboratory to perform the torsional tests.

CHAPTER:

4. EXPERIMENTAL PROGRAM

The present chapter deals with the experimental work performed as part of this research study. The chapter is sub-divided into three main parts: (i) preparation of the specimens, including casting, strengthening and test setup; (ii) detailed analysis of the results, with overall general behaviour of beams, evolution of steel and CFRP strains, crack spacing, comparison of different strengthening configurations (minimum and maximum strengthened beams), analysis of deformation through digital image correlation; and finally (iii) a summary of the main conclusions of the experimental study.

4.1. PREPARATION

4.1.1. SPECIMENS

The experimental programme consists of ten thin walled tubular RC beams with an outer cross section of 400 mm × 400 mm and inner hollow cross section of 200 mm × 200 mm. The total length of each beam is 1900 mm, with the effective torsional study area being the central 1000 mm. As shown in Figure 4.1, the longitudinal reinforcement comprise eight bars with a diameter of 10 mm, while the shear reinforcement is provided by four-legged stirrups with a diameter of 8 mm spaced at 200 mm. Additional stirrups are provided at both ends along a length of 450 mm, with a spacing of 100 mm to avoid premature local failures due to the development of high strain gradients in the loading and clamping regions. Two reference beams are cast with concrete strength class C25/30. One of the reference beams only includes one stirrup in the study zone, whereas the other beam has four stirrups. All the eight strengthened beams are also cast with C25/30 concrete strength class. Each steel stirrup of transverse reinforcement consists of eight legs with two legs on each wall of the beam, as shown in Figure 4.1.

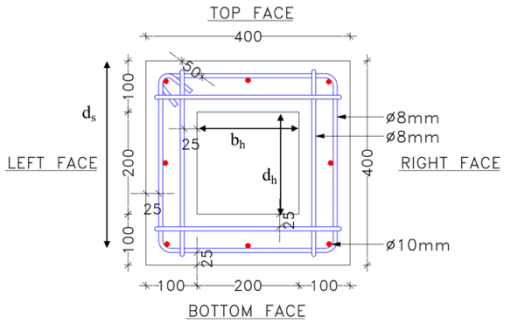

(a)

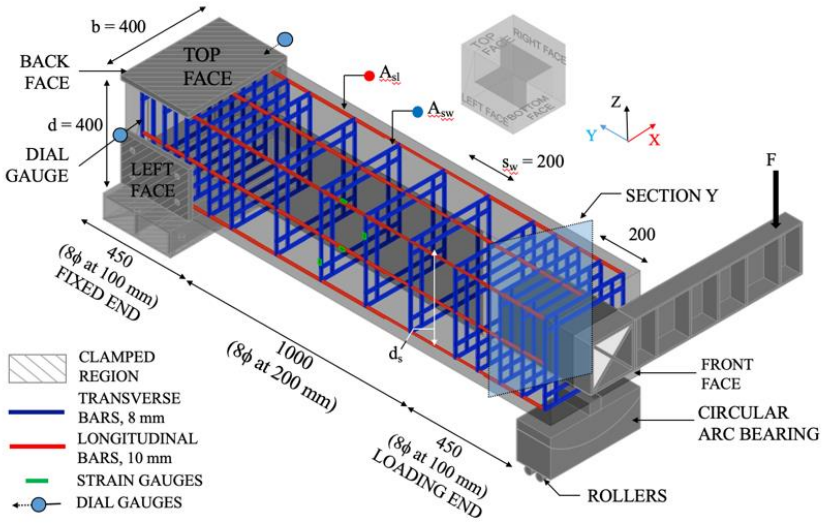

(b)

Figure 4.1 Beam details (a) Cross section (b) Longitudinal details (all dimensions are in mm)

The manufacturing of the beam specimens involved the following steps:

- Preparation of the steel cages (Figure 4.2a);
- Attaching strain gauges on transverse and longitudinal steel reinforcement on top and left faces, closer to the central section of the beam, 850 mm (Figure 4.2b);
- Inserting the steel cages into the formwork (Figure 4.2c);
- Casting the ready-mix concrete.

(a)

(b)

(c)

Figure 4.2 Specimens' preparation (a) Steel cage (b) Strain gauges on steel reinforcement and (c) Formwork

4.1.2. STRENGTHENING

The adopted strengthening configurations are based on the results of the FE analysis (as discussed in section 3.3) and are illustrated in Figure 4.3. Eight strengthening configurations are adopted by changing the longitudinal and transverse CFRP reinforcement strengthening ratios, number of strengthening faces (four and three) and the type of CFRP laminate (straight and L-type). The eight strengthened beams are divided into three series according to the implemented strengthening scheme:

1. Series 1: beams strengthened on all four faces, with varying longitudinal and transverse CFRP reinforcement using straight laminates. The laminates are distributed on the four faces, as shown in Figure 4.3;
2. Series 2: beams strengthened only on three faces (no strengthening on the top face) but otherwise adopting the same scheme as for some of the beams in series 1, as shown in Figure 4.4;
3. Series 3: beams strengthened on four faces using the same minimum and maximum strengthening ratios of series 1, but with specifically manufactured L-type CFRP laminates, as shown in Figure 4.5. To achieve the maximum strengthening configuration (S4FL_L4S10), two laminates are placed in the same slit to avoid the corner discontinuity.

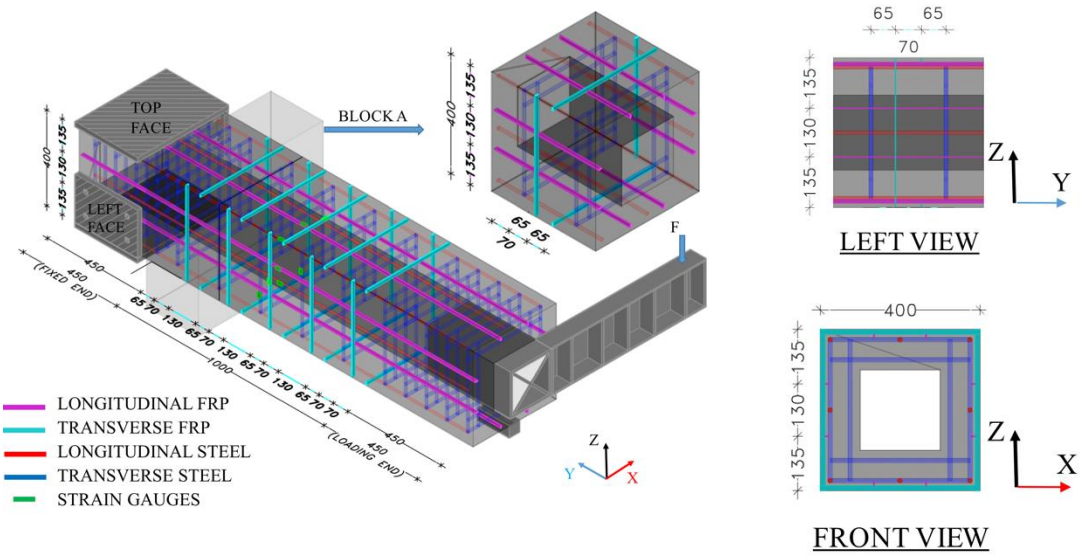
TOP FACE
LEFT FACE
BLOCK A
F
LONGITUDINAL FRP
TRANSVERSE FRP
LONGITUDINAL STEEL
TRANSVERSE STEEL
STRAIN GAUGES
(FIXED END)
(LOADING END)
65 65
70
LEFT VIEW
400
FRONT VIEW

(a)

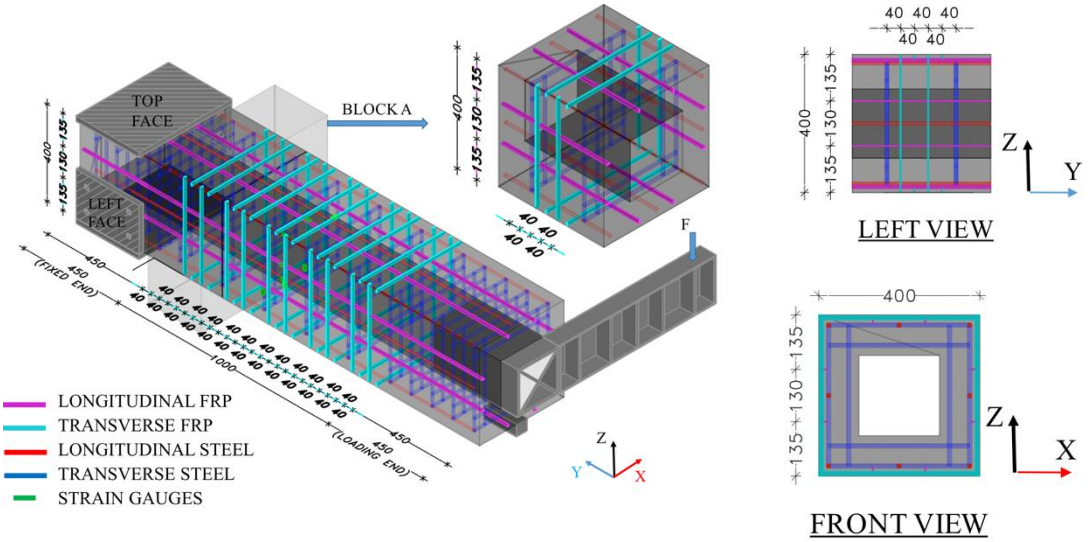
TOP FACE
LEFT FACE
BLOCK A
F
LONGITUDINAL FRP
TRANSVERSE FRP
LONGITUDINAL STEEL
TRANSVERSE STEEL
STRAIN GAUGES
(FIXED END)
(LOADING END)
40 40 40
40 40
LEFT VIEW
400
FRONT VIEW

(b)

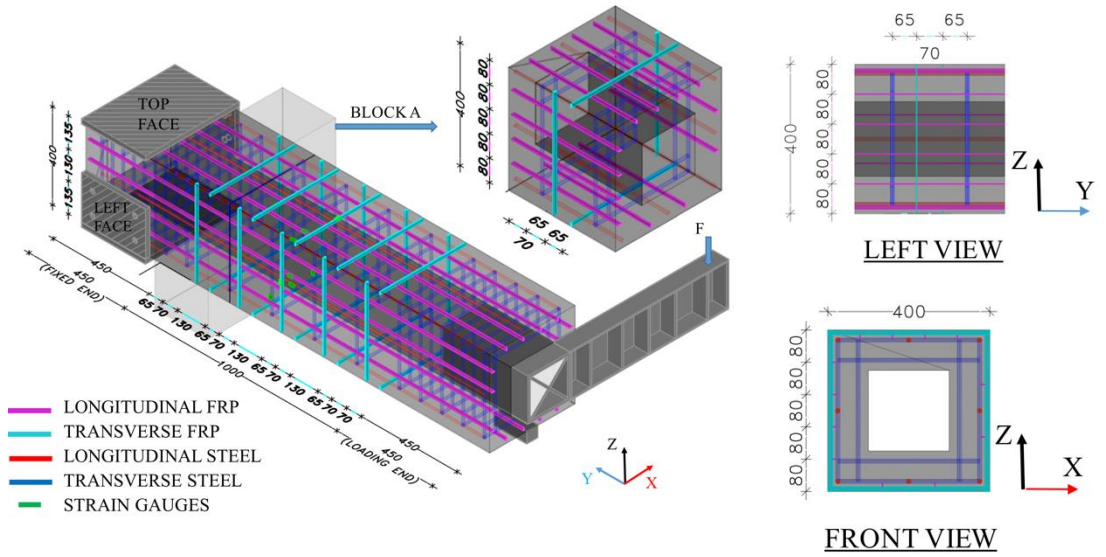

(c)

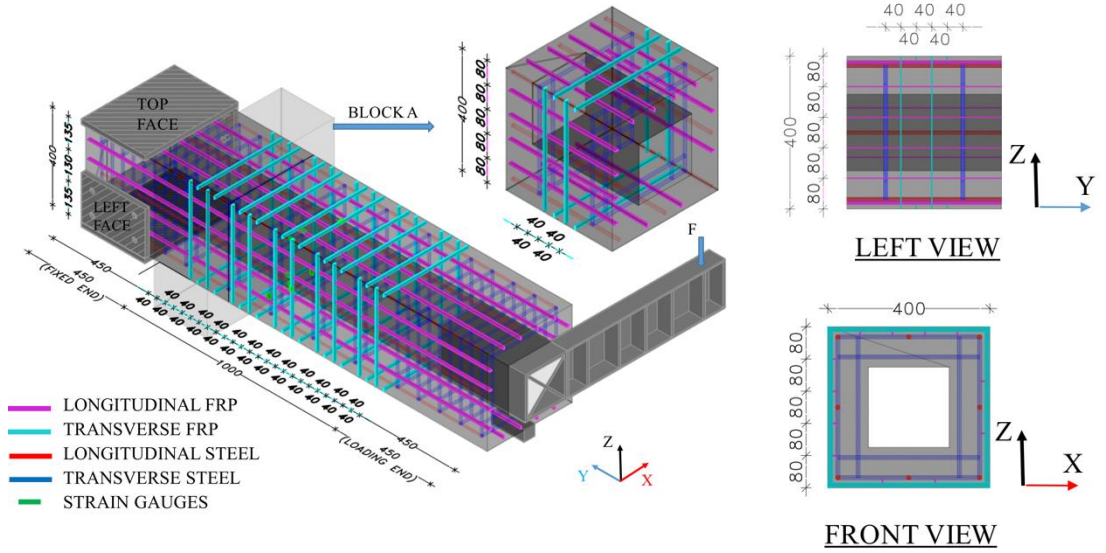

(d)

Figure 4.3 Series one strengthening configurations (a) S4F_L2S5 (b) S4F_L2S10 (c) S4F_L4S5 and (d) S4F_L4S10

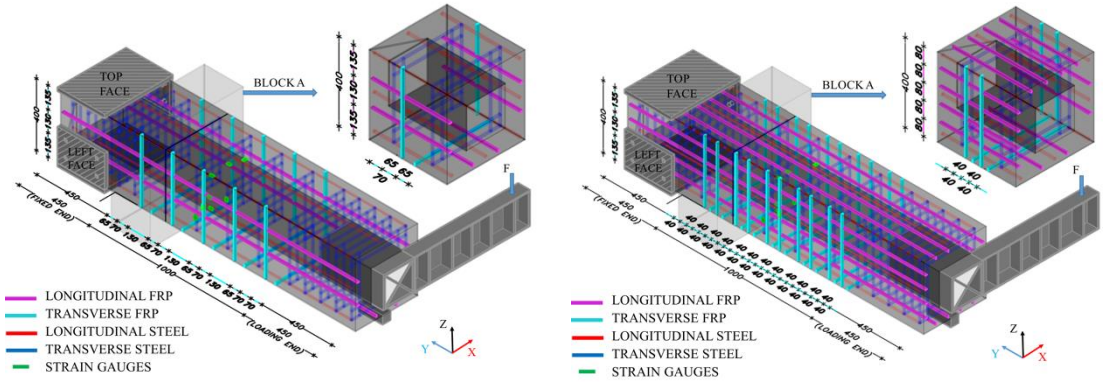

(a) (b)

Figure 4.4 Series two strengthening configurations (a) S3F_L2S5 and (b) S3F_L4S10

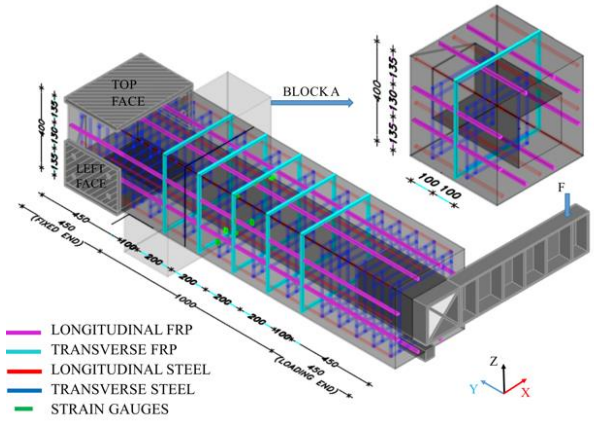

(a)

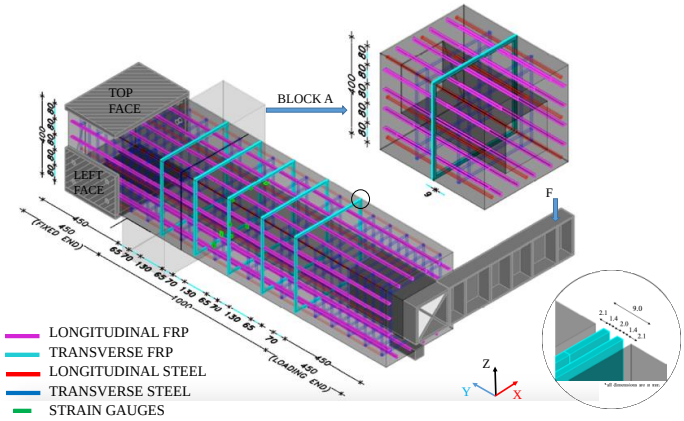

(b)

Figure 4.5 Series three strengthening configurations (a) S4FL_L2S5 and (b) S4FL_L4S10

The total equivalent longitudinal, $\rho_{l,eq}$, and transverse, $\rho_{w,eq}$, reinforcement ratios are calculated according to equation 4.3 and equation 4.4, respectively, which include both the internal steel bars and the CFRP strengthening systems converted to equivalent steel reinforcement ratios (see Figures 4.1 and 4.3 for the meaning of some of the symbols):

$$\rho_{l,eq} = \frac{A_{sl}}{\left(bd_s - b_h d_h\right)} + \left[\frac{A_f E_f}{E_s}\frac{1}{\left(bd_f - b_h d_h\right)}\right] \quad 4.3$$

$$\rho_{w,eq} = \frac{A_{sw}}{\left(b_w s_w\right)} + \left[\frac{A_f E_f}{E_s}\frac{1}{\left(bs_f\right)}\right] \quad 4.4$$

In equations 4.3 and 4.4, A_{sl} is the cross sectional area of the longitudinal steel bars, b and d_s are the breadth and the internal lever arm, A_f and d_f are the cross sectional area and the internal lever arm of the longitudinal CFRP, E_s and E_f are the modulus of elasticity of the steel and CFRP, b_w is the width of the web (100 mm), b_h and d_h are the breadth and depth of the hollow section, A_{sw} (two bars of 8 mm diameter per wall component) and s_w are the cross sectional area and the spacing of the transverse reinforcement. The values of these variables for each specimen are presented in Table 4.1.

Table 4.1 Details of beams, reinforcement and strengthening ratios, and spacing of laminates

Beam	A_{sl} (mm^2)	ρ_{sl} (%)	ρ_{fl} (%)	$\rho_{l,eq}$ (%)	A_{sw} (mm^2)	ρ_{sw} (%)	ρ_{fw} (%)	$\rho_{w,eq}$ (%)	s_{fl} (mm)	s_{fw} (mm)
S4F_L2S5 (Figure 4.3a)	628	0.571	0.096	0.667	100.48	0.502	0.071	0.573	134	65
S4F_L2S10 (Figure 4.3b)	628	0.571	0.096	0.667	100.48	0.502	0.141	0.644	134	40
S4F_L4S5 (Figure 4.3c)	628	0.571	0.192	0.763	100.48	0.502	0.071	0.573	80	65
S4F_L4S10 (Figure 4.3d)	628	0.571	0.192	0.763	100.48	0.502	0.141	0.644	80	40
S3F_L2S5 (Figure 4.4a)	628	0.571	0.072	0.643	100.48	0.502	0.053	0.555	134	65
S3F_L4S10 (Figure 4.4b)	628	0.571	0.144	0.715	100.48	0.502	0.106	0.608	80	40
S4FL_L2S5 (Figure 4.5a)	628	0.571	0.096	0.667	100.48	0.502	0.071	0.573	134	200
S4FL_L4S10 (Figure 4.5b)	628	0.571	0.192	0.763	100.48	0.502	0.141	0.644	80	200

During the strengthening, the longitudinal CFRP laminates are placed deeper (before) than the transverse CFRP laminates. Hence, the grooves for the longitudinal CFRP

laminates are executed with a depth of 22 mm, while those for the transverse laminates are only 12 mm deep. It is noted that the selected groove depths are smaller than recommended in the ACI guidelines (ACI 440.2R-08 2008) due to the small concrete cover, which is representative of existing deficient structures. This, however, does not compromise the bond conditions for the CFRP laminates. Epoxy 220 resin and CFRP laminates with a cross section of 10 mm × 1.4 mm from Clever reinforcement Iberica are used for all the beams. The L-CFRP laminates are maunfactured using conventional strips, which are post-treated to enable bending, as shown in Figure 4.6.

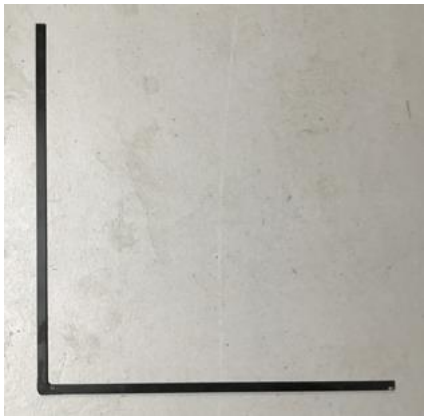

Figure 4.6 L-CFRP laminates used for strengthening in series three

The strengthening involved the following steps:

- Slits of about 5 mm width are opened at the predefined locations using cutting machines;
- The slits are cleaned with compressed air to remove the dust and to ensure proper bonding between epoxy and concrete substrate;
- The CFRP laminates are cleaned with acetone and then the strain gauges are bonded in the pre-established locations;
- The two componets of epoxy are mixed in 1:4 ratio according to the specifications, and applied inside the slits and on the two larger surfaces of the CFRP laminates;
- CFRP laminates are introduced inside the slits and the excess epoxy is removed. The adhesive is let to cure for a week.

Images of beams S4F_L2S10 (series one) and S4FL_L4S10 (series three), before and after strengthening, are shown in Figure 4.7. For the beams of series three, the strengthening was executed while the beams were kept vertical to have easy access to all

four faces at the same time. In case of series one, two faces where strengthened simlutaneously and then the beam was rotated to strengthen the remaining two faces.

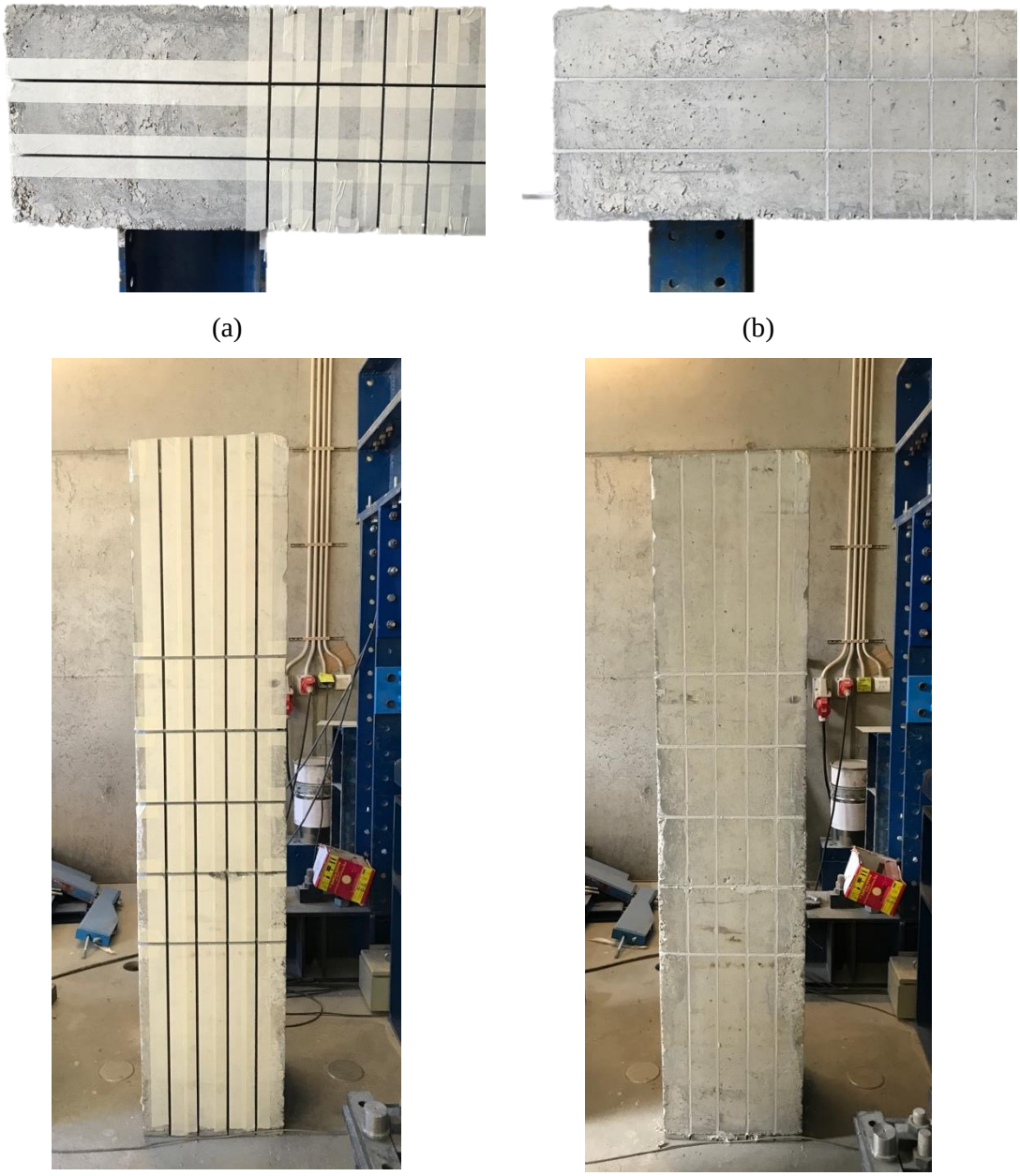

(a) (b)

(c) (d)

Figure 4.7 Strengthening images of beam S4F_L2S10 (a) & (b) and of beam S4FL_L4S10 (c) & (d): (a) & (c) Location of slits (b) & (d) Appearance after strengthening

4.1.3. TEST SETUP

The test setup to perform the experimental investigation on the torsional behaviour of tubular RC elements is shown in Figure 4.8. It consists of a fixed and a loading end mechanical system to ensure, as much as possible, clamping and pure torsional loading

conditions. The fixed end of the beam involves steel profiles and a hydraulic jack to secure and avoid any transversal translations or rotations taking place during the tests. In the front end, the beam rests on a pinned support and a circular arc bearing (CAB), which allows the free rotation of the beam at an arc radius of 350 mm from the centre of the beam's cross section to avoid any additional eccentric forces during the tests. The CAB rests on rollers allowing axial deformation of the beam in Y-direction (Figure 4.5a: co-ordinates). The direction and rotation of the CAB and rollers are shown in Figure 4.8(b) and Figure 4.8(c). The load is applied through a L type steel profile, part of which is inside the hollow section of the beam up to a length of 300 mm. The other part of this steel loading beam is connected to a load cell at 750 mm from the centre of the beam through multiple hinges to allow the rotation of the steel loading section with as much minimum friction as possible. Two steel jackets of 52 mm wide, separated at 250 mm are fastened in the loading end of the beam in the over reinforced region to ensure the applied moment is transferred to the central study area. The tests are performed under displacement control at a displacement rate of 20 $\mu m / s$, with an internal LVDT controlling the actuator.

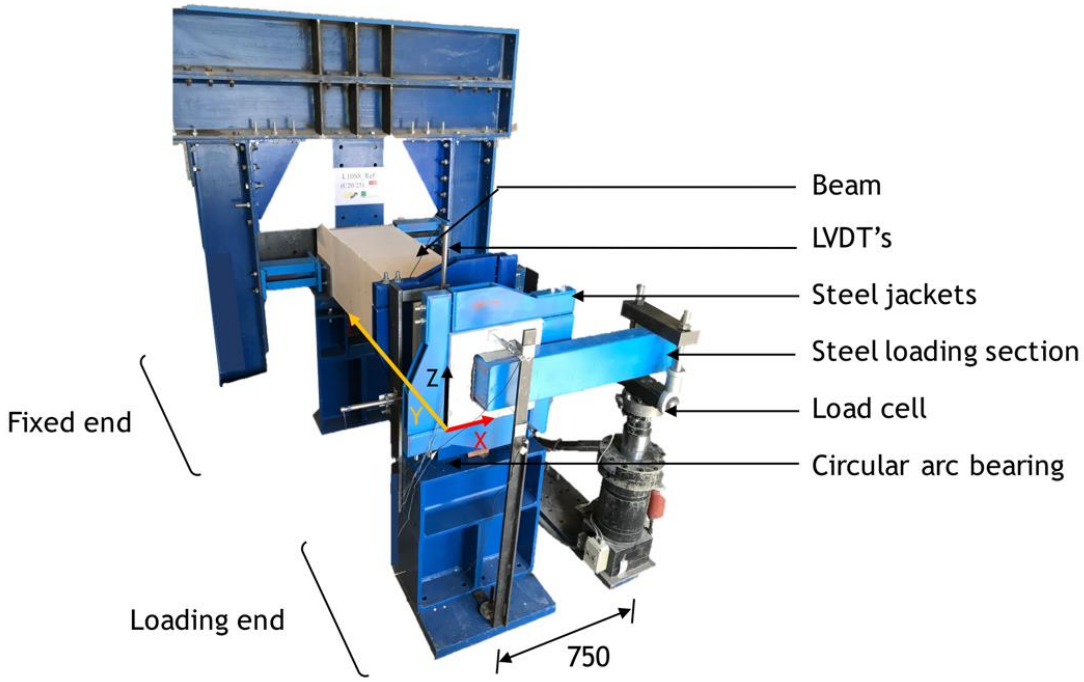

(a)

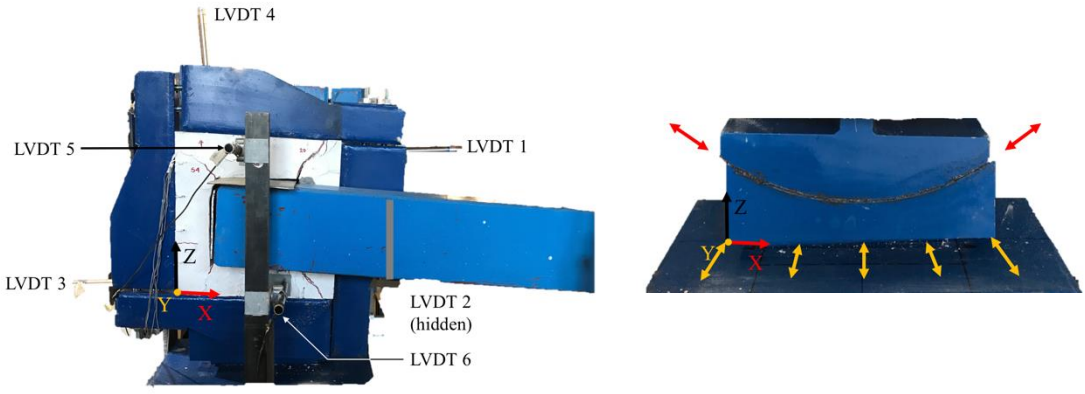

(b) (c)

Figure 4.8 (a) Test setup (b) LVDT locations and (c) Circular arc bearing (CAB)

The torsional angle of rotation is measured at a distance of 200 mm (section Y in Figure 4.1b) from the front face of the beam. The coordinates of LVDT's are shown in Table 4.2 according to the reference system shown in Figure 4.8(a). To measure the axial deformation of the beams, LVDT's are placed at the two end sections of the beam, as shown in Figure 4.8a, Figure 4.8b and Figure 4.13b. Dial gauges are attached to the right and left face extremities of the beam (fixed end) to measure transverse translations (Figure 4.1b). Four strain gauges are attached to the steel reinforcement in the central section of the beam (Y=850 mm), two on the longitudinal bars and two on the transverse bars (on top and left face) as shown in Figure 4.1 b and Figure 4.13b. Four strain gauges are also installed on the CFRP laminates, as close as possible to the central section of the beam, as illustrated in Figure 4.13b. 2D Digital image correlation (DIC) is performed on the left face to measure the concrete strain field and the cracking process. The results of DIC are discussed in detail in section 4.2.4.

Table 4.2 Location of linear variable differential transducers (LVDT) according to the coordinate system XYZ presented in Figure 4.1

	X (mm)	Y (mm)	Z (mm)
LVDT 1	400	200	350
LVDT 2	350	200	0
LVDT 3	0	200	50
LVDT 4	50	200	400
LVDT 5	150	350	0
LVDT 6	250	50	0
LVDT 7	200	350	1900

4.2. RESULTS

4.2.1. PROPERTIES OF INTERVENIENT MATERIALS

Concrete cylinders were cast along with the beams to evaluate the average concrete compressive strength, and modulus of elasticity, at 28 days. Three and five cylinders were tested to determine the E_{cm} and f_{cm}, respectively, according to EN 12390-3 (2009). Each cylinder had a diameter of 150 mm and a height of 300 mm. For the E_{cm} and f_{cm}, values of 34.53 GPa (3.5%) and 31.80 MPa (2.8%) were obtained (the values in the parenthesis are coefficient of variation). Five samples of the steel bars for 8 mm and 10 mm diameter were tested to determine the average values of the modulus of elasticity, E_{sm}, yield stress, f_{ym}, and tensile strength, f_{um}, according to EN 10002-1 (ISO 6892-1 2009) and the values are presented in Table 4.3.

Table 4.3 Properties of the steel reinforcement

Property	ϕ 8 (mm)	COV (%)	ϕ 10 (mm)	COV (%)
Modulus of elasticity, $E_{sm}(GPa)$	195.98	0.45	205.73	10.25
Yield stress, $f_{ym}(MPa)$	566.71	7.45	449.49	2.69
Yield strain, $\varepsilon_{ym}(\mu\varepsilon)$	3.06	11.53	2.46	22.87
Tensile strength, $f_{um}(MPa)$	680.27	4.74	560.99	1.48
Strain at tensile strength, $\varepsilon_{um}(\mu\varepsilon)$	0.074	10.15	0.128	7.53

The tensile properties of the CFK 150/2000 S&P laminates were characterized by uniaxial tensile tests on 3 samples carried out according to ISO 527-5 (ISO 1997). The average elastic modulus, E_{fm}, and tensile strength, f_{fu}, for the four batches of CFRP laminates used in the experimental program are shown in Table 4.4. The tensile tests on batch 4 were performed on straight laminates, before transforming them into L-shape. It must be noted that the tensile strength and the modulus of elasticity in the transition zone are expected to be lower than those of straight laminates (J. Barros et al. 2016). S&P Resin 220 epoxy adhesive was used to bond the CFRP laminates to the concrete substrate. The instantaneous and long term tensile behaviour of this adhesive was investigated by Costa and Barros (Costa and Barros 2015). At 3 days, the elastic modulus ($E_{0.5-2.5\%}$) attained a stabilized value, and the tensile strength and the $E_{0.5-2.5\%}$, determined according to the

ISO 527-2 recommendations (ISO527-2 1993), were about 20 MPa and 7 GPa, respectively.

Table 4.4 Properties of CFRP laminates

	E_{fm} (GPa)	Co.V. (%)	f_{fu} (MPa)	Co.V. (%)
Batch 1	205.04	1.20	2346	5.60
Batch 2	199.83	1.40	1982	3.30
Batch 3	198.77	1.35	1879	0.48
Batch 4	196.20	0.13	2276	0.60

The reference beams are identified by the general acronym of *Ref_bS*, where: *Ref* represents a reference beam; *b* identifies the number of steel stirrups in the central study zone (1000 mm of length). The general acronym for the strengthened beams is *Sx_LyTz*, where S represents a strengthened beam and *x* represents the number of strengthened faces of the beam. Series one is represented with 'S4F' meaning the beam is strengthened on four faces, series two with 'S3F' and series three with 'S4FL', indicating the strengthening is carried out with L-laminates. *Ly* is the number (*y*) of CFRP laminates in the longitudinal direction (parallel to the Y axis – longitudinal reinforcement); *Tz* is the number (*z*) of CFRP laminates in the transversal direction (parallel to the Z axis – transverse reinforcement).

To assess the influence of the existing percentage of steel stirrups in the monitored zone of the beam, one of the reference beams of concrete strength class C25/30 included only one stirrup in this zone (Ref_1S), while the other reference beam (C25/30) was reinforced with 4 steel stirrups (Ref_4S). All the strengthened beams had 4 steel stirrups in the monitored zone. Beams S4F_L2S5, S4F_L2S10 and S4F_L4S5 were strengthened with the CFRP laminates of the first batch, while S4F_L4S10, S3F_L2S5 and S3F_L4S10 beams were strengthened with the CFRP laminates of the second batch in both the longitudinal and transverse direction. In series 3 (beams S4FL_L2S5 and S4F_L4S10) the longitudinal laminates were from the 3rd batch and the special L-laminates in the transverse direction were from the 4th batch.

4.2.2. GENERAL BEAM BEHAVIOUR

The torsional angle of rotation *vs*. torsional moment of beam S4F_L2S10 is represented in Figure 4.9, and is used to introduce the parameters that were observed experimentally and that will be discussed in detail. The experimental torsional response of this representative beam can be decomposed into the following main phases:

1) linear response up to the formation of visible cracks in the external faces of the beam $(\theta_{t,cr}, M_{t,cr})$. The stiffness of this phase is characterized by the inclination of the line connecting the test initiation and the point corresponding to $(\theta_{t,cr}, M_{t,cr})$, $k_{t,lin} = M_{t,cr} / \theta_{t,cr}$. Analysing in depth the shape of $M_{t,cr} - \theta_{t,cr}$ in this phase, a certain extent of nonlinearity is verified by the formation of few cracks in the loading branch of the beams, due to the high tensile strains (cracks) developed in the loading zone;

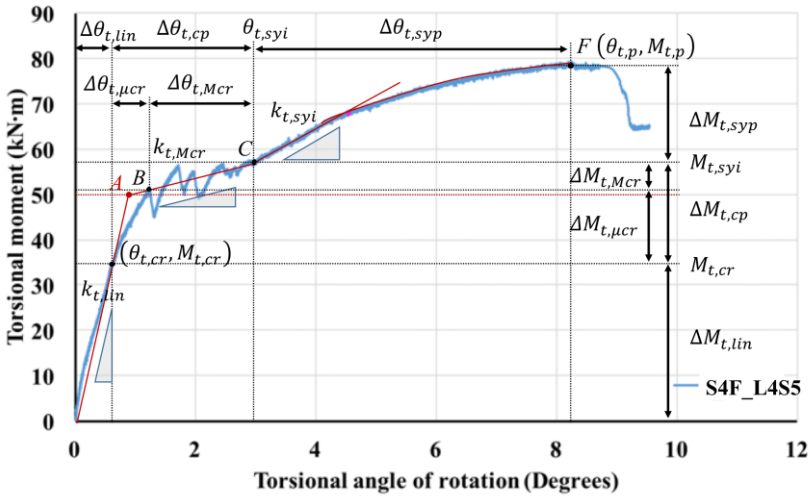

Figure 4.9 Torsional moment *vs*. torsional angle of rotation of S4F_L2S10

2) A crack propagation phase, where the development of new cracks are accompanied by a sudden drop in torsional resistance. The relative loss in torsional resistance decreases with increasing the applied torsional capacity until no new torsional cracks develop (point C) and energy is primarily dissipated trough the increasing crack width. This cracking phase (identified by the subscript '*cp*') can be decomposed in two sub-stages, one from crack initiation up to the first drop in the torsional moment capacity, identified by point *B*, and the other sub-stage from point *B* to *C*. Deep analysis of the obtained results has pointed out that the crack stabilization process almost coincides with the yield initiation of the steel reinforcement. Yielding of the longitudinal and transverse reinforcement took

place simultaneously in Ref_4S, whereas in case of strengthened beams it takes place either in the longitudinal reinforcement or in the transverse reinforcement. Therefore, to simplify the analysis without compromising the reliability on the relevant conclusions, it is assumed that the crack stabilization process coincides with the occurrence of first yield of the steel reinforcement. The last point C represents the yield initiation of the steel reinforcement, identified by $\theta_{t,syi}$ and $M_{t,syi}$. These first and second sub-stages are characterized by the propagation of micro- and macro-cracks, therefore the respective subscripts, μ_{cr} and M_{cr}, are used for their identification. These micro- and macro-crack propagation sub-stages are identified by the following respective increment of torsional angle and torsional moment: $\Delta\theta_{t,\mu cr}$, $\Delta M_{t,\mu cr}$, $\Delta\theta_{t,Mcr}$, $\Delta M_{t,Mcr}$. The macro-crack propagation sub-stage is also identified by the stiffness, $k_{t,Mcr} = \Delta M_{t,Mcr} / \Delta\theta_{t,Mcr}$, which is the inclination of a line that best fits the experimental response of this sub-stage.

3) The third phase covers the stage from yield initiation in the steel reinforcement $(\theta_{t,syi}, M_{t,syi})$ up to the peak load $(\theta_{t,p}, M_{t,p})$. The CFRP strengthening systems are mainly activated in this phase by increasing the stiffness and the torsional capacity. Following an initial stage of almost constant stiffness, the stiffness gradually decreases due to the yielding of more steel bars, as well as debonding between reinforcement and surrounding concrete. Debonding of the CFRP NSM reinforcement can contribute to this decrease in stiffness in the case of the strengthened beams. The increment of torsional moment and torsional angle in this elasto-plastic cracked stage is presented by $\Delta M_{t,cp}$ and $\Delta\theta_{t,cp}$.

4.2.3. DETAILED RESULTS

In this section, the results of all strengthened beams are presented in terms of torsional moment *vs.* torsional angle of rotation, evolution of steel and CFRP strains, influence of CFRP laminates in the longitudinal and transverse strengthening, crack spacing, crack orientation and failure modes.

4.2.3.1. Torsional moment *vs.* torsional angle of rotation

The $M_t - \theta_t$ of all tested beams are presented in Figure 4.10, and the relevant results are included in Table 4.5, Table 4.6 and Table 4.7 in terms of torsional moment, torsional angle of rotation and stiffness. As the same concrete strength (C25/30) was adopted for

all specimens in this experimental programme, $k_{t,lin}$ was expected to be the same for all tested beams. However, as reported in Table 4.7, some differences were observed. This can be attributed to material variability and the reliance of $k_{t,lin}$ on the definition of point $(\theta_{t,cr}, M_{t,cr})$, whose determination has the expected uncertainty on the detection of the crack initiation as well as the presence of non-linearity. This difficulty is even amplified due to the probability of similar crack occurrence on all four external faces, and the application of different strengthening systems. Beams with maximum longitudinal reinforcement in series one (33.01%) and L-laminate strengthening (19.36%) have shown a considerable decrease in the corresponding value.

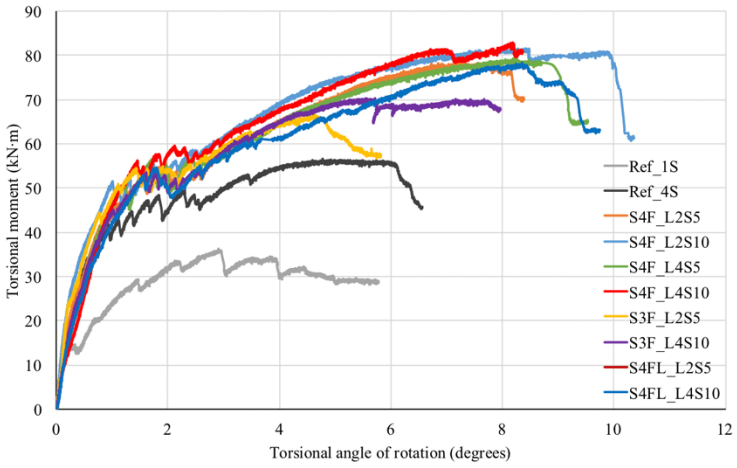

(a)

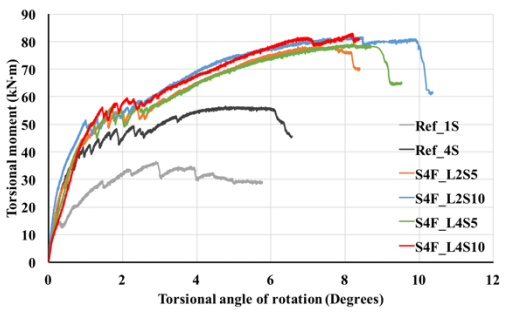

(b)

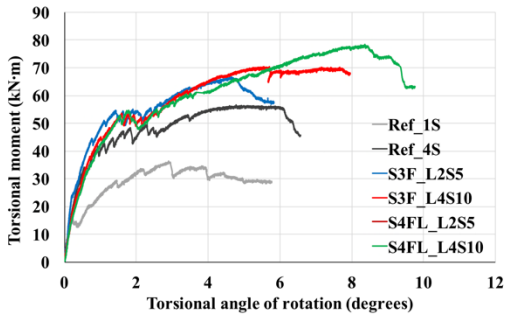

(c)

Figure 4.10 Torsional moment *vs.* torsional angle of rotation (a) All beams (b) Series one beams and (c) Series two (three face strengthening) and series three (L-laminate strengthening)

In series one, apart from beam S4F_L2S5, the other strengthening configurations have provided an increase on the $M_{t,cr}$, while increase of $\theta_{t,cr}$ was only registered in the two strengthening configurations with four longitudinal CFRP laminates (S4F_L4S5 and S4F_L4S10). In series two, beams have decreased torsional cracking moment and only

beam S3F_L2S5 has increased angle of rotation. This is due to the early cracking on the unstrengthened surface of the beam. In case of series three, S4FL_L2S5 has shown a decrease in both values, while these increased in beam S4FL_L4S110.

Regarding point A with cracking angle $\theta_{t,A}$ and cracking moment $M_{t,A}$, average values of 0.73 degrees and 47.15 kN.m were obtained for beams in series one, with much higher COV for the $\theta_{t,A}$ (38%) than for $M_{t,A}$ (13%) due to its higher susceptibility to $k_{t,lin}$. In any case, a tendency in the increase of $\theta_{t,A}$ with increasing percentage of longitudinal CFRP laminates is evident (almost double), while the increase of $M_{t,A}$ in the strengthened beams was not so accentuated (17.57%). Similarly, in case of series two and series three, $\theta_{t,A}$ and $M_{t,A}$ have an average increase of 28.73% and 10.11%.

Table 4.5 Experimental results of beams in terms of torsional moment, M_t at different stages

Beam	$M_{t,cr}$ (kN.m)	$\left(\frac{M^S_{t,cr}-M^R_{t,cr}}{M^R_{t,cr}}\right)\%$	$M_{t,A}$ (kN.m)	$M_{t,Mcr}$ (kN.m)	$M_{t,syi}$ (kN.m)	$\left(\frac{M^S_{t,syi}-M^R_{t,syi}}{M^R_{t,syi}}\right)\%$	$M_{t,p}$ (kN.m)	$\left(\frac{M^S_{t,p}-M^R_{t,p}}{M^R_{t,p}}\right)\%$
Ref_4S	28.01	-	40.02	41.44	47.29	-	56.69	-
S4F_L2S5	25.04	-10.61	41.99	44.43	55.23	16.79	78.30	38.11
S4F_L2S10	28.46	1.64	48.26	51.17	57.63	21.87	81.69	44.09
S4F_L4S5	34.41	22.87	50.27	50.40	56.40	19.27	79.37	39.99
S4F_L4S10	39.26	40.17	55.18	55.51	59.39	25.58	83.02	46.43
S3F_L2S5	26.57	-5.14	44.03	44.78	55.57	17.51	70.27	23.94
S3F_L4S10	24.83	-10.98	42.59	46.52	55.72	17.83	77.05	35.90
S4FL_L2S5	30.75	9.80	43.47	44.31	53.72	13.61	67.89	19.75
S4FL_L4S10	32.69	16.71	50.88	52.45	60.99	28.98	78.35	38.19

$M^{S/R}_{t,cr}$: S and R stand for, respectively, strengthened and reference beam

Table 4.6 Experimental results of beams in terms of torsional angle of rotation, θ_t at different stages

Beam	$\theta_{t,cr}$ (deg.)	$\left(\frac{\theta^S_{t,cr}-\theta^R_{t,cr}}{\theta^R_{t,cr}}\right)\%$	$\theta_{t,A}$ (deg.)	$\theta_{t,Mcr}$ (deg.)	$\theta_{t,syi}$ (deg.)	$\left(\frac{\theta^S_{t,syi}-\theta^R_{t,syi}}{\theta^R_{t,syi}}\right)\%$	$\theta_{t,p}$ (deg.)	$\left(\frac{\theta^S_{t,p}-\theta^R_{t,p}}{\theta^R_{t,p}}\right)\%$	$\frac{\theta_{t,p}}{\theta_{t,syi}}$	$\theta_{t,u}$ (deg.)	$\left(\frac{\theta^S_{t,u}-\theta^R_{t,u}}{\theta^R_{t,u}}\right)\%$
Ref_4S	0.39	-	0.54	0.93	2.77	-	4.78	-	1.73	6.09	-
S4F_L2S5	0.33	-14.43	0.57	0.88	2.76	-0.44	7.31	53.01	2.65	8.19	34.33
S4F_L2S10	0.30	-23.20	0.50	0.99	2.57	-7.24	8.40	75.83	3.27	9.91	62.65
S4F_L4S5	0.62	59.28	0.92	1.19	2.94	5.97	8.23	72.21	2.80	8.90	46.13

S4F_L4S10	0.78	101.88	1.14	1.45	2.97	7.22	8.19	71.43	2.76	8.37	37.40
S3F_L2S5	0.44	13.85	0.72	1.02	2.78	0.48	5.71	19.48	2.05	7.79	27.86
S3F_L4S10	0.33	-13.74	0.70	1.24	2.82	1.73	7.14	49.42	2.53	7.14	17.21
S4FL_L2S5	0.69	78.09	0.62	1.38	3.52	26.97	6.98	46.12	1.99	7.46	22.38
S4FL_L4S10	0.63	62.89	0.94	1.54	4.40	59.00	8.36	74.83	1.90	9.35	53.47

$\theta_{t,cr}^{S/R}$: S and R stand for, respectively, strengthened and reference beam

Table 4.7 Experimental results of beams in terms of torsional stiffness, k_t at different stages

Beam	$k_{t,lin}$ (kN.m/deg.)	$\left(\frac{k_{t,lin}^{S}-k_{t,lin}^{R}}{k_{t,lin}^{R}}\right)$	$k_{t,Mcr}$ (kN.m/deg.)	$\left(\frac{k_{t,Mcr}^{S}-k_{t,Mcr}^{R}}{k_{t,Mcr}^{R}}\right)$	$k_{t,syi}$ (kN.m/deg.)	$\left(\frac{k_{t,syi}^{S}-k_{t,syi}^{R}}{k_{t,syi}^{R}}\right)$
Ref_4S	69.80	%	4.02	%	7.36	%
S4F_L2S5	64.46	-7.66	5.77	43.64	6.10	-17.06
S4F_L2S10	87.30	25.07	5.97	48.60	7.69	4.58
S4F_L4S5	45.08	-35.41	3.74	-7.03	7.49	1.81
S4F_L4S10	48.43	-30.61	3.42	-14.84	6.20	-15.76
S3F_L2S5	66.81	-4.28	4.48	11.41	9.88	34.30
S3F_L4S10	63.21	-9.45	6.05	50.47	6.46	-12.18
S4FL_L2S5	43.14	-38.19	4.75	18.30	6.64	-9.79
S4FL_L4S10	49.38	-29.26	5.07	26.08	4.97	-32.48

$k_{t,cr}^{S/R}$: S and R stand for, respectively, strengthened and reference beam

The stiffness at the macro-crack propagation, $k_{t,Mcr}$, increased in the beams strengthened with 2 longitudinal CFRP laminates and decreased in the beams strengthened with 4 longitudinal CFRP laminates in series one. In case of the other two series, the stiffness of all the beams have increased. This phase is highly influenced by the crack opening, crack sliding, formation of new cracks, spacing of the CFRP laminates and concrete strength. As the variation level was very small, it can be concluded that, for the adopted strengthening configurations, $k_{t,Mcr}$ is not significantly affected. The stabilization of macro-crack formation stage is considered to be coincident with yielding of the steel reinforcement (phase 3) at $M_{t,syi}$ and $\theta_{t,syi}$. This phase is dependant on both the longitudinal and transverse CFRP strengthening reinforcement ratios, since the higher the reinforcement ratio, the higher is the torsional moment and the angle of rotation at yield initiation.

Regarding the torsional moment at yield initiation of the steel reinforcement, $M_{t,syi}$, transverse CFRP laminates seem to be more effective than longitudinal ones, except in beam S3F_L4S10 of series two due a premature failure in the over-reinforced loading region. The torsional angle at yield initiation, $\theta_{t,syi}$, increased only in the beams with the highest percentage of longitudinal CFRP laminates and beam S4FL_L2S5, though only by 14.74%. The adopted strengthening configurations did not change significantly the stiffness at steel yield initiation, $k_{t,syi}$, with respect to the reference beam (except beam S3F_L4S10). An average value of 6.87 kN.m/deg. with COV of 11% was observed for the $k_{t,syi}$ of the strengthened beams tested in series one. Both beams in series two were characterized by a higher value, though the increase for beam S3F_L2S5 was marginal. Both beams in series three had a poorer performance due to the full formation of a higher number of cracks with respect to other beams. The stiffness of this phase seems to be mainly dependent on the spacing of the CFRP laminates.

Regarding the torsional moment at peak load $(M_{t,p})$ the increase provided by the adopted strengthened configurations varied between 18% and 46%, with the largest increase in the beams with the highest percentage of transverse CFRP laminates in every series. The adopted strengthened configurations were also very effective in increasing the torsional angle at peak load $(\theta_{t,p})$, which can be taken as a ductility indicator. This increase ranged between 20% and 76% and the minimum values were observed for the beams of series

two, due to early cracking on the unstrengthened top surface. However, it must be noted that beam S3F_L4S10 still registered an increase of 20%. No clear conclusions can be extracted for the dominance of longitudinal versus transverse CFRP laminates on the torsional deformability of this type of RC beams. In order to evaluate the ductility of the strengthened beams, a ductility index calculated as $\theta_{t,p}/\theta_{t,syi}$ is also introduced in Table 4.6, confirming the above-mentioned results. The experimental values of the angle of rotation measured at failure, i.e. the ultimate torsional angle, $\theta_{t,u}$, are also reported in Table 4.6. All the examined strengthening schemes led to a significant increase in $\theta_{t,u}$, except for beam S3F_L2S5, which failed prematurely at a low value of 66.65 kN.m (5.81 degrees, $\theta_{t,u}$). Beam S4F_L2S10, which had the highest amount of transverse CFRP laminates, showed the highest increase (63%).

Figure 4.11(a) compares the $M_t - \theta_t$ response of the two reference RC beams, the Ref_1S with only one steel stirrup in the monitored span, and the Ref_4S with four steel stirrups in this span. This simple comparison confirms that by increasing the reinforcement ratio of existing steel stirrups (ρ_{sw}) from 0.050% to 0.502%, the torsional moment and torsional angle at crack initiation and at peak load increase significantly. This indicates that lower is the ρ_{sw} the larger is the potential of the CFRP laminates in increasing the torsional resistance and deformability of this type of RC structures. This is in line with the interaction observed between existing steel stirrups and NSM CFRP laminates applied for increasing the shear capacity of RC beams, where available experimental research (Dias and Barros 2013b) and analytical models (Bianco, Monti, and Barros 2014) demonstrate that the strengthening effectiveness decreases for a higher existing percentage of steel stirrups.

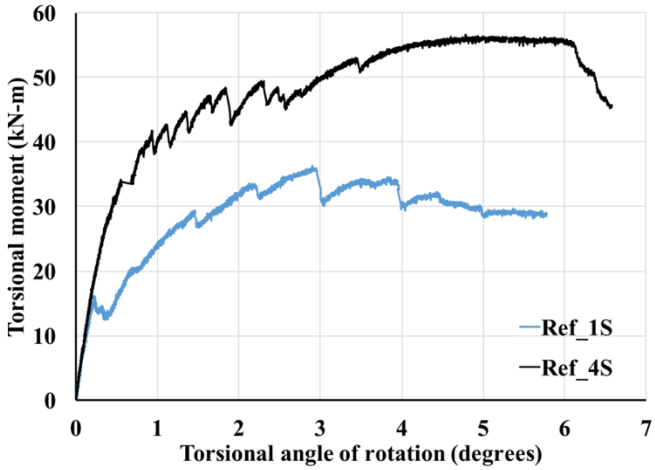

(a)

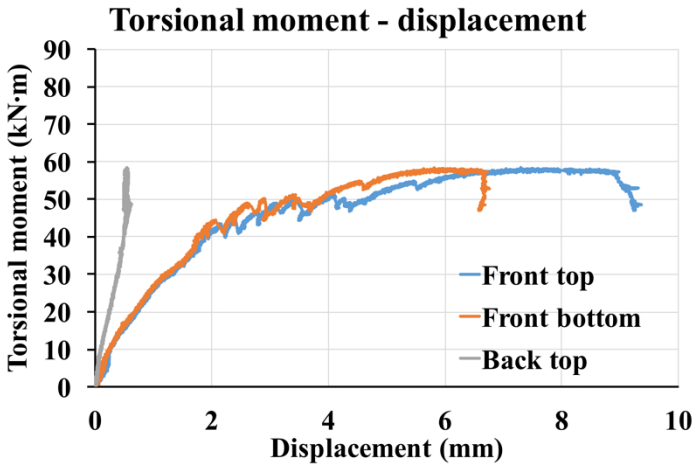

(b)

Figure 4.11 (a) Torsional moment *vs.* torsional angle of rotation of reference beams and (d) Torsional moment *vs.* elongation of Ref_4S

Figure 4.11b shows the relationship between the applied torsional moment *vs.* the axial deformability of the Ref_4S beam, where the axial deformability was recorded in the clamping and loading extremities by the LVDT's placed according to the schematic representation shown in Figure 4.13b. For the axial deformation, positive values are assumed for elongation. It is shown that the LVDT's positioned at the top and bottom flanges of the extremity at the loaded zone recorded almost equal displacement of elongation up to the torsional strength of the beam. The LVDT placed at the top flange of the extremity at the clamping zone also registered an elongation of the beam, but as expected, of much smaller value. The elongation and the corresponding beam's axial deformation at torsional strength was 6.69 mm and 3.52‰ in the Ref_4S beam. The corresponding average values of 10.97 mm and 5.77‰ for series one strengthened beams,

with a Co.V of 11.2%, indicate that all the strengthened beams in series one experienced similar elongation, of about double that of the reference beam. In case of series two and series three the average values of 7.09 mm and 7.67 mm with 3.73‰ and 4.04‰, also indicate that the beams experienced elongation. The elongation is mainly caused by the axial component of the crack opening (Y-axis) developed during the loading process of the beam. The strengthened beams presented larger axial deformation than the reference beam mainly due to the higher torsional deformability at failure. The graphs of torsional moment *vs.* axial deformation for all the strengthened beams are shown in Figure 4.12.

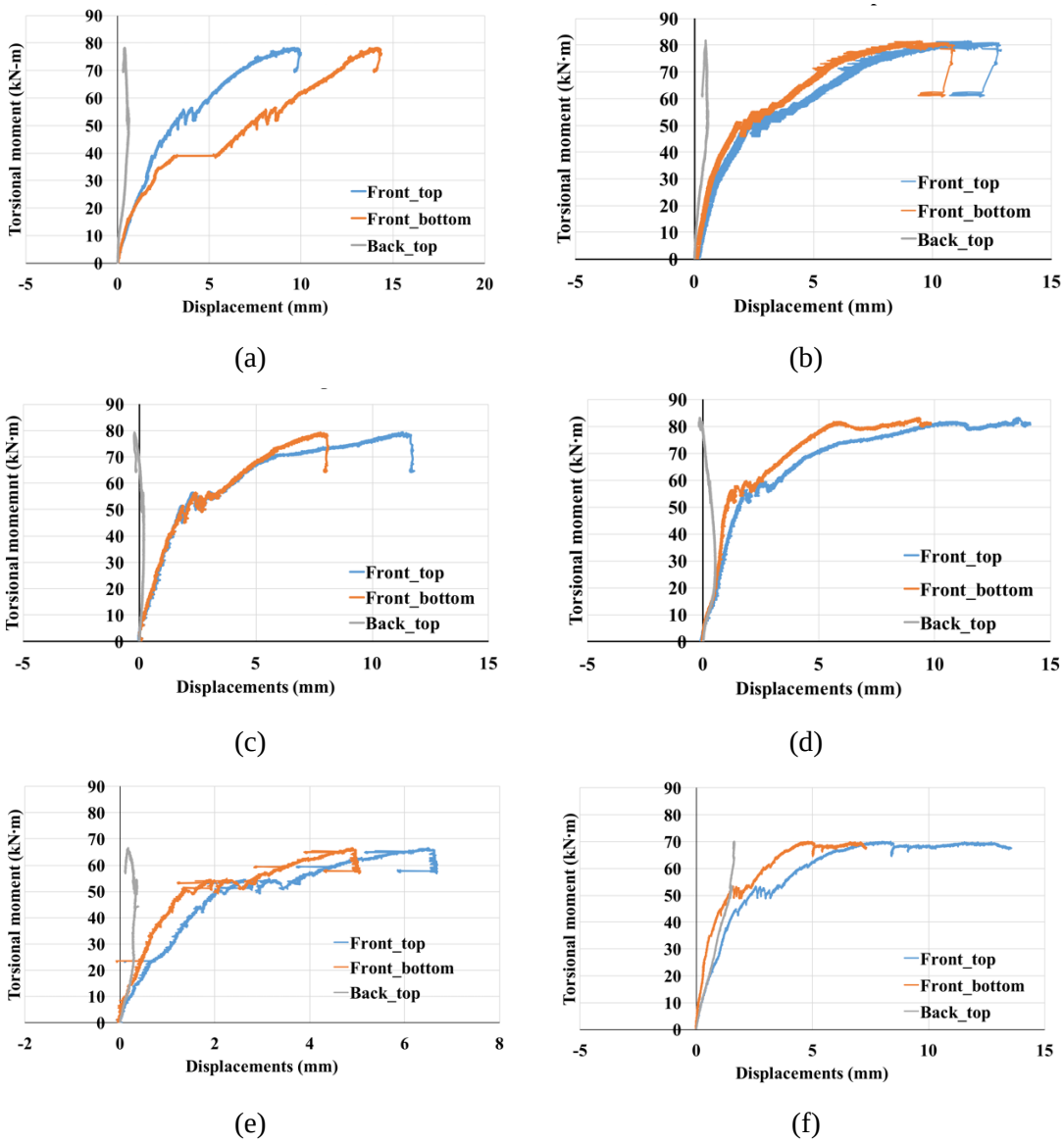

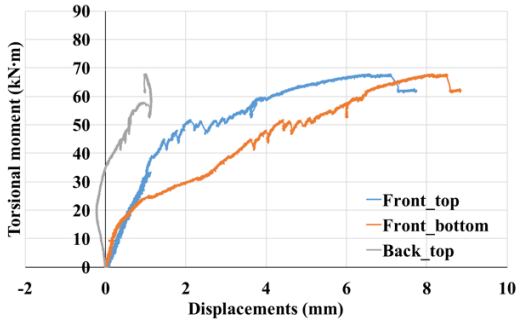

(g)

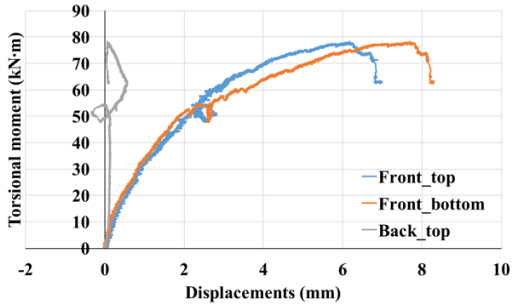

(h)

Figure 4.12 Torsional moment *vs.* elongation of beam (a) S4F_L2S5 (b) S4F_L2S10 (c) S4F_L4S5 (d) S4F_L4S10 (e) S3F_L2S5 (f) S3F_L4S10 (g) S4FL_L2S5 and (h) S4FL_L4S10

4.2.3.2. Strains in the steel reinforcements and CFRP laminates

The relationship between the strains registered in the strain gauges (SG) applied in the steel reinforcements and the torsional angle for the reference and strengthened beams are presented in Figure 4.13a and Figure 4.14. The vertical dashed (red colour) and dotted (blue colour) lines indicate the yielding strain in longitudinal and transverse steel reinforcements at 2675 $\mu\varepsilon$ and 3060 $\mu\varepsilon$, respectively. The location and designation of the adopted SG's are indicated in Figure 4.13b, while their precise co-ordinates are presented in Table 4.8 according to the coordinate system adopted in Figure 4.8a. In case of beams in series two, where no strengthening is applied on the top surface, the strain gauges on the CFRP laminates were installed on the right face, as close as possible to the central section. The strain gauges on the steel reinforcement were installed on the top surface for all of the beams in the experimental program. Unfortunately some of the SG did not function properly during the tests and their values are not presented. The letters L and T in the adopted acronym represent the strain gauges in longitudinal and transversal direction for the reinforcements, while S and F represent steel and CFRP-laminate. For instance, SG_LS1 indicates strain gauge number 1 (applied on the top face of the beam, Figure 4.13b) installed on a longitudinal steel bar; SG_TF2 indicates strain gauge number 2 (applied on a lateral face of the beam, Figure 4.13b) installed on the transverse CFRP laminate.

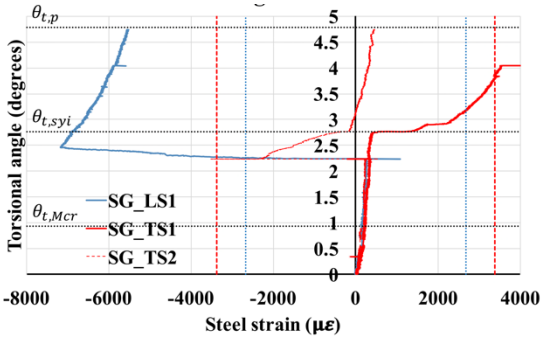

(a)

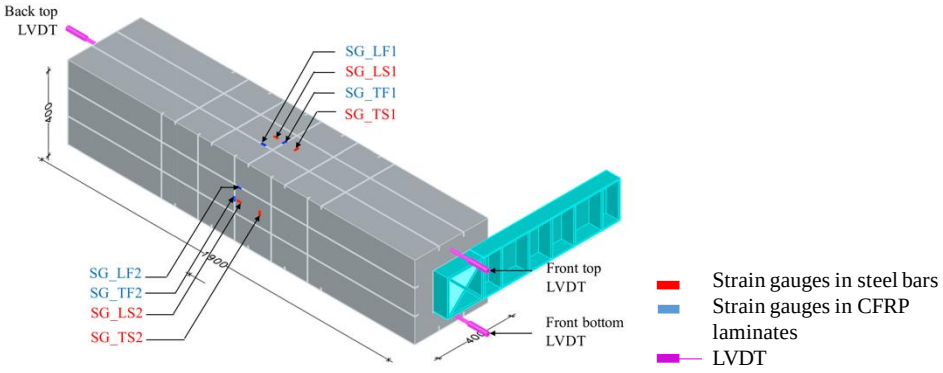

(b)

Figure 4.13 (a) Torsional angle *vs.* steel strain in Ref_4S (b) Location of strain gauges and LVDT's

Table 4.8 Location of strain gauges according to the co-ordinate system adopted in Figure 4.8a

Strain gauge (SG)	X (mm)	Y (mm)	Z (mm)
SG_LS1	200	950	367
SG_TS1	200	850	375
SG_LS2	33	950	200
SG_TS2	25	850	200
SG_LF1	135	950	380
SG_TF1	200	915	390
SG_LF2	20	950	265
SG_TF2	10	985	200

LS – SG on longitudinal steel reinforcement; TS – SG on transverse steel reinforcement;

LF – SG on longitudinal CFRP laminate; TF – SG on transverse CFRP laminate

The values of steel and CFRP strains at $\theta_{t,syi}$, $\theta_{t,p}$ and $\theta_{t,u}$ (when the test has ended) are presented in Table 4.9 and Table 4.10. In Figure 4.14 and Figure 4.15 horizontal lines are also added at $\theta_{t,Mcr}$, $\theta_{t,syi}$ and $\theta_{t,p}$. As expected, Figure 4.14 shows that up to $\theta_{t,Mcr}$ the

steel strains are very small due to the almost inactivation of the reinforcement. Abrupt increase in the strains are recorded between $\theta_{t,Mcr}$ and $\theta_{t,syi}$, i.e., during the crack propagation stage. This also happens in the strengthened beams, not only in the steel reinforcement, but also in the CFRP laminates. However, in the Ref_4S beam two of the three SG have presented an abrupt increase of negative strain values (compression), while in the strengthened beams, as expected, the abrupt increase of strain was always positive (tensile strain) in both the steel reinforcement and the CFRP laminates. The abrupt increase of negative strain in the Ref_4S might be justified by a local phenomenon related to the relative distance between the SG (where these values were recorded) and the closest crack. If a dominant sliding develops along a crack crossed by the reinforcement, a local curvature can be developed in the reinforcement at the cracked section. If a SG is localized in this zone, it can record negative strain values.

Table 4.9 Evolution of steel strain at yield initiation $(\theta_{t,syi})$, peak moment $(\theta_{t,p})$ and ultimate moment $(\theta_{t,u})$

Beam	Strain gauges	Strain at $\theta_{t,syi}(\mu\varepsilon)$	Strain at $\theta_{t,p}(\mu\varepsilon)$	Strain at $\theta_{t,u}(\mu\varepsilon)$
Ref_4S	SG_LS1	-6847	-5536	-5087
	SG_TS1	1244	19825	19825
	SG_LS2	-	-	-
	SG_TS2	-213	471	16069
S4F_L2S5	SG_LS1	1592	1479	1233
	SG_TS1	-	-	-
	SG_LS2	-	-	-
	SG_TS2	-	-	-
S4F_L2S10	SG_LS1	2757	606	20327
	SG_TS1	717	941	1434
	SG_LS2	1882	2005	2185
	SG_TS2	1210	1322	18063
S4F_L4S10	SG_LS1	1569	2488	2331
	SG_TS1	2129	2420	2376
	SG_LS2	1827	2140	2107
	SG_TS2	717	807	807
S3F_L2S5	SG_LS1	2174	3250	3350

	SG_TS1	1423	1435	19655
	SG_TS2	1020	1210	20719
S3F_L4S10	SG_LS2	1424	1916	21234
	SG_TS2	1479	2454	18377
S4FL_L4S10	SG_TS1	1109	2936	2745
	SG_LS2	4852	2543	1983

Table 4.10 Evolution of CFRP strain at yield initiation $(\theta_{t,syi})$, peak moment $(\theta_{t,p})$ and ultimate moment $(\theta_{t,u})$

Beam	Strain gauges	Strain at $\theta_{t,syi}(\mu\varepsilon)$	Strain at $\theta_{t,p}(\mu\varepsilon)$	Strain at $\theta_{t,u}(\mu\varepsilon)$
S4F_L2S5	SG_LF1	2302	4120	4120
	SG_TF1	3093	5771	6891
	SG_LF2	680	1190	1190
	SG_TF2	2632	4581	4581
S4F_L2S10	SG_LF1	2796	6214	10977
	SG_TF1	3624	8013	6937
	SG_LF2	62	6043	6385
	SG_TF2	986	5397	6054
S4F_L4S5	SG_LF1	112	7188	6621
	SG_TF1	1095	11046	10426
	SG_LF2	4023	7032	6535
	SG_TF2	102	5927	5379
S4F_L4S10	SG_LF1	641	2635	2685
	SG_TF1	2528	3914	3950
	SG_LF2	12	909	933
	SG_TF2	-102	1543	1572
S3F_L2S5	SG_LF1	97	800	1500
	SG_TF1	330	2839	2804
	SG_LF2	484	2919	4319
	SG_TF2	-32	1067	1627
S3F_L4S10	SG_LF1	2447	4099	4545
	SG_TF1	2004	3233	3484
	SG_LF2	1414	3416	3966
	SG_TF2	1179	1831	2017

S4FL_L2S5	SG_LF1	4904	5675	5249
	SG_TF1	1032	2506	2700
	SG_LF2	2519	4264	4579
	SG_TF2	-120	2652	5979
S4FL_L4S10	SG_LF1	1175	4039	4012
	SG_TF1	2063	3674	3364
	SG_LF2	3326	4542	4169
	SG_TF2	815	2634	2826

After the abrupt increase in the strains recorded in the steel reinforcements, Ref_4S presented a gradient of strains higher than the ones registered in the SG applied in the strengthened beams (apart the exception of the strain recorded in the SG_TS1 of S4F_L4S10 beam). This can be justified by the contribution of the CFRP laminates crossing the cracks, by promoting the development of a higher number of cracks, but of smaller crack width. No clear tendency is detected in the type of reinforcement (longitudinal or transversal) where the maximum strains have occurred, since this depends significantly on the relative position between the SG and the closest crack. Unfortunately, the SG in Beams S4F_L4S5 and S4FL_L2S5 were faulty and the relevant data could not be recorded.

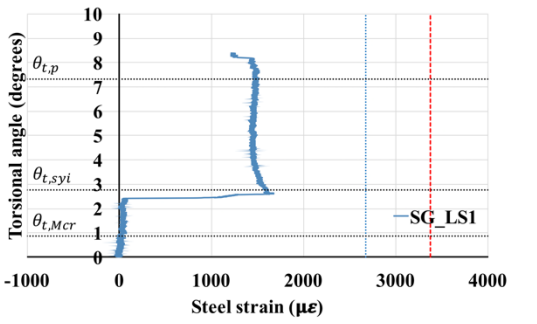

(a)

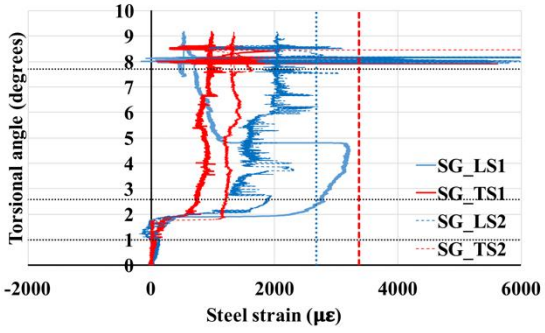

(b)

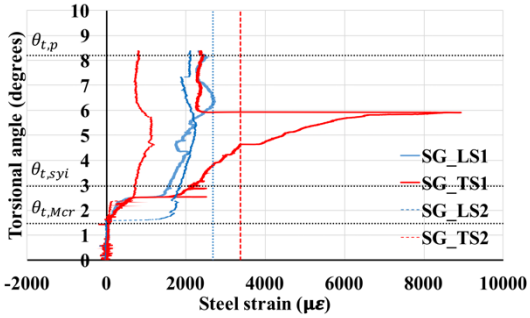

(c)

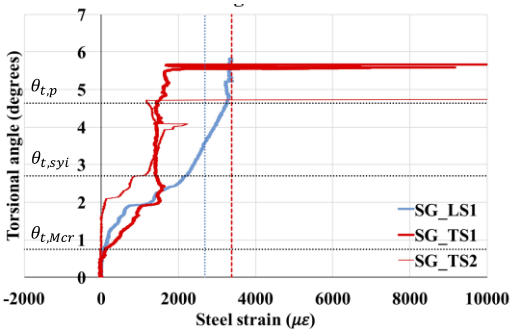

(d)

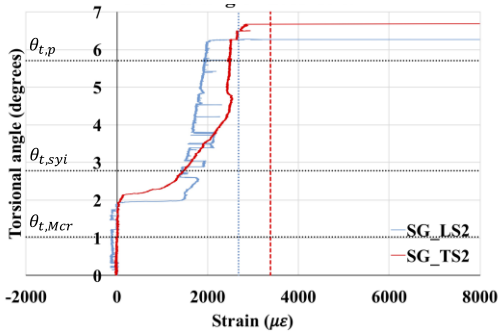

(e)

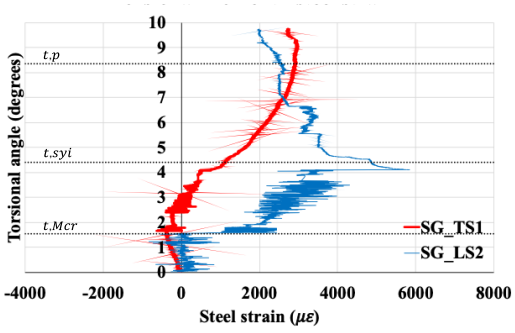

(f)

Figure 4.14 Torsional angle *vs.* steel strain evolution of all beams (a) S4F_L2S5 (b) S4F_L2S10 (c) S4F_L4S10 (d) S3F_L2S5 (e) S3F_L4S10 and (f) S4FL_L4S10

Regarding the strains in the CFRP laminates (Figure 4.15), overall the maximum strains occurred at the location of SG_TF1 i.e., in the transverse CFRP laminate located on the top face of strengthened beams in series one (Figure 4.13b). In case of beams in series two and series three, the maximum strains were recorded by different strain gauges. Like the SG installed in the steel bars, the gradient of strain in the CFRP laminates was also quite dependent on the relative position of the SG to the closest crack. Figure 4.15 and Table 4.10 show that the maximum strain in the CFRP laminates at $\theta_{t,p}$ was 11.05‰, which corresponds to 88.50% of the ultimate tensile strain of these laminates in beam S4F_L2S10 of series one. In series two, maximum strain of 4.54‰ is attained in S3F_L4S10 corresponding to 40% of its ultimate tensile strain. Similarly, in series three, beam S4FL_L2S5 has reached the maximum strain of 5.79‰, which corresponds to 46.64‰ of the ultimate tensile strain. The premature delamination of CFRP in corners due to bond failure or stress concentration, usually occurring in EBR-based torsional strengthening configurations (Panchacharam and Belarbi 2002), is not observed in any of the adopted NSM strengthening configurations.

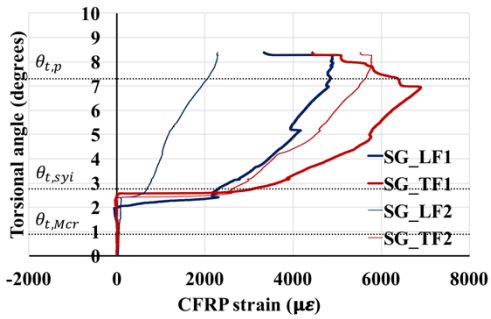

(a)

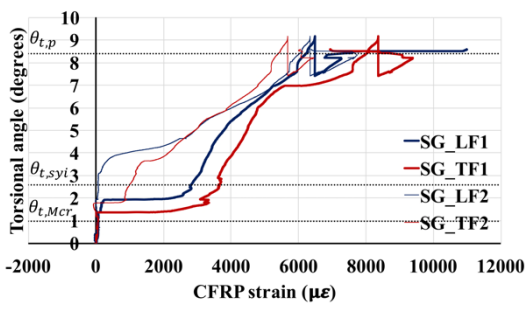

(b)

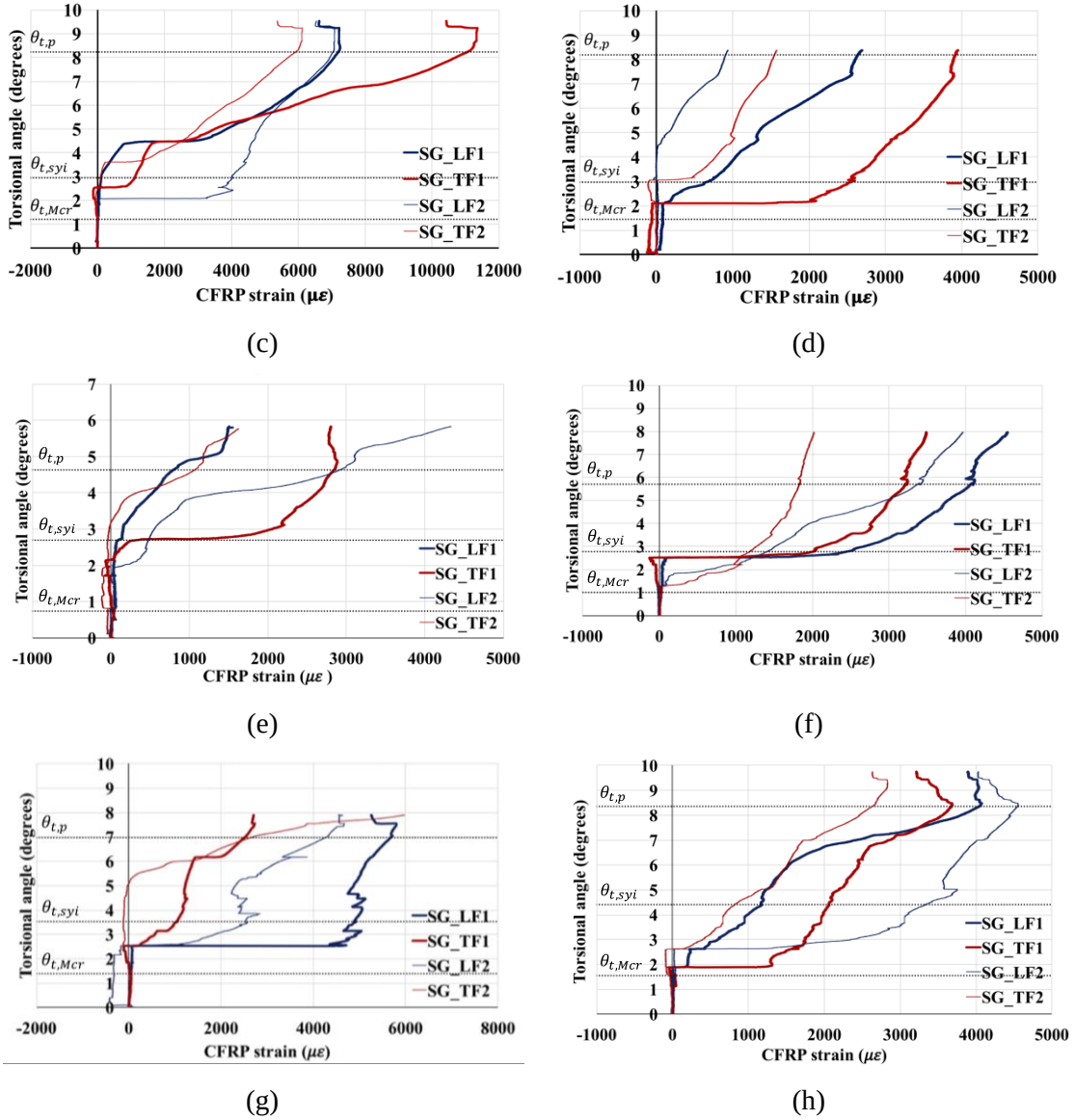

Figure 4.15 Torsional angle *vs.* CFRP strains of all beams (a) S4F_L2S5 (b) S4F_L2S10 (c) S4F_L4S5 (d) S4F_L4S10 (e) S3F_L2S5 (f) S3F_L4S10 (g) S4FL_L2S5 and (h) S4FL_L4S10

4.2.3.3. Influence of CFRP strengthening ratios on the torsional performance of the tested beams: Series one

In order to assess the influence of the longitudinal CFRP strengthening ratio on the torsional behaviour of the strengthened beams, the torsional angle *vs.* torsional moment $(M_t - \theta_t)$ of beams S4F_L2S5 and S4F_L4S5 are compared in Figure 4.16a and, for S4F_L2S10 and S4F_L4S10 are compared in Figure 4.16b. For these adopted longitudinal strengthening configurations it is observed that increasing ρ_{fl} from 0.096 to 0.192 (Table 4.1) had marginal contribution in terms of torsional capacity and deformability. The $M_t - \theta_t$ of the S4F_L2S5 and S4F_L2S10 beams are compared in

Figure 4.16c, while this comparison for the S4F_L4S5 and S4F_L4S10 is shown in Figure 4.16d, in order to assess the influence of the transverse CFRP strengthening ratio on torsional behaviour of the tested strengthened beams. For these adopted transverse strengthening configurations, it is verified that increasing ρ_{fw} from 0.071 to 0.141 (Table 4.1) had similar increase in both groups of beams in terms of torsional capacity, but limited to 4.45%. The increase is mainly relevant for the moment at macro-crack initiation ($M_{t,Mcr}$) that increased by 12.65%. The stiffness for torsional deformation above $\theta_{t,Mcr}$ was marginally affected by the adopted ρ_{fw}. In terms of maximum torsional deformation, an increase is observed in the first group, while in the second group it has decreased. However, it should be mentioned that the test of S4F_L4S10 beam was ended prematurely to avoid damage in some of the LVDTs. It is expected that the ultimate torsional deformation would also have increased with the increase of ρ_{fw}.

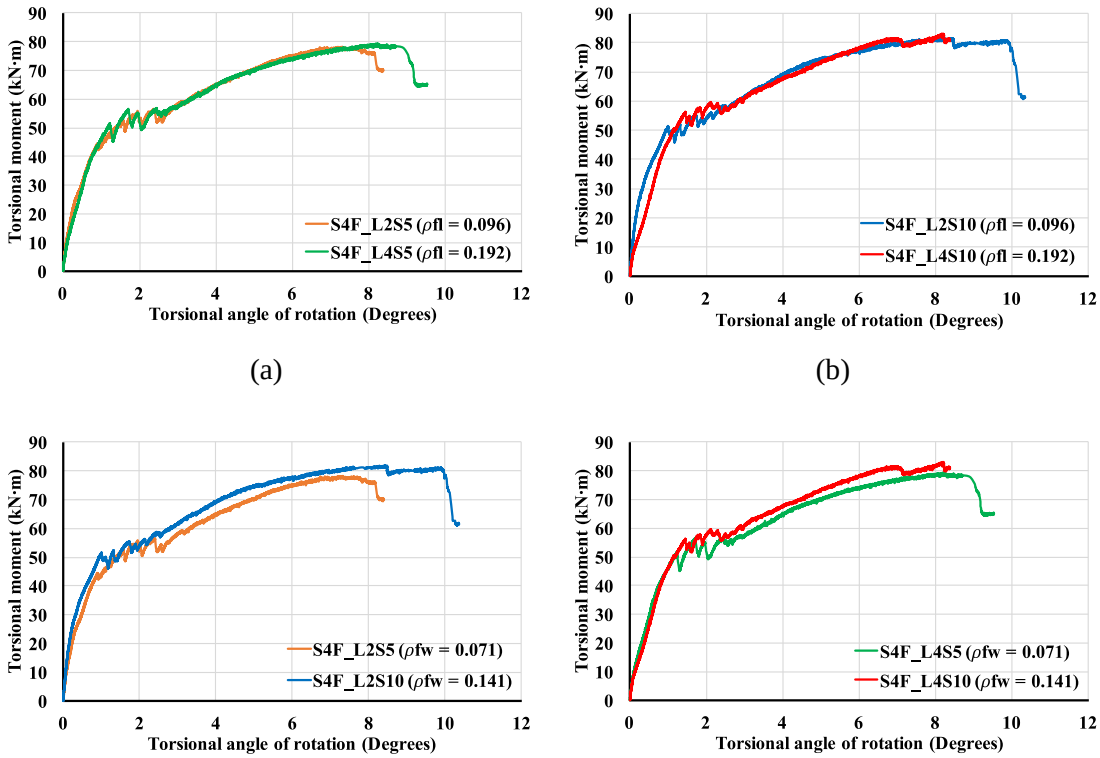

Figure 4.16 Influence of CFRP strengthening ratios (a) and (b) Longitudinal (c) and (d) Transverse

4.2.3.4. Crack spacing and orientation, and failure modes

The average crack spacing (s_{rm}) and average crack orientation (α_{crm}) are determined according to the strategy described in Figure 4.17 and, calculated using equations 4.5 and 4.6. s_{rm} is calculated as an average, of average crack spacing of only full cracks on each face of the monitored span, according to equation 4.5, where s_i (i=1 to n) is crack spacing and n is number of cracks. α_{crm} is evaluated as an average crack inclination along the four faces of the beam using equation 4.6. Each inclination is determined by an imaginary line connecting the cracks from one edge to the other on each face as shown in Figure 4.17b. The values of s_{rm} and α_{crm} for the tested beams are presented in Table 4.11, while Figure 4.18 and Figure 4.19 represent the crack pattern at the failure of the reference and strengthened beams, respectively.

$$s_{rm} = \frac{s_1 + s_2 + s_3 + ... + s_n}{n} \quad 4.5$$

$$\alpha_{crm} = \frac{\tan^{-1}\left(\frac{y}{x_1}\right) + \tan^{-1}\left(\frac{y}{x_2}\right) + \tan^{-1}\left(\frac{y}{x_3}\right) + ... + \tan^{-1}\left(\frac{y}{x_n}\right)}{n} \quad 4.6$$

Table 4.11 Average crack spacing (s_{rm}) and crack orientation (α_{crm}) of all beams, strengthened and reference beams

Beam	Average crack spacing s_{rm} (mm)	$\left(\frac{s_{rm}^{S} - s_{rm}^{R\_4S}}{s_{rm}^{R\_4S}}\right)100$ (%)	Average crack orientation, α_{crm} (degrees)
Ref_1S	417.92	-	49.61
Ref_4S	200.28	-	50.09
S4F_L2S5	132.59	-33.80	51.34
S4F_L2S10	104.48	-47.83	53.70
S4F_L4S5	133.33	-33.43	49.13
S4F_L4S10	101.37	-49.38	49.32
S3F_L2S5	169.20	-15.52	49.33
S3F_L4S10	139.90	-30.15	50.83
S4FL_L2S5	119.68	-40.24	49.88
S4FL_L4S10	88.71	-55.71	51.79

s_{rm}^{S/R_4S} : S and R stand for strengthened and reference beam, respectively

In the reference beams (Figure 4.18) the s_{rm} of Ref_4S (200 mm) is less than half the s_{rm} of Ref_1S (412mm), evidencing the high influence of the existing percentage of steel stirrups, with consequent impact on the torsional performance, as already described. However, the α_{crm} was equal in these two beams (50 degrees).

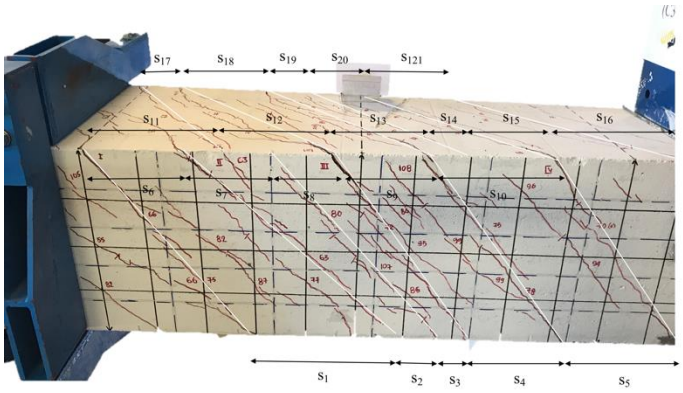

(a)

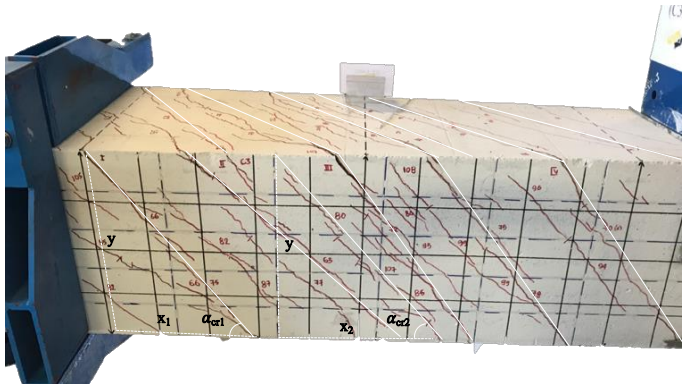

(b)

Figure 4.17 Schematic procedure to determine (a) Average crack spacing (s_{rm}) and (b) Average angle of inclination (α_{crm})

Regarding the strengthened beams (Figure 4.19) it is verified that the transverse CFRP laminates are more effective than the longitudinal CFRP laminates in decreasing the s_{rm}. In fact, the s_{rm} of the beams reinforced with the highest transverse strengthening ratio (S4F_L2S10 and S4F_L4S10 beams) in series one is almost equal, with an average value of 102 mm, whereas the s_{rm} of the beams reinforced with the lowest transverse strengthening ratio (S4F_L2S5 and S4F_L4S5 beams) is equal to 133 mm. The α_{crm} in the strengthened beams is almost equal to the one of the reference beams, varying between 49 and 54 degrees.

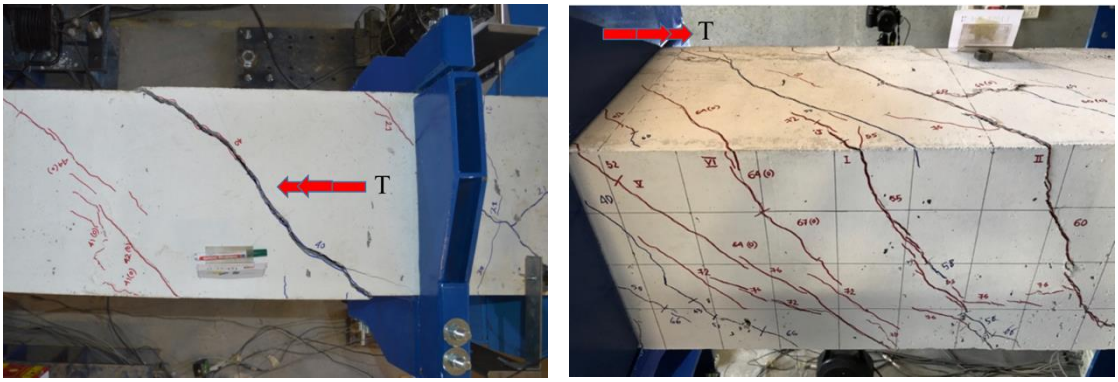

(a) (b)

Figure 4.18 Crack pattern at failure of reference beams (a) Ref_1S and (b) Ref_4S

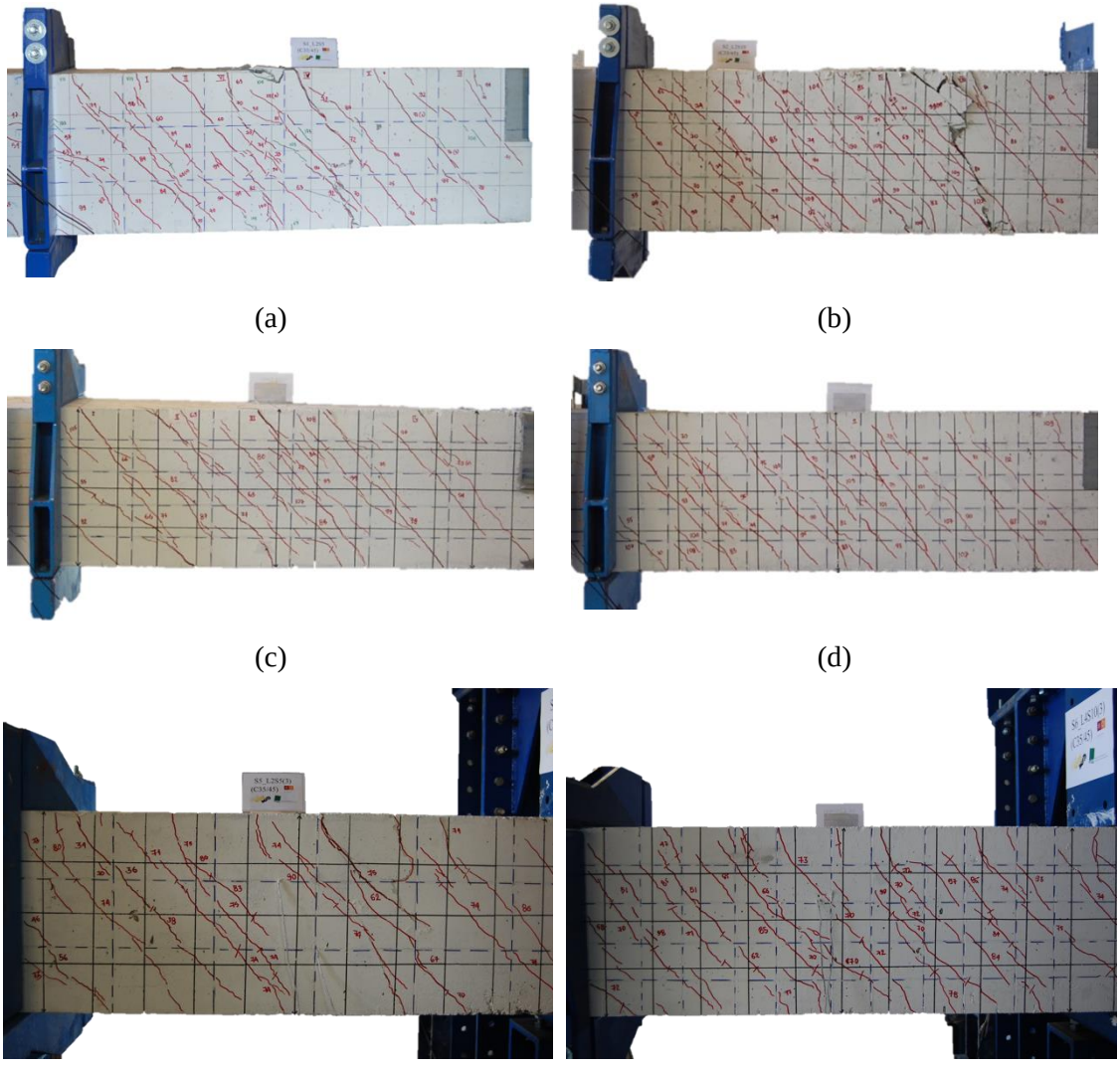

(a) (b)

(c) (d)

(e) (f)

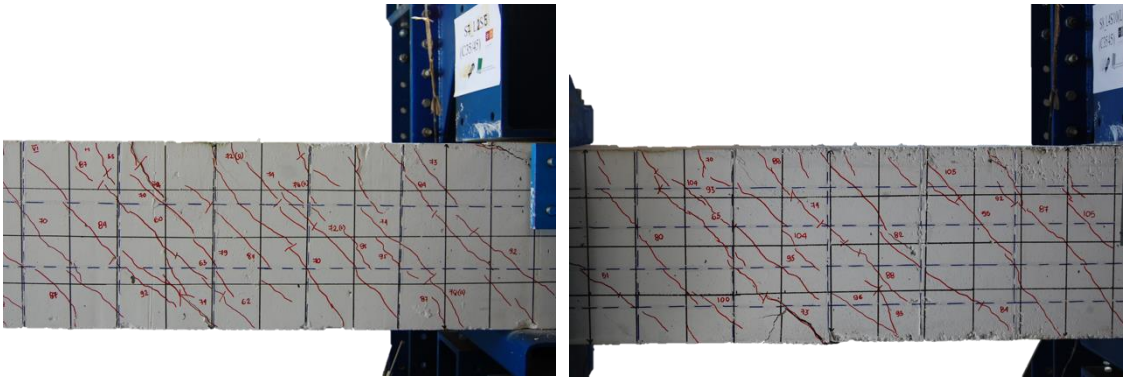

(g) (h)

Figure 4.19 Crack pattern of beams at failure (a) S4F_L2S5 (b) S4F_L2S10 (c) S4F_L4S5 (d) S4F_L4S10 (e) S3F_L2S5 (f) S3F_L2S10 (g) S4FL_L4S5 and (h) S4FL_L4S10

The post failure right face images of the strengthened beams in series two and series three are also shown in Figure 4.19. The reduction in s_{rm} in series two is lower, due to strengthening on only three faces of the beam. Since the cracking is larger on the unstrengthened top face, it increases the overall average crack spacing of the beams. All the four faces of beam S3F_L2S5 are shown in Figure 4.20. Beams S3F_L4S10 and S4FL_L4S10, with higher strengthening ratio in their respective series have more cracks due to higher torsional moment and ductility. In series three with L-laminate strengthening, the crack spacing, s_{rm} is reduced by 47.98% (average value) with respect to Ref_4S, showing the effectiveness of L-laminate strengthening. They also have the maximum reduction of crack spacing, considering both minimum and maximum strengthened beams. In terms of α_{crm} there is no much variation observed in strengthened beams, as the variation is between 49.88 – 51.79 degrees.

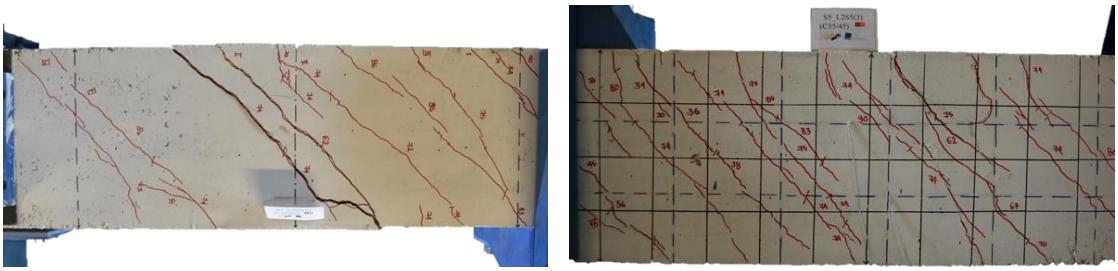

(a) (b)

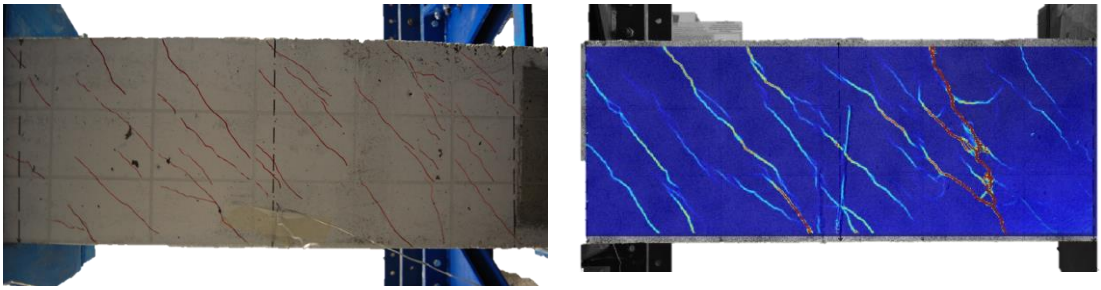

(c) (d)

Figure 4.20 Beam S3F_L2S5 faces after failure (a) Top (b) Right (c) Bottom & (d) Left

The Ref_1S beam had a brittle concrete failure (Figure 4.18a) with the formation of very small number of wider cracks due to the existence of only one stirrup in the beam's central study zone. However, Ref_4S has failed in a much more ductile behaviour due to the formation of several cracks and the contribution of the four steel stirrups (as seen in Figure 4.13a, longitudinal and transverse reinforcements have yielded). The S4F_L2S5 and S4F_L2S10 beams failed by CFRP rupture on the longitudinal laminate followed by concrete crushing (with spalling) on the right and top face (Figure 4.19a, Figure 4.21a and Figure 4.22a, and Figure 4.19b, Figure 4.21b and Figure 4.22b). S4F_L4S5 beam also failed with CFRP rupture (longitudinal laminate) and crushing of concrete but on the left and top surfaces (Figure 4.19c and Figure 4.22c). S4F_L4S10 beam had a premature concrete failure on the top surface between the steel jackets, due to load concentration from the steel loading section (Figure 4.19d and Figure 4.22d) inserted inside the hollow section of the beam. In spite of this, beam S4F_L4S10 presented the maximum torsional capacity. In S4F_L2S5, S4F_L2S10 and S4F_L4S10 beams the rupture of CFRP laminates was confirmed by post-testing inspections, shown in Figure 4.21.

In series two, beam S3F_L2S5 failed by concrete crushing on the top surface as expected, due to unstrengthening of CFRP laminates, leading to the formation of wider cracks. Beam S3F_L4S10 also failed by concrete crushing, but prematurely in between the two steel encasings like S4F_L4S10 of series one, due to stress concentration around the steel loading section. If premature failure did not occur, the beam was expected to fail on the unstrengthened top surface of the beam like in S3F_L2S5. In series three, both the beams (S4FL_L2S5 and S4FL_L4S10) failed by CFRP rupture on the longitudinal laminates followed by concrete crushing on the left face, closer to the fixed end. The failure locations of all the beams are shown in Figure 4.22.

(a) (b)

Figure 4.21 CFRP rupture in beams (a) S4F_L2S5: top face and (b) S4F_L2S10: top face

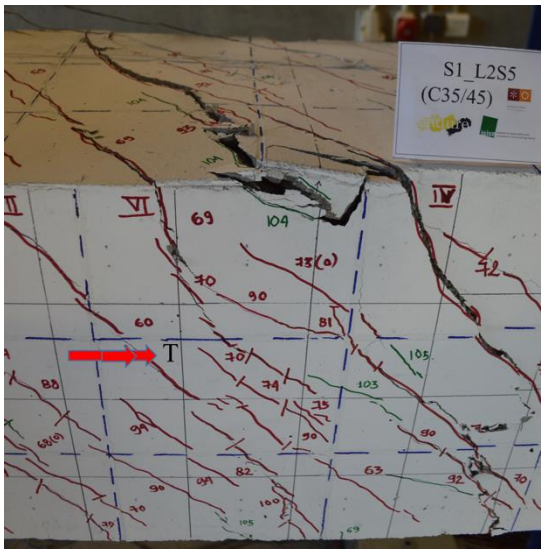

(a)

(b)

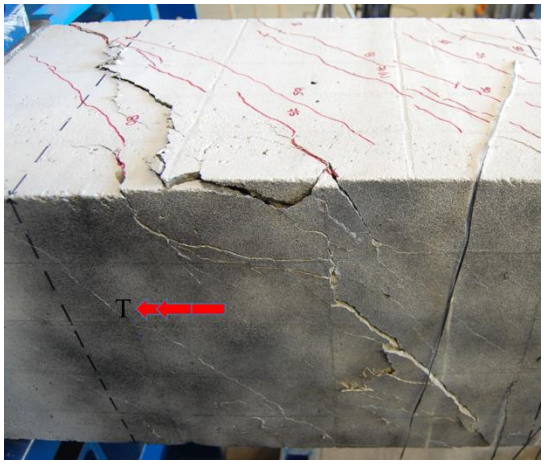

(c)

(d)

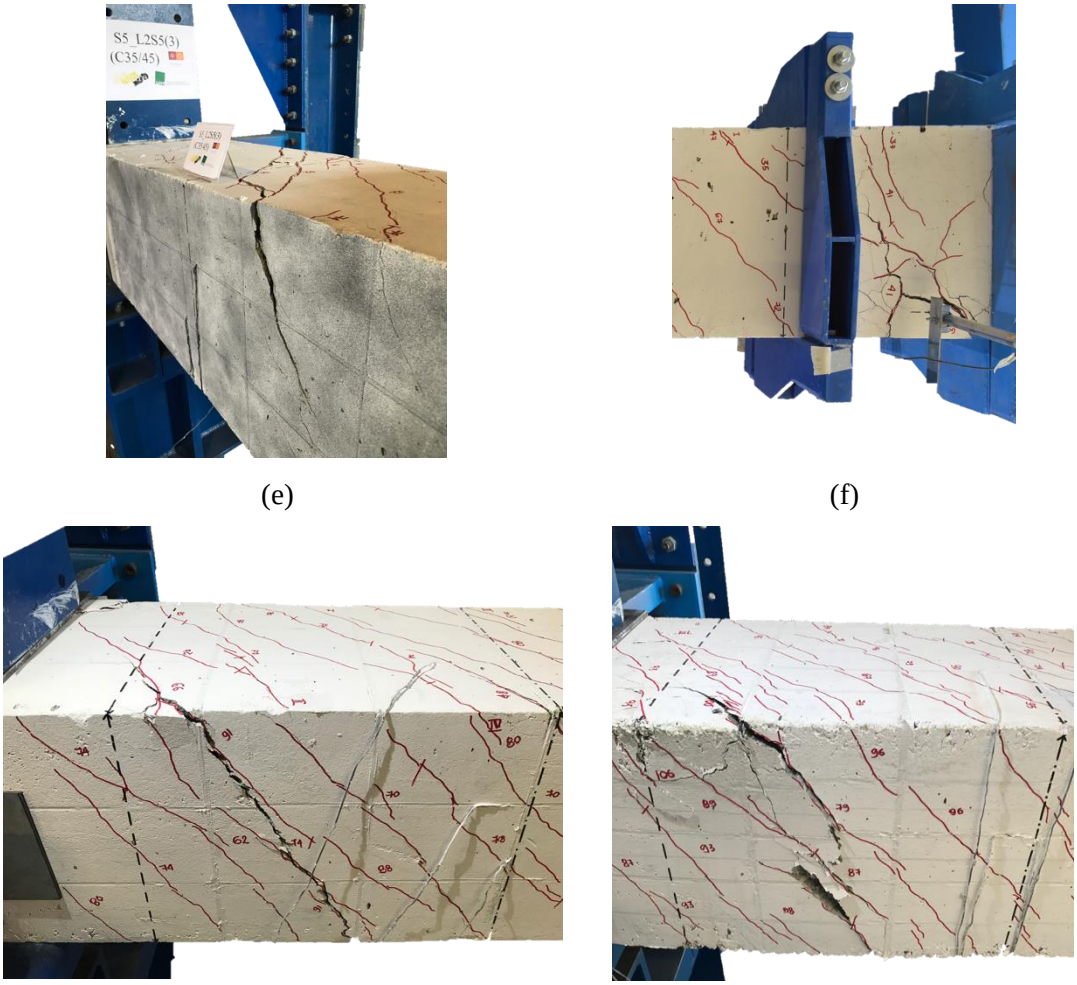

(e) (f)

(g) (h)

Figure 4.22 Failure configuration of all strengthened beams (a) S4F_L2S5 (b) S4F_L2S10 (c) S4F_L4S5 (d) S4F_L4S10 (e) S3F_L2S5 (f) S3F_L2S10 (g) S4FL_L4S5 and (h) S4FL_L4S10

4.2.4. DIGITAL IMAGE CORRELATION

2D digital image correlation (DIC) was used to monitor the behaviour of the strengthened beams to help in understanding the crack evolution and fracture mechanism of thin-walled tubular reinforced concrete structures. DIC was used to estimate the distribution of deformations on the left face of the beam in the central study zone of 1000 mm, by representing the principal tensile strain fields. The camera used to capture the images included a CMOS sensor with 24 mm by 36 mm, with approximately 36 MPix, and pictures are taken at a time interval of 10 seconds using lenses with a focal distance of 44 mm. The camera was mounted on a tripod at a distance of 1.22 m from the concrete surface. In order to have uniform lighting during the tests and to capture the images, two

LED lights are used. A speckle pattern is created on the surface using a very thin spray of Acrylic spray paint.

In order to explain the crack pattern and fracture of concrete, the cracks are categorized into the following and the schematic presentation of these cracks are shown in Figure 4.23:

1. Primary cracks (type I): cracks running throughout the face length, 400 mm;
2. Secondary cracks (type II): cracks subdivided into type A and B
    a. Type A (IIa): new cracks running for more than half the face length, 200 mm;
    b. Type B (IIb): originating from existing primary cracks for more than 200 mm length;
3. Tertiary cracks: subdivided into type A and B cracks
    a. Type A (IIIa): new cracks running less than half the face length (200 mm);
    b. Type B (IIIb): cracks originating from existing primary or secondary cracks, with length less than 200 mm.

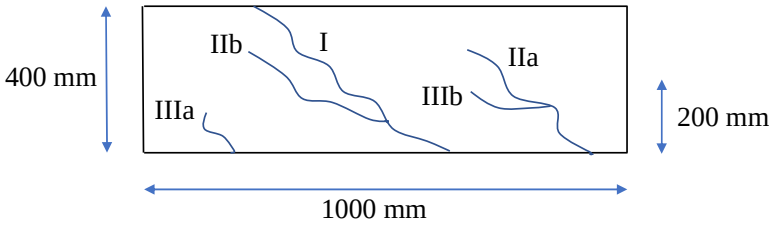

Figure 4.23 Schematic representation of cracks

Beam S4F_L4S5 is used to describe the crack evolution according to the DIC. Step by step development of cracks depending on the important stages of cracking is presented in Figure 4.24, while the corresponding points of CFRP strain evolution are presented in Figure 4.25. The longitudinal and transverse CFRP laminates are presented by white dotted lines in Figure 4.24 and, the transverse and longitudinal steel reinforcement by yellow dotted lines in all the images. The strain grading scale in the DIC images is varied between '0 – 0.1', where '0' presents no crack and '0.1' presents the cracks with maximum surface strain in the analysis. The maximum surface strains of concrete in each beam can be different. The rest of the strengthened beams follow a similar pattern, whose differences are mainly dependent on the strengthening ratios of CFRP laminates, since the steel reinforcement is maintained same in all the beams.

In beam S4F_L4S5, the crack initiates in the over reinforced region, where the torsional cracking moment, $M_{t,cr}$, is registered. The cracking then spreads into the central study region of 1000 mm, from both the loading and the fixed ends at 1.89° and 54.11 kN.m, with the formation of secondary and tertiary cracks (IIIa). The first abrupt jump in the steel strain evolution at this stage is observed in transverse steel reinforcement, shown in Figure 4.14c (SG_TS2). The beam enters in the macro/micro crack propagation phase, where the cracking mainly taking place in the central region with the development of critical cracks, leading to the failure of the beam at later stages. At this stage, the moment carrying capacity is mainly resisted by steel reinforcements in case of reference beam as seen in Figure 4.13a and in case of strengthened beams, from concrete to steel (Figure 4.14c) and CFRP reinforcements (Figure 4.25). In case of reference beam, a sudden abrupt increase in steel strains between 4000-6000 micro strain is obtained, whereas in case of strengthened beams (S4F_L4S5) it is limited to 2000 micro strain (Figure 4.14c), since the moment carrying capacity is shared between the steel and CFRP laminates.

At 2.44° and 56.72 kN.m, a primary crack is formed in the middle of the beam along with a few tertiary cracks, which later interconnect to form primary and secondary cracks. At this stage the strain jump in both the steel and CFRP transverse reinforcement (Figure 4.25: point ‘c’) is also recorded. As the applied torsional moment is increased, the crack propagation continues mainly with generation of secondary and tertiary cracks, instead of primary cracks due to the presence of longitudinal and transverse CFRP laminates successfully avoiding the formation of primary cracks, resulting in higher angle of rotation increasing the ductility performance and the torsional moment carrying capacity of the beam (5.99°, 73.74 kN.m: Figure 4.24g and point g in Figure 4.25). Almost every DIC image corresponds to a change in the strain of longitudinal or transverse CFRP laminates. It is clearly observed in Figure 4.24 (d-k) that the longitudinal and the transverse CFRP laminates arrest the crack growth at four locations (position of longitudinal CFRP laminates) along the depth of the beam and at five locations (position of transverse CFRP laminates), generating many secondary and tertiary cracks rather than the primary cracks (cracks running full length of the beam, 400 mm).

θ_t / M_t	DIC	$M_t - \theta_t$	Remarks
0.34°/ 20.78 kN.m	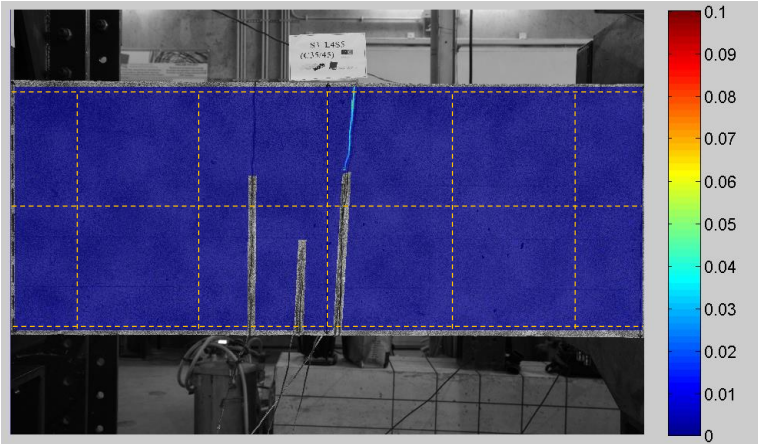	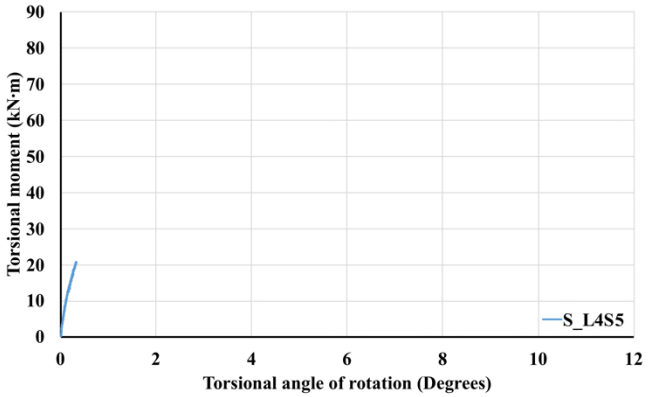	Linear phase
1.89°/ 54.11 kN.m	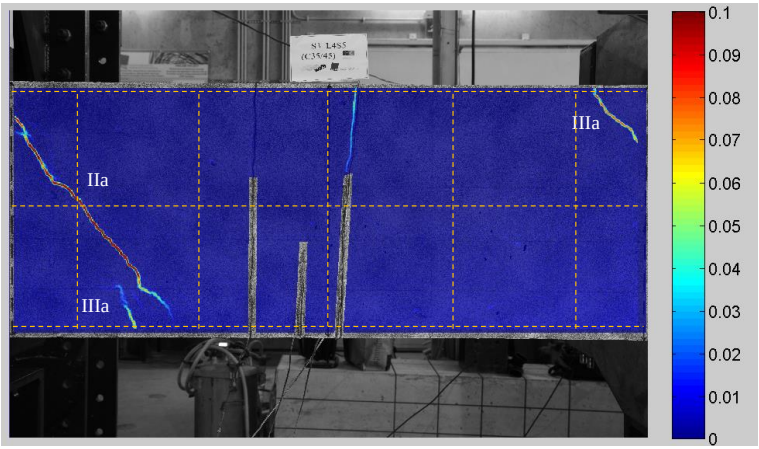	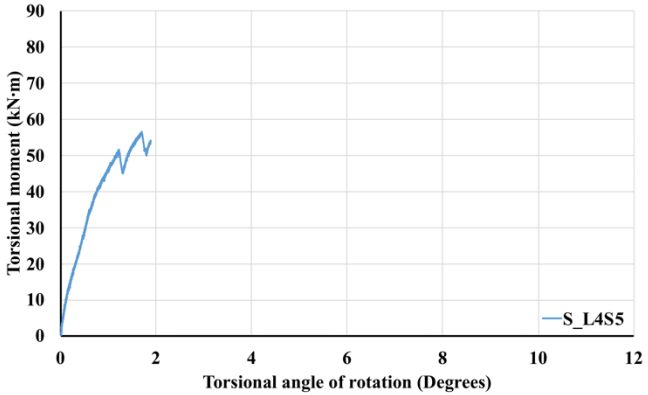	Crack propagation phase

(a)

(b)

2.44°/ 56.72 kN.m

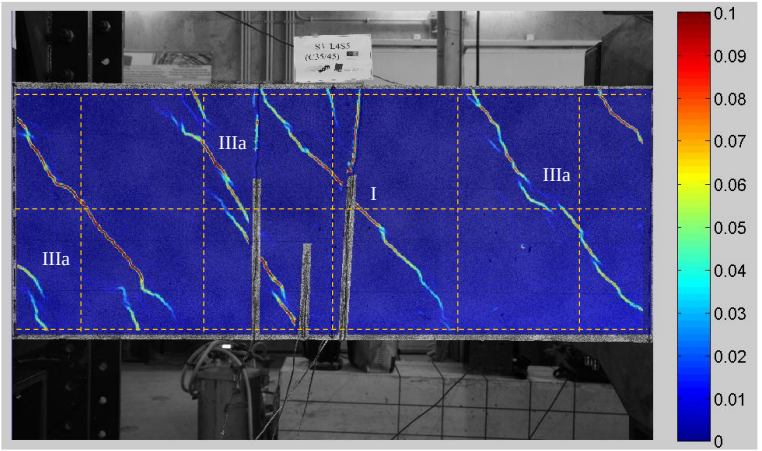

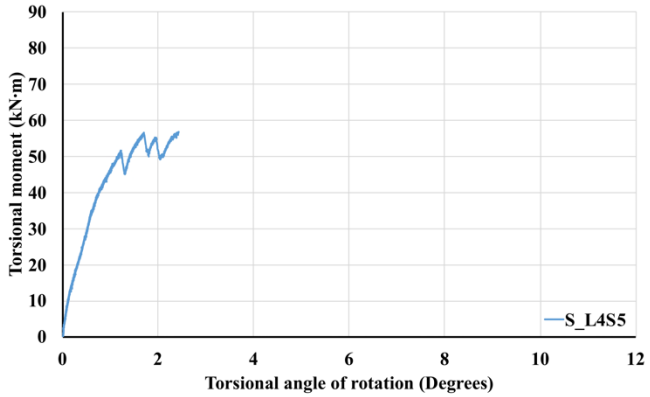

Termination of crack propagation phase and initiation of steel yielding phase

(c)

3.43°/ 60.99 kN.m

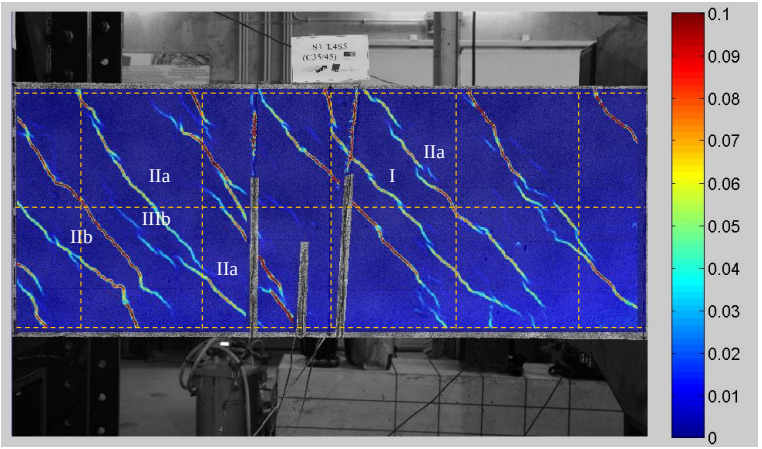

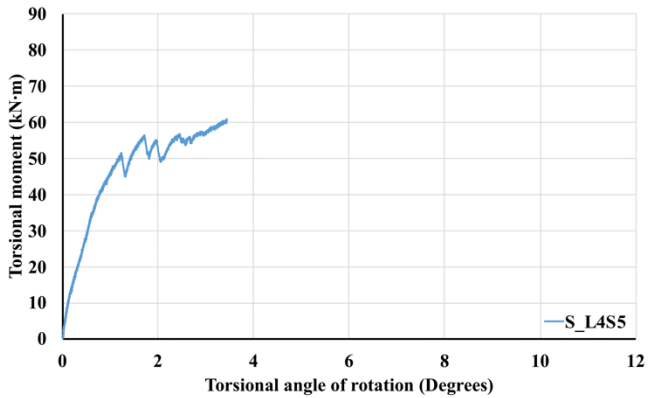

Steel yielding phase

(d)

4.51°/
68.12
kN.m

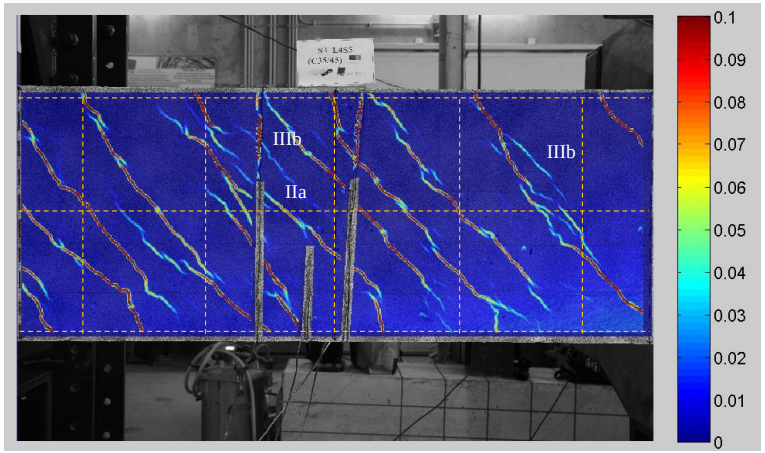

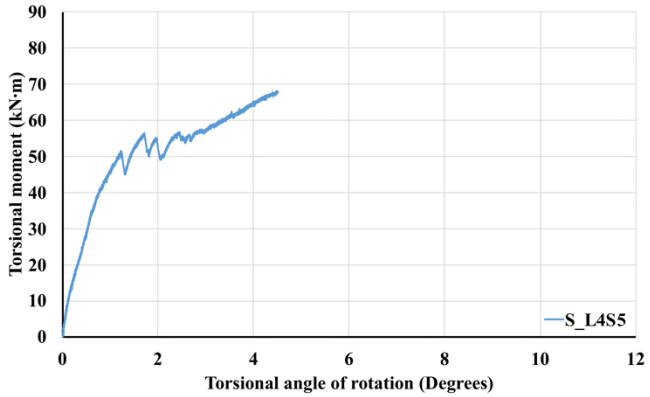

Cracking

(e)

5.22°/
70.92
kN.m

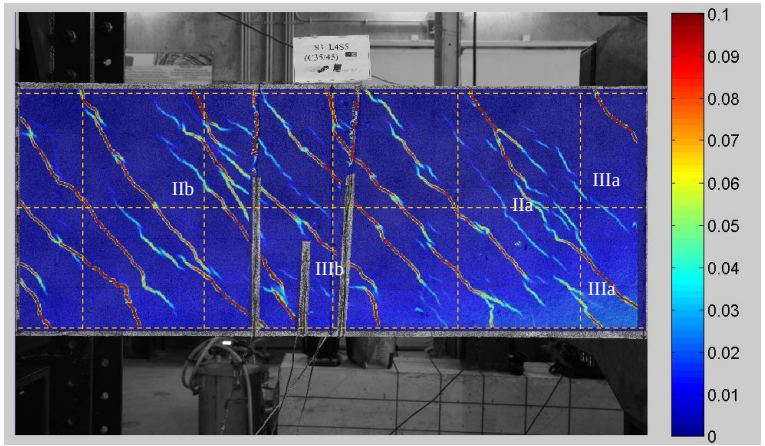

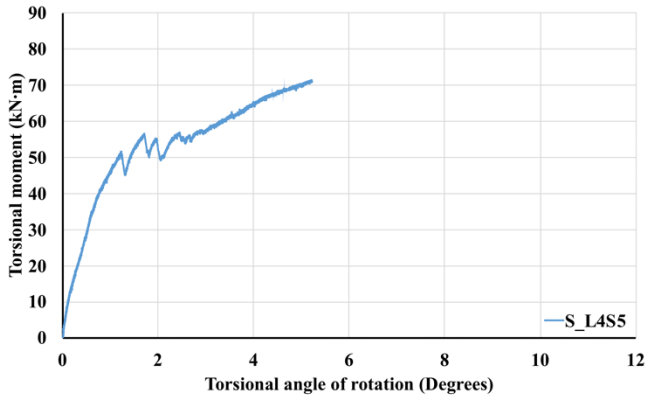

Cracking

(f)

5.99°/
73.74
kN.m

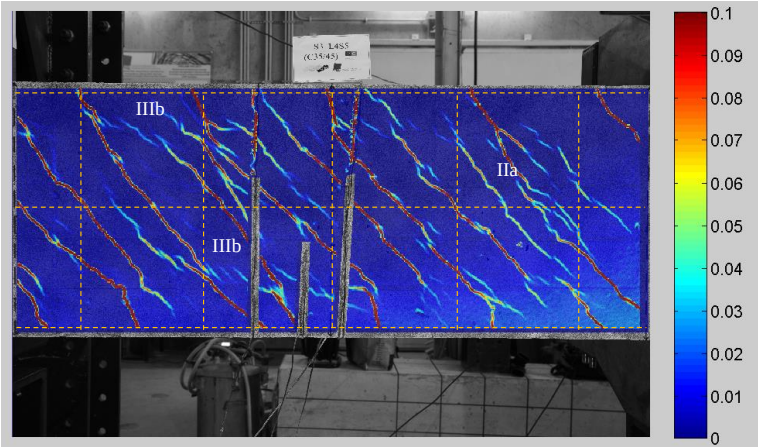

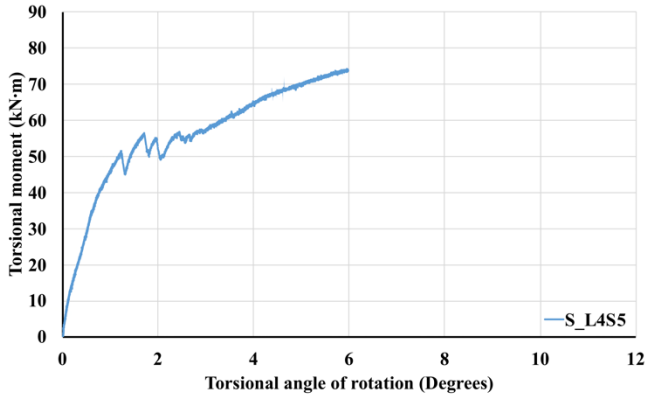

Cracking

(g)

7.39°/
77.34
kN.m

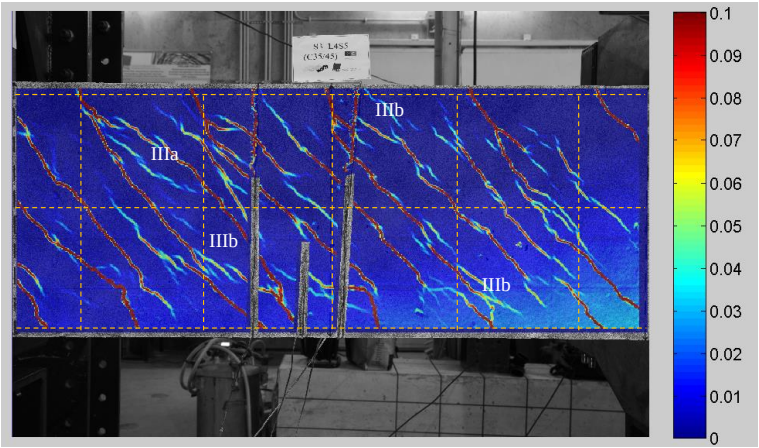

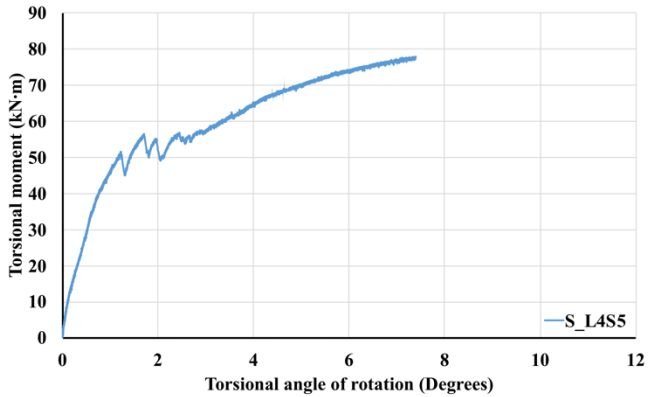

Cracking

(h)

8.44°/ 77.95 kN.m

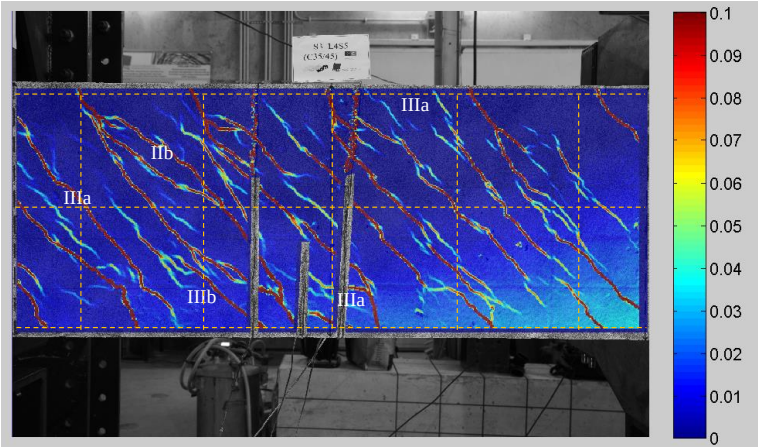

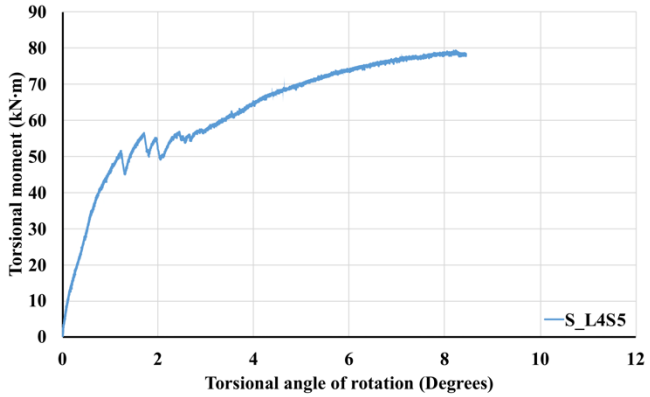

Peak torsional moment

(i)

9.44°/ 64.78 kN.m

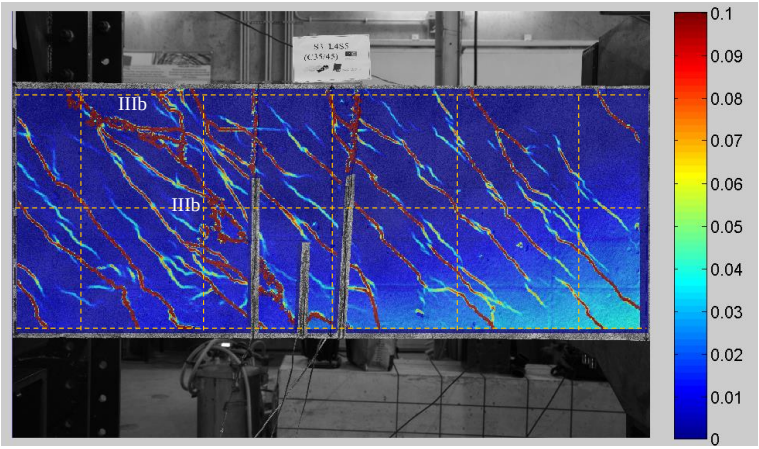

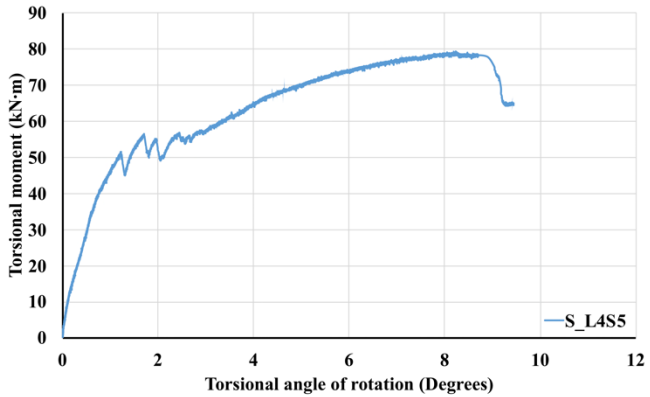

After failure

(j)

9.53°/ 64.92 kN.m

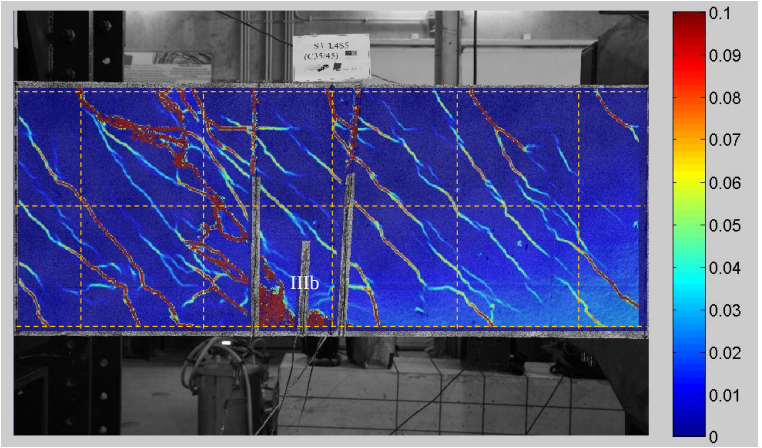

End of test

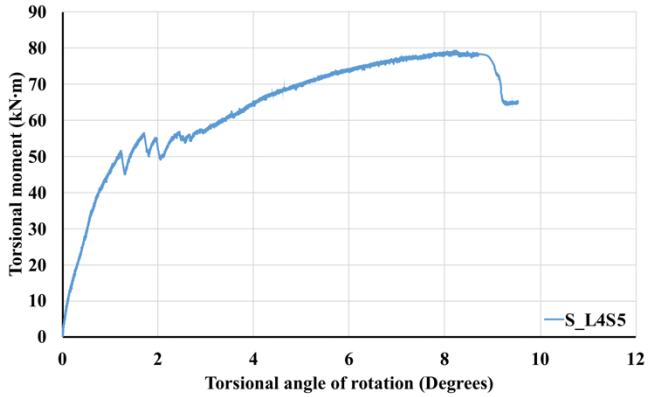

(k)

Figure 4.24 Crack evolution of beam S4F_L4S5 captured by digital image correlation (DIC)

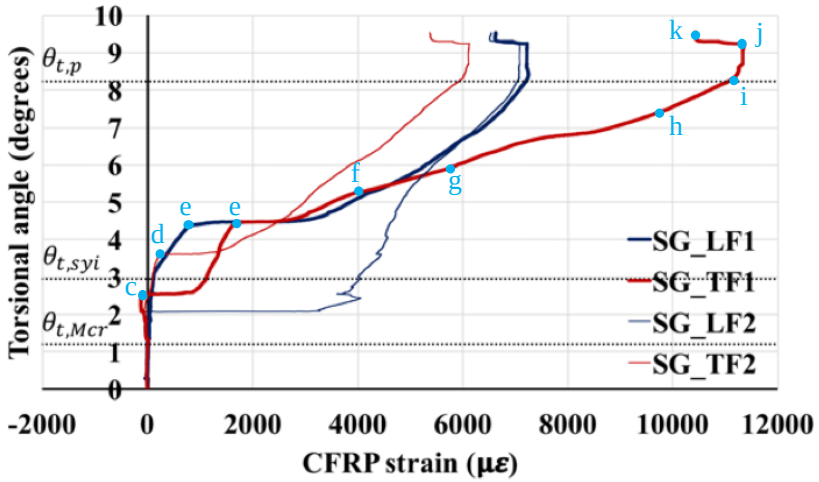

Figure 4.25 CFRP strain *vs.* torsional angle of rotation of beam S4F_L4S5

Crack stabilization is reached when yielding of steel reinforcement takes place. New crack formation and widening of existing tertiary and secondary cracks are noticed at a lower rate. Interlinking of existing cracks, between all three type of cracks also take place at this stage (5.99°, 73.74 kN.m). Few of the steel reinforcements have yielded and the CFRP laminates are totally active in resisting the torsional moment. It is confirmed by the change in the stiffness response of the CFRP laminates, leading to higher contribution, shown in Figure 4.25. More cracks are formed at the top and bottom approximate locations of the steel longitudinal reinforcement, which can be due to their yielding. Peak torsional moment is reached in Figure 4.24i (8.44°, 77.95 kN.m and point 'i' in Figure 4.25), leading to interconnection of cracks leading to the failure of the beam (9.44°, 64.78 kN.m) and entering into the torsional softening response of the beam.

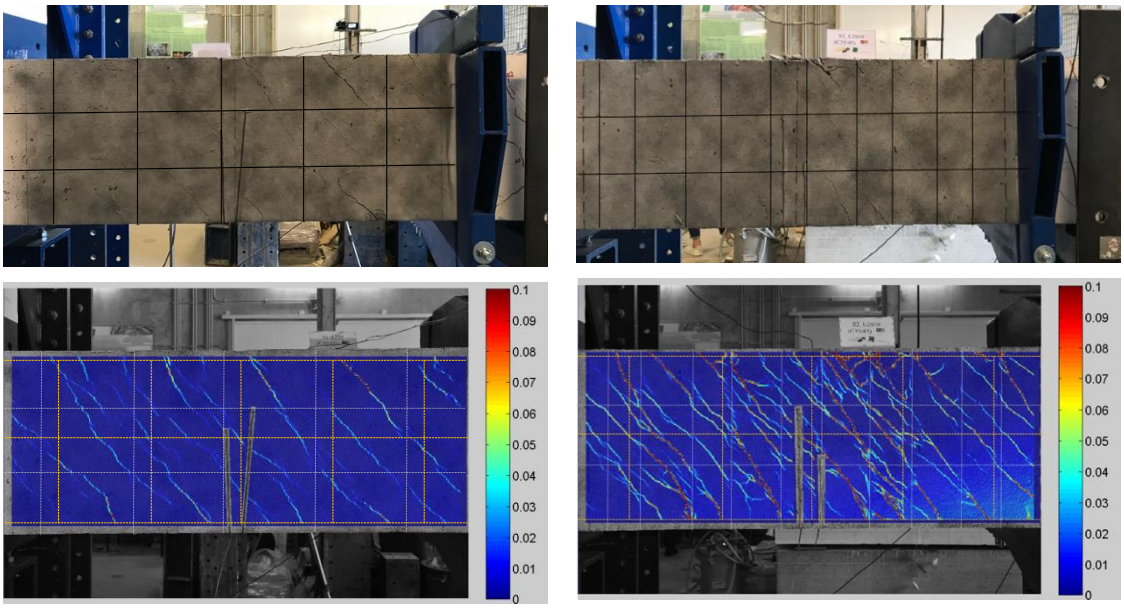

(a) (b)

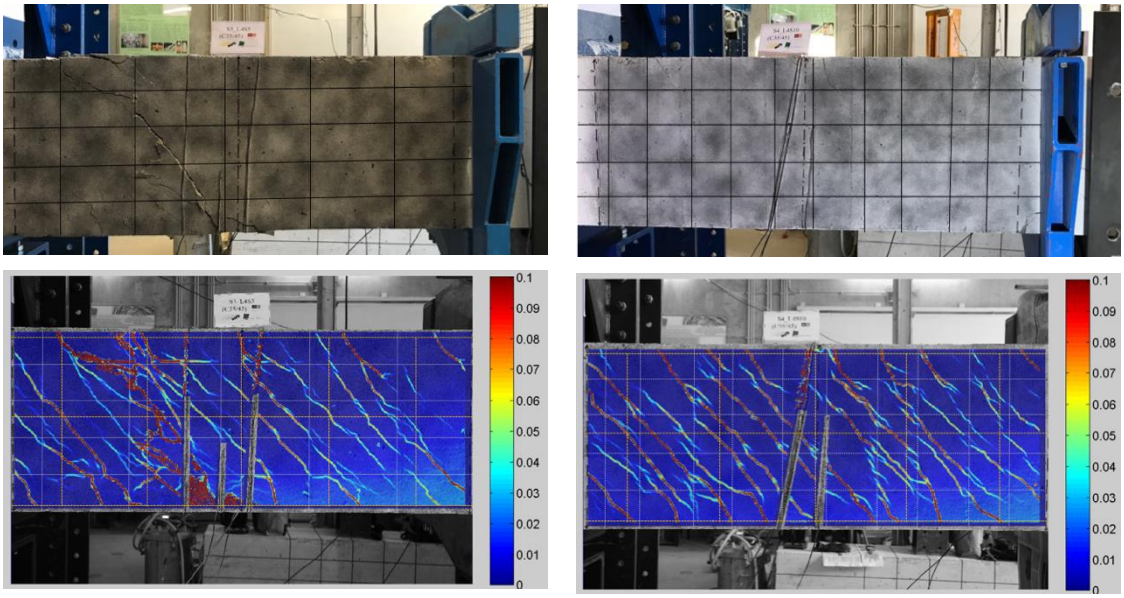

(c) (d)

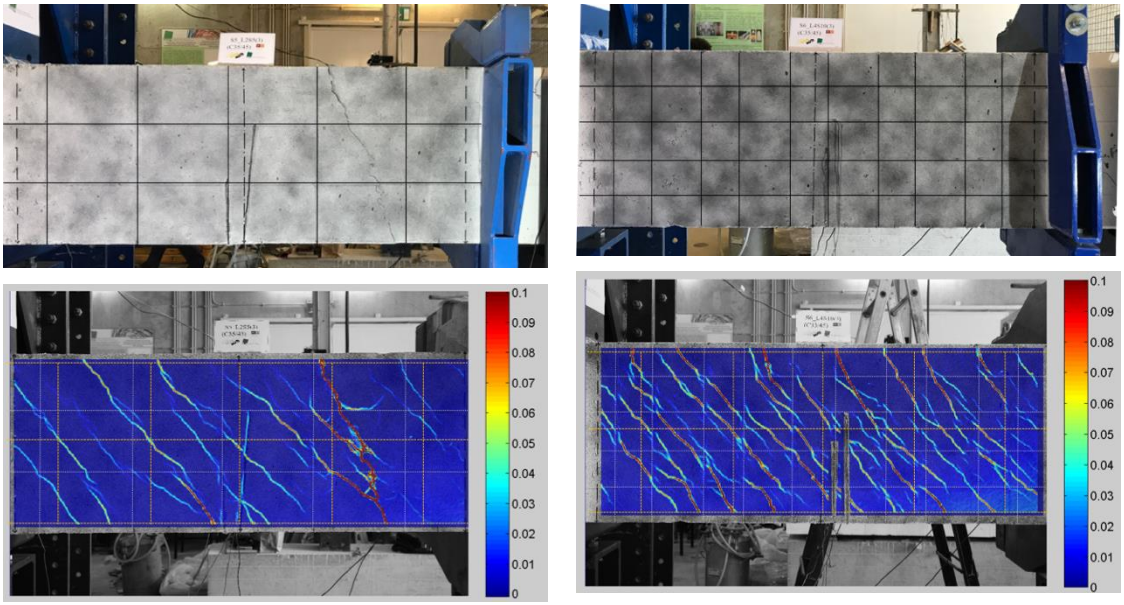

(e) (f)

Figure 4.26 DIC results (a) S4F_L2S5 (b) S4F_L2S10 (c) S4F_L4S5 (d) S4F_L4S10 (e) S3F_L2S5 and (f) S3F_L4S10

Figure 4.26 shows the surface strain distribution of all the beams tested with DIC, in which the CFRP laminates are presented by white dotted lines both in horizontal and longitudinal direction, and by black lines in real images. The DIC analysis helps in understanding:

- The crack growth/evolution in thin-walled elements subjected to torsion, which is invisible to the naked eye (mainly in initial stages);

- Every new crack formed is clearly linked to a change in steel or CFRP strain variation;
- The interlinking of many secondary and tertiary cracks, leading to the formation of primary cracks ultimately resulting in the failure of the beam;
- The contribution of CFRP laminates in resisting torsion is mainly dependant on their reinforcement ratios.

From the results it can be concluded that the CFRP laminates successfully arrest the crack growth by breaking the primary cracks into tertiary cracks at initial stages (Figure 4.24c, IIIa) and into secondary cracks at higher moment (Figure 4.24i, IIb). However, at higher angle of rotation (closer to peak moments), interconnection of tertiary and primary cracks take place leading to the failure of the beam (Figure 4.24j). In few cases, it is also noticed that the crack develops along the bond between CFRP and concrete, only at the critical crack location closer to the failure stages (Figure 4.26c, top longitudinal CFRP laminate). In most of the cracks at laminate location the strain is lower, especially at the overlapping of longitudinal and transverse laminates, due to multiple layers of CFRP laminates (Figure 4.26d, along lower longitudinal CFRP laminate) resisting the applied torsion.

Beam S4F_L2S5 is shown in Figure 4.26(a), where the failure of the beam is not captured by the DIC as it takes place on the top and partial right surface, whereas the DIC is measured on the left face. The cracks are spaced at an average distance of 142.86 mm. The average crack spacing is calculated considering only the cracks which run full length on the left face (type I crack) and is shown in Table 4.12. However, the average crack spacing considering all the four faces of the beams using equations 4.5 and 4.6, are also presented in the table for comparison. The results show that the difference between both (using DIC and equations 4.5 and 4.6) values vary by an average of 5.25%, which can be due to the difficulty in measuring and identifying the accurate origin of the cracks.

Table 4.12 Average crack spacing based on DIC results

Beam	Average crack spacing according to DIC (mm): left face	Average crack spacing (mm): all faces	DIC/average of four faces (%)
Ref_4S	163.76	200.28	81.77
S4F_L2S5	142.86	132.59	107.75
S4F_L2S10	120.00	104.48	114.86
S4F_L4S5	139.58	133.33	104.69
S4F_L4S10	114.00	101.37	112.46
S3F_L2S5	186.07	169.20	109.97
S3F_L4S10	120.45	139.90	86.10
Average			102.51

The results of S4F_L2S10 with twice the transverse CFRP laminates with respect to S4F_L2S5 is shown in Figure 4.26b. In this case too, the failure is obtained on the top and right faces. Higher number of cracks are formed in the beam (S4F_L2S10) due to higher torsional moment obtained. The CFRP laminates are successful in arresting the crack propagation with lower crack spacing of 120 mm. Beam S4F_L2S5 failed by concrete crushing on the unstrengthened top surface and partial failure on the left face captured by DIC. The average crack spacing is 186 mm, which is the highest with respect to the other beams, due to early failure of the beam. However, considerable improvement in the torsional moment carrying capacity (18%) is obtained. Figure 4.26d, shows the results of beam S4F_L4S10 with maximum strengthening. The failure is not captured by the DIC due to premature failure of the beam in the over-reinforced region of the loading end. Beam S3F_L2S5 is shown in Figure 4.26e, where the failure takes place on the top and partial left face captured by the DIC.

4.2.5. COMPARISON

In the current section, comparison of beams with similar CFRP strengthening ratios both in longitudinal and transverse direction is performed. It is categorized into two parts, (i) with minimum strengthening ratio, involving beams of the type S*x*_L2S5 and (ii) with maximum strengthening ratio of types S*x*_L4S10. These variations are adopted to investigate the influence of different strengthening proposals like, the four-face

strengthening, three face strengthening, and application of straight and L-laminate in NSM torsional strengthening.

4.2.5.1. Beams strengthened with minimum strengthening ratios: S*x*_L2S5

Beams S4F_L2S5, S3F_L2S5 and S4FL_L2S5 with the minimum strengthening ratio in each series are compared in this section. Beam S4F_L2S5 is strengthened on four faces with straight CFRP laminates, beam S3F_L2S5 is strengthened only on three faces with straight CFRP laminates. Finally, beam S4FL_L2S5 is strengthened with L-CFRP laminate on all the four faces of the beam. The strengthening ratios of the beams are presented in Table 4.1 and the results are compared in Table 4.13, Table 4.14, Table 4.15 and Table 4.16. The $M_t - \theta_t$ response is shown in Figure 4.27.

The linear torsional stiffness, $k_{t,lin}$, has reduced in all the three series by an average of 6.13%, which can be neglected considering the percentage variation and the difficulty in detecting torsional cracking moment as discussed in section 4.2.3.1. In terms of torsional cracking moment, $M_{t,cr}$, and torsional angle, $\theta_{t,cr}$, all the beams have also reduced performance. The values of $M_{t,cr}$ and $\theta_{t,cr}$, for all the beams are in similar range except beam S3F_L2S5 in $\theta_{t,cr}$ due to early cracking (premature failure).

Table 4.13 Experimental results of minimum strengthening ratio beams in terms of M_t, torsional moment

Beam	$M_{t,cr}$ (kN.m)	$\left(\frac{M^S_{t,cr}-M^R_{t,cr}}{M^R_{t,cr}}\right)$	$M_{t,A}$ (kN.m)	$M_{t,syi}$ (kN.m)	$\left(\frac{M^S_{t,syi}-M^R_{t,syi}}{M^R_{t,syi}}\right)$	$M_{t,p}$ (kN.m)	$\left(\frac{M^S_{t,p}-M^R_{t,p}}{M^R_{t,p}}\right)$
Ref_4S	28.01	-	40.02	47.29	-	56.69	-
S4F_L2S5	25.04	-10.61	41.99	55.23	16.79	78.30	38.11
S3F_L2S5	23.69	-15.43	42.82	56.28	19.02	66.65	17.57
S4FL_L2S5	24.93	-10.98	42.59	55.72	17.83	77.05	35.90

Table 4.14 Experimental results of minimum strengthening ratio beams in terms of θ_t, angle of rotation

Beam	$\theta_{t,cr}$ (deg.)	$\left(\frac{\theta^S_{t,cr}-\theta^R_{t,cr}}{\theta^R_{t,cr}}\right)$	$\theta_{t,A}$ (deg.)	$\theta_{t,syi}$ (deg.)	$\left(\frac{\theta^S_{t,syi}-\theta^R_{t,syi}}{\theta^R_{t,syi}}\right)$	$\theta_{t,p}$ (deg.)	$\left(\frac{\theta^S_{t,p}-\theta^R_{t,p}}{\theta^R_{t,p}}\right)$
Ref_4S	0.39	-	0.54	2.77	-	4.78	-
S4F_L2S5	0.33	-14.43	0.57	2.76	-0.44	7.31	53.01
S3F_L2S5	0.21	-45.62	0.57	2.70	-2.39	4.63	-3.17
S4FL_L2S5	0.34	-13.74	0.70	2.82	1.73	7.14	49.42

Table 4.15 Experimental results of minimum strengthening ratio beams in terms of k_t , stiffness

Beam	$k_{t,lin}$ (kN.m/deg.)	$\left(\frac{k_{t,lin}^{S}-k_{t,lin}^{R}}{k_{t,lin}^{R}}\right)$	$k_{t,Mcr}$ (kN.m/deg.)	$\left(\frac{k_{t,Mcr}^{S}-k_{t,Mcr}^{R}}{k_{t,Mcr}^{R}}\right)$	$k_{t,syi}$ (kN.m/deg.)	$\left(\frac{k_{t,syi}^{S}-k_{t,syi}^{R}}{k_{t,syi}^{R}}\right)$
Ref_4S	69.80	-	4.02	-	7.36	-
S4F_L2S5	64.46	-7.66	5.77	43.64	6.10	-17.06
S3F_L2S5	68.91	-1.28	4.88	21.52	7.44	1.12
S4FL_L2S5	63.21	-9.45	6.05	50.47	6.46	-12.18

All beams have improved stiffness at macro cracking stage $k_{t,Mcr}$, due to the contribution of CFRP laminates. It is dependent on the CFRP laminate location (strengthening arrangement) and crack location, since the strengthening ratio of CFRP laminates (except beam S3F_L2S5) is maintained the same. S4F_L2S5 presented the best response due to effective activation and higher contribution of the CFRP laminates, where three of the four strain gauges in the CFRP have registered more than 4000 $\mu\varepsilon$, Figure 4.15a. In terms of torsional moment at steel yielding, $M_{t,syi}$, all the beams have registered an average increase of 17.88%. In case of torsional angle of rotation at steel yielding, the differences in values are not so different with respect to the reference beam. Considering the peak moment, $M_{t,p}$, all three beams have shown increased torsional moment carrying capacity by an average of 30.41%. In terms of torsional angle of rotation at peak moment, beams S4F_L2S5 and S4FL_L2S5 have increased by 50%, whereas beam S3F_L2S5 had early failure on the top surface of the beam.

Considering the peak moment and torsional angle of rotation at peak moment, beam S4F_L2S5 had the best performance with respect to other strengthening configurations in minimum strengthened beams. Beam S4FL_L2S5 had equally good performance, even though the difference between beam S4FL_L2S5 and S4F_L2S5 in terms of peak moment and angle of rotation at peak moment is very less. In both these beams, the strengthening configuration has promoted formation of more cracks of smaller crack width, resulting in higher contribution of the concrete and the reinforcements. It can be seen in Figure 4.15a of torsional moment *vs.* CFRP strain evolution, Figure 4.19a of crack pattern and in Table 4.11 of crack spacing, increasing the torsional capacity and deformability of the beam response, due to effective utilization of the CFRP laminates since they cross more cracks. Comparing the strains, beam S4F_L2S5 has attained the maximum strain of 6.90‰ in the top transverse CFRP laminate.

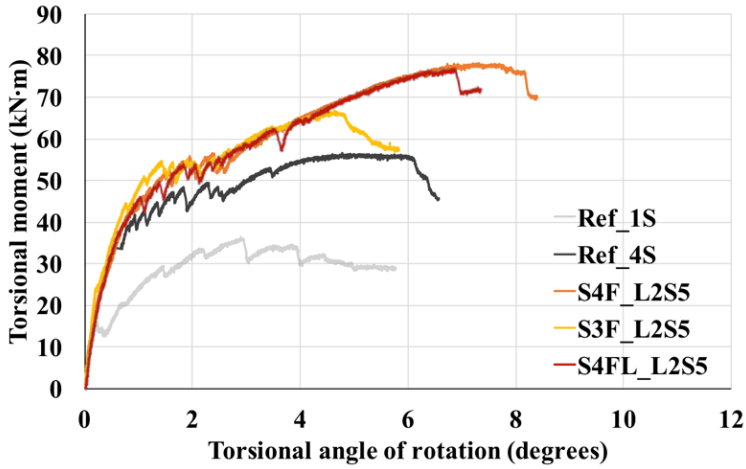

Figure 4.27 Torsional moment *vs.* torsional angle of rotation of beams with minimum strengthening ratio in the experimental campaign

Beam S3F_L2S5 follows almost similar response of $M_t - \theta_t$ as S4F_L2S5 up to 4.20º angle of rotation and then deviates entering the softening phase due to formation of critical crack on the left face of the beam. The DIC images just before and after 4.20° angle of rotation is used for comparison in Figure 4.28a and b, and in Figure 4.28c and d in beams S4F_L2S5 and S3F_L2S5, respectively. The critical crack is represented by white box in Figure 4.28b of beam S3F_L2S5, where coalescence of two primary cracks takes place resulting in the beam failure being closer to the longitudinal steel reinforcement, and between both the longitudinal and transverse CFRP reinforcements. In case of beam S4F_L2S5 it can be seen that the beam continues increasing the torsional moment capacity (Figure 4.27) with the formation of new cracks with lower tensile strains (Figure 4.28). Still the performance of the beam S3F_L2S5 with three face strengthening is better in comparison to reference beams, providing a very good increase in torsional moment capacity and stiffness.

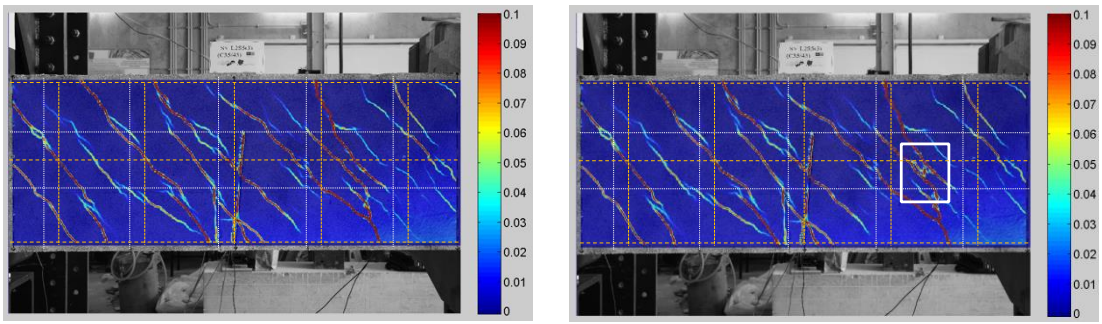

(a) (b)

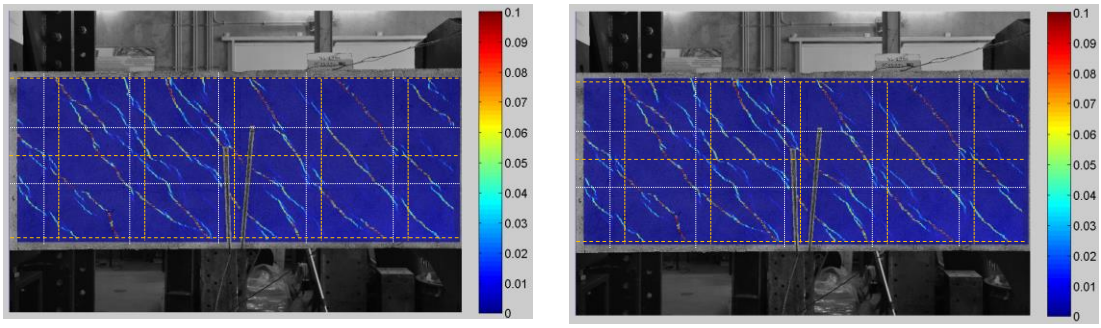

(c) (d)

Figure 4.28 DIC results (a) and (b) Beam S3F_L2S5 (before and after 4.20°), (c) and (d) Beam S4F_L2S5 (before and after 4.20°)

More cracks are formed in S4FL_L2S5 as shown in Figure 4.19g and Figure 4.24c and d, due to the wider spacing of the CFRP transverse laminates on all the four faces (200 mm). In beams S4F_L2S5 and S3F_L2S5 the CFRP laminates are distributed over the surface of the beam as presented in Figure 4.4 and Figure 4.5. In terms of cracks spacing, s_{rm}, an overall average reduction of 29.9% is obtained with respect to all the minimum strengthened beams, shown in Table 4.16. Beam S4FL_L2S5 with L-laminates has the maximum decrease in crack spacing and the minimum decrease is registered in beam S3F_L2S5, due to wider cracking on the unstrengthened top surface, increasing the overall average crack spacing of the beam.

Table 4.16 Experimental results of minimum strengthening ratio beams in terms of s_{rm}, crack spacing and α_{crm}, crack orientation

Beam	Crack spacing (mm, s_{rm})	$\left(\frac{s_{rm}^{S} - s_{rm}^{R\_4S}}{s_{rm}^{R\_4S}}\right)$	Crack orientation (degrees, α_{crm})
Ref_1S	417.92	-	49.61
Ref_4S	200.28	-	50.09
S4F_L2S5	132.28	-33.80	51.34
S3F_L2S5	169.20	-15.52	49.33
S4FL_L2S5	119.68	-40.24	49.88

4.2.5.2. Beams strengthened with maximum strengthening ratio: S*x*_L4S10

The $M_t - \theta_t$ relation for second set of beams with higher strengthening ratios i.e., S4F_L4S10, S3F_L4S10 and S4FL_L4S10 are compared in Figure 4.29, and the results are presented in Table 4.17, Table 4.18, Table 4.19 and Table 4.20 in terms of M_t, θ_t, k_t, s_{rm} and α_{crm}. In beam S4F_L4S10, the transverse laminates are spaced at an average distance of 100 mm and in beam S4FL_L4S10 the laminates are spaced at 200 mm with double layer of CFRP laminates maintaining the same reinforcement ratio. Like in minimum strengthened beams, series one beam S4F_L4S10 had the best performance in $M_{t,p}$ followed by series three and series two. This is due to the early activation of the transverse CFRP laminates, as they cross many spiral cracks generated by torsion. In case of series three, the torsional spiral cracks are interrupted by two transverse laminates placed in the same slit, whereas in case of series one, only one laminate is placed in each slit (also on series two), resulting in different bond conditions of the CFRP to concrete substrate. Since two laminates are placed in the same slit in series three, the applied moment is resisted by both the laminates resulting in lower tensile strain in transverse laminates than in series one. This is confirmed from the strain distribution (Figure 4.15d, f and h), where the longitudinal laminates reach higher strain than the transverse laminates unlike in series one beam where the transverse laminates have attained higher CFRP strains.

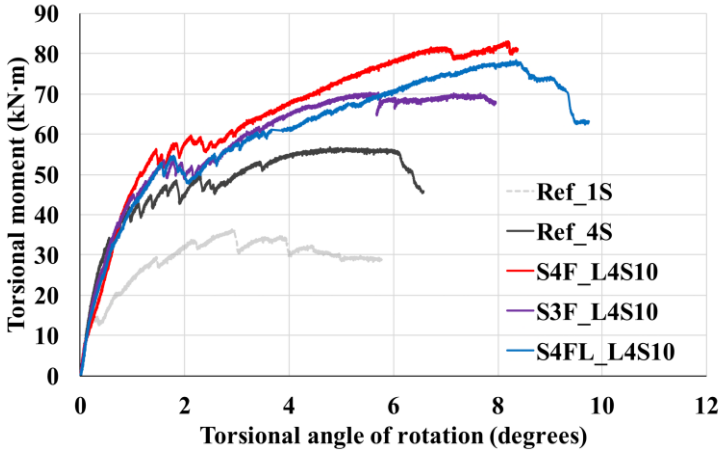

Figure 4.29 Torsional moment *vs.* torsional angle of rotation of beams with maximum strengthening ratio in the experimental campaign

Figure 4.30, shows the crack pattern on the right face of the beams with maximum strengthened ratios of all the series. As seen, beam S4F_L4S10 has more cracks, mainly

of the secondary and tertiary type cracks due to successful arrest in crack propagation by the CFRP laminates. In case of series three, many full primary cracks (crack running throughout the face) are formed, rather than secondary or tertiary cracks. Considering the crack spacing, series three has the maximum decrease, followed by series one and series three (Table 4.20). It should be noted that the crack spacing is calculated as an average spacing of only fully developed cracks on each face of the beam. The linear torsional stiffness of all the three strengthened beams are smaller with respect to the reference beam Ref_4S. In terms of torsional cracking moment and angle of rotation, series one and series three have improved performance. All the three series have increased the torsional moment as well as torsional angle of rotation at steel yielding, due to the contribution of CFRP laminates in resisting the applied torsional moment.

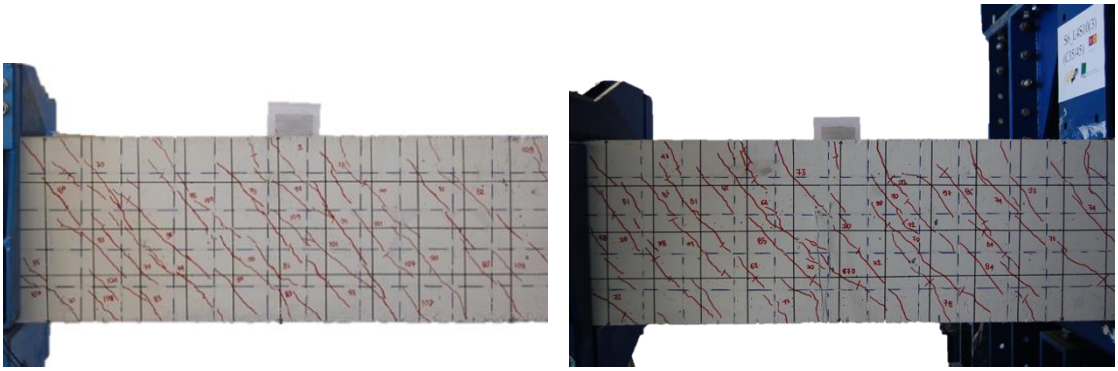

(a) (b)

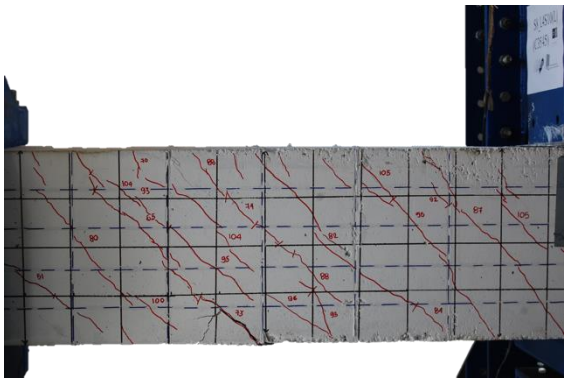

(c)

Figure 4.30 Crack patterns on right face of beams (a) S4F_L4S10 (b) S3F_L4S10 and (c) S4FL_L4S10

Beams S4F_L4S10 and S3F_L4S10 both experienced early premature failure in the over-reinforced region, thereby limiting the maximum torsional capacity and the angle of rotation at peak moment. However, beam S4F_L4S10 still had the maximum torsional capacity at peak, $M_{t,p}$, with respect to all the strengthened beams.

Table 4.17 Experimental results of maximum strengthening ratio beams in terms of M_t, torsional moment

Beam	$M_{t,cr}$ (kN.m)	$\left(\frac{M^S_{t,cr}-M^R_{t,cr}}{M^R_{t,cr}}\right)$	$M_{t,A}$ (kN.m)	$M_{t,syi}$ (kN.m)	$\left(\frac{M^S_{t,syi}-M^R_{t,syi}}{M^R_{t,syi}}\right)$	$M_{t,p}$ (kN.m)	$\left(\frac{M^S_{t,p}-M^R_{t,p}}{M^R_{t,p}}\right)$
Ref_4S	28.01	-	40.02	47.29	-	56.69	-
S4F_L4S10	39.26	40.17	55.18	59.39	25.58	83.02	46.43
S3F_L4S10	26.57	-5.14	44.03	55.57	17.51	70.27	23.94
S4FL_L4S10	32.69	16.71	50.88	60.99	28.98	78.35	38.19

Table 4.18 Experimental results of maximum strengthening ratio beams in terms of θ_t, angle of rotation

Beam	$\theta_{t,cr}$ (deg.)	$\left(\frac{\theta^S_{t,cr}-\theta^R_{t,cr}}{\theta^R_{t,cr}}\right)$	$\theta_{t,A}$ (deg.)	$\theta_{t,syi}$ (deg.)	$\left(\frac{\theta^S_{t,syi}-\theta^R_{t,syi}}{\theta^R_{t,syi}}\right)$	$\theta_{t,p}$ (deg.)	$\left(\frac{\theta^S_{t,p}-\theta^R_{t,p}}{\theta^R_{t,p}}\right)$
Ref_4S	0.39	-	0.54	2.77	-	4.78	-
S4F_L4S10	0.78	101.88	1.14	2.97	7.22	8.19	71.43
S3F_L4S10	0.44	13.85	0.72	2.78	0.48	5.71	19.48
S4FL_L4S10	0.63	62.89	0.94	4.40	59.00	8.36	74.83

Table 4.19 Experimental results of maximum strengthening ratio beams in terms of k_t , stiffness

Beam	$k_{t,lin}$ (kN.m/deg.)	$\left(\frac{k_{t,lin}^{S}-k_{t,lin}^{R}}{k_{t,lin}^{R}}\right)$	$k_{t,Mcr}$ (kN.m/deg.)	$\left(\frac{k_{t,Mcr}^{S}-k_{t,Mcr}^{R}}{k_{t,Mcr}^{R}}\right)$	$k_{t,syi}$ (kN.m/deg.)	$\left(\frac{k_{t,syi}^{S}-k_{t,syi}^{R}}{k_{t,syi}^{R}}\right)$
Ref_4S	69.80	-	4.02	-	7.36	-
S4F_L4S10	48.43	-30.61	3.42	-14.84	6.20	-15.76
S3F_L4S10	66.81	-4.28	4.48	11.41	9.88	34.30
S4FL_L4S10	49.38	-29.26	5.07	26.08	4.97	-32.48

Table 4.20 Experimental results of maximum strengthening ratio beams in terms of s_{rm}, crack spacing and α_{crm}, crack orientation

Beam	Crack spacing (mm, s_{rm})	$\left(\frac{s_{rm}^{S} - s_{rm}^{R\_4S}}{s_{rm}^{R\_4S}}\right)$	Crack orientation (degrees, α_{crm})
Ref_1S	417.92	-	49.61
Ref_4S	200.28	-	50.09
S4F_L4S10	101.37	-49.39	49.32
S3F_L4S10	139.90	-30.15	50.83
S4FL_L4S10	88.71	-55.71	51.79

Figure 4.31 shows beams with three face strengthening failure due to wider cracking on the unstrengthened top surface of the beams, even though good increase in torsional moment and angle of rotation is observed. Series one strengthening had the best performance in terms of maximum torsional moment, due to the strengthening configuration of the CFRP laminates, mainly limiting the spiral cracking pattern in torsion. The purpose of providing corner continuity was applied by reinforcing beams with L-laminates. These beams had the maximum ductile performance with good increase in torsional moment, $M_{t,p}$ and torsional angle of rotation, $\theta_{t,p}$.

(a)

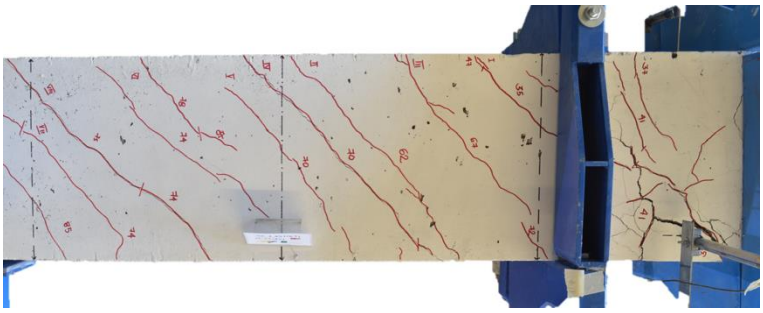

(b)

Figure 4.31 Unstrengthened face (top) of beam (a) S3F_L2S5 and (b) S3F_L4S10

4.3. CONCLUSIONS:

The current chapter describes in detail the experimental work on torsional strengthening of thin walled tubular reinforced concrete structures. It involved testing of ten beams in three series. The key parameters of this study were (a) the evaluation of new test setup for torsional strengthening (b) variation of longitudinal CFRP reinforcement ratio (c) variation of transverse CFRP reinforcement ratio (d) variation of different strengthening configurations with straight and L-CFRP laminates, and (e) variation of conventional stirrups. According to the results obtained and the discussion carried out in the chapter, the following conclusions are drawn from it:

- The conceived test setup is successful in assessing the performance of torsional tests;
- The adopted NSM-CFRP strengthening configurations provided an overall improved behaviour in maximum torsional moment, $M_{t,p}$ (between 18% and 46%), in $\theta_{t,p}$ (19% - 76%), $M_{t,cr}$ (10% - 40%), stiffness after crack stabilized stage (1%-34%) and $M_{t,syi}$ (14% - 29%);
- Most of the steel reinforcements both in the longitudinal and transverse directions have yielded, f_{ym} before the peak torsional moment is reached. The CFRP reinforcements have reached strains of 11358 $\mu\varepsilon$ (88.5% of its tensile capacity) proving their efficacy in torsional applications;
- Series one and series three strengthening configurations had really good performance in terms of peak torsional moment and torsional angle of rotation at peak moment;
- Series one and series three beams had the most ductile behaviour;
- Contribution of transverse CFRP laminates are more influential than the longitudinal CFRP laminates in many aspects like $M_{t,p}$, $\theta_{t,p}$, s_{rm} and arrest in crack propagation;
- All strengthened beams have undergone elongation (0.53%) due to crack sliding and crack opening. Considering the average spiral crack spacing, the CFRP strengthened beams have decreased crack spacing between 16% - 56%, being very effective in reducing the crack growth and limiting the crack width;
- Most of the beams failed by CFRP rupture followed by concrete crushing. However, in series two failure was by concrete crushing on the unstrengthened surface. Beam S4F_L4S10 (series one) and beam S3F_L4S10 failed prematurely in the over-reinforced region in loading region;
- The application of DIC for strain measurements help in understanding the crack evolution and fracture process in torsion.

CHAPTER:

5. ANALYTICAL FORMULATION

This chapter reviews the torsional resistance offered by longitudinal and transverse reinforcement according to space truss theory and discusses the development of models that can be used for the design of strengthening solutions using NSM CFRP laminates. Basic approaches such as the skew bending theory and space truss analogy are presented in Chapter 2 and new equations are proposed here with the aim of providing simple, yet effective models that can be easily introduced in current design practice. The proposed equations are based on the experimental evidence gathered from the testing programme discussed in Chapter 4 and implements some of the concepts already established in the current literature, such as the compressive strut angle according to the modified compression field theory and effective strain values for the contribution of FRP laminates at ultimate limit state.

5.1 SPACE TRUSS THEORY

A brief introduction on space truss theory is presented in Chapter 2 (Section 2.1.2). Hence the current section describes the amount of transverse and longitudinal steel reinforcement necessary to resist applied torsional moment based on the theory in the following sections. In space truss theory the torsional moment is assumed to be resisted by closed shear flow (q) acting on the walls of the thin walled tube (Figure 5.1a), both in solid and hollow sections, MacGregor and Ghoneim (1995). The section is assumed as a space truss where concrete has little to no contribution in resisting torsion after cracking. The transverse and longitudinal reinforcement act as tension chords and the concrete between the cracks act as diagonal struts inclined at 45 degrees to the longitudinal axis of the member.

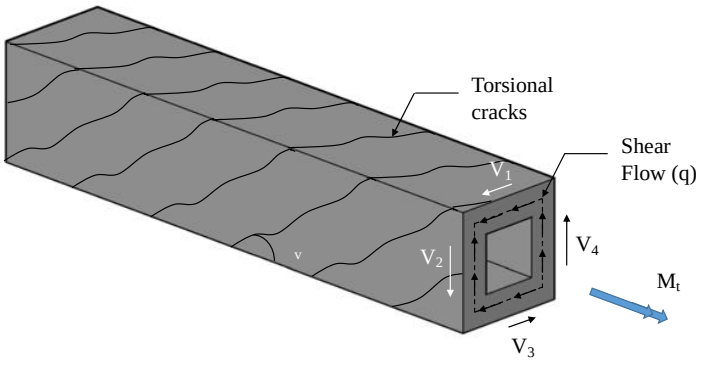

(a)

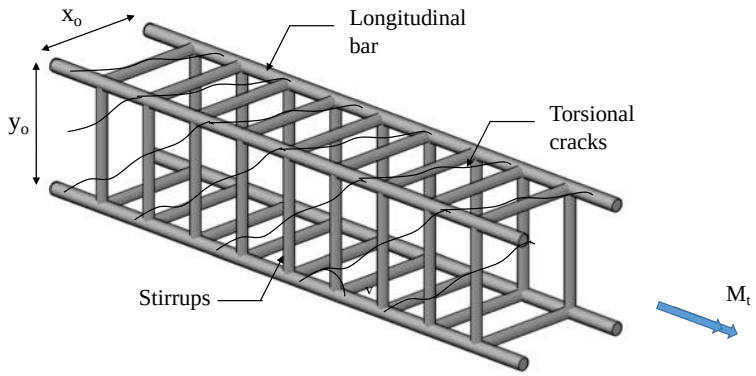

(b)

Figure 5.1 (a) Thin-walled tube analogy and (b) Space-truss analogy

5.1.1 EVALUATION OF TRANSVERSE REINFORCEMENT

The shear flow (q) on each wall is the shear force (V) acting per unit length of the perimeter at any point of the tubular structure and calculated according to equation 5.1. To quantify the shear force on each wall, the shear stress is multiplied by the corresponding length of the wall as shown in equation 5.2.

$$q = \tau t = \frac{M_t}{2A_0} \qquad 5.1$$

$$V_2 = \frac{M_t}{2A_0} y_0 \qquad 5.2$$

Where A_0 is the area enclosed by the centre line of the exterior most transverse reinforcement including the hollow area, V_2 is the shear force shown in Figure 5.1a, t is the wall thickness and y_0 is the length of the leg of the stirrup in the corresponding wall. A portion of the wall is presented in Figure 5.2 along with the forces developed in the stirrups to resist the applied torsional action.

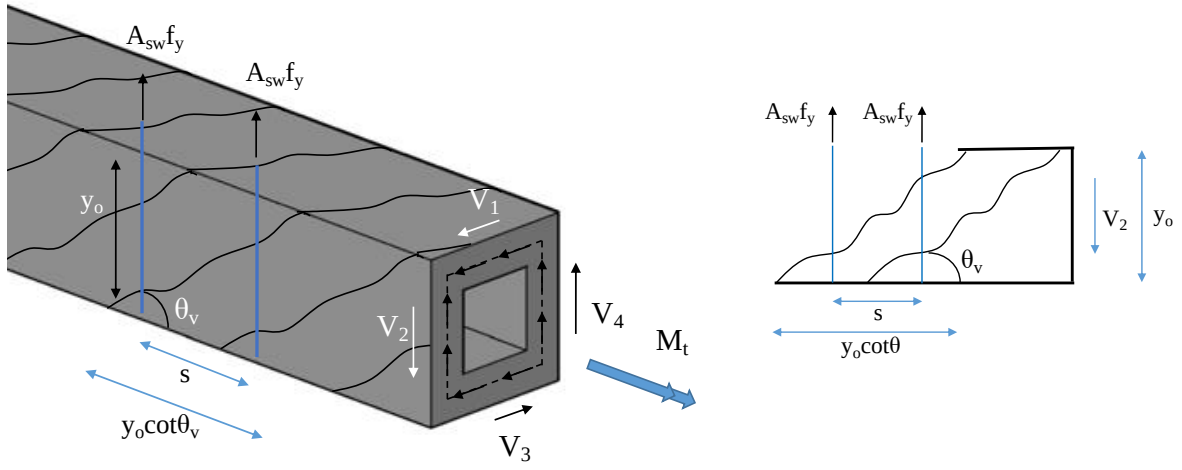

(a) (b)

Figure 5.2 Portion of a vertical side (a) 3D (b) 2D

The vertical shear force V_2 is resisted by the shear reinforcement (equation 5.3) crossing a single crack (two stirrups in the case of the beam illustrated in Figure 5.2). In evaluating the torsional moment resistance offered by the stirrups, only the leg of each stirrup embedded in the side wall under evaluation is considered when determining the A_{sw}, as the other legs do not offer resistance to the same component of shear flow. Substituting equation 5.2 into 5.3 yields equation 5.4, which gives the torsional capacity of the element as a function of the transverse reinforcement and can be used to determine the amount of transverse reinforcement necessary to resist the applied torsion.

$$V_2 = \frac{A_{sw} f_y y_0}{s} \cot\theta \qquad 5.3$$

$$M_t = \frac{2A_0 A_{sw} f_y}{s} \cot\theta \qquad 5.4$$

The angle of inclination (θ) of the compressive strut has been shown to vary between 30° and 45°. In the present work, the angle is evaluated using the modified compression field theory, as discussed in section 5.3.1.3.

5.1.2 EVALUATION OF LONGITUDINAL REINFORCEMENT

The amount of longitudinal reinforcement necessary to resist torsion is determined through force equilibrium. As shown in Figure 5.3, the shear force V_2 acting in the vertical direction is decomposed into the diagonal force D_2 along the compressive strut direction at an angle (θ_v)

(equation 5.5) and the axial force N_2 (equation 5.6). As the shear flow is considered to be constant along each side, in thin-walled beams subjected to pure torsion, the forces D_2 and N_2 are assumed to act at mid height of the wall and the axial force N_2 is shared between the top and the bottom reinforcement bar. Similarly, forces V_1, V_3 and V_4 (Figure 5.2a), and their axial components N_1, N_3 and N_4 act on the walls of a rectangular beam. As a result, the total force (N) acting on each wall is as shown in equation 5.7.

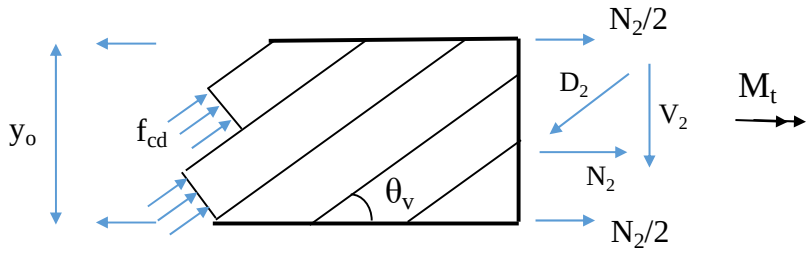

Figure 5.3 Resolution of forces for longitudinal reinforcement

$$D_2 = \frac{V_2}{\sin\theta} \qquad 5.5$$

$$N_2 = V_2 \cot\theta \qquad 5.6$$

$$N = 2\left(N_1 + N_2\right) \qquad 5.7$$

Substituting equation 5.2 and 5.6 in 5.7 yields equation 5.8, where $2\left(x_0 + y_0\right)$ is the perimeter of the closed stirrup (u_k), shown in Figure 5.1b. Assuming yielding of the reinforcement at failure, the longitudinal reinforcement resisting the axial force is $N = A_l f_{yl}$. This leads to equation 5.9, which can be easily used to determine the area of longitudinal reinforcement necessary to resist the applied torsion.

$$N = \frac{M_t}{2A_0} 2\left(x_0 + y_0\right)\cot\theta \qquad 5.8$$

$$A_l = \frac{M_t u_k}{2A_0 f_{yl}} \cot\theta \qquad 5.9$$

The equations discussed above (based on the concepts of thin walled beams and space truss analogy) will be applied and extended as shown in the following sections to predict the torsional capacity of thin-walled tubular reinforced concrete structures strengthened with near surface mounted CFRP laminates.

5.2 PREDICTIVE PERFORMANCE OF STANDARD CODES

In order to evaluate the predictive performance of the codes presented in Chapter 2 (section 2.2), the torsional cracking moment and the peak torsional capacity is calculated and compared with the experimental results in this section. The results of reference beam, Ref_4S of the current experimental campaign is presented and compared in Table 5.1 and then the experimental results of reference beam (C1 and C2) of Al-Bayati et al. (2016), is presented and compared in Table 5.2. The peak torsional moment capacity of the beam Ref_4S from the experimental test is 56.69 kN.m and the torsional cracking moment is 28.01 kN.m.

Table 5.1 Analytical results of the current experimental campaign using EuroCode 2 (2004), NTC-CNR (2018), ACI 318 (2011) and DR_AS-3600 (2017)

Codes	Cracking moment (kN·m) $T_{cr,ana}$	$T_{cr,ana}/T_{cr,\exp}$	Concrete crushing (kN·m)	$M_{t,ana}$		$M_{t,ana}/M_{t,\exp}$
				Transverse steel contribution (kN·m)	Longitudinal steel contribution (kN·m)	
EuroCode 2 (2004)	54.20	1.94	149.88	-	42.34	0.75
NTC-CNR (2018)	-	-	371.95	91.11	64.52	1.14
ACI 318 (2011)	29.78	1.06	-	60.74	-	1.07
DR_AS-3600 (2017)	29.77	1.06	-	56.61	-	1.00

As seen from the table, the EuroCode 2 (2004) overestimates the torsional cracking moment by almost twice, whereas the ACI 318 (2011) and DR_AS-3600 (2017) are closer to the experimental results. The ACI 318 (2011) and DR_AS-3600 (2017) have same results, since they follow the same equation for the calculation of cracking moment.

In the above Table 5.1, the torsional capacity of NTC-CNR (2018) is taken as the minimum of longitudinal and transverse steel contribution and compared with the experimental result. The EuroCode 2 (2004) is conservative in estimating the torsional capacity. In case of NTC-CNR (2018), ACI 318 (2011) and DR_AS-3600 (2017), the torsional moment is over-estimated. In these three approaches, the main difference is in the estimation of the area for calculation. In NTC-CNR (2018), the outer cross sectional area is taken for evaluation, in ACI 318 (2011), it is taken as $A_o = 2A_{cp}/3$ (A_{cp} being the area of outer cross section) and in DR_AS-3600 (2017), it is taken as $A_o = 0.85A_{oh}$ (A_{oh} being the inner center line area of exterior transverse torsional reinforcement). The DR_AS-3600 (2017), is more appropriate since the outer layer of concrete (outside the transverse reinforcement) becomes ineffective in torsional resistance after torsional cracking. In case of EuroCode 2 (2004), the inner area of walls connected by their centre-line is considered for evaluation. In all the above calculations the compressive strut angle is taken as 45 degrees.

Similarly, the codes are applied for the reference beams in Al-Bayati et al. (2016), and the results are presented in Table 5.2. The experimental average torsional cracking moment and average peak torsional moment capacity of the two reference beams (C1 and C2) are 4.52 kN.m and 6.77 kN.m.

Table 5.2 Analytical results of the Al-Bayati et al. (2016) experimental campaign using EuroCode 2 (2004), NTC-CNR (2018), ACI 318 (2011) and DR_AS-3600 (2017)

Codes	Cracking moment (kN·m) $T_{cr,ana}$	$T_{cr,ana}/T_{cr,\exp}$	Concrete crushing (kN·m)	$M_{t,ana}$		$M_{t,ana}/M_{t,\exp}$
				Transverse steel contribution (kN·m)	Longitudinal steel contribution (kN·m)	
EuroCode 2 (2004)	8.95	1.98	29.45	-	15.62	2.31
NTC-CNR (2018)	-	-	79.50	9.27	20.44	1.37

ACI 318 (2011)	3.79	0.84	-	6.18	-	0.91
DR_AS-3600 (2017)	3.79	0.84	-	5.55	-	0.82

The EuroCode 2 (2004) over predicts the torsional cracking capacity like in the first case, and the ACI 318 (2011) and DR_AS-3600 (2017) provide conservative estimates. In case of the torsional capacity prediction, EuroCode 2 (2004) over predicts by more than 200%. It must be noted that the capacity is evaluated based on the longitudinal reinforcement. The Italian code also over-estimates the torsional capacity. However, the ACI and Australian code provide conservative values in this case.

5.3 ANALYTICAL FORMULATIONS

The different methods and equations available to calculate the torsional capacity of RC members according to current codes are discussed in Chapter 2 (section 2.2). EuroCode 2 (2004) proposes equations to determine the shear stress on each wall based on applied torsional moment, limitation of the concrete compressive struts and contribution of longitudinal reinforcement. When designing the transverse reinforcement, the requirements are the same as for shear reinforcement, provided that the links are well anchored (90 degree hooks). In NTC-CNR (2018), the contribution of concrete, longitudinal reinforcement and transverse reinforcement are calculated and the minimum value is taken as the torsional capacity of the member. In ACI 318 (2011), the torsional strength is calculated based on the amount of transverse reinforcement. In case of combined shear and torsion, the necessary transverse reinforcement is provided as the sum of the required shear reinforcement and torsional reinforcement. It also provides an equation to calculate minimum area of longitudinal reinforcement to resist torsion. The Australian code DR_AS-3600 (2017) gives equations to calculate the torsional cracking moment and the torsional moment capacity according to the amount of transverse reinforcement.

Based on an implementation of the space truss analogy, current design equations and the experimental observations reported in Chapter 4, two approaches are proposed in the following sections to evaluate the contribution of CFRP strengthening to the total torsional capacity of a

reinforced concrete element. The first approach (Section 5.2) adopts the same space truss approach used in ModelCode (1990), EuroCode 2 (2004) and NTC-CNR (2018) along with the implementation of an effective strain to estimate the contribution of the transverse NSM reinforcement to the overall torsional capacity. The MCFT is used to evaluate the compressive strut angle (θ_v), since it is capable of predicting with good accuracy the shear strength, taking into account the tensile stress of concrete and the diagonal compressive strut angle. A second approach, described in section 5.4, is also proposed on the basis of the simplified modified compressive field theory developed by Bianco (BSMCFT, Baghi & Barros (2017)). While the first approach is more suitable for implementation in current design recommendations, the second model implements a more rational approach and it is more suited for numerical implementation.

5.3.1 EVALUATION OF TORSIONAL MOMENT

According to the space truss analogy, the torsional moment carrying capacity of a member is considered to be provided by the total transverse reinforcement (equation 5.10) as the sum of the contribution of the steel stirrups (equation 5.11) and the NSM CFRP laminates. The ultimate capacity of the member should also be limited by the concrete diagonal compressive strut failure $(M_{t,Rd,\max})$. As described in section 5.3.2, appropriate longitudinal reinforcement should also be provided to resist the additional axial forces originating from the applied torsional moment.

$$M_t = M_{t,s} + M_{t,f} \tag{5.10}$$

$$M_{t,s} = \frac{2A_o A_{sw} f_y}{s}\cot\theta_v \tag{5.11}$$

$$M_{t,Rd,\max} = 2\nu\alpha_{cw} f_{cd} A_k t_{ef,i} \sin\theta_v \cos\theta_v \tag{5.12}$$

Equation 5.11 gives the contribution of transverse steel reinforcement, where: A_0 is the area enclosed by the centre line of the exterior transverse reinforcement including the hollow area (Figure 5.4); A_{sw} is the area of transverse reinforcement (calculated as the area of only external legs); f_y is the yield stress of the transverse reinforcement; s is the spacing of transverse bars and θ_v is the angle of the diagonal compressive strut evaluated according to section 5.3.1.3, using modified compressive field theory.

Equation 5.12 provides the limit of concrete crushing by diagonal compressive strut failure, where: ν is the strength reduction factor for cracked concrete in shear, $\nu = 0.6\left(1-\frac{f_{ck}}{250}\right)$; α_{cw} is the coefficient taking into account the stress in the compression chord (taken as '1' for non-prestressed structures); f_{cd} is the design compressive strength (to be taken as mean strength when evaluating experimental work); A_k is the area enclosed by the centre walls of the element (300 × 300 mm^2); and $t_{ef,i}$ is the effective thickness of the wall. $t_{ef,i}$ is evaluated according to equation 5.13, where A is the cross sectional area (400 × 400 mm^2) and u is the perimeter of the cross section (4 × 400 = 1600 mm). The most important design parameters are also presented in Figure 5.4.

$$t_{ef,i} = \frac{A}{u} \qquad 5.13$$

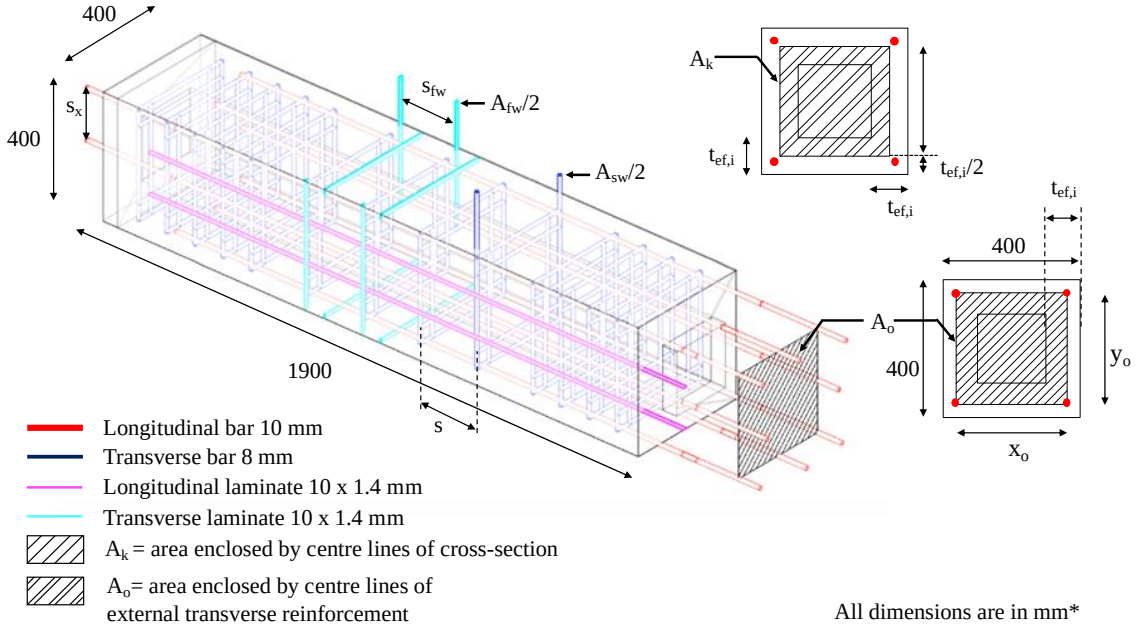

Figure 5.4 Details of analytical terms used in the equations

5.3.1.1 CFRP contribution

The contribution of NSM CFRP laminates to the torsional moment capacity can be calculated according to equation 5.16. The equation is similar to equation 5.11, where the yield strength of steel reinforcement is replaced by an effective design strength, $E_{fw}\varepsilon_{fe,w}$, being mobilised in

the FRP reinforcement just before failure and corresponding to an effective tensile strain. In equation 5.16, A_{fw} is the cross sectional area of transverse CFRP laminate per wall component; E_{fw} is the modulus of elasticity of the CFRP; $\varepsilon_{fe,w}$ is the effective strain of the CFRP and s_{fw} is the spacing of the transverse CFRP laminates.

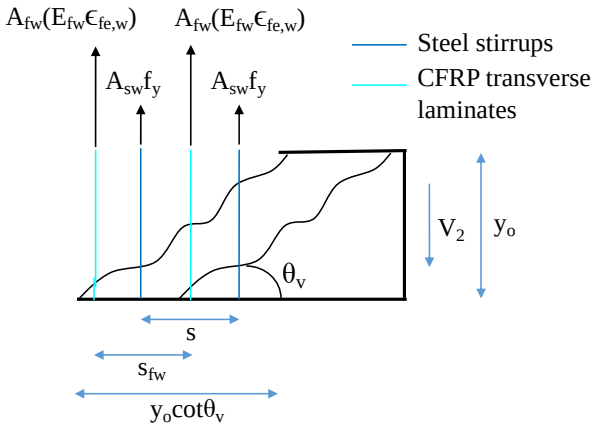

Figure 5.5 Wall portion of an element with CFRP laminates

The basis for equation 5.16 is shown in Figure 5.5, where a crack is intercepted, for example, by two CFRP laminates and two steel transverse bars. As discussed in section 5.1.1, the shear force (equation 5.2) is equated to equation 5.14 for equilibrium. That is, the shear force should be balanced by the summation of forces from the transverse steel bars and CFRP laminates (Figure 5.5 and equations 5.15), leading to the total resistance (equation 5.10) of the reinforced concrete member in torsion.

$$V_2 = \left(\frac{A_{sw} f_y y_0}{s}\cot\theta_v\right) + \left(\frac{A_{fw}(E_{fw}\varepsilon_{fe,w})y_0}{s_{fw}}\cot\theta_v\right) \qquad 5.14$$

$$\frac{M_t}{2A_0} y_0 = \left(\frac{A_{sw} f_y y_0}{s}\cot\theta_v\right) + \left(\frac{A_{fw}(E_{fw}\varepsilon_{fe,w})y_0}{s_{fw}}\cot\theta_v\right)$$

$$M_t = 2A_0\left(\frac{A_{sw} f_y}{s}\cot\theta_v\right) + 2A_0\left(\frac{A_{fw}(E_{fw}\varepsilon_{fe,w})}{s_{fw}}\cot\theta_v\right) \qquad 5.15$$

$$M_t = M_{t,s} + M_{t,f}$$

$$M_{t,f} = 2A_o\frac{A_{fw}\left(E_{fw}\varepsilon_{fe,w}\right)}{s_{fw}}\cot\theta_v \qquad 5.16$$

As many researchers have suggested and discussed over the past decades, the main problem in predicting the contribution of FRP laminates in flexure, shear or torsion, is the estimation of the effective strain of the FRP, which is a function of many parameters, mainly concrete

compressive strength, modulus of elasticity of the FRP reinforcement, FRP reinforcement ratio and the ultimate tensile strain of the FRP.

In the current proposal, only two strengthening configurations are considered, (i) 3-face (or U strengthening) and (ii) 4-face strengthening. In 4-face strengthening, two different sets of equations are proposed to estimate the effective strain in elements with transverse reinforcement ratios above and below 0.10% (i.e. $\rho_{fw} > 0.1$ and $\rho_{fw} < 0.1$). The two different equations account for the interaction between the existing steel reinforcement and the NSM FRP reinforcement and that higher steel reinforcement ratios lead to a lower effectiveness of the strengthening material. The basic equations for the effective strain are adopted from FIB bulletin 14 (2001), which were originally developed for externaly bonded FRP, but account for the better performance of NSM FRP compared to EBR FRP (Dias and Barros (2013), Barros, Dias, and Lima (2007), El-Hacha and Rizkalla (2004) etc.). According to the results obtained in the current experimental programme, all the beams have failed by CFRP tensile rupture, followed by concrete crushing or premature failure in the over-reinforced region of the beams (stress concentration by steel loading section), while no failure at the corner of the FRP reinforcement has been observed. The proposed equations predict average strain of the FRP laminate, whereas in experiments most of the FRP strain gauges pass through cracks, registering higher strain values. The calculation of effective strain and the angle of concrete strut angle are described in sections 5.3.1.2 and 5.3.1.3.

5.3.1.2 Effective strain

The effective strain equations are adopted from FIB (2001), according to which the effective strain in the FRP is a function of the concrete compressive strength, modulus of elasticity of the FRP laminate, strengthening reinforcement ratio and ultimate strain of the FRP material. In the case of NSM FRP, however, the effectiveness of the FRP material has been shown to be higher than for EBR as a result of the higher bonded area of the FRP laminates with the surrounding concrete. Therefore, the equations originally developed for EBR FRP are modified to account for the higher effective strain that is expected to be developed in the FRP at failure. It should be noted that, the FRP laminates were found to fail in tension during the experimental tests discussed in Chapter 4, tensile failure of the FRP was the result of twisting of the laminate with large crack openings.

As also shown by experimental evidence, the higher the strengthening ratio, the lower is the contribution of the strengthening material, i.e. the FRP laminates reach lower strain values when higher percentages of the strengthening material are provided. To account for this behaviour, two equations are proposed to assess the design contribution of the NSM FRP. Equation 5.17 gives the effective strain ($\varepsilon_{fe,w}^{4F}$) for 4-face strengthening with transverse reinforcement ratios lower than 0.10%, while equation 5.18 is proposed for transverse reinforcement ratios greater than 0.10%. When strengthening is carried out only on 3-faces, a lower strain is expected to be mobilised in the FRP reinforcement at failure, as also observed in the experimental tests, and Equation 5.19 can be used to predict the effective strain for this configuration ($\varepsilon_{fe,w}^{3F}$). The constants used for the three predictive equations are derived based on an inverse analysis of the experimental results, the target of which was to minimise the error between predicted and experimental results.

$$\varepsilon_{fe,w}^{4F} = 0.32\left[\frac{f_{cm}^{2/3}}{E_{fw}\rho_{fw}}\right]^{0.15}\varepsilon_{fu,w} \qquad \rho_{fw} \leq 0.1 \qquad 5.17$$

$$\varepsilon_{fe,w}^{4F} = 0.23\left[\frac{f_{cm}^{2/3}}{E_{fw}\rho_{fw}}\right]^{0.15}\varepsilon_{fu,w} \qquad \rho_{fw} > 0.1 \qquad 5.18$$

$$\varepsilon_{fe,w}^{3F} = 0.14\left[\frac{f_{cm}^{2/3}}{E_{fw}\rho_{fw}}\right]^{0.15}\varepsilon_{fu,w} \qquad 5.19$$

According to the strengthening configurations, the effective strains are calculated from equations 5.17 - 5.19, and then the respective values are applied in equation 5.16 to obtain the transverse torsional FRP laminate contribution. The respective values for the experimental programme are presented in Table 5.3, where E_{sw} = 195975 MPa, breadth b = 200 mm and s_{fw} = 200 mm. The reinforcement ratios (ρ_{fw}) are calculated as an avergae of all the four faces, to incorporate the unstrengthened top face of three face strengthened beams. Beams with higher CFRP strengthening ratio (maximum strengthened beams in all series), have the maximum CFRP contribution to torsional resistance, even though the effective strain capacity is lower than most of the minimum strengthened beams. The effective strain values from the proposed equations predict lower strain values with respect to the experimental results. This can be attributed to the fact that the experimental strain are localised values and can tend to overestimate average strains if the gauges are located in the proximity of a crack. In addition,

the model assumes that all links intersected by a crack contibute equally to the torsional resistance and the use of conservative values for the average effective strain is more suitable for design.

Table 5.3 Evaluation of transverse reinforcement ratio (equation 4.4), transverse effective strain (equations 5.17, 5.18 and 5.19) and transverse torsional moment (equation 5.16) for the current experimental campaign

Beam	A_{fw} (mm^2)		E_{fw}	ρ_{fw}			$\varepsilon_{fe,w}$	$M_{t,f}$
	Left/ Right	Top/ Bottom	(GPa)	Left/ Right	Top/ Bottom	Average	$(\mu\varepsilon)$	(kN.m)
S4F_L2S5	28	28	205.04	0.00732	0.00732	0.00732	2740	18.796
S4F_L2S10	56	56	205.04	0.00146	0.00146	0.00146	1770	24.351
S4F_L4S5	28	28	205.04	0.00073	0.00073	0.00073	2740	18.896
S4F_L4S10	56	56	199.83	0.00143	0.00143	0.00143	1590	21.245
S3F_L2S5	28	14	199.83	0.00071	0.00036	0.00054	1120	7.491
S3F_L4S10	56	28	199.83	0.00143	0.00071	0.00107	1010	13.502
S4FL_L2S5	28	28	196.20	0.00070	0.00070	0.00070	2770	18.209
S4FL_L4S10	56	56	196.20	0.00140	0.00140	0.00140	1790	23.590

5.3.1.3 MCFT for compressive strut angle

The angle of inclination (θ_v) of the compressive strut is determined according to equation 5.20, using the simplified modified compression field theory from Bentz *et al.* (2006). MCFT is a modified version of compression-field theory for reinforced concrete in torsion and shear, where the concrete after cracking is treated as new material with stress-strain characteristics. The principal compressive stress was found to be not only a function of principal compressive strain but also on principal tensile strain. The compressive field theory equations were updated to consider average principal tensile stresses in cracked concrete obtaining geometric, equilibrium and constitutive relationships for MCFT. The developed constitutive relations are adopted for both the compressive stress-strain relation as well as the tensile stress-strain relation for cracked concrete. The MCFT takes into account the tensile stresses between the cracks, which increase the ability of concrete to resist shear. The shear strength of a section is

a function of β, a factor that takes into account the effect of tensile stress in cracked concrete (strain effect), and θ_v, the angle of the diagonal compressive stress (also related to the size of the element). Both β and θ_v are mainly dependant on the longitudinal strain, ε_x, and can be estimated using equations 5.21 and 5.20, respectively.

ε_x is taken as the longitudinal reinforcement yield strain if the longitudinal reinforcement has yielded. If not, it is calculated using equation 5.23 and 5.24, where v_c is the concrete shear strength and v is the overall shear stress. The evaluation of θ_v is an iterative procedure as described in section 5.4.3 and Bentz et al. (2006). In any case, for the current approach since the experimental results have proved the yielding of the longitudinal reinforcement, ε_x is taken as the yield strain of longitudinal reinforcement. s_{xe} is determined using equation 5.22, where s_x is taken as the vertical distance between bars in the x-direction (Figure 5.4) and a_g is the maximum coarse aggregate size. In equation 5.23, E_s is the modulus of elasticity of the steel reinforcement, ρ_{sl} is the reinforcement ratio in the x-direction (longitudinal reinforcement).

$$\theta_v = \left(29 + 7000\varepsilon_x\right)\left(0.88 + \frac{s_{xe}}{2500}\right) \leq 75\,\text{deg} \qquad 5.20$$

$$\beta = \frac{0.4}{1+1500\varepsilon_x}\frac{1300}{1000+s_{xe}} \qquad 5.21$$

$$s_{xe} = \frac{35 s_x}{a_g + 16} \qquad 5.22$$

$$\varepsilon_x = \frac{f_{sx}}{E_s} = \frac{v\cot\theta - v_c/\cot\theta}{E_{sl}\rho_{sl}} \qquad 5.23$$

$$v = v_c + v_s = \beta\sqrt{f_c'} + \rho_{fw} f_{yl}\cot\theta_v \qquad 5.24$$

The corresponding values calculated according to the above equations for the current experimental programme are s_x = 162 mm, a_g = 12.5 mm, s_{xe} = 199, ε_x = 2460 $\mu\varepsilon$ (yield strain of longitudinal reinforcement in the present case), θ_v = 44.34° and $M_{t,Rd,\max}$ = 99.89 kN.m.

5.3.2 LONGITUDINAL REINFORCEMENT

The contribution of the longitudinal CFRP laminates is estimated based on the space truss analogy, similar to the longitudinal steel reinforcement, and implementing the equations described in section 5.1.2. The axial force (N), obtained from the decomposition of the applied torsional moment, should be resisted by the combined action of longitudinal steel and longitudinal CFRP laminates. Assuming the longitudinal reinforcement yields at failure, which was the case for all beams tested as part of this research study, and limiting the strain in the CFRP laminates to the estimated effective strain (ε_{fe}), the contribution of the longitudinal CFRP laminates is obtained according to equations 5.25 and 5.26, where $M_{t,fl}$ is the contribution of longitudinal FRP laminates; A_{fl} is the total area of the longitudinal FRP strengthening of the cross section; E_f is the modulus of elasticity of the longitudinal FRP laminates; ε_{fe} is the effective strain of the laminates calculated using equation 5.27 (see Section 5.3.1.2); u_k is the perimeter of area A_k (area of lines connecting the centre of walls).

$$\frac{M_t}{2A_0}2(x_0+y_0)\cot\theta_v = A_l f_{yl} + A_{fl}\left(E_f \varepsilon_{fe}\right)$$

$$M_t = \frac{2A_0\left(A_l f_{yl}\right)}{u_k \cot\theta_v} + \frac{2A_0\left(A_{fl}\left(E_f \varepsilon_{fe}\right)\right)}{u_k \cot\theta_v} \qquad 5.25$$

$$M_t = M_{t,sl} + M_{t,fl}$$

$$M_{t,fl} = 2A_o \frac{\sum A_{fl}\left(E_f \varepsilon_{fe}\right)}{u_k \cot\theta_v} \qquad 5.26$$

$$\varepsilon_{fe} = 0.17\left[\frac{f_{cm}^{2/3}}{E_f \rho_{fl}}\right]^{0.30} \varepsilon_{fu,l} \qquad 5.27$$

Table 5.4 Evaluation of longitudinal contribution of FRP laminates (using equation 5.26 and 5.27)

Beam	A_{fl} (mm^2)	ρ_{fl} ($\mu\varepsilon$)	E_f (MPa)	$\varepsilon_{fu,l}$ ($\mu\varepsilon$)	ε_{fe} ($\mu\varepsilon$)	$M_{t,fl}$ (kN.m)
S4F_L2S5	112	945	205037	12832	897	3.2186
S4F_L2S10	112	945	205037	12832	897	3.2186
S4F_L4S5	224	1891	205037	12832	728	5.2287
S4F_L4S10	224	1891	199833	11398	657	4.5969

S3F_L2S5	84	691	199833	11398	150	0.3925
S3F_L4S10	168	1383	199833	11398	101	0.5325
S4FL_L2S5	112	917	198766	9787	697	2.4245
S4FL_L4S10	224	1834	198766	9787	566	3.9387

5.3.3 APPLICATION

Table 5.5 shows the results of analytical prediction according to the proposed equations from 5.10 - 5.22 for transverse steel reinforcement and transverse CFRP reinforcement. The experimental values of shear force and torsional moment are presented and compared to the analytical predictions.

Table 5.5 Analytical results according to the proposed equations and their comparison with the current experimental results

Beams	$M_{t,s}$ (kN.m)	$M_{t,fw}$ (kN.m)	$M_{t,ana} = M_{t,s} + M_{t,fw}$ (kN.m)	$V_{t,ana}$ (kN)	$M_{t,\exp}$ (kN.m)	$V_{t,\exp}$ (kN)	$M_{t,\exp} / M_{t,ana}$	$V_{t,\exp} / V_{t,ana}$	Failure (Experimental)	Failure (Analytical)
Ref_4S	55.71	-	55.71	81.44	56.69	82.88	1.018	1.02	Concrete crushing	Steel yielding
S_L2S5	55.71	18.80	74.51	108.93	78.30	114.47	1.051	1.05	FRP rupture	FRP
S_L2S10	55.71	24.35	80.06	117.05	81.69	119.43	1.020	1.02	FRP rupture	FRP
S_L4S5	55.71	18.80	74.51	108.93	79.37	116.03	1.065	1.07	FRP rupture	FRP
S_L4S10	55.71	21.25	76.95	112.51	83.02	121.37	1.079	1.08	Premature concrete failure	FRP
S_L2S5(3)	55.71	7.49	63.20	92.40	66.65	97.45	1.055	1.06	Concrete crushing	Yielding + FRP
S_L4S10(3)	55.71	13.50	69.21	101.18	70.27	102.73	1.015	1.02	Premature concrete failure	Yielding + FRP
S_L2S5(L)	55.71	18.21	73.92	108.07	67.89	112.64	0.918	1.04	FRP rupture	FRP
S_L4S10(L)	55.71	23.59	79.30	115.93	78.35	114.54	0.988	0.99	FRP rupture	FRP
Average							**1.024**	**1.037**		
Standard deviation							**5.20%**	**2.87%**		
Co-efficient of variation							**5.10%**	**2.77%**		

FRP = strain in FRP exceeds FRP strain

$V_{t,\exp} = \frac{M_{t,\exp}}{2A_0} y_0$; A_0 = 116964 mm^2 and y_0 = 342 mm.

The analytical predictions are in very good agreement with the experimental results, with a co-efficient of variation of 5.1%. To verify the proposed formulations, they are also applied to the available experimental data of Al-Bayati et al. (2016) and the results are shown in Table 5.6. They are also in good accordance with the experimental values with a coefficient of variation of 8.6%.

Table 5.6 Proposed analytical prediction for Al-Bayati et al. (2016)

Beams	$M_{t,s}$ (kN.m)	$M_{t,fw}$ (kN.m)	$M_{t,ana} = M_{t,s} + M_{t,fw}$ (kN.m)	$M_{t,\exp}$ (kN.m)	$M_{t,\exp} / M_{t,ana}$	Failure type
Ref (C1 & C2)	5.719	-	5.719	6.770	1.183	Concrete crushing
EF	5.719	3.463	9.182	7.799	0.964	Concrete cover delamination
EU1	5.719	1.582	7.301	7.219	1.133	Concrete crushing (unstrengthened surface)
EU2	5.719	1.410	7.301	7.129	1.120	Concrete crushing (unstrengthened surface)
Average					**1.072**	
Standard deviation					**9.47%**	
Co-efficient of variation					**8.60%**	

5.4 EVALUATION OF SHEAR FORCE USING BSMCFT:

In order to evaluate the shear force in each wall, Bianco's simplified modified compressive field theory is used as described in Baghi & Barros (2017). The theory is a combination of the simplified modified compression field theory (Bentz *et al.* 2006) and the simplified approach of Bianco *et al.* (2014) to evaluate the shear force (V_f) contribution of NSM FRP laminates.

5.4.1 BACKGROUND TO BIANCO ET AL. (2014)

The shear force contribution of NSM FRP laminates in the beam is determined using the simplified approach described in Bianco *et al.* (2014), hereafter referred to as BSMCFT. The original version of the constitutive law presented in Bianco et al. (2011) is based on the bond length available in the NSM FRP laminates crossing the shear crack. Due to the complexity of the original model, Bianco et al. (2014) proposed a simplified approach based on the use of an average bond length, a bi-linear local bond stress-slip $\tau(\delta)$ relation, a semi-pyramid concrete fracture surface and four modes of failure caused by an imposed end slip as shown in Figure 5.6: 1) debonding; 2) tensile rupture of the laminate; 3) concrete semi-pyramid tensile fracture and; 4) a mixed shallow semi-pyramid with debonding failure.

During the loading process a single, critical diagonal crack (CDC) is formed at an angle θ_v with respect to the longitudinal axis of the beam. After the crack formation, with every increase in load step (t_n), the CDC $\gamma(t_n)$ progressively widens. This crack opening is resisted by the laminates crossing the crack by bond to the surrounding concrete through an effective bond length L_{fi}, which is taken as the shorter length of the laminate divided by the CDC.

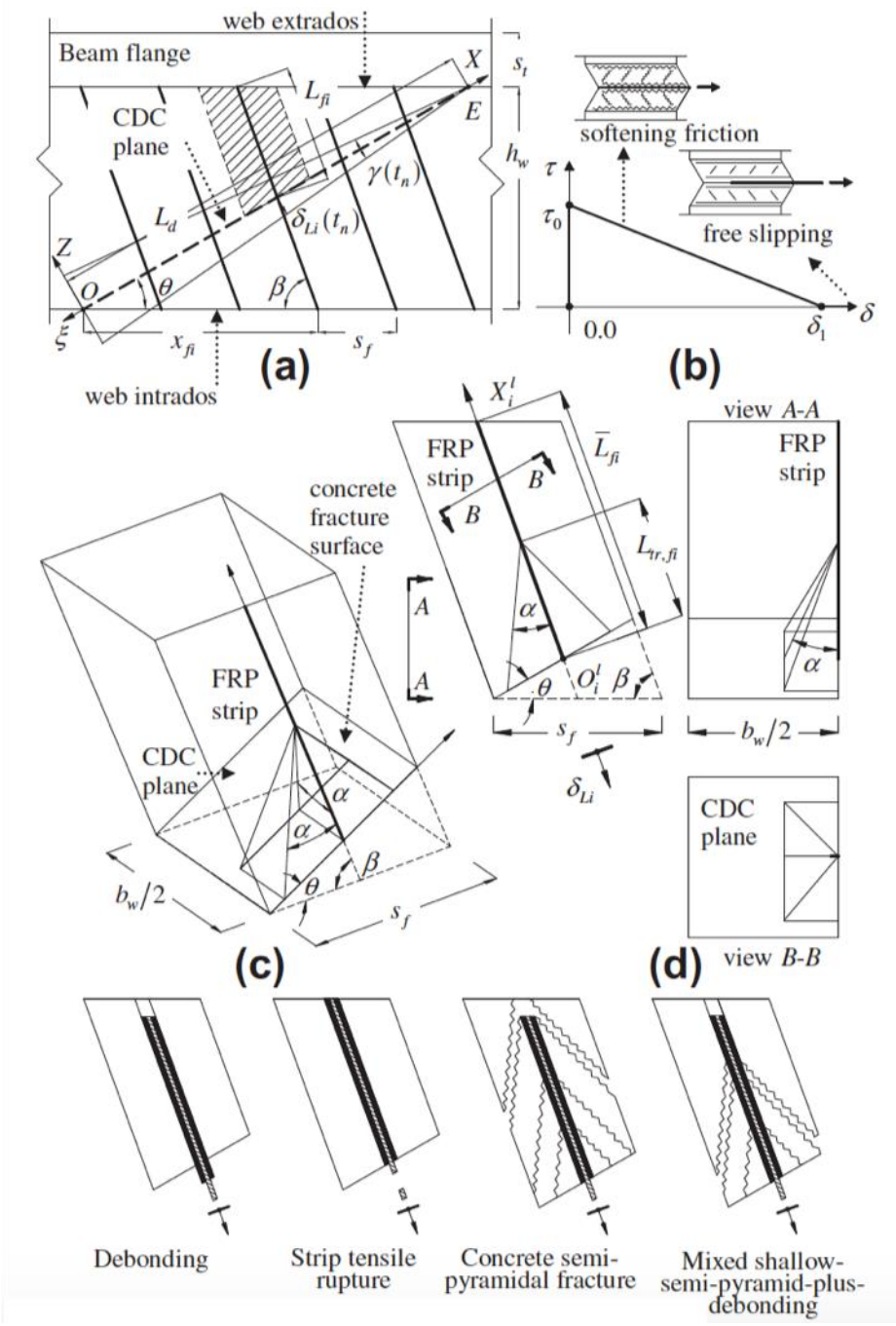

Figure 5.6 Schematic representation of Bianco et al. (2014) model

The procedure to evaluate the shear force V_f follows the steps below:

1. Definition of the input parameters: height of beam (h), breadth (b), angle of semi-pyramid cone (α), concrete compressive strength (f_{cm}), spacing of FRP laminates (s_f), angle of FRP laminates (β), tensile strength of FRP laminates (f_{fu}), modulus of elasticity of FRP laminates (E_{fw}), width (a_f) and depth (b_f) of FRP laminates, bond-slip $(\tau_0 - \delta_1)$ values and CDC angle (θ_v).

2. Evaluation of average available bond length ($\overline{L}_{Rfi}$) using equation 5.28 and the integer number of FRP laminates crossing the CDC ($N^{l}_{f,\text{int}}$) using eqaution 5.29;

$$\overline{L}_{Rfi} = \frac{h\ \sin\theta_v\left(\cot\theta_v + \cot\beta\right)}{4\sin(\theta_v + \beta)} \qquad 5.28$$

$$N^{l}_{f,\text{int}} = round\left[h_w \frac{\cot\theta_v + \cot\beta}{s_{fw}}\right] \qquad 5.29$$

3. Evaluation of constants, including geometric constants, mechanical constants and bond-modelling constants;

   a. The geometric constants are: effective perimeter of FRP laminate cross section (L_p) equation 5.30; cross sectional area of the prism surrounding the concrete (A_c) using equation 5.31; and length of the CDC (L_d) according to equation 5.32.

$$L_p = 2\left(a_f + b_f\right) \qquad 5.30$$

$$A_c = s_w \frac{b_w}{2} \qquad 5.31$$

$$L_d = \frac{h_w}{\sin\theta_v} \qquad 5.32$$

   b. The mechanical constants are: FRP laminate tensile strength; concrete tensile strength (f_{ctm}); and Young's modulus (E_c) using equations 5.33 through 5.35

$$V_f^{tr} = a_f b_f f_{fu} \qquad 5.33$$

$$f_{ctm} = 1.4\left(\frac{f_{cm} - 8}{10}\right)^{2/3} \qquad 5.34$$

$$E_c = 2.15\times10^4\left(\frac{f_{ctm}}{10}\right)^{2/3} \qquad 5.35$$

f_{fu} is the tensile strength of the FRP laminate and f_{ctm} is the concrete tensile strength.

   c. The bond-modelling constants are: bond modelling constant; integration constant (C_3); constant of differential equation (λ); effective resisting

bond length (L_{Rfe}); and corresponding maximum bond force (V_{f1}^{bd}), using equations 5.36 through 5.39.

$$J_1 = \frac{L_p}{A_f}\left[\frac{1}{E_f} + \frac{A_f}{A_c E_c}\right] \qquad 5.36$$

$$C_3 = \frac{V_f^{tr} J_1}{L_p \lambda},\ \frac{1}{\lambda^2} = \frac{\delta_1}{\tau_b J_1} \qquad 5.37$$

$$L_{Rfe} = \frac{\pi}{2\lambda} \qquad 5.38$$

$$V_{f1}^{bd} = \frac{L_p \lambda \delta_1}{J_1} \qquad 5.39$$

4. Evaluation of reduction factor (η) and equivalent average resisting bond length $(\bar{L}_{Rfi}^{eq})$ using equation 5.40;

$$\bar{L}_{Rfi}^{eq} = \eta \bar{L}_{Rfi} \qquad 5.40$$

where

$$\eta = \begin{cases} \dfrac{f_{ctm}}{f_{ctm}^{*}} & if\ f_{ctm} < f_{ctm}^{'} \\ 1 & if\ f_{ctm} > f_{ctm}^{'} \end{cases} \qquad 5.41$$

$$f_{ctm}^{*} = \frac{L_p \lambda \delta_1 \sin(\lambda L_{Rfi})}{J_1 \cdot \min(L_{Rfi}\tan\alpha, {}^{b_w}\!/_{2}) \cdot \min(s_f \sin\beta, 2L_{Rfi}\tan\alpha)} \qquad 5.42$$

In which L_{Rfi} should be

$$L_{Rfi} = \begin{cases} \overline{L_{Rfi}} & if\ \bar{L}_{Rfi} \le L_{Rfe} \\ L_{Rfe} & if\ \bar{L}_{Rfi} > L_{Rfe} \end{cases} \qquad 5.43$$

5. Assessment of the imposed end slip value (δ_{Lu}) according to equation 5.44, for which the maximum force $V_{fi}(\bar{L}_{Rfi}^{eq}; \delta_{Li})$ in the constitutive law for the corresponding bond length $\bar{L}_{Rfi}^{eq}$ is achieved;

$$\delta_{Lu} = \begin{cases} \delta_{L1}(\bar{L}_{Rfi}^{eq}) & if\ V_{f1}^{bd} < V_f^{tr} \\ \min\left[\delta_{L1}(\bar{L}_{Rfi}^{eq}); \delta_{L1}(V_f^{tr})\right] & f\ V_{f1}^{bd} \geq V_f^{tr} \end{cases} \quad 5.44$$

where

$$\delta_{L1}(\bar{L}_{Rfi}^{eq}) = \begin{cases} \delta_1[1-\cos(\lambda \bar{L}_{Rfi}^{eq})] & if\ \bar{L}_{Rfi}^{eq} \leq L_{Rfe} \\ \delta_1 & if\ \bar{L}_{Rfi}^{eq} > L_{Rfe} \end{cases} \quad 5.45$$

and

$$\delta_{L1}(V_f^{tr}) = \delta_1 \left\{1-\cos\left[-\arcsin\frac{C_3}{\delta_1}\right]\right\} \quad 5.46$$

6. Evaluation of the maximum effective capacity of the NSM FRP laminate $(V_{fi,eff}^{\max})$ with equation 5.47 with equivalent average resisting bond length $(\bar{L}_{Rfi}^{eq})$;

$$V_{fi,eff}^{\max} = V_{fi,eff}(\gamma_{\max}) = \frac{\delta_1 A_2}{2L_d A_3 \gamma_{\max}}\left[\frac{\pi}{2} - \arcsin\psi - \psi\sqrt{1-\psi^2}\right] \quad 5.47$$

where

$$A_2 = \frac{L_p \lambda}{J_1};\ A_3 = \frac{\sin(\theta_v+\beta)}{2\delta_1};\ \gamma_{\max} = \frac{2\delta_{Lu}}{L_d \sin(\theta_v+\beta)}$$
$$\psi = (1-A_3)\gamma_{\max} L_d \quad 5.48$$

7. Prediction of the shear strength contribution provided by the NSM FRP laminates (equation 5.49);

$$V_{fd} = \frac{1}{\gamma_{Rd}} V_f = \frac{1}{\gamma_{Rd}}(2N_{f,\text{int}}^{l} V_{fi,eff}^{\max} \sin\beta) \quad 5.49$$

γ_{Rd} is the partial safety factor, which can be assumed to range between 1.1-1.2 for design. In the current case, it is taken as '1' to assess the predictive performance.

5.4.2 BACKGROUND TO BAGHI & BARROS (2017)

As described earlier, Baghi & Barros (2017) proposed the combination of Bianco approach with SMCFT to determine the shear force contribution of CFRP laminates in NSM strengthening. The formulation proposed to evaluate the shear stress is shown in equation 5.50, which is the addition of FRP shear stress contribution to the concrete and steel shear contribution derived according to MCFT.

$$\nu = \nu_c + \nu_s + \nu_f$$
$$\nu = \beta\sqrt{f_c'} + \rho_{fw} f_{yl} \cot\theta_v + \frac{V_f}{b_w d} \qquad 5.50$$

5.4.3 APPLICATION

Baghi & Barros (2017) approach is used to evaluate the shear force in each wall of the experimental beams subjected to torsion. The main difference with the original formulation is that, while the CDC in shear rotates at the crack tip and gradually widens (Bianco et al. 2014), in case of torsion it is assumed to widen uniformly along the crack. However, all the calculations remain the same, since the simplified approach is adopted to evaluate the average bond length resisting the shear force by the NSM FRP laminates.

The following algorithm is used to calculate the shear force according to Bianco's simplified modified compression field theory (BSMCFT):

1. Assume : ε_x
2. Calculate : s_{xe} using equation 5.22
3. Calculate : θ_v and β using equation 5.20 and 5.21
4. Calculate : V_{fw} using equations 5.28 - 5.49
5. Calculate : $\nu = \nu_c + \nu_s + \nu_{fw}$ using equation 5.50
6. Calculate : $\varepsilon_x = \dfrac{\nu\cot\theta_v - \nu_c \big/ \cot\theta_v}{E_{sl}\rho_{sl}}$
7. Compare ε_x of step 6 with ε_x of step 1
8. Return to step 2, until the tolerance $\left(\dfrac{\left|\varepsilon_x(step6) - \varepsilon_x(step1)\right|}{\varepsilon_{syl}} < 1\times10^{-6}\right)$ is reached

9. If : ε_x (step 6) $> \varepsilon_{syl}$, then take $\varepsilon_x = \varepsilon_{syl}$ and repeat calculations up to shear stress evaluation (step 5).

In case of beams strengthened only on three faces, the beams fail earlier due to the lower capacity of the unstrengthened top surface. The above approach evaluates the shear force on each leg/wall of the beam. So in order to evaluate the shear force contribution of the beams strengthened on three faces, equation 5.51 (minimum strengthened beam) and equation 5.52 (maximum strengthened beam) are used to determine the average shear force.

$$V_{S3F\_L2S5} = \frac{\left[\left(3*V^{S4F\_L2S5}\right)+\left(1*V^{Ref\_4S}\right)\right]}{4} \qquad 5.51$$

$$V_{S3F\_L4S10} = \frac{\left[\left(3*V^{S4F\_L4S10}\right)+\left(1*V^{Ref\_4S}\right)\right]}{4} \qquad 5.52$$

The above algorithm is applied for the reference and strengthened beams of the current experimental programme and the results are presented in Table 5.7.

Table 5.7 Shear force evaluation according to BSMCFT, for the experimental data

Beam	θ_v (deg.)	β	ν_c (MPa)	ν_s (MPa)	ν_f (MPa)	ν (MPa)	V (kN)
Ref_4S	44.35	0.093	0.522	1.456		1.978	72.38
S4F_L2S5	44.35	0.093	0.522	1.456	0.833	2.810	102.86
S4F_L2S10	44.35	0.093	0.522	1.456	1.666	3.644	133.35
S4F_L4S5	44.35	0.093	0.522	1.456	0.833	2.810	102.86
S4F_L4S10	44.35	0.093	0.522	1.456	1.667	3.645	133.40
S3F_L2S5	44.35	0.093	0.522	1.456	0.833	2.811	95.26
S3F_L4S10	44.35	0.093	0.522	1.456	1.667	3.645	118.14
S4FL_L2S5	44.35	0.093	0.522	1.456	0.834	2.811	102.90
S4FL_L4S10	44.35	0.093	0.522	1.456	0.822	2.800	102.48

ν_c = concrete shear stress, ν_s = steel shear stress, ν_f = FRP shear stress, ν = shear stress and V = Shear force, α =25 degrees, β = 90 degrees, a_f =1.4 (S4F and S3F beams) and 2.8 mm (S4FL beams), b_f = 10 mm, s_f = 200/100 mm, τ_0 = 13 MPa, δ_1 = 5 mm.

The results obtained from both analytical approaches are presented in Table 5.8 and compared with the experimental results. Both approaches predict very well the experimental results. The under prediction of the load capacity of beams S4F_L4S10 and S3F_L4S10 using BSMCFT can be attributed to the fact that these beams had a premature failure in the over-reinforced region of the beams.

Table 5.8 Comparison of experimental results with both analytical approaches

Beam	Experimental results		Analytical results		V_{exp}/V_{ana}	V_{exp}/V_{ana}
	Torsional moment, M_t (kN.m)	Shear force, V (kN)	Shear force, V (kN) I approach	Shear force, V (kN) BSMCFT	I approach	BSMCFT
Ref_4S	56.69	82.88	81.44	72.38	1.02	1.15
S4F_L2S5	78.30	114.47	108.93	102.86	1.05	1.11
S4F_L2S10	81.69	119.43	117.05	133.35	1.02	0.90
S4F_L4S5	79.37	116.03	108.93	102.86	1.07	1.13
S4F_L4S10	83.02	121.37	112.51	133.40	1.08	0.91
S3F_L2S5	66.65	97.45	92.40	95.26	1.06	1.02
S3F_L4S10	70.27	102.73	101.18	118.14	1.02	0.87
S4FL_L2S5	77.05	112.64	108.07	102.89	1.04	1.10
S4FL_L4S10	78.35	114.54	115.93	102.48	0.99	1.12
Average					**1.04**	**1.03**
Standard deviation					**2.87%**	**11.17%**
Coefficient of variation					**2.77%**	**10.81%**

5.5 CONCLUSIONS

The proposed analytical equations to predict the torsional moment capacity of transverse steel and FRP reinforcements, effective strain of FRP laminates and compressive strut angle in first approach are based on thin-walled space truss analogy, the basis for many codes, as it is considered simple and effective in calculating the torsional resistance of reinforced concrete member. The contribution of the transverse reinforcement is

evaluated based on the vertical shear force resisted by the transverse reinforcements (steel and CFRP laminates) crossing the cracks. Similarly, the longitudinal reinforcements are accounted for by considering the transformed axial force to be resisted by the CFRP and steel reinforcements. The effective strain limitation for the CFRP laminates are adapted from existing FIB (2001) formulations for shear and EBR, and updated to the current NSM FRP torsional strengthening equations. The compressive strut angle is calculated based on the modified compressive field theory, as it takes into account the tensile contribution of concrete between cracks. The proposed equations predict well the torsional moment carrying capacity of thin-walled tubular reinforced concrete structures with a standard deviation of 5.2% and coefficient of variation of 5.1%. Approach I is based on an empirical approach and is validated against the available research data. Although the approach is simple and can be easily implemented in current design guidelines, more experimental data is necessary to validate it further and to obtain a more reliable estimate of effective strain for different reinforcement types and layouts.

The second approach adopted in the current chapter to evaluate the shear force contribution of the FRP laminates of the current experimental data, is an implementation of the BSMCFT described in Baghi & Barros (2017). It combines MCFT with shear force evaluation of NSM FRP laminates described in Bianco et al. (2014) taking into account the resisting bond length of the FRP laminates and the concrete semi-pyramid area. The obtained results are in very good agreement with the experimental results with a standard deviation of 11.2% and a coefficient of variation of 10.8%.

CHAPTER:

6. CONCLUSIONS

The use of near surface mounted FRP reinforcement has been shown to provide excellent advantages and superior performance as both a flexural and shear strengthening solution. However, the application of NSM FRP in torsional strengthening has been very limited. The main aim of the current research was to exploit the benefits of NSM FRP reinforcement and assess its performance in torsional strengthening of thin walled tubular RC structures so as to expand the use of this innovative technique and find alternative solutions to the increasingly important problems related to our aging infrastructure.

The complex nature of torsional behaviour in RC beams was firstly investigated through the implementation of a detailed non-linear numerical analysis. This initial investigation assisted the design of a bespoke testing frame, along with all required support and loading fixtures, and enabled a preliminary assessment of different torsional strengthening schemes. The best NSM FRP configurations were subsequently tested during the experimental phase of this research study and analytical models were developed to predict the torsional behaviour of the tested beams and propose simple, yet safe, design recommendations. Based on the discussions presented in the previous chapters, the main conclusions are summarised in the following.

6.1. NUMERICAL RESULTS

A non-linear numerical finite element analysis was performed to assist with the preparation of the experimental work and assess the suitability of different strengthening strategies using NSM FRP. After the model was successfully calibrated against available experimental data, a study was carried out to assess the influence of key parameters on overall torsional response. The parameters investigated included: longitudinal and transverse steel reinforcement ratios; concrete compressive strength and different strengthening configurations for the experimental work.

The main conclusions from this preliminary investigation are summarised below.

- The ratios of both transverse and longitudinal reinforcement affect the post-cracking torsional stiffness of the beam. An increase in the reinforcement ratios

leads to an increase in the stiffness of the elasto-plastic range and results into a higher ultimate torsional moment carrying capacity;

- An increase in concrete strength results into an increase in the torsional cracking moment and torsional capacity at yield initiation of the steel reinforcement;
- All the proposed strengthening configurations with variations in both longitudinal and transverse direction, improved the torsional moment capacity (7%-15%);
- The FRP laminates are effective in reducing the crack propagation as well as widening of the cracks;
- The stiffness of the CFRP laminates influences the stiffness response of the overall behaviour of the beam: the higher is the stiffness of the FRP material, the stiffer the response and the earlier the FRP material starts resisting the torsional moment.

6.2. EXPERIMENTAL RESULTS

Ten beams, including two reference and eight strengthened beams, were tested to assess the performance of NSM CFRP as torsional strengthening system. Different strengthening configurations were examined, including four face strengthening and three face strengthening systems, using straight laminates and L-CFRP laminates. Based on the results obtained from the preliminary numerical FE analysis, four different combinations of longitudinal and transverse CFRP reinforcement were explored in series one. In series two, strengthening was performed on three faces, while series three involved strengthening with L-CFRP laminates on four faces. Considering the overall performance of the strengthened beams, the proposed strengthening strategies improved the overall response of the beams providing important experimental evidence that NSM CFRP reinforcement is an efficient strengthening solution for thin-walled tubular reinforced concrete structures.

The following results were obtained from the experimental work:

- All strengthening configurations improved the ultimate torsional moment carrying capacity of the beams (18%-46%);
- All three series of beams had improved ductility performance (17%-63%);
- Most of the steel reinforcements yielded before failure;

- The CFRP reinforcement was effectively utilised, mobilising up to 88.5‰ of its tensile strength;
- All strengthening configurations resulted in a reduced average crack spacing (between 16% to 56%), indicating that the use of NSM FRP reinforcement is effective in limiting the crack growth and reducing crack width;
- DIC measurements help in understanding the crack evolution process;
- Four face strengthening configurations (series one and three) perform better than a three face strengthening layout (series two) due to failure on the unstrengthened top face;
- Most of the beams failed by tensile rupture of CFRP followed by concrete crushing (series one and three), series two strengthened beams failed by concrete crushing on the unstrengthened surface and two beams, S4F_L4S10 and S3F_L4S10 failed prematurely in the over-reinforced loading section of the beam.

6.3. ANALYTICAL WORK

Analytical equations are derived based on the space truss analogy to determine the torsional moment capacity of beams strengthened with NSM FRP laminates. The torsional contribution of the FRP laminates is estimated on the basis of a limiting effective strain, while the inclination of the diagonal compressive strut is determined according to the modified compression field theory (MCFT). Three equations are proposed to evaluate the effective strain based on the reinforcement ratio of CFRP laminates, concrete compressive strength, reinforcement ratio and modulus of elasticity of the FRP material. The proposed equations provide a conservative estimate of the tensile strain that can be safely developed in the NSM FRP reinforcement and can be easily incorporated in simple design rules.

The proposed simplified design model predicts well the torsional capacity of the tested beams with a standard deviation of 5.2% (5.1% Coefficient of variation). The equations are also applied to available research work, predicting well the results with 9.5% standard deviation (8.6% Coefficient of variation).

The shear force in each wall of the beam is evaluated using the BSMCFT approach described in Baghi & Barros (2017), which is a combination of Bianco et al. (2014) to evaluate FRP laminate shear force and MCFT (Approach 2). The obtained results are in good accordance with the experimental results with a standard deviation of 11.2% (coefficient of variation of 10.8%).

6.4. RECOMMENDATIONS FOR FUTURE WORK

Although the main objectives of the proposed research were successfully achieved, further research questions arose during the various phases of this study and the following issues should be considered in future work.

- As the main target application is the strengthening of bridge girders, additional experimental tests should be performed on high strength concrete beams. The higher strength concrete is expected to influence the geometry of the space truss and possibly affect the bond performance of the NSM FRP reinforcement and the magnitude of strain that can be effectively mobilized in the FRP reinforcement;
- In terms of strengthening, placing the transverse laminates first (interior) and then the longitudinal laminates. It is seen that the transverse laminates are contributing more to the torsional resistance than the longitudinal laminates. Deeper the placement of the transverse laminates, higher the contribution in torsional resistance;
- Validate and improve the effective strain predicting equations, both for transverse and longitudinal CFRP laminates, when additional data become available.
- Application of pre-stress to the FRP laminates, in order to have an early contribution of laminates in the serviceability limit state. A preliminary analysis was performed in Chapter 3 (section 3.3.2) but an experimental investigation should assess the practicalities of developing feasible solutions;
- Explore additional strengthening configurations and FRP reinforcement types, for example FRP ropes in a continuous spiral configuration;
- New type of loading section, possibly like a steel collar covering the beam externally, in order to avoid premature failure of beams;
- Use of 3D DIC to assess in more detail the torsional deformation of the elements and how this affects failure of the NSM FRP longitudinal and transverse reinforcement. The FRP strips or bars are subjected to a complex combination of

stresses (parallel and transverse to the fibres) and this would affect their effectiveness and failure mode.

- Numerical simulation of experimentally tested beams to validate the adopted constitutive models. Once validated, performing strengthening assessment on real case studies and to explore new strengthening configurations.

REFERENCES

ACI 318. 2011. *Building Code Requirements for Structural Concrete and Commentary (ACI 318M-11). American Concrete Institute, Farmington Hills, MI*. doi:10.1016/0262-5075(85)90032-6.

ACI 440.2R-08. 2008. *Guide for the Design and Construction of Externally Bonded FRP Systems for Strengthening Existing Structures*. *ACI Committee 440*.

Akhtaruzzaman, Ali. 1990. "Design of Rectangular Beams Under Torsion, Bending & Shear." *Journal of King Abdulaziz University-Engineering Sciences* 2 (1): 133–51. doi:10.4197/Eng.2-1.9.

Al-Bayati, G., R. Al-Mahaidi, and R. Kalfat. 2017. "Torsional Strengthening of Reinforced Concrete Beams Using Different Configurations of NSM FRP with Epoxy Resins and Cement-Based Adhesives." *Composite Structures* 168: 569–81. doi:10.1016/j.compstruct.2016.12.045.

Al-Bayati, G, R Al-Mahaidi, and R Kalfat. 2016. "Torsional Strengthening of Reinforced Concrete Beams Using Different Configurations of NSM FRP with Epoxy Resins and Cement-Based Adhesives." *Composite Structures*. doi:10.1016/j.compstruct.2016.12.045.

Al-Bayati, Ghaidak, Riadh Al-Mahaidi, M. Javad Hashemi, and Robin Kalfat. 2018. "Torsional Strengthening of RC Beams Using NSM CFRP Rope and Innovative Adhesives." *Composite Structures* 187 (December 2017). Elsevier: 190–202. doi:10.1016/j.compstruct.2017.12.016.

Al-Mahaidi, Riadh, and Adrian. K Y Hii. 2007. "Bond Behaviour of CFRP Reinforcement for Torsional Strengthening of Solid and Box-Section RC Beams." *Composites Part B: Engineering* 38 (5–6): 720–31. doi:10.1016/j.compositesb.2006.06.018.

Alkhrdaji, By Tarek, and Jay Thomas. 2002. "Methods of Upgrading Concrete Structures." *Concrete Repair Bulletin*.

Anderson, Paul. 1935. "Experiments with Concrete in Torsion." *ASCE* Volume 100: pp 949–83.

Baghi, Hadi, and Joaquim A.O. Barros. 2017. "New Approach to Predict Shear Capacity of Reinforced Concrete Beams Strengthened with Near-Surface-Mounted Technique." *ACI Structural Journal* 114 (1): 137–48. doi:10.14359/51689433.

Barros, J. A O, and S. J E Dias. 2006. “Near Surface Mounted CFRP Laminates for Shear Strengthening of Concrete Beams.” *Cement and Concrete Composites* 28 (3): 276–92. doi:10.1016/j.cemconcomp.2005.11.003.

Barros, J. a O, S. J E Dias, and J. L T Lima. 2007. “Efficacy of CFRP-Based Techniques for the Flexural and Shear Strengthening of Concrete Beams.” *Cement and Concrete Composites* 29 (3): 203–17. doi:10.1016/j.cemconcomp.2006.09.001.

Barros, J.A.O., Matteo Breveglieri, A. Ventura-Gouveia, Gláucia M. Dalfré, and Alessandra Aprile. 2013. “Model to Simulate the Behavior of RC Beams Shear Strengthenend with ETS Bars.” *FraMCoS-8 Fracture Mechanics of Concrete and Concrete Structures*, 505–16.

Barros, J.A.O., and A.S. Fortes. 2004. “Flexural Strengthening of Concrete Beams with CFRP Laminates Bonded into Slits.” *Cement and Concrete Composites* 27 (4): 471–80. doi:10.1016/j.cemconcomp.2004.07.004.

Barros, J A.O., Mohammadali Rezazadeh, João P.S. Laranjeira, Mohammad R.M. Hosseini, Mohammad Mastali, and Honeyeh Ramezansefat. 2017. “Simultaneous Flexural and Punching Strengthening of RC Slabs According to a New Hybrid Technique Using U-Shape CFRP Laminates.” *Composite Structures* 159. Elsevier Ltd: 600–614. doi:10.1016/j.compstruct.2016.10.009.

Barros, J, M Rezazadeh, I Costa, H Baghi, MRM Hosseini, M Mastali, and J Laranjeira. 2016. “Flexural and Shear/Punching Strengthening of RC Beams/Slabs Using Hybrid NSM-ETS Technique with Innovative CFRP Laminates.” In *The Sixth International Conference on Structural Engineering, Mechanics and Computation*, 37–44.

Barros, Joaquim A. 2016. “Debilities and Strengths of FEM-Based Constitutive Models for the Material Nonlinear Analysis of Steel Fibre Reinforced Concrete Structures.” In *Proceedings of the 9th International Conference on Fracture Mechanics of Concrete and Concrete Structures*. FraMCoS-9, V. Saouma, J. Bolander and E. Landis (Eds), California,. doi:May 29-June 1, 2016.

Beaupré, D. 1999. “Bond Strength of Shotcrete Repair.” *Shotcrete Magazine*. http://www.shotcrete.org/pdf_files/Sp99Beaupre.pdf.

Bentz, Evan C., Frank J. Vecchio, and Michael P. Collins. 2006. “Simplified Modified Compression Field Theory for Calculating Shear Strength of Reinforced Concrete Elements.” *ACI Structural Journal* 103 (4): 614–24. doi:10.14359/16438.

Bianco, Vincenzo, Giorgio Monti, and J. A.O. Barros. 2011. “Theoritical Model and

Computational Procedure to Evaluate the NSM FRP Strips Shear Strength Contribution to a RC Beam." *ASCE Journal of Structural Engineering* 137(11): 1359–72.

Bianco, Vincenzo, Giorgio Monti, and J. A.O. Barros. 2014. "Design Formula to Evaluate the NSM FRP Strips Shear Strength Contribution to a RC Beam." *Composites Part B: Engineering* 56. Elsevier Ltd: 960–71. doi:10.1016/j.compositesb.2013.09.001.

BS EN 12390-3 (2009). 2009. "Testing Hardened Concrete." Vol. 3.

Chalioris, C.E. 2007. "Behavioural Model of FRP Strengthened Reinforced Concrete Beams under Torsion." *Journal of Composites for Construction* 11 (2): 192–200. doi:10.1061/(ASCE)1090-0268(2007)11:2(192).

Chalioris, Constantin E. 2008. "Torsional Strengthening of Rectangular and Flanged Beams Using Carbon Fibre-Reinforced-Polymers - Experimental Study." *Construction and Building Materials* 22 (1): 21–29. doi:10.1016/j.conbuildmat.2006.09.003.

Costa, Inês G., and Joaquim A O Barros. 2015. "Tensile Creep of a Structural Epoxy Adhesive: Experimental and Analytical Characterization." *International Journal of Adhesion & Adhesives* 59 (12): 115–24. doi:10.1002/pssb.201451168.

Cowan, H. J. 1950. "Elastic Theory for Torsional Strength of Rectanglar Reinforced Concrete Beams."

Csikós, Ádám, and István Hegedûs. 1998. "Torsion of Reinforced Concrete Beams." *2nd Int. PhD Symposium in Civil Engineering Budapest*, 1–9.

Deifalla, A., A. Awad, and M. Elgarhy. 2013. "Effectiveness of Externally Bonded CFRP Strips for Strengthening Flanged Beams under Torsion: An Experimental Study." *Engineering Structures* 56. Elsevier Ltd: 2065–75. doi:10.1016/j.engstruct.2013.08.027.

Deifalla, A, and A Ghobarah. 2005. "Simplified Analysis for Torsionaly Strengthened RC Beams Using FRP." In *Proceedings of International Symposium on Bond Behaviour of FRP in Structures (BBFS 2005), Hong Kong, December 5-7, 2005*.

Deifalla, A, and A Ghobarah. 2010. "Strengthening RC T-Beams Subjected to Combined Torsion and Shear Using FRP Fabrics : Experimental Study." *JOURNAL OF COMPOSITES FOR CONSTRUCTION © ASCE / MAY/JUNE 2010*, no. June: 301–12.

Dias, S. J E, and J. A O Barros. 2013a. "Shear Strengthening of RC Beams with NSM CFRP Laminates: Experimental Research and Analytical Formulation." *Composite*

Structures 99: 477–90. doi:10.1016/j.compstruct.2012.09.026.

Dias, S.J.E., and J.A.O. Barros. 2008. "Shear Strengthening of T Cross Section Reinforced Concrete Beams by Near-Surface Mounted Technique." *Journal of Composites for Construction* 12 (3): 300–311. doi:10.1061/(ASCE)1090-0268(2008)12:3(300).

Dias, S.J.E, and J.A.O. Barros. 2013b. "Shear Strengthening of RC Beams with NSM CFRP Laminates: Experimental Research and Analytical Formulation." *Composite Structures Journal* 99: 477–90. doi:http://dx.doi.org/10.1016/j.compstruct.2012.09.026.

DR_AS-3600. 2017. "Australian Standard: Concrete Structures."

El-Hacha, Raafat, and Sami H. Rizkalla. 2004. "Near-Surface-Mounted Fiber-Reinforced Polymer Reinforcements for Flexural Strengthening of Concrete Structures." *ACI Structural Journal* 101 (5): 717–26. doi:10.14359/13394.

Emmons, Peter H, Alexander M Vaysburd, and J Thomas. 1998. "Strengthening Concrete Structures, Part I." *Concrete International* 19 (3): 53–58.

EuroCode 2. 2004. "EN 1992-1-1:2004 - Eurocode 2: Design of Concrete Structures - Part 1-1: General Rules and Rules for Buildings." *CEN, Brussels*.

FIB. 2001. "Externally Bonded FRP Reinforcement for RC Structures." *Bulletin 14*. Vol. 14. http://scholar.google.com/scholar?hl=en&btnG=Search&q=intitle:Externally+bonded+FRP+reinforcement+for+RC+structures#0.

Gosbell, T, and R Meggs. 2002. "West Gate Bridge Approach Spans FRP Strengthening Melbourne, Australia." In *Proceedings of IABSE Symposium: Towards a Better Built Environment Innovation, Sustainability, Information Technology*, 330–31.

Hii, Adrian. K Y, and Riadh Al-Mahaidi. 2006. "An Experimental and Numerical Investigation on Torsional Strengthening of Solid and Box-Section RC Beams Using CFRP Laminates." *Composite Structures* 75 (1–4): 213–21. doi:10.1016/j.compstruct.2006.04.050.

Hsu, Thomas T.C C, and Y.L Mo. 1985. "Softening of Concrete in Torsional Members-Design Recommendations" 82 (4): 443–52.

Hsu, Thomas T.C, and Y.L Mo. 1985. "Softening of Concrete in Torsional Members - Theory and Tests" 82 (4): 290–303.

ISO, 527-5. 1997. "Plastics — Determination of Tensile Properties - Part 5: Test Conditions for Unidirectional Fibre-Reinforced Plastic Composites." *International*

Organisation for Standardization (ISO), Geneva, Switzerland. Vol. 1. http://www.chemshow.cn/UploadFile/datum/1000/huayangyq2008w_2009420145250792688.pdf.

ISO 6892-1. 2009. "Metallic Materials — Tensile Testing — Part 1: Method of Test at Room Temperature." *Metallic Materials*. Vol. 2009.

ISO527-2. 1993. "Plastics - Determination of Tensile Properties - Part 2: Test Conditions for Moulding and Extrusion Plastics." *International Organisation for Standardization (ISO), Geneva, Switzerland*.

Jing, Meng, Werasak Raongjant, and Zhongxian Li. 2007. "Torsional Strengthening of Reinforced Concrete Box Beams Using Carbon Fiber Reinforced Polymer." *Composite Structures* 78 (2): 264–70. doi:10.1016/j.compstruct.2005.10.017.

Karayannis, Chris G. 2000. "Smeared Crack Analysis for Plain Concrete in Torsion." *ASCE Journal of Structural Engineering*, no. June: 638–45.

Karayannis, Chris G., and C.E. Chalioris. 2000. "Experimental Validation of Smeared Analysis for Plain Concrete in Torsion." *ASCE Journal of Structural Engineering* 126 (6): 638–45. doi:10.1016/S0065-2113(03)81001-5.

Khalifa, Ahmed, and Antonio Nanni. 2000. "Improving Shear Capacity of Existing RC T-Section Beams Using CFRP Composites." *Cement and Concrete Composites* 22 (3): 165–74. doi:10.1016/S0958-9465(99)00051-7.

Lorenzis, De L., and Antonio Nanni. 2001. "Shear Strengthening of Reinforced Concrete Beams with Near-Surface Mounted Fiber-Reinforced Polymer Rods." *ACI Structural Journal* 98(1) (98): 60–68.

Lorenzis, Laura De, Antonio Nanni, and Antonio La Tegola. 2000. "Strengthening of Reinforced Concrete Structures with Near Surface Mounted FRP Rods." In *International Meeting on Composite Materials, PLAST 2000*, 1–8. Milan, Italy.

MacGregor, J. G, and M. G. Ghoneim. 1995. "Design for Torsion." *ACI Structural Journal* 92: 211–18.

ModelCode. 1990. "BEF-FIP Model Code."

N., Lessig. 1959. "Determination of Load Carrying Capacity of Reinforced Concrete Element with Rectangular Cross-Section Subjected to Flexure with Torsion." In *Proceedings, Concrete and Reinforced Concrete Institute, Moscow*, 28:5–28.

Nanni, Antonio, Marco Di Ludovico, and Renato Parretti. 2004. "Shear Strengthening of a PC Bridge Girder with NSM CFRP Rectangular Bars." *Advances in Structural Engineering* 7 (4): 97–109. doi:10.1260/1369433041653570.

NTC-CNR. 2018. “Norme Tecniche per Le Costruzioni - NTC 2018.”

Panchacharam, Saravanan, and Belarbi Abdeldjelil. 2002. “Torsional Behavior of Reinforced Concrete Beams Strengthened with FRP Composites.” In *First FIB Congress, Osaka, Japan, October 13-19,2002*, 1–11.

Panchacharam, Saravanan, and Abdeldjelil Belarbi. 2002. “Torsional Behavior of Reinforced Concrete Beams Strengthened with FRP Composites.” In *First FIB Congress on Concrete Structures in 21st Century, Osaka, Japan, October 13-19,2002*, 1–11.

Rausch, Ernst. 1938. “Berechnung Des Eisenbetons Gegen Verdrehung (Torsion) Und Abscheren.”

Rezazadeh, M., H. Ramezansefat, and J. Barros. 2016. “NSM CFRP Prestressing Techniques with Strengthening Potential for Simultaneously Enhancing Load Capacity and Ductility Performance.” *Composites for Construction Journal* 20 (5). doi:10.1061/(ASCE)CC.1943-5614.0000679.

Rodriguez, M, and R Park. 1991. “Repair and Strengthening of Reinforced Concrete Buildings for Seismic Resistance.Pdf.” *Earthquake Spectra* 7 (No. 3): 439–59.

Schladitz, F., and M. Curbach. 2009. “Increase in the Torsional Resistance of Reinforced Concrete Members Using Textile Reinforced Concrete (TRC).” In *Concrete Repair, Rehabilitation and Retrofitting II*, 1095–1100. http://ftp.ing.unibs.it/~plizzari/CD/Pdf/154.pdf.

Vecchio, Frank J, and Michael P Collins. 1986. “The Modified Compression-Field Theory for Reinforced Concrete Elements Subjected to Shear.” *ACI Journal Proceedings* 83 (2): 219–31. doi:10.14359/10416.

Ventura-Gouveia, A., J.A.O. Barros, A. F. M. Azevedo, and J.M. Sena-Cruz. 2008. “Multi-Fixed Smeared 3D Crack Model to Simulate the Behavior of Fiber Reinforced Concrete Structures.” *CCC2008-Challenges for Civil Construction*, 11.

ANNEX: CHAPTER 4

EXPERIMENTAL WORK

DIGITAL IMAGE CORRELATION (DIC)

1. Ref_4S

Data	Images	Torsional moment *vs.* torsional angle of rotation	Remarks
0.221°/ 19.133 kN.m	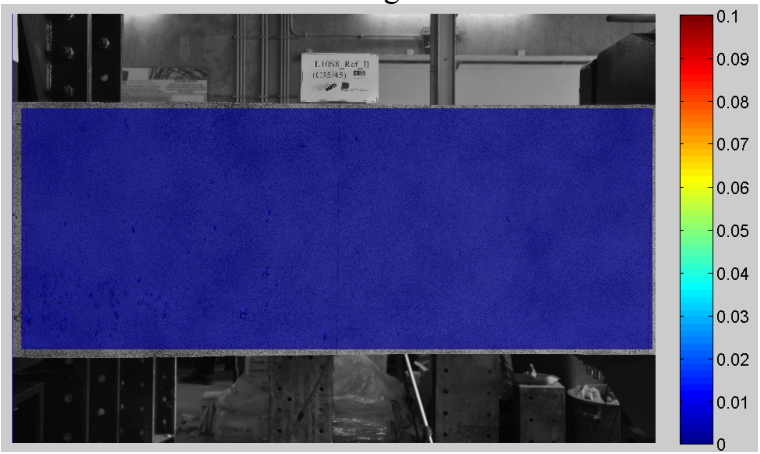	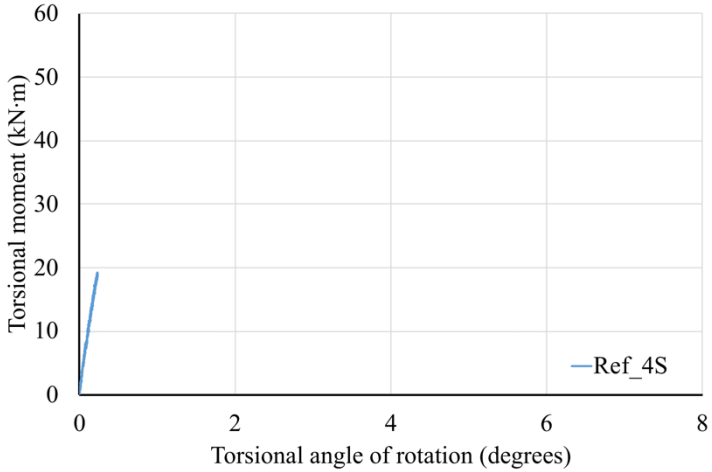	No cracks, linear section
0.488°/ 30.870 kN.m	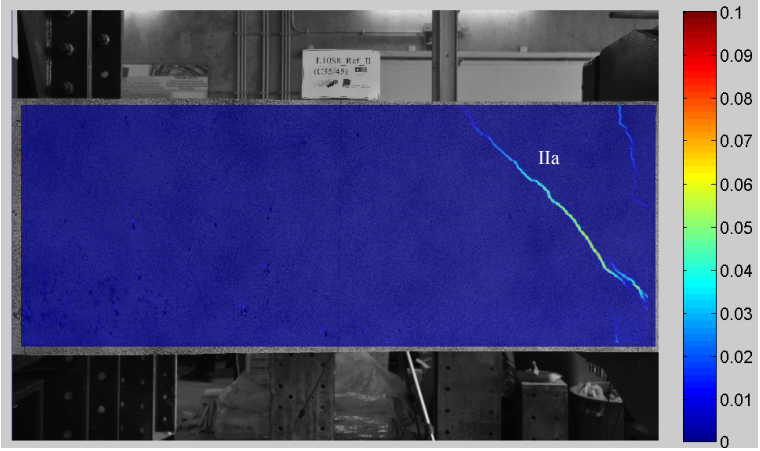	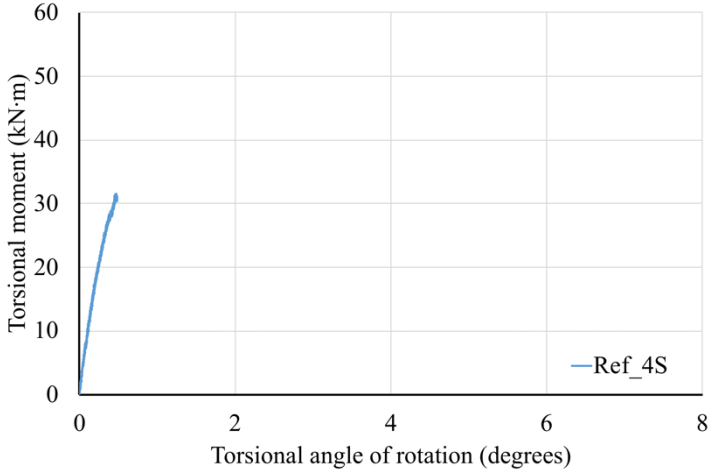	Torsional cracking moment

1.210°/
41.475
kN.m

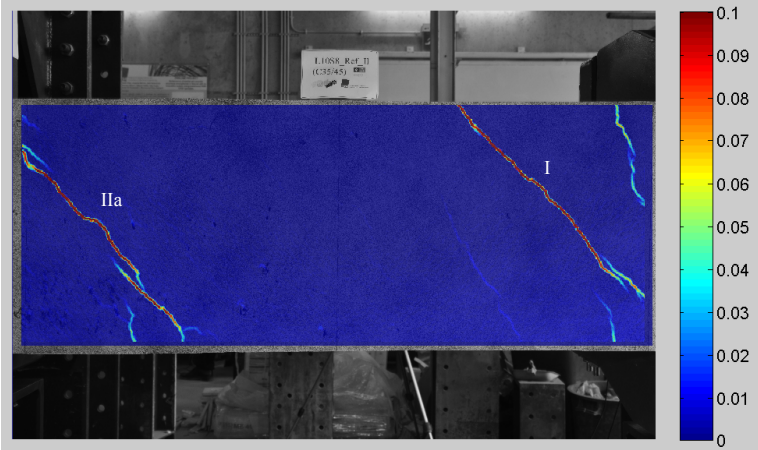

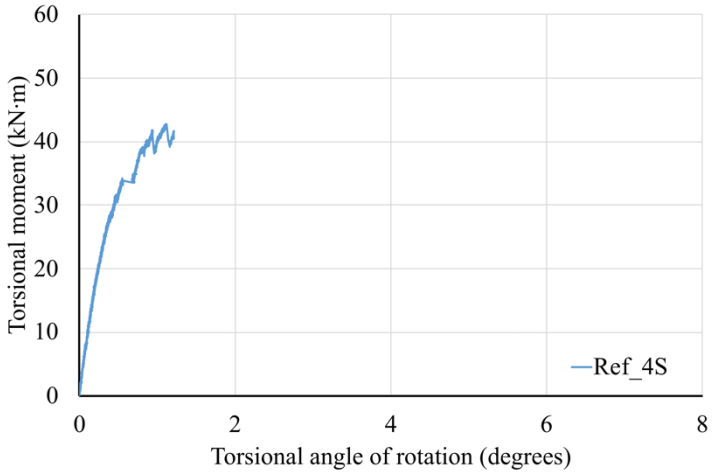

Macro
cracking

1.597°/
46.418
kN.m

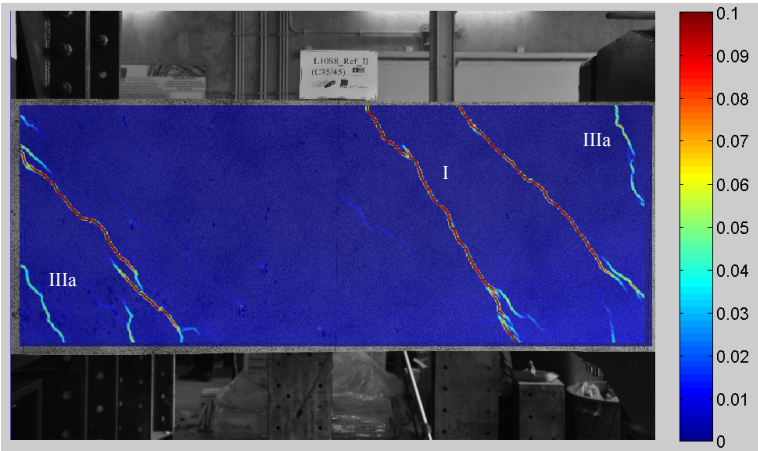

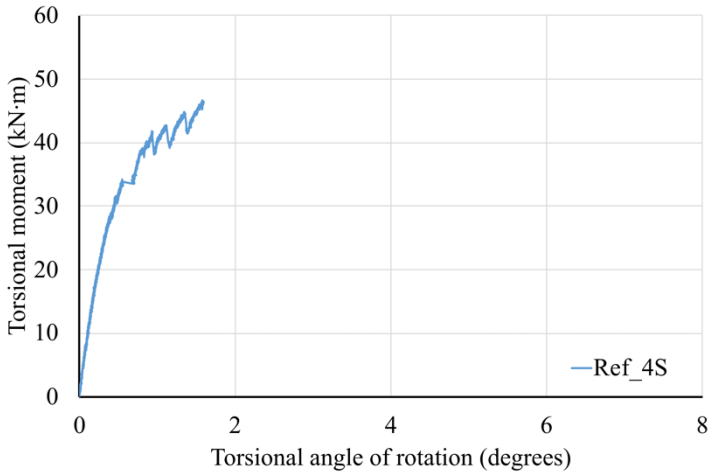

Crack
propagation

1.734°/
46.493
kN.m

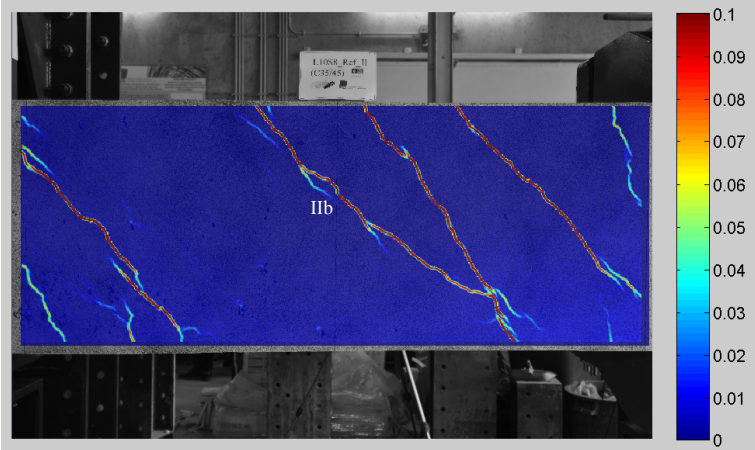

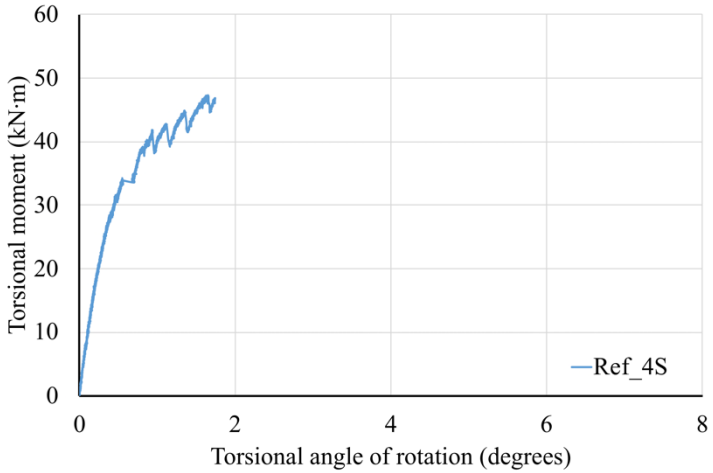

2.771°/
47.363
kN.m

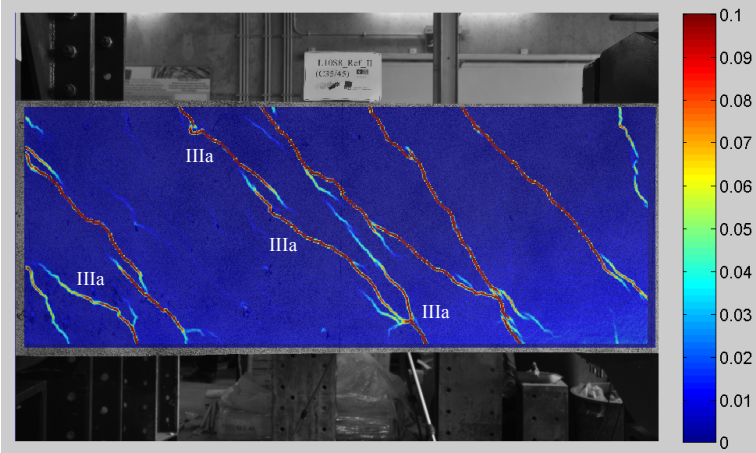

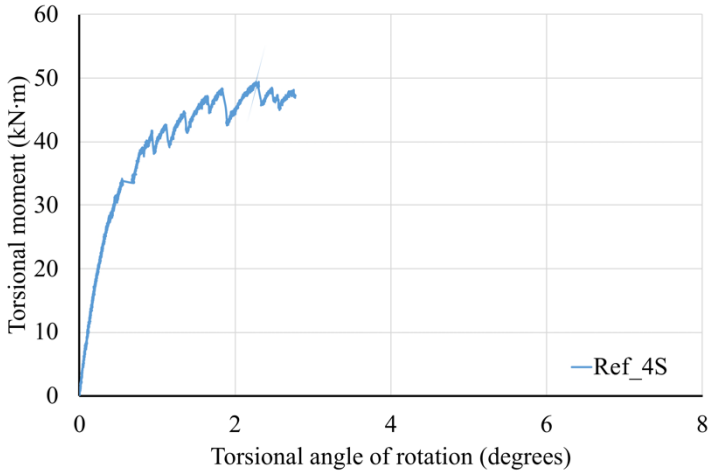

Yield
initiation

3.704°/
53.393
kN.m

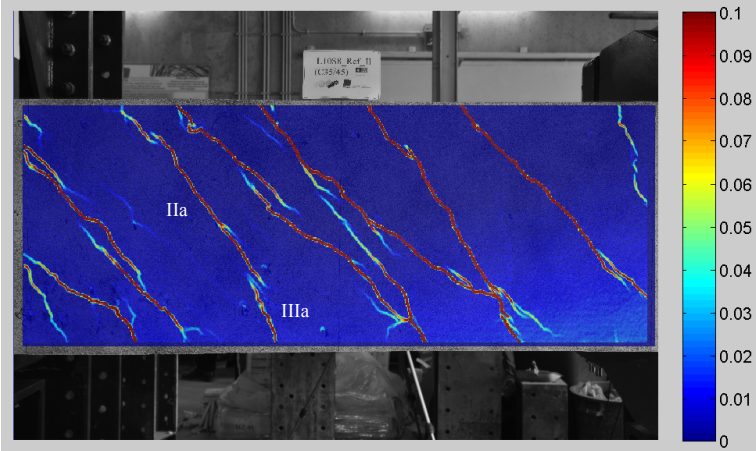

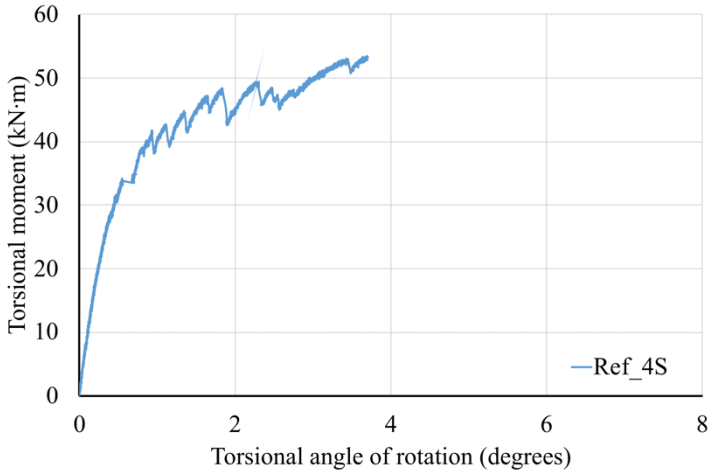

4.696°/
56.010
kN.m

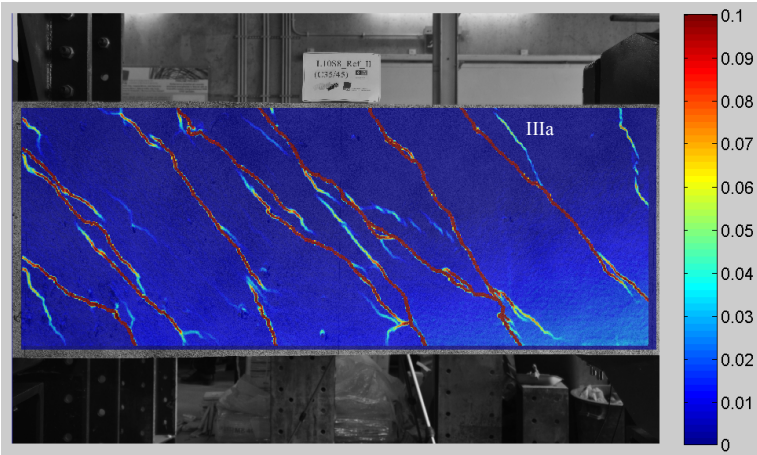

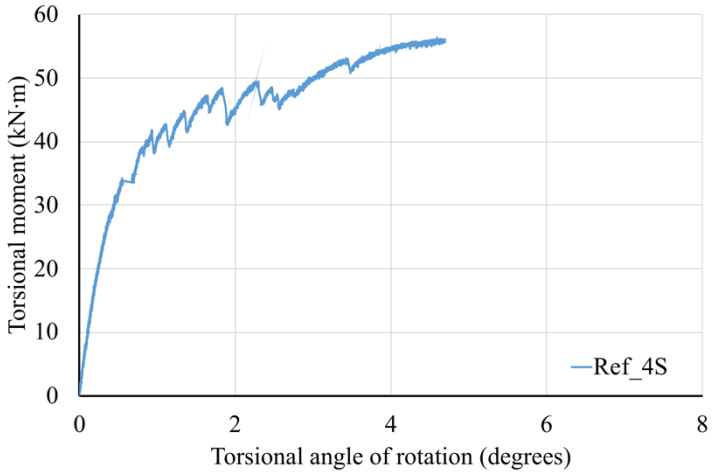

5.467°/
55.845
kN.m

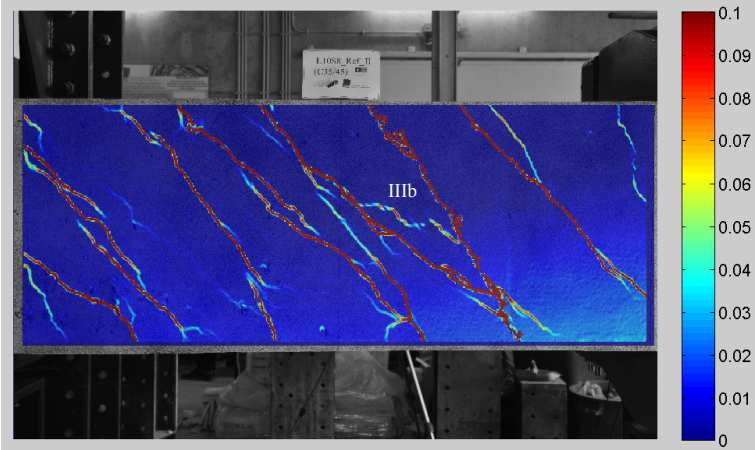

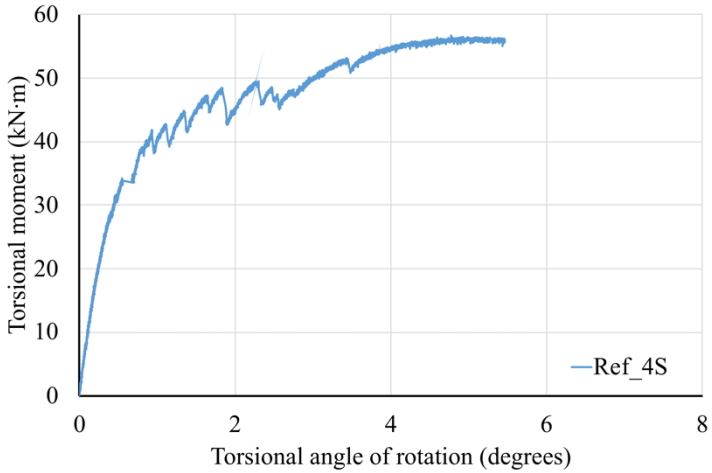

Peak
torsional
moment

6.565°/
45.458
kN.m

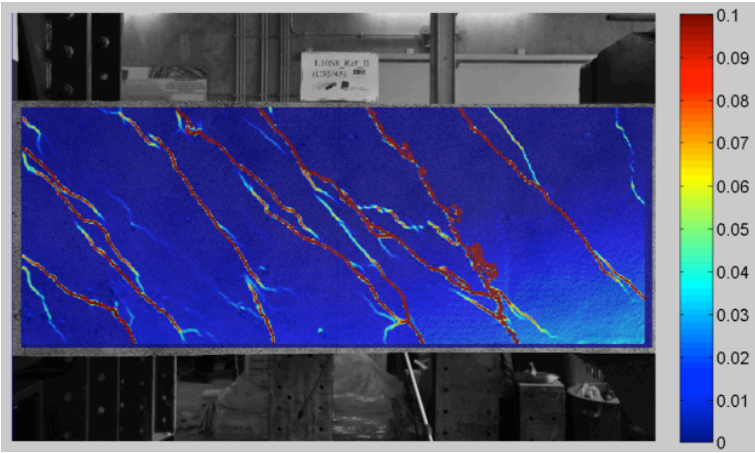

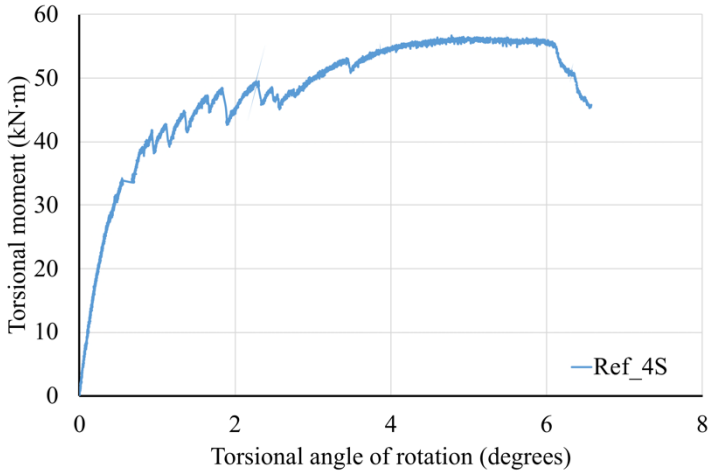

After failure

2. Beam: S4F_L2S5

Data	Images	Torsional moment *vs.* torsional angle of rotation	Remarks
0.318°/ 25.11 kN.m	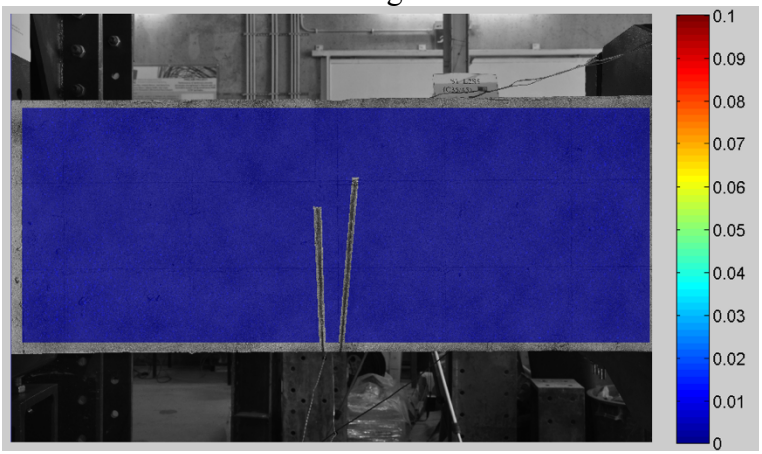	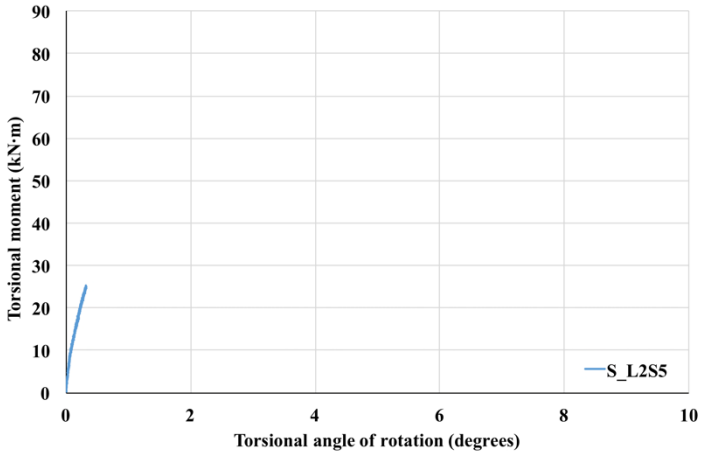	No cracks, linear section
1.447°/ 50.865 kN.m	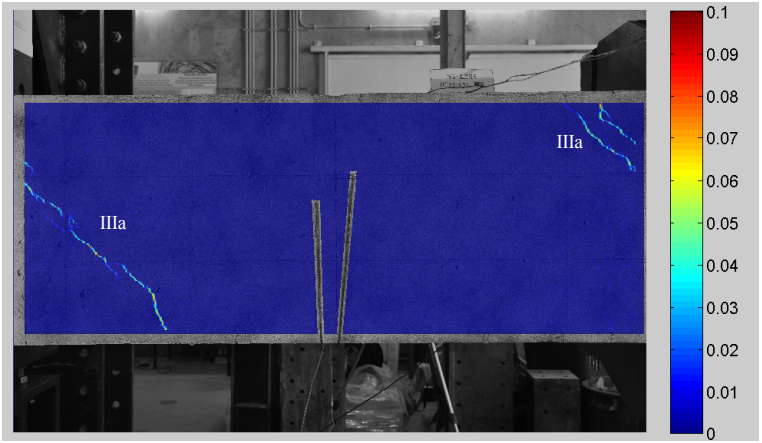	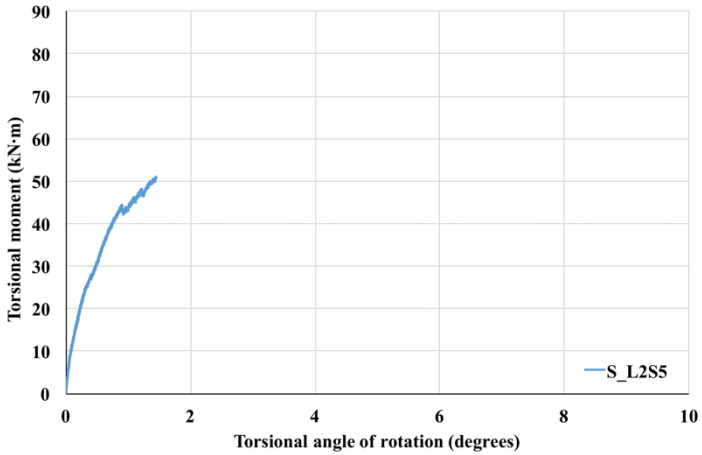	Torsional cracking

1.939°/ 55.225 kN.m

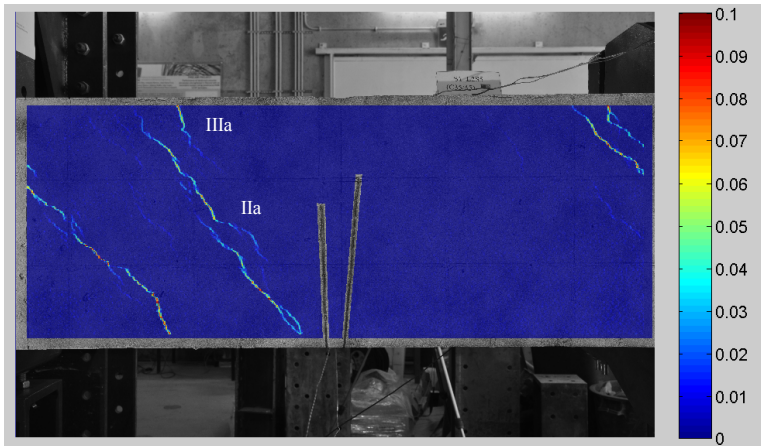

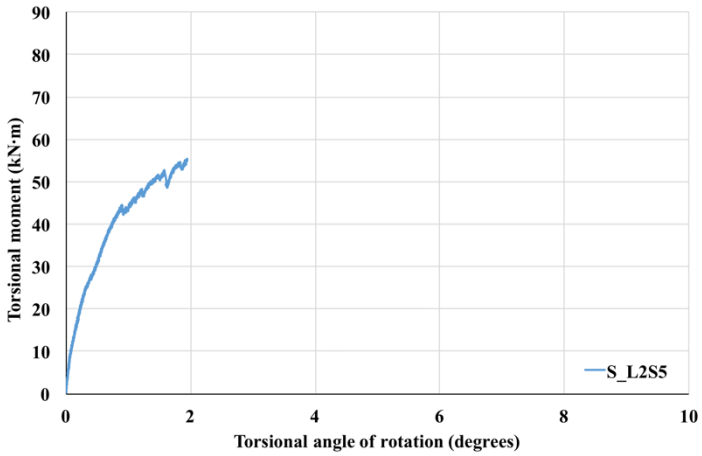

Macro cracking

2.488°/ 52.485 kN.m

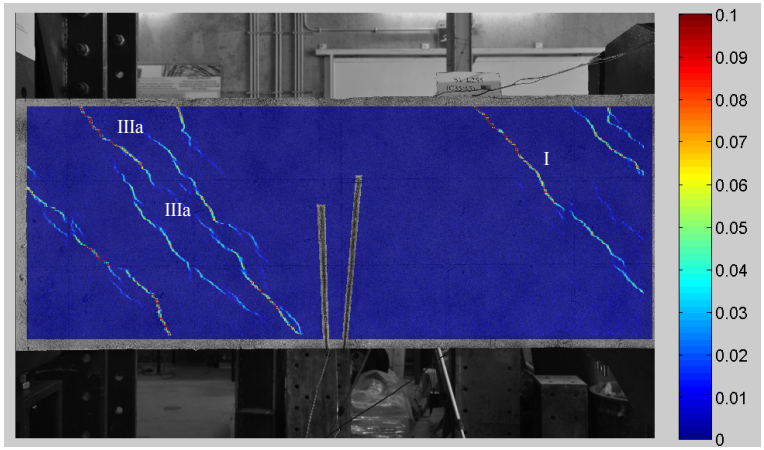

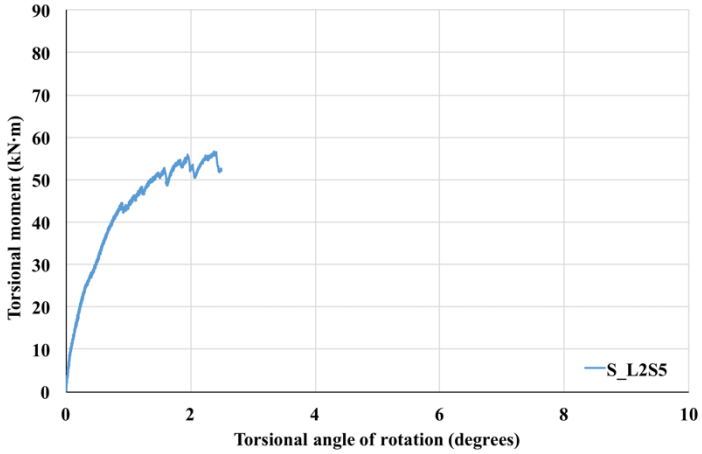

2.830°/
56.235
kN.m

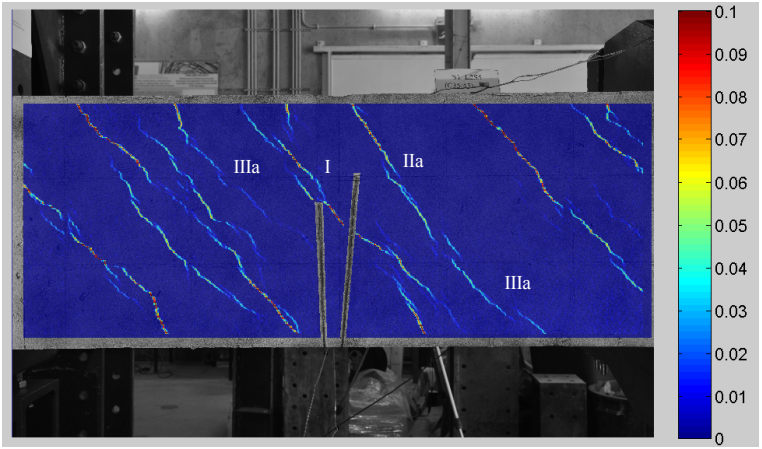

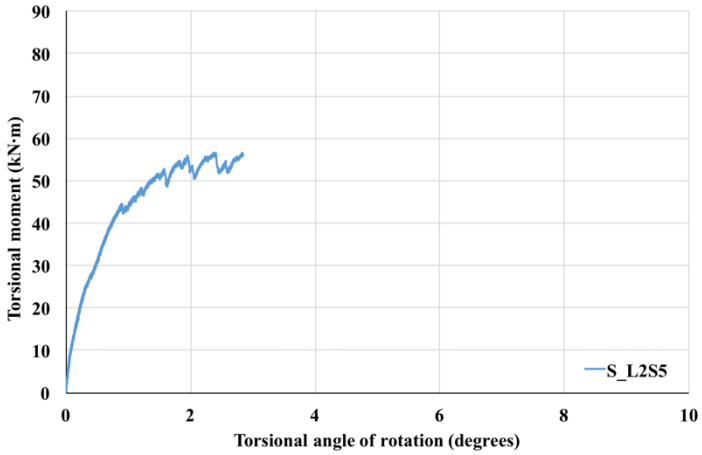

Yield
initiation

4.106°/
65.438
kN.m

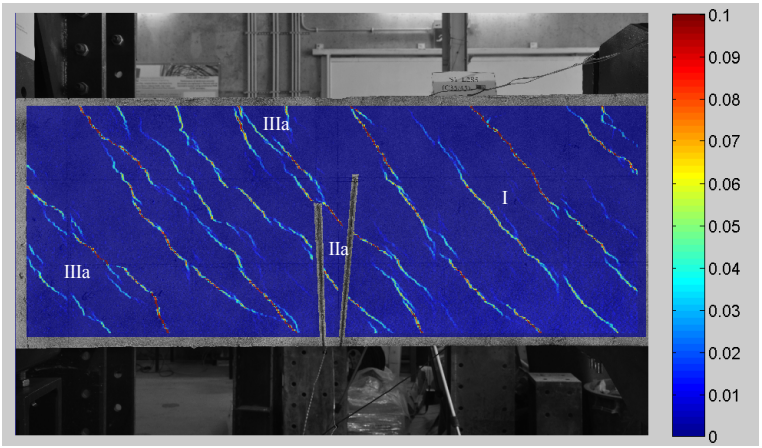

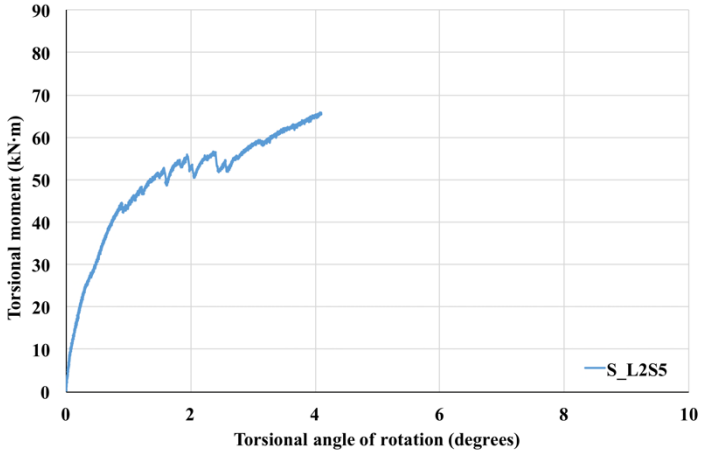

5.693°/
73.823
kN.m

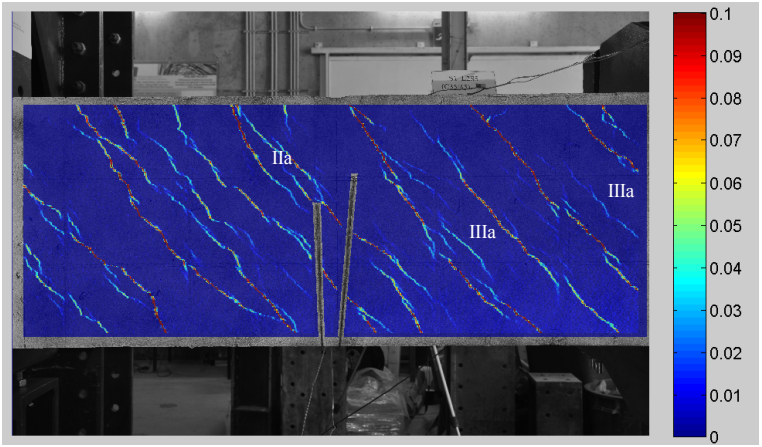

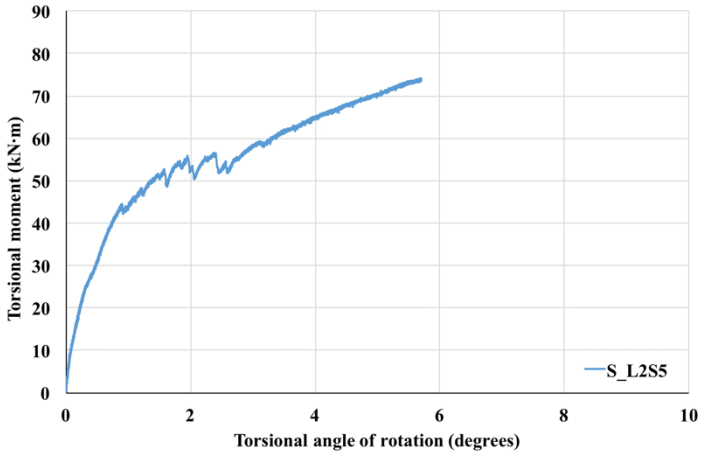

8.387°/
70.110
kN.m

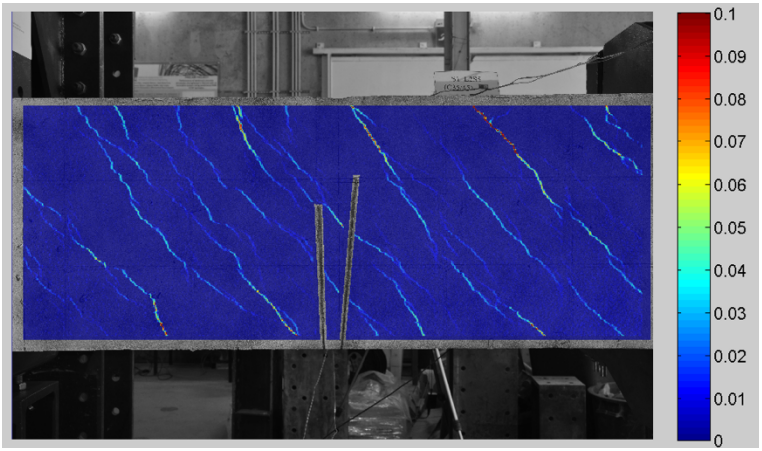

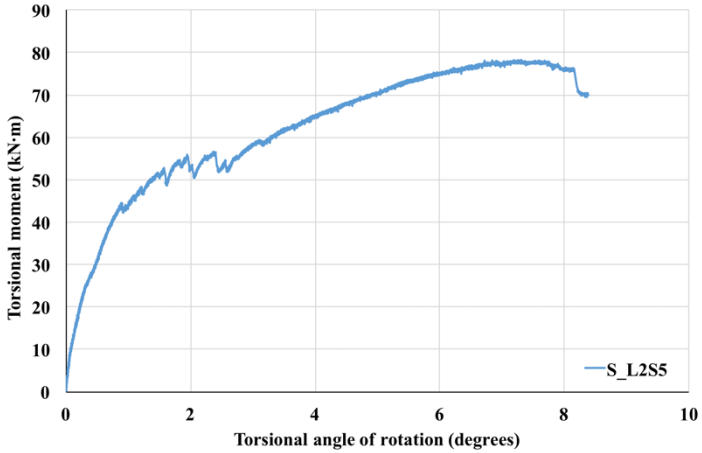

After
failure

3. Beam S4F_L2S10

Data	Images	Torsional moment *vs.* torsional angle of rotation	Remarks
0.493°/ 36.548 kN.m	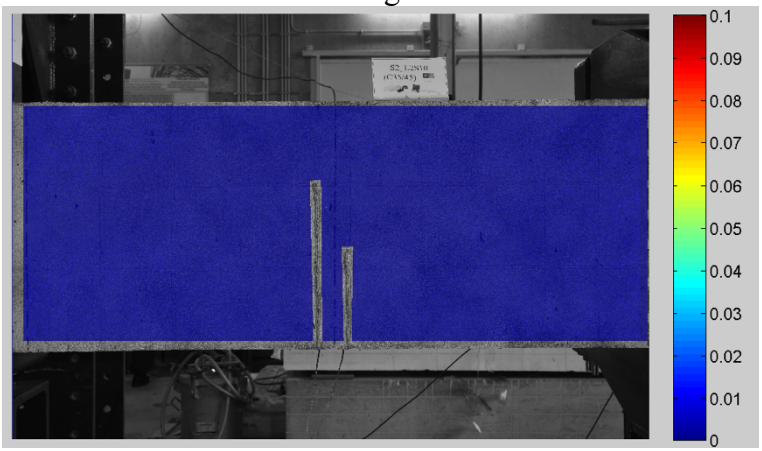	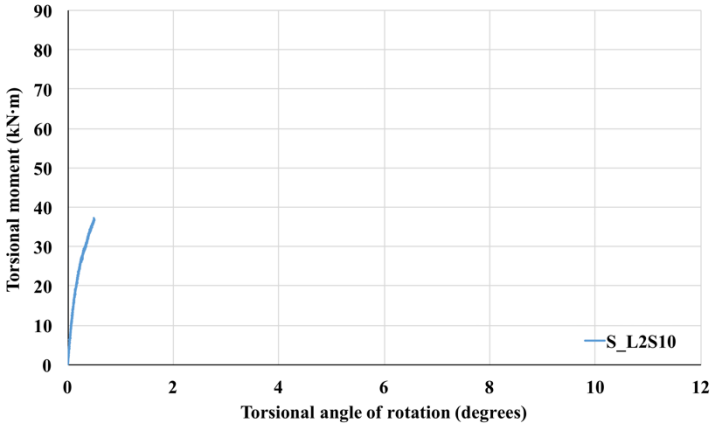	No cracks, linear section
1.381°/ 49.350 kN.m	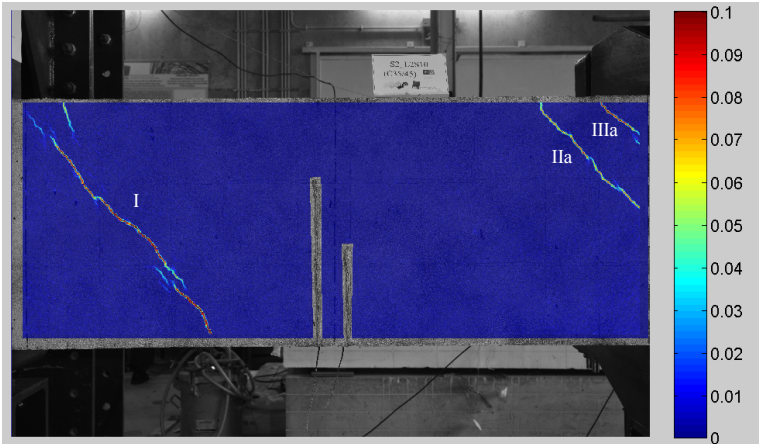	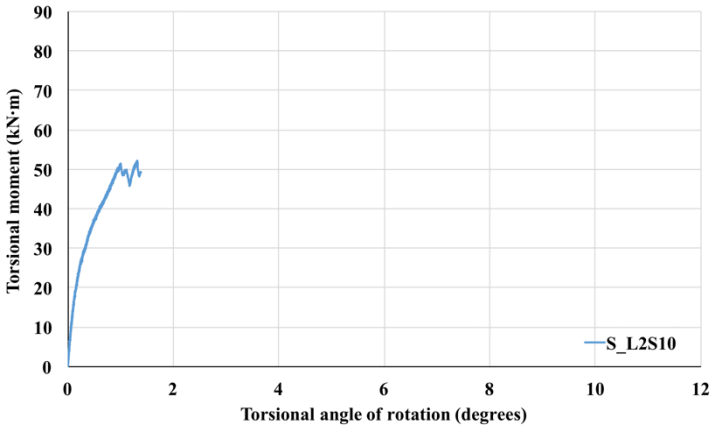	Torsional cracking moment

1.861°/
53.558
kN.m

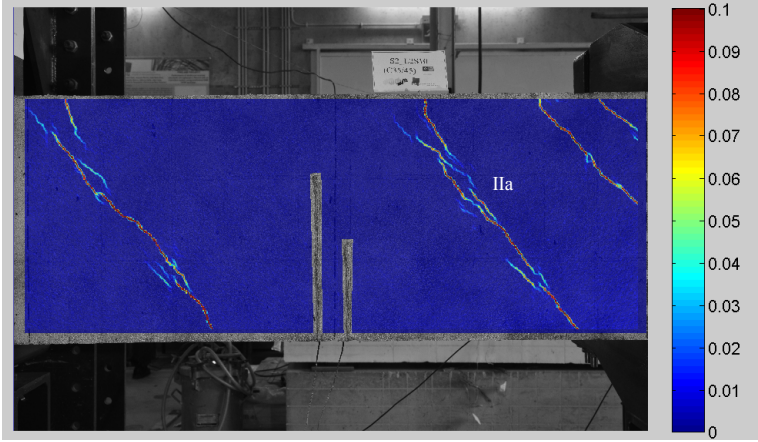

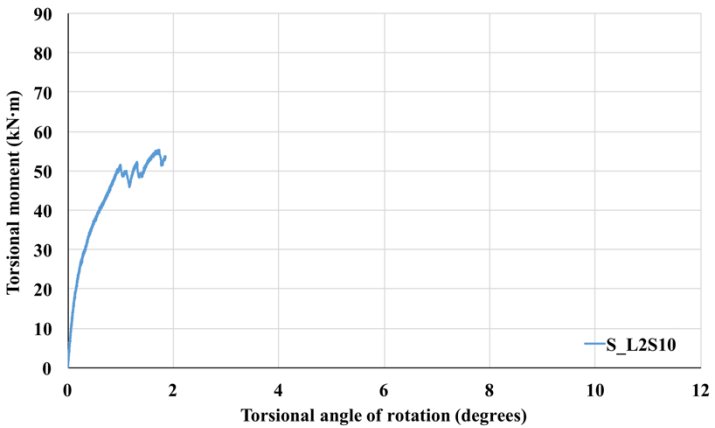

Macro
crack
propagation

2.037°/
54.863
kN.m

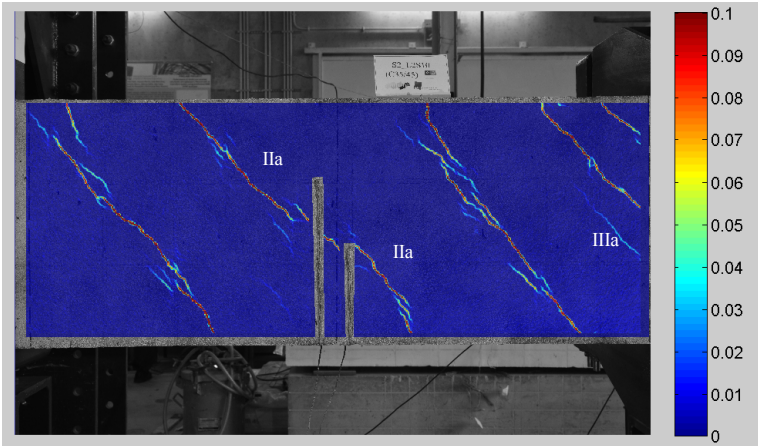

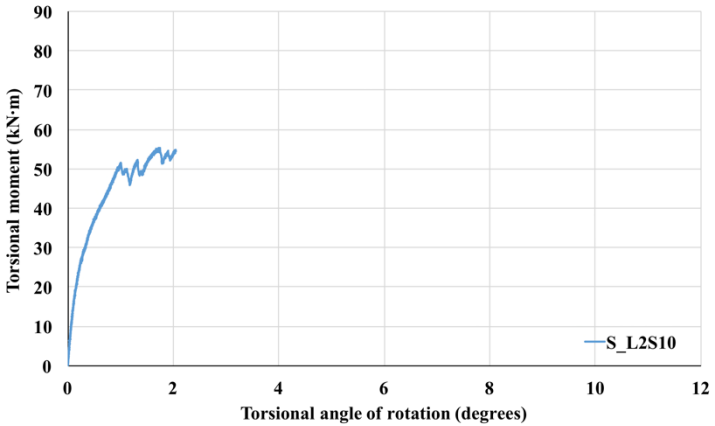

2.977°/
61.193
kN.m

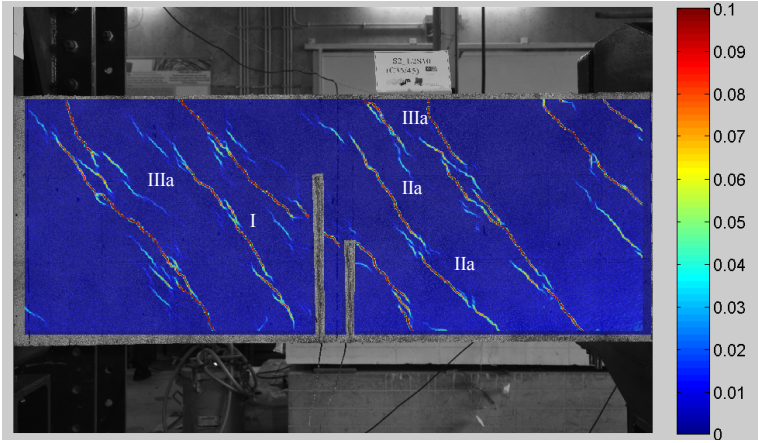

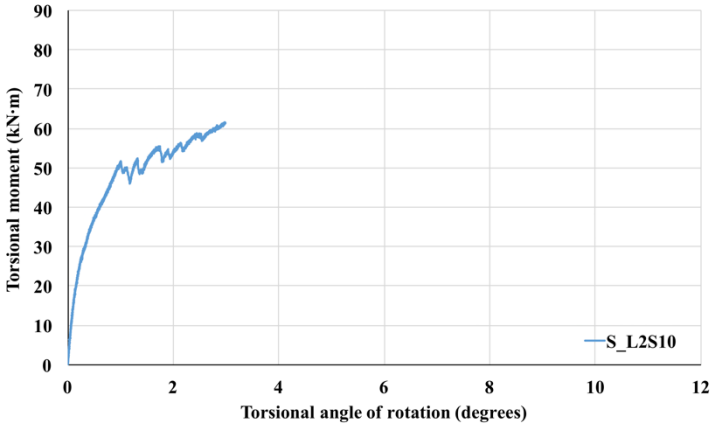

Yield
initiation

3.550°/
65.565
kN.m

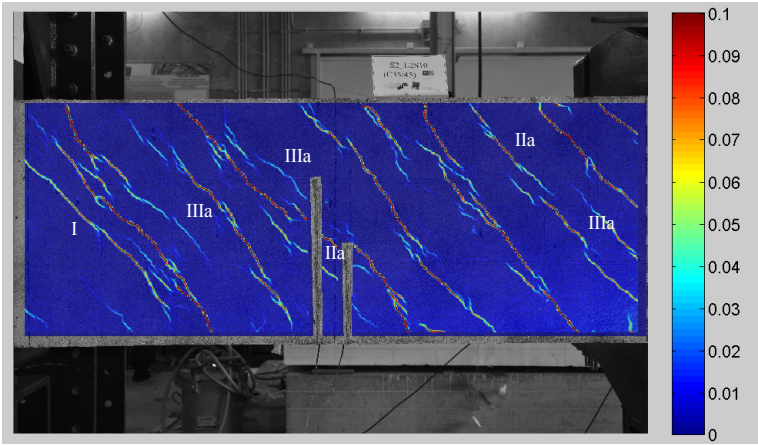

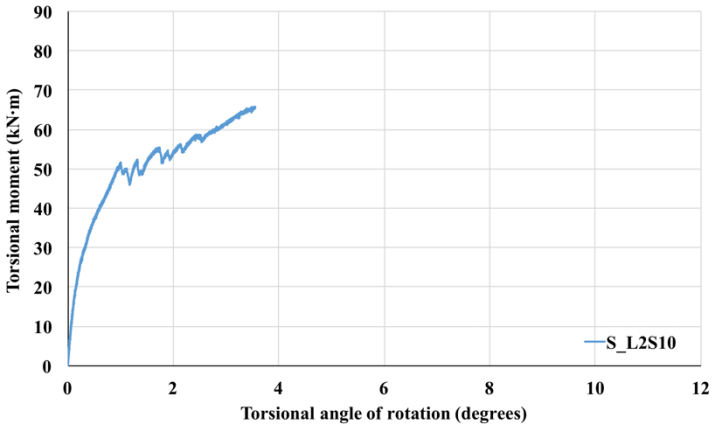

4.341°/
71.250
kN.m

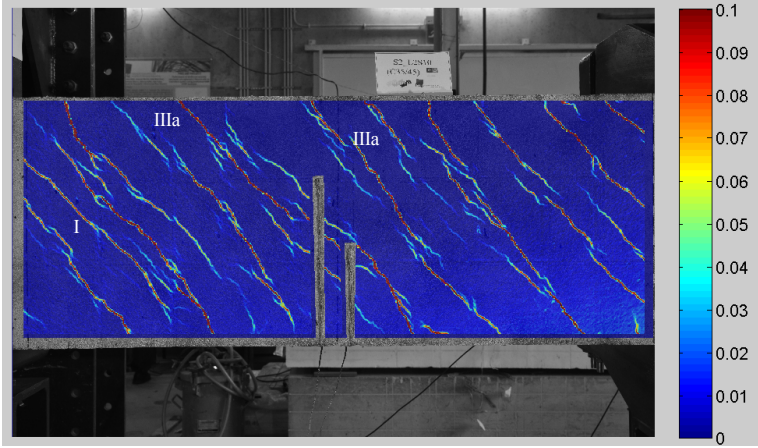

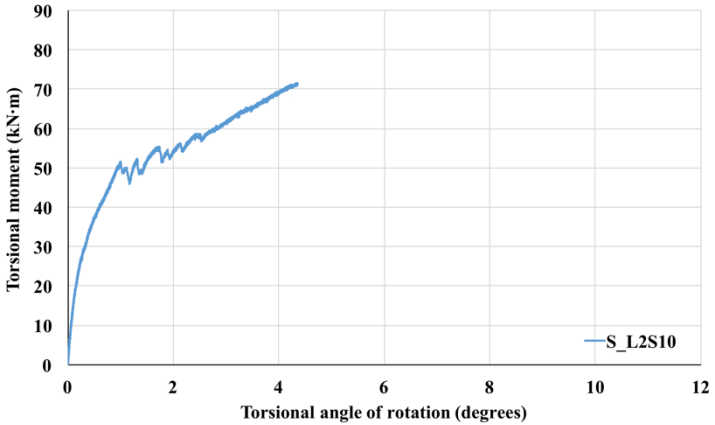

5.399°/
75.728
kN.m

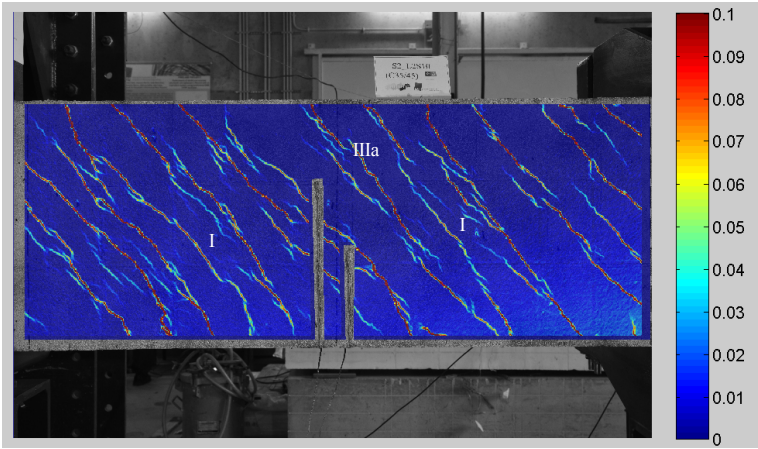

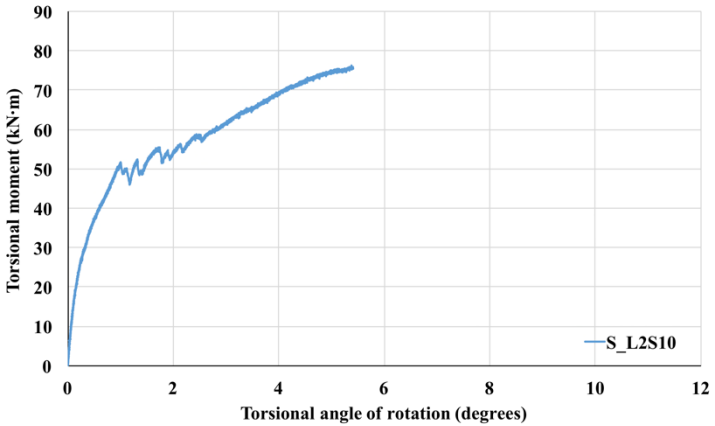

7.048°/
79.455
kN.m

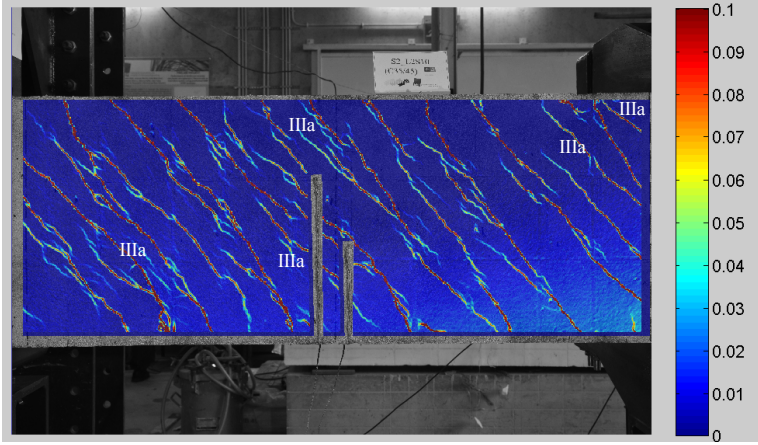

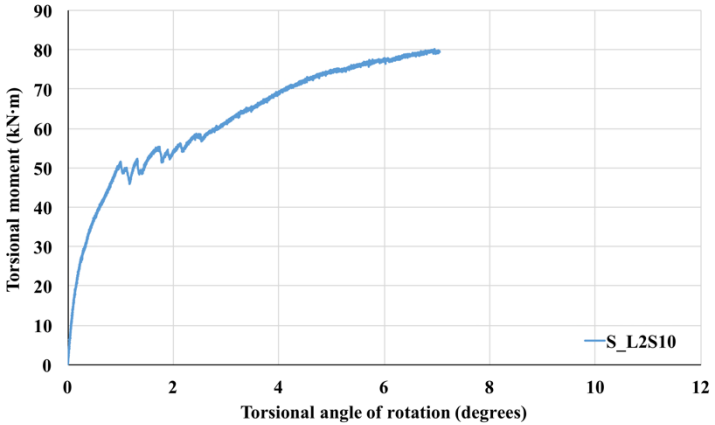

9.357°/
79.680
kN.m

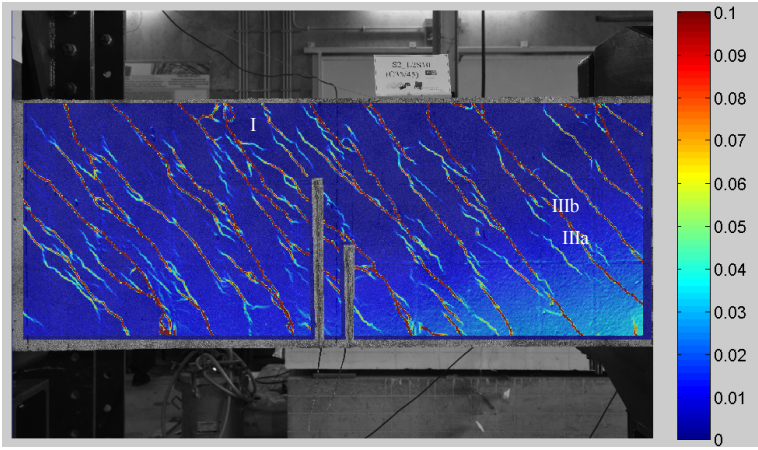

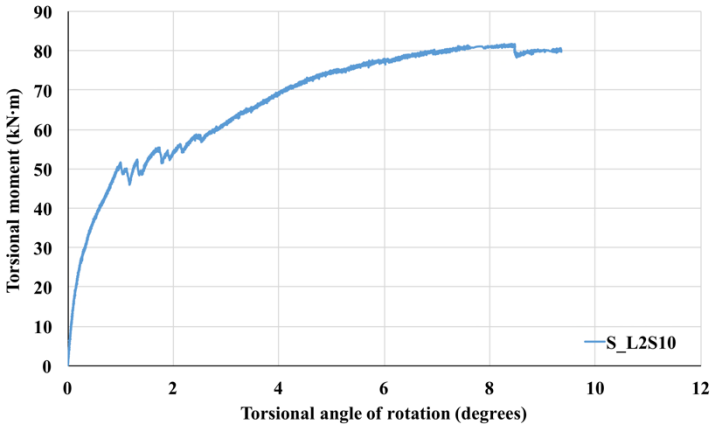

Peak
torsional
moment

9.748°/
80.580
kN.m

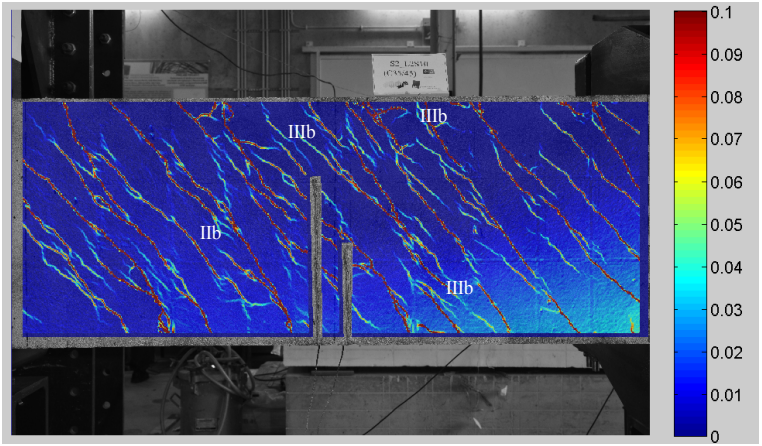

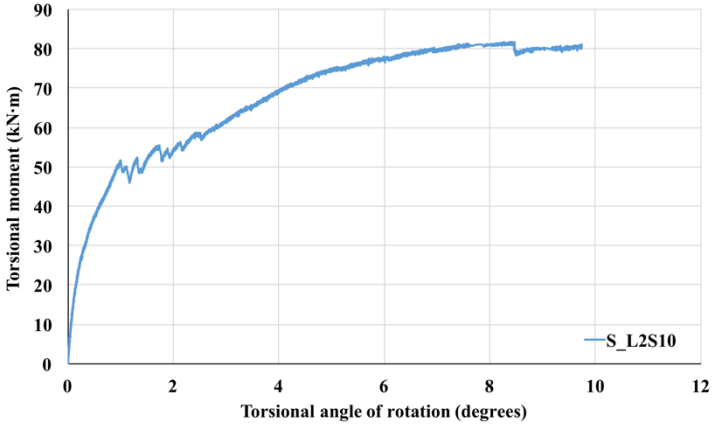

9.890°/
80.580
kN.m

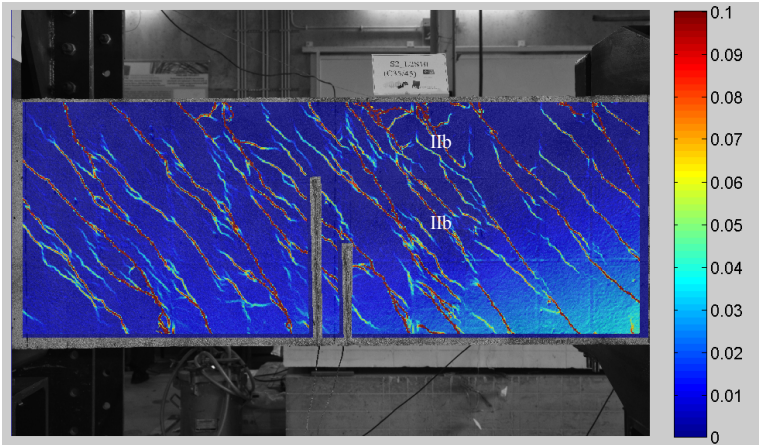

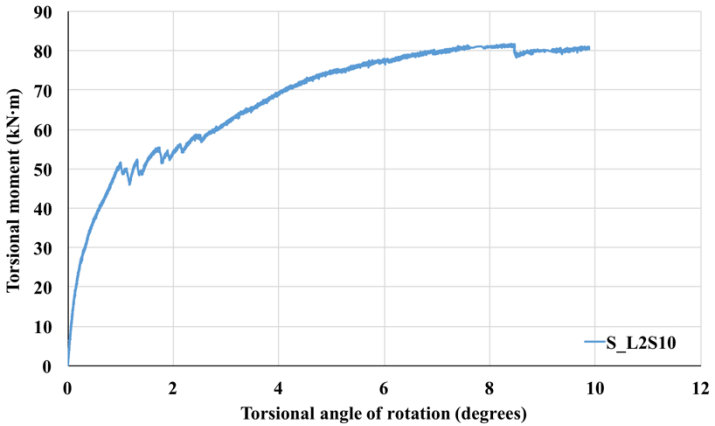

10.352°/ 61.380 kN.m

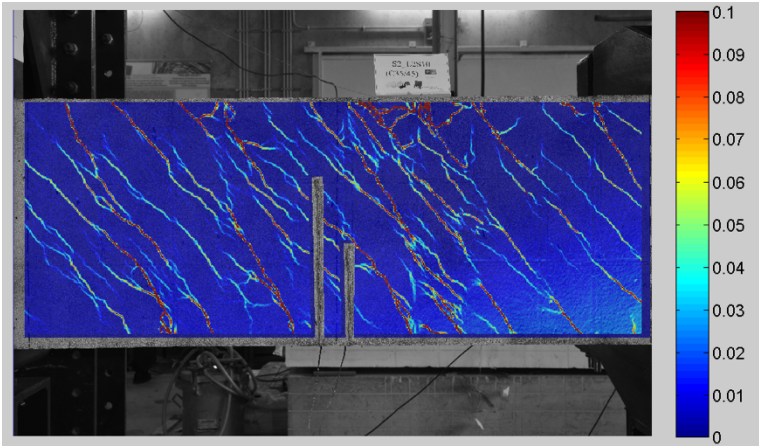

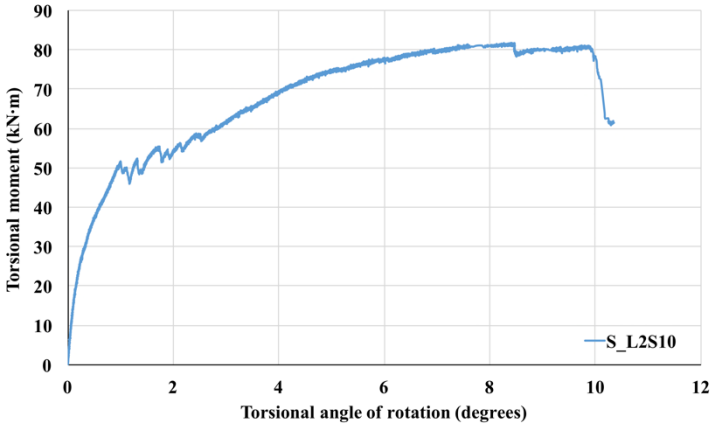

After failure

4. Beam S4F_L4S10

Data	Images	Torsional moment *vs.* torsional angle of rotation	Remarks
0.766°/ 38.888 kN.m	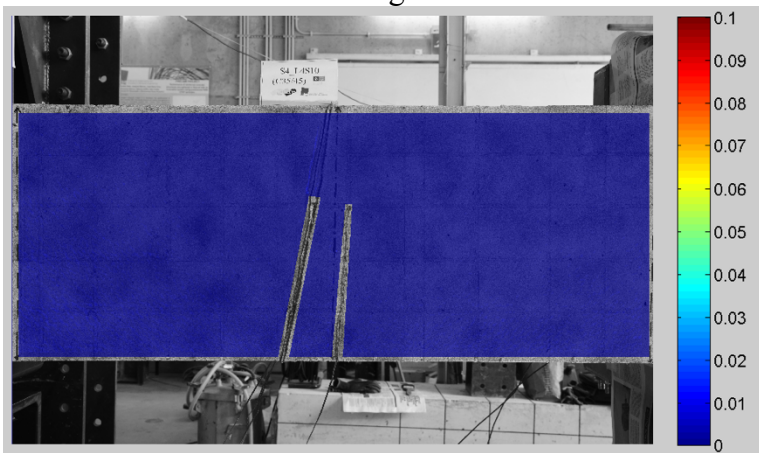	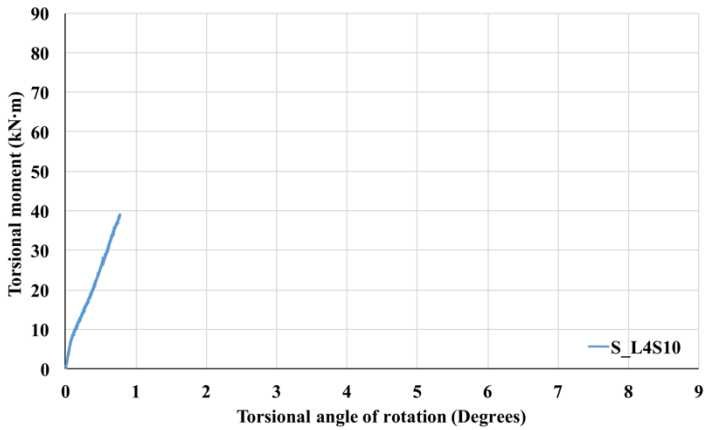	No cracks, linear section
1.384°/ 54.810 kN.m	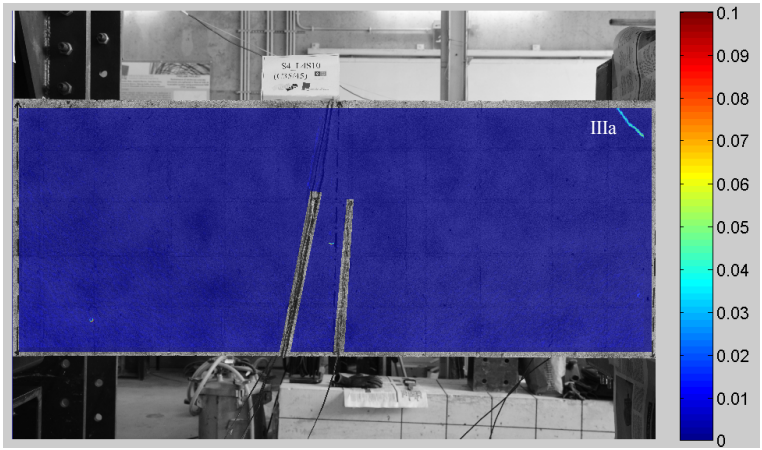	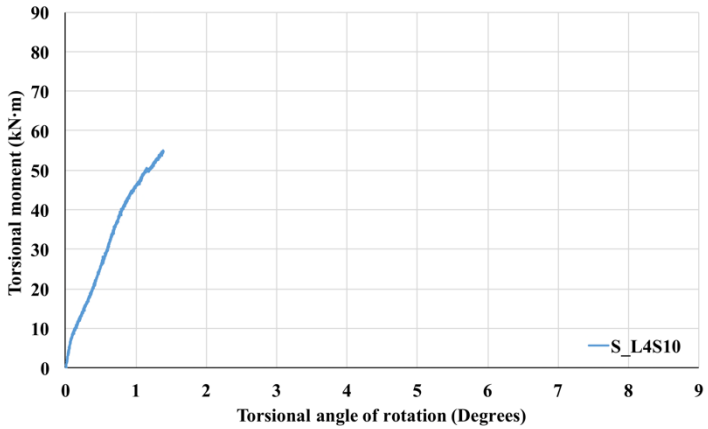	Torsional cracking moment

1.711°/
55.155
kN.m

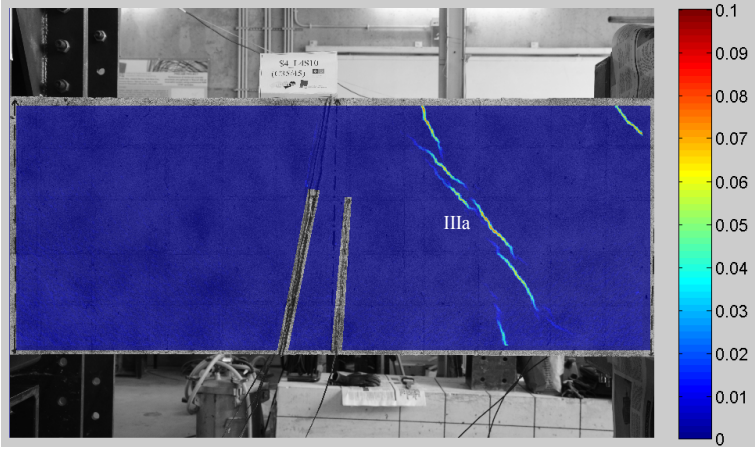

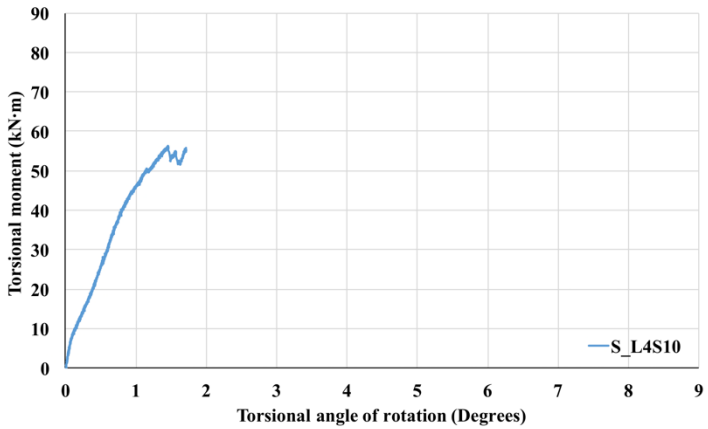

Macro
cracking

2.010°/
57.795
kN.m

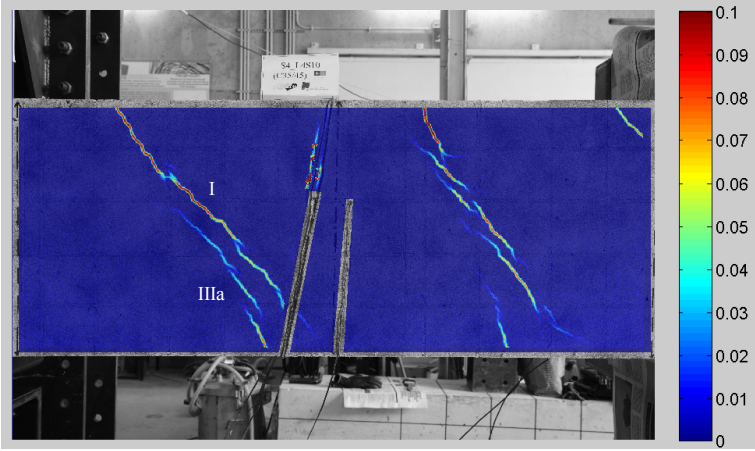

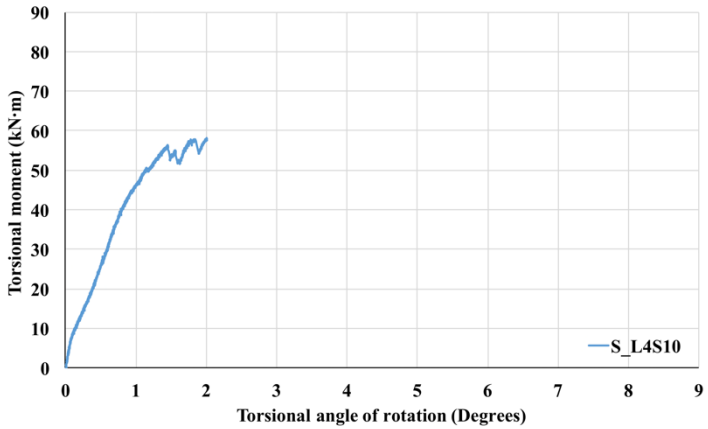

2.330°/
57.780
kN.m

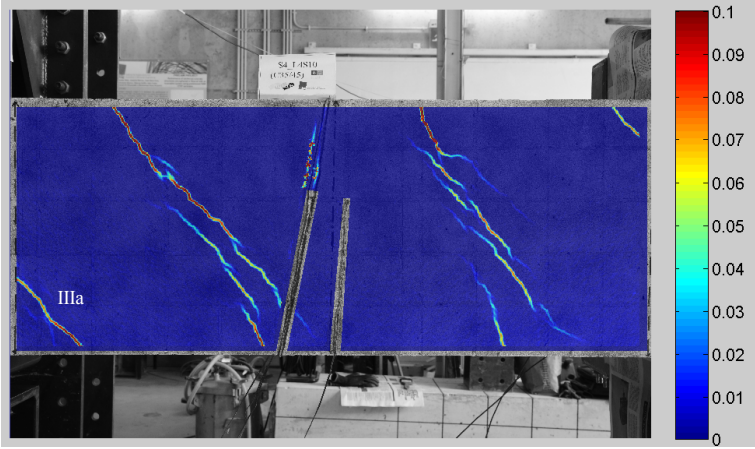

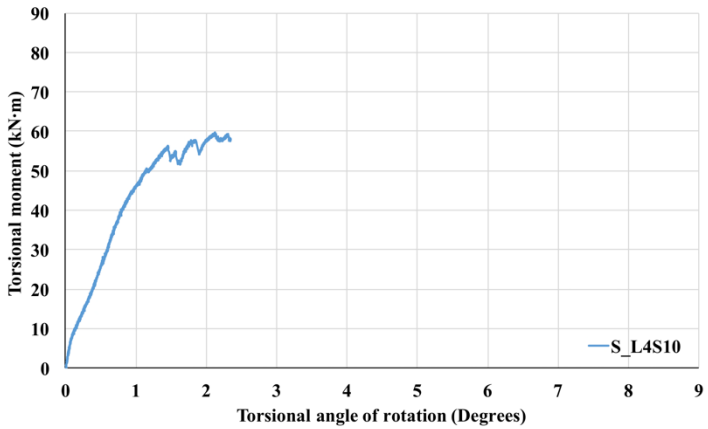

2.546°/
57.338
kN.m

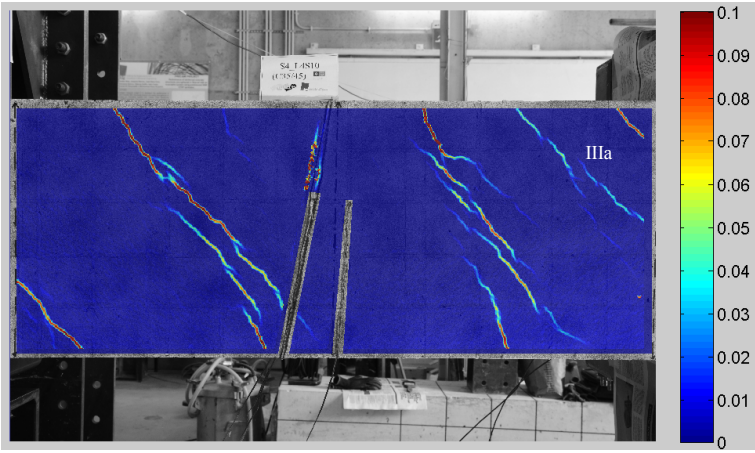

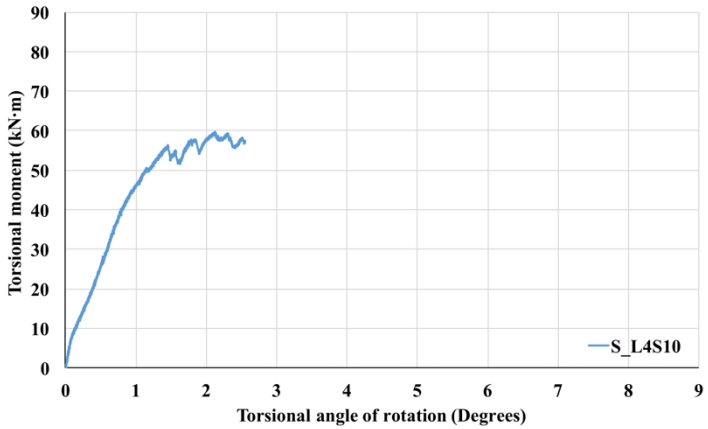

3.693°/
65.595
kN.m

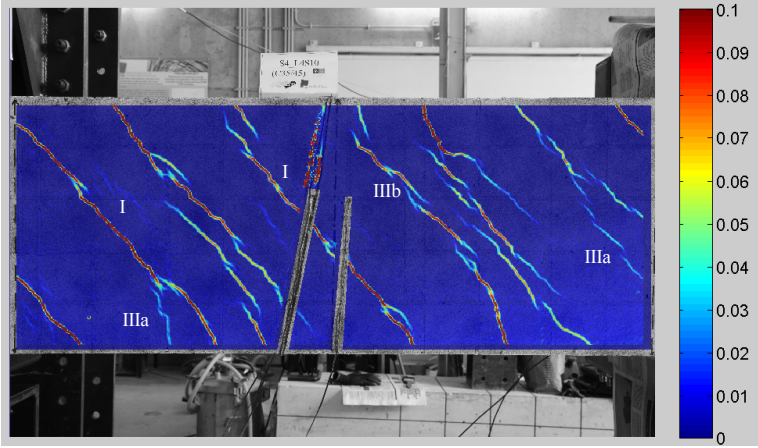

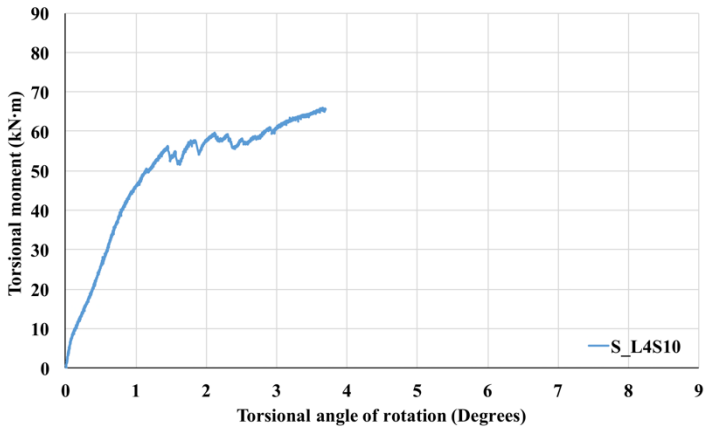

Yield
initiation

4.118°/
68.423
kN.m

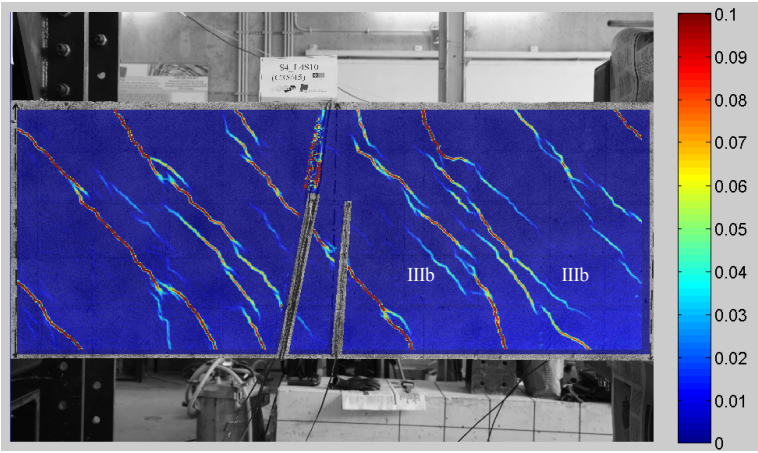

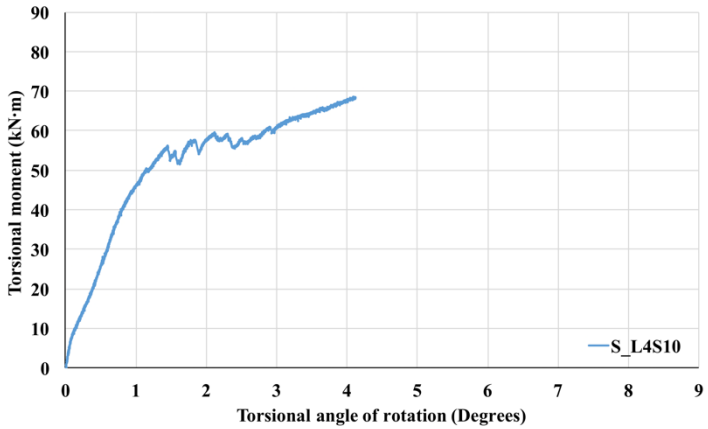

4.410°/
69.698
kN.m

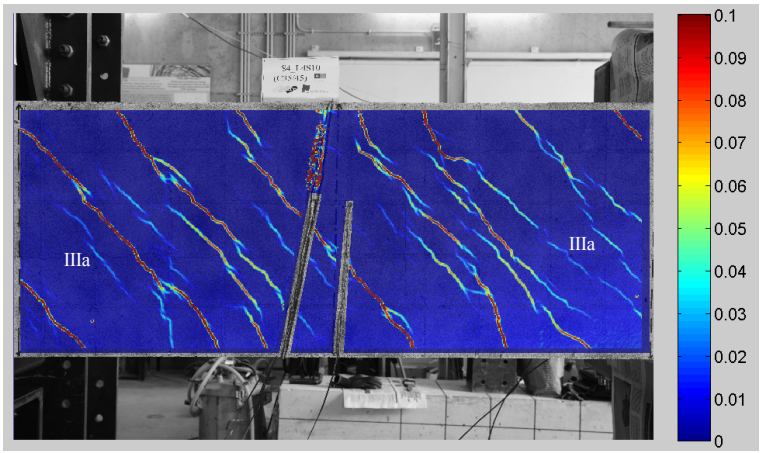

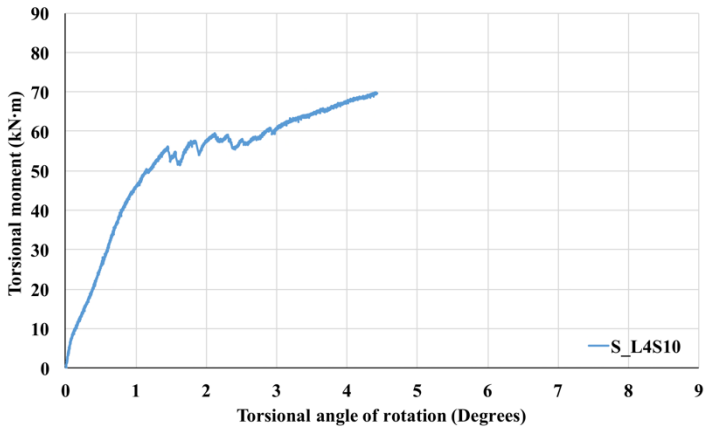

4.824°/
72.150
kN.m

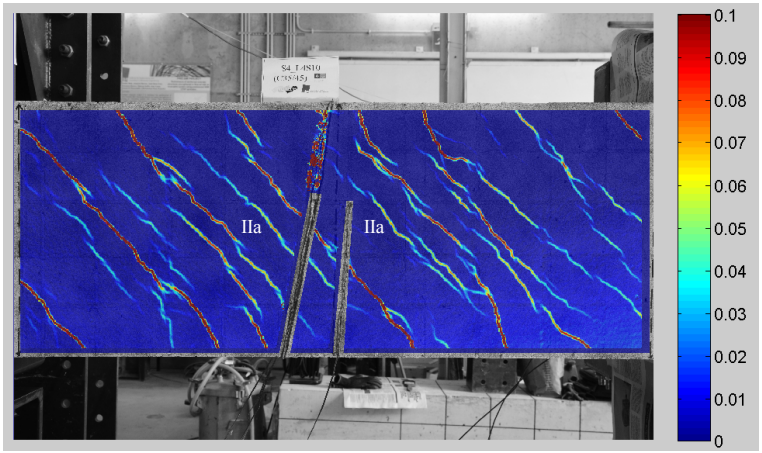

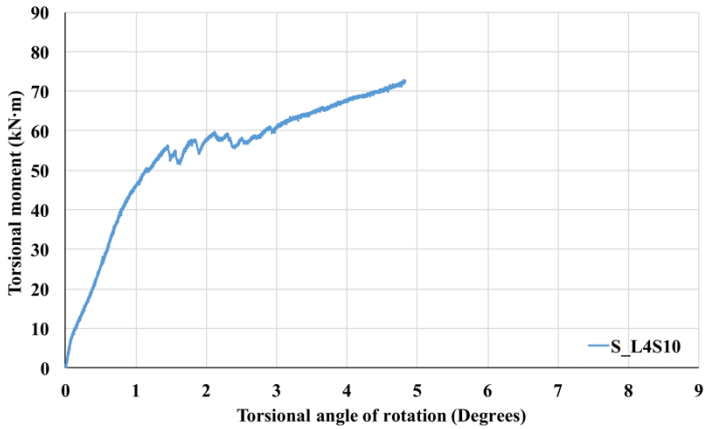

5.667°/
76.560
kN.m

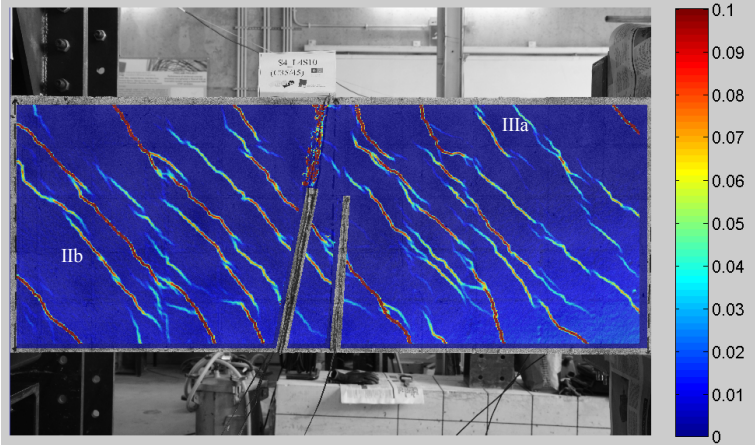

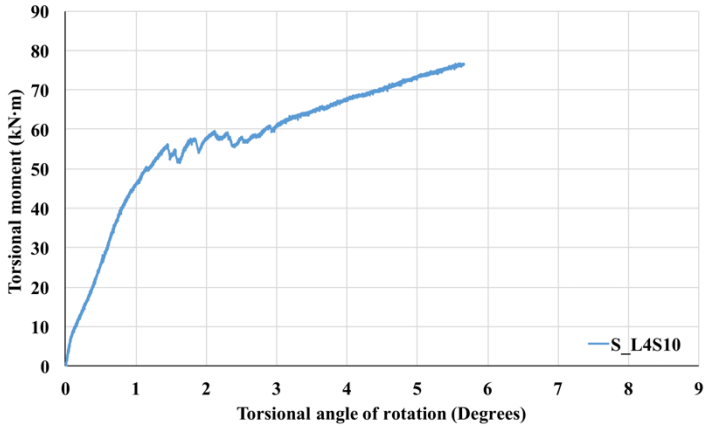

6.222°/
79.065
kN.m

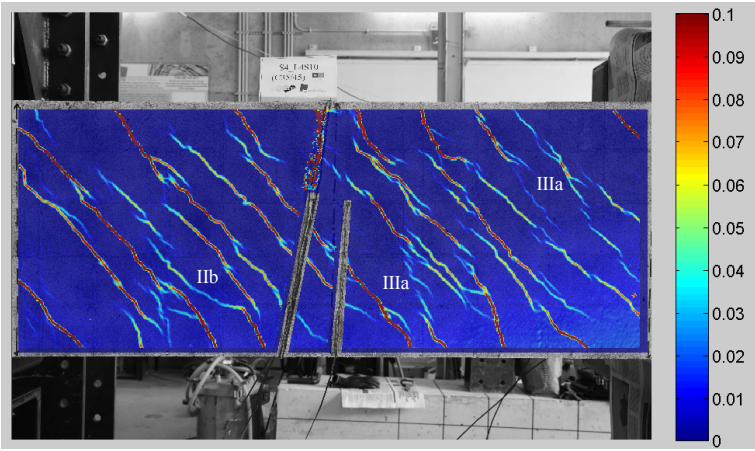

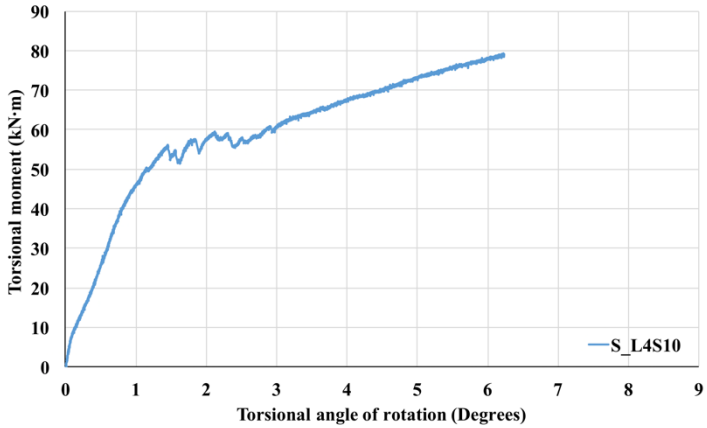

6.877°/
81.300
kN.m

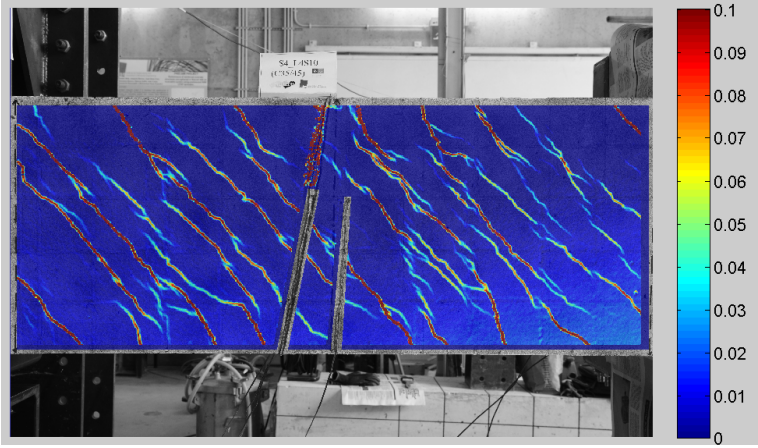

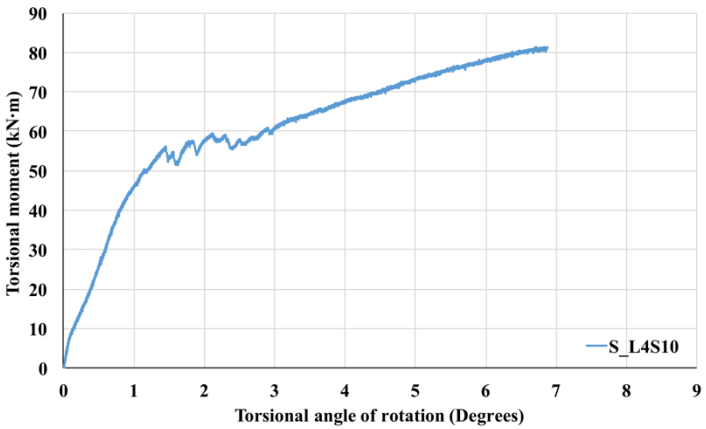

Peak
torsional
moment

7.747°/
80.580
kN.m

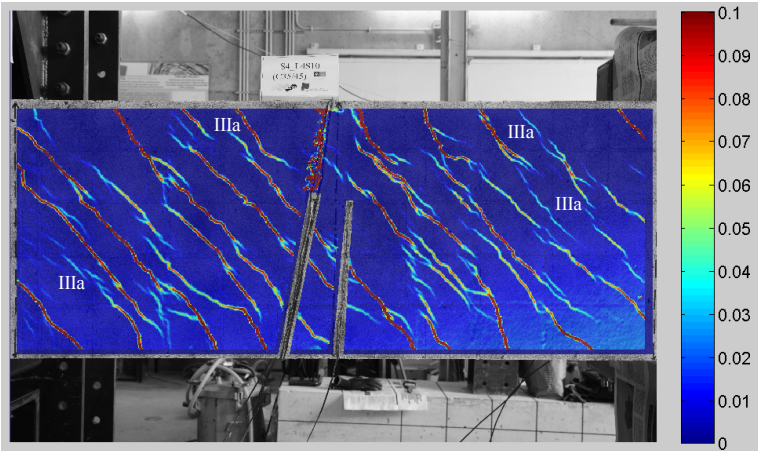

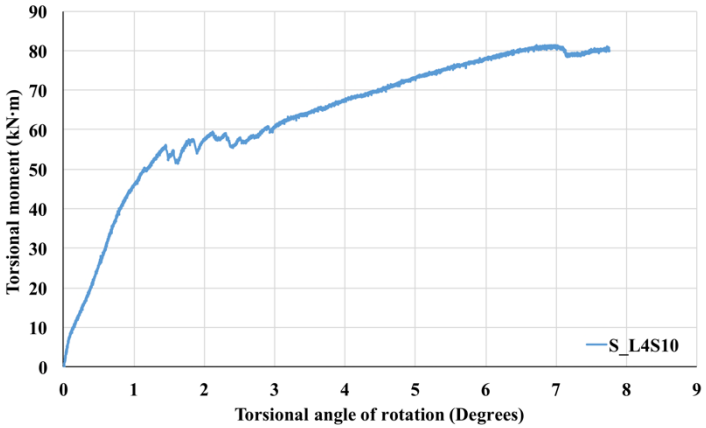

8.056°/
82.110
kN.m

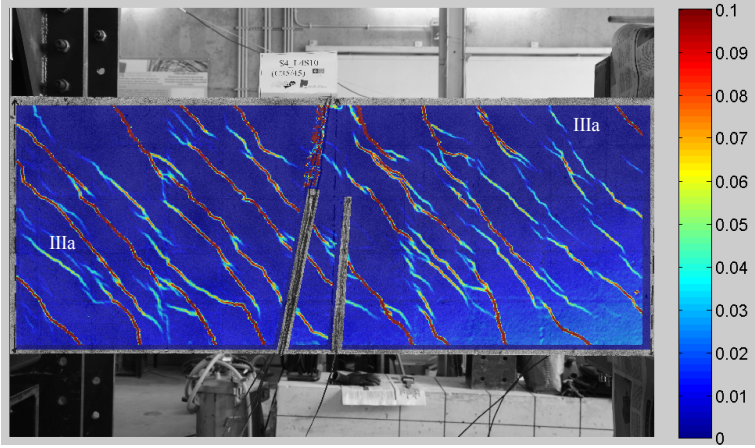

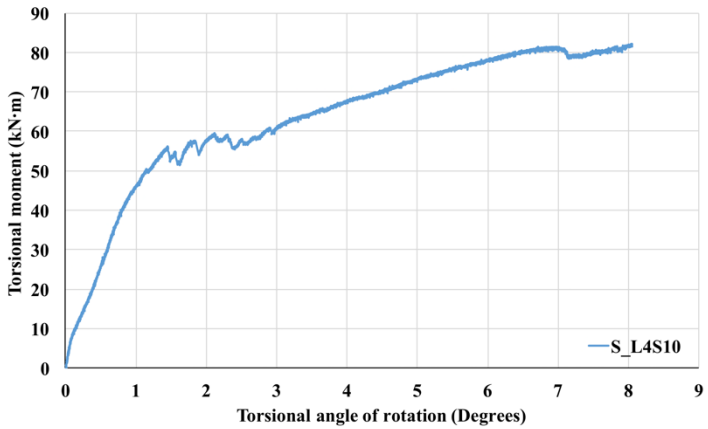

8.372°/
80.895
kN.m

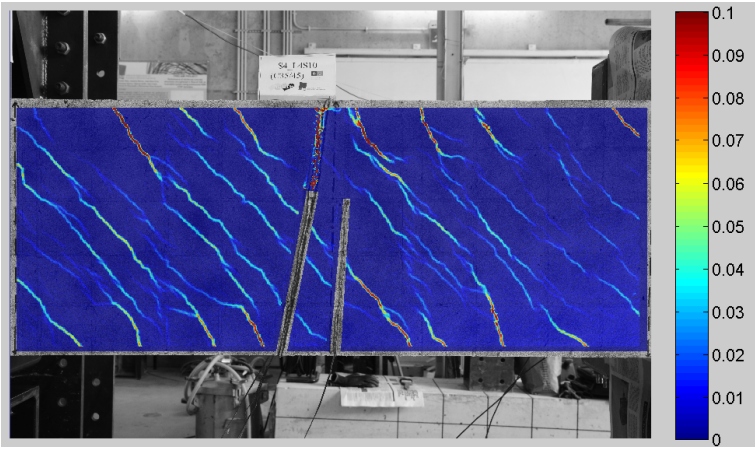

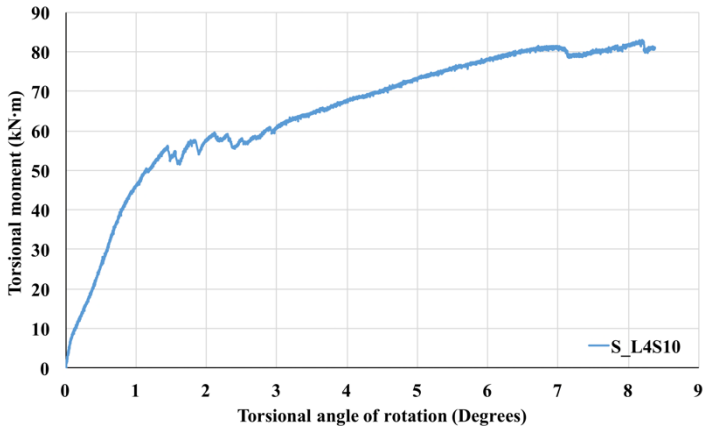

After
failure

5. S3F_L2S5

Data	Images	Torsional moment *vs.* torsional angle of rotation	Remarks
0.338°/ 27.563 kN.m	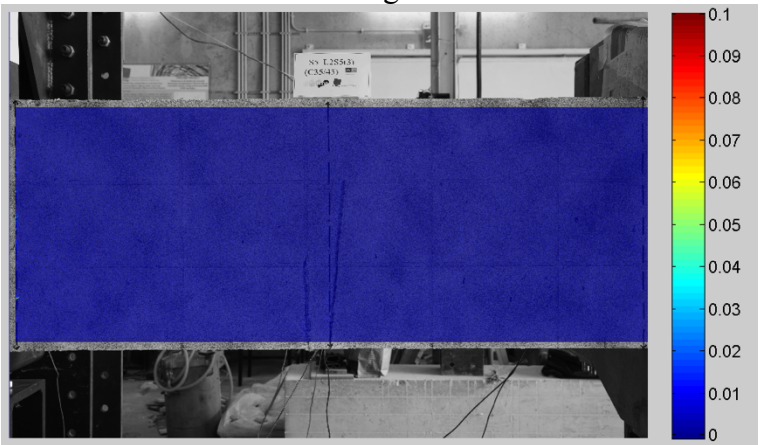	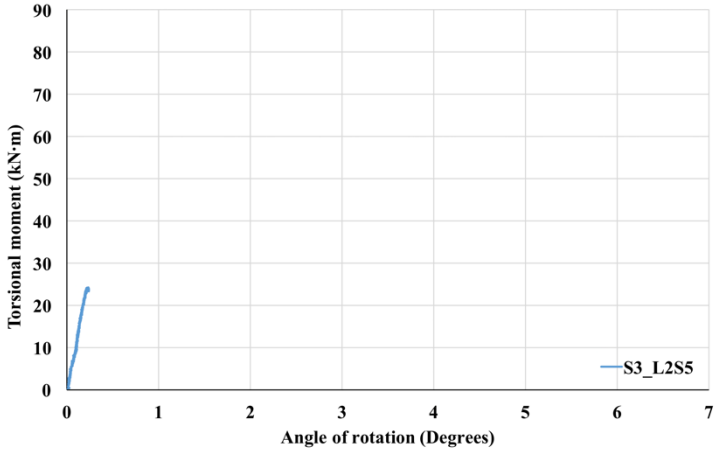	No cracks, linear section
1.020°/ 48.188 kN.m	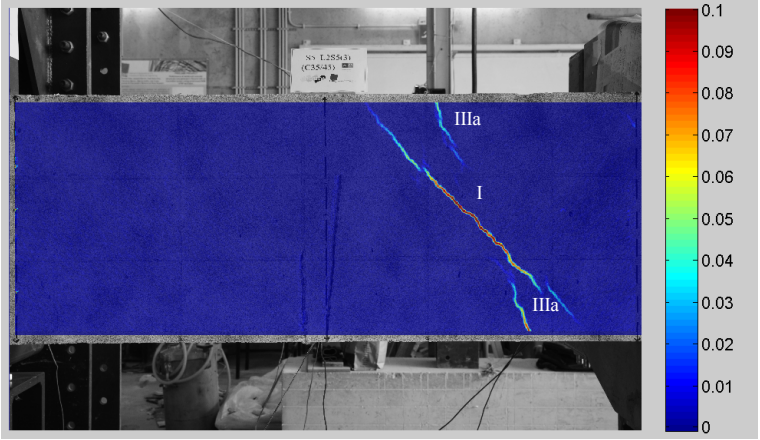	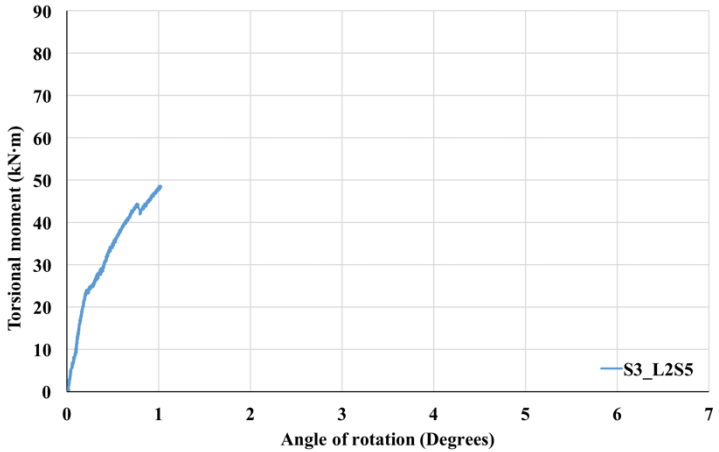	Torsional cracking moment

1.593°/
53.258
kN.m

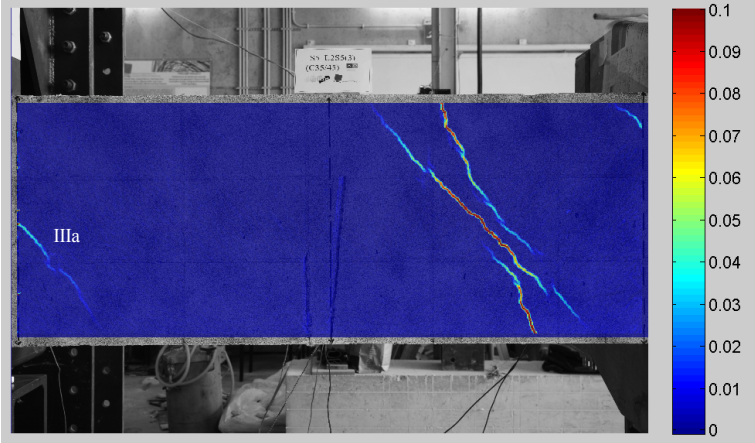

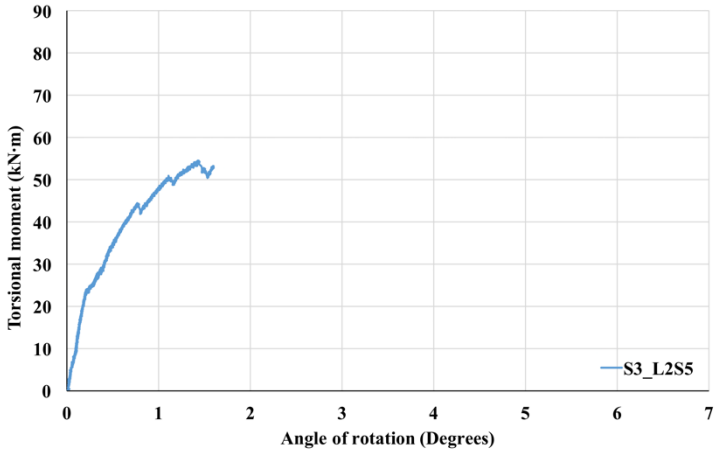

Macro
cracking

1.793°/
52.628
kN.m

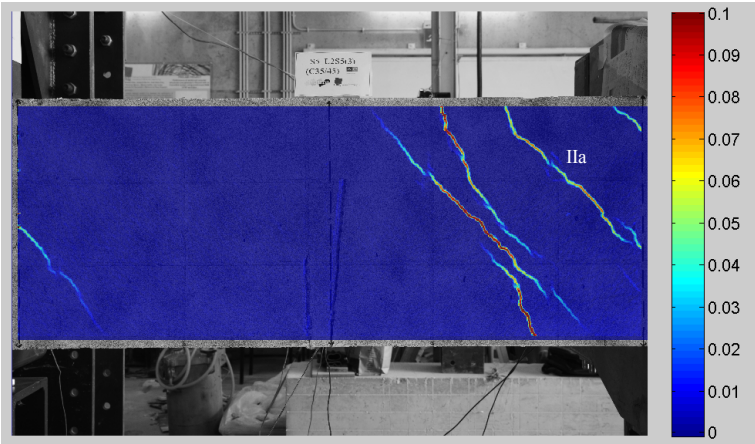

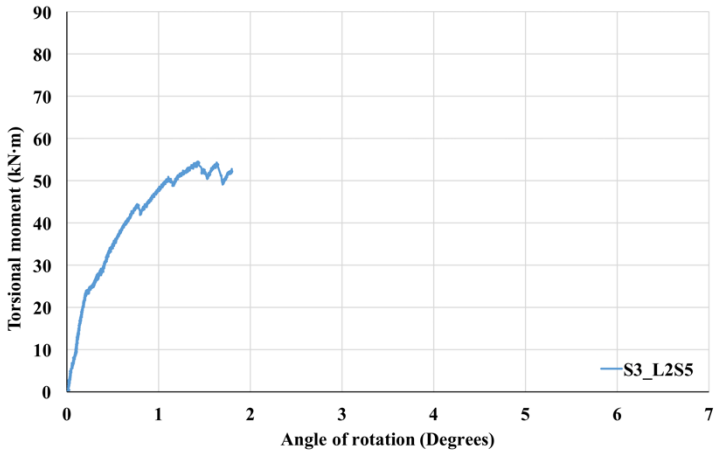

1.974°/
53.993
kN.m

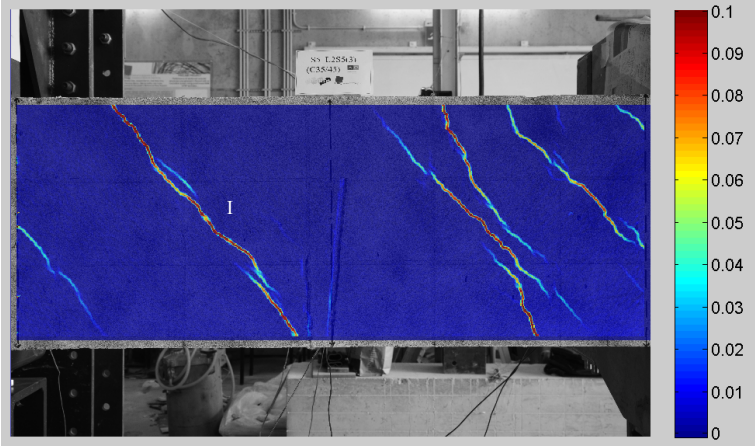

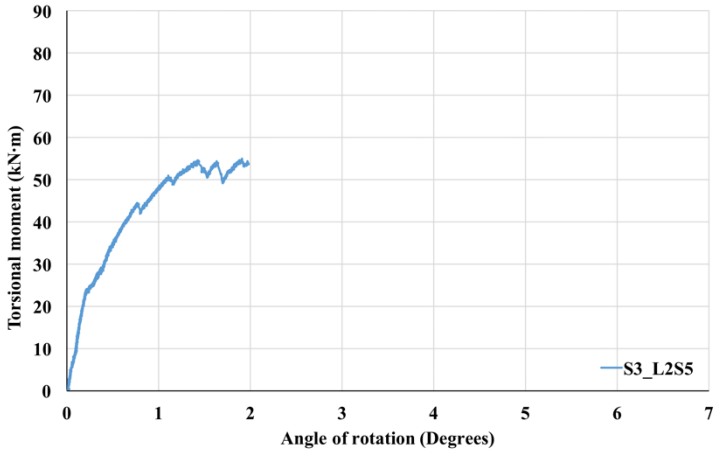

2.203°/
51.803
kN.m

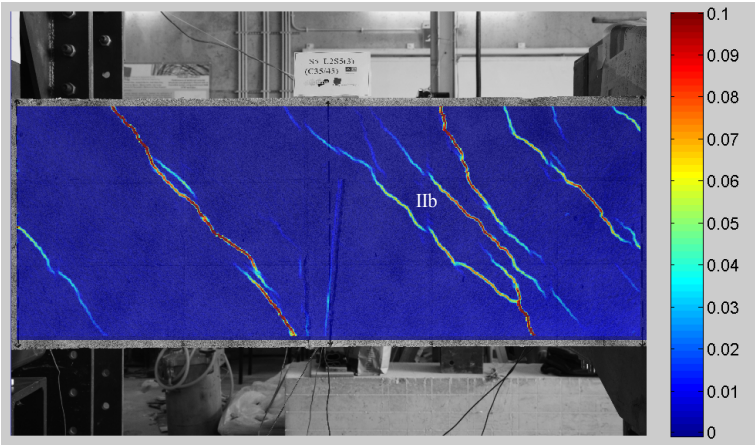

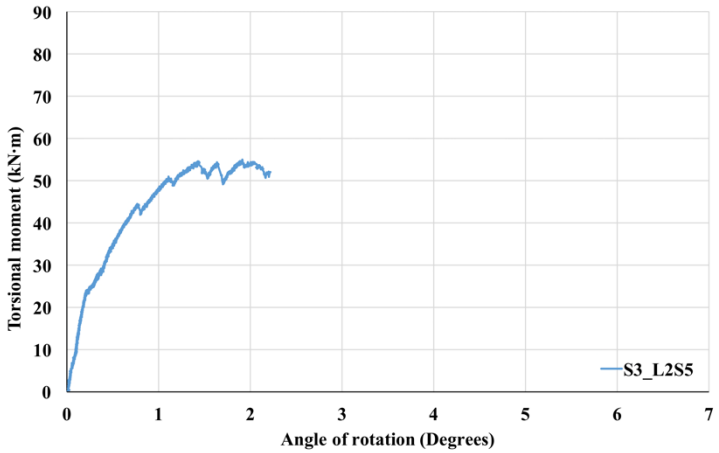

2.723°/
56.303
kN.m

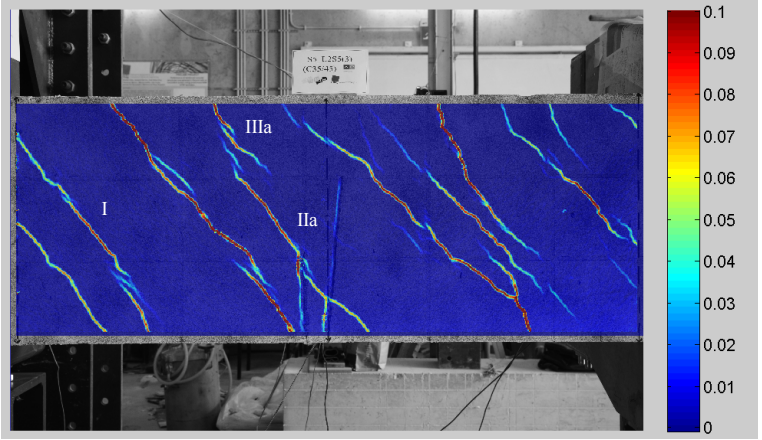

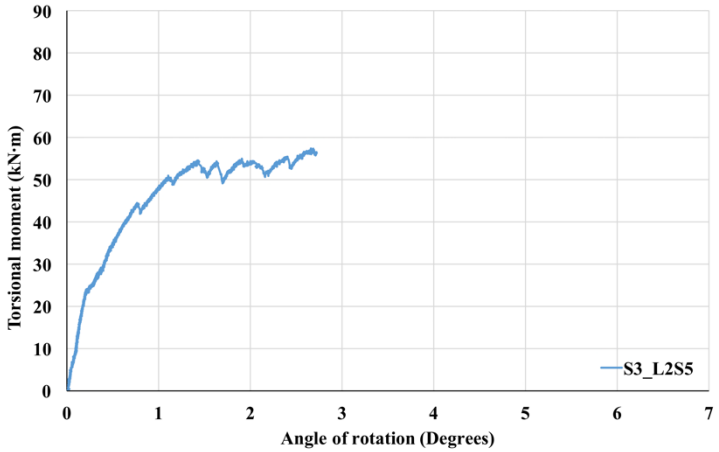

Yield
initiation

3.699°/
63.075
kN.m

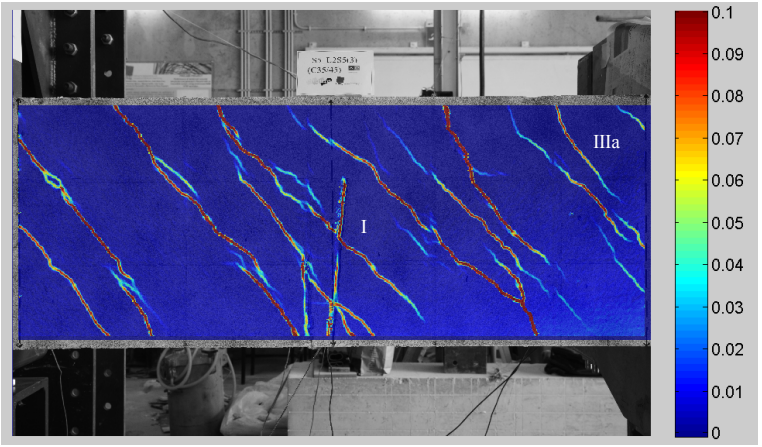

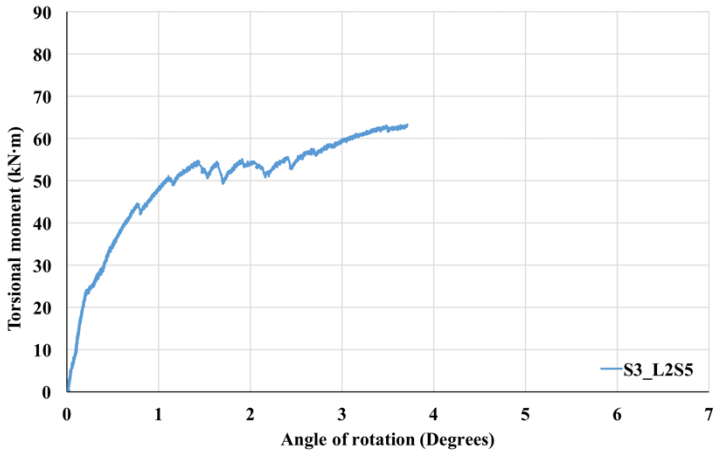

5.280°/
59.843
kN.m

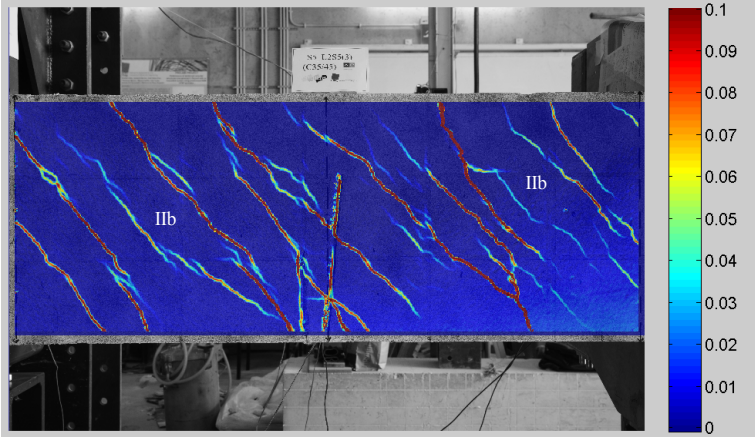

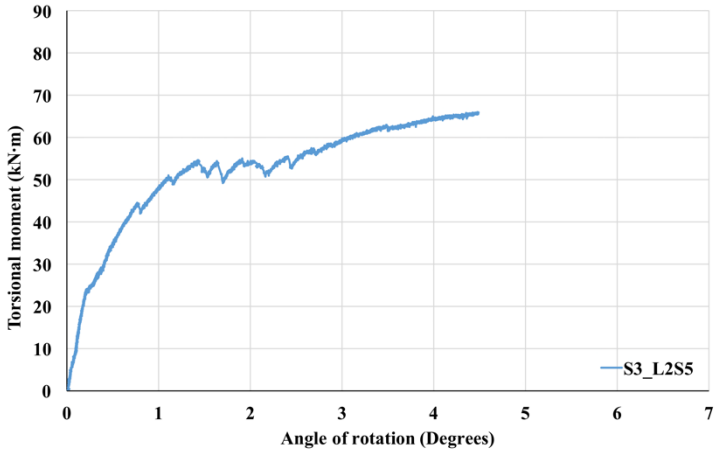

5.156°/
61.410
kN.m

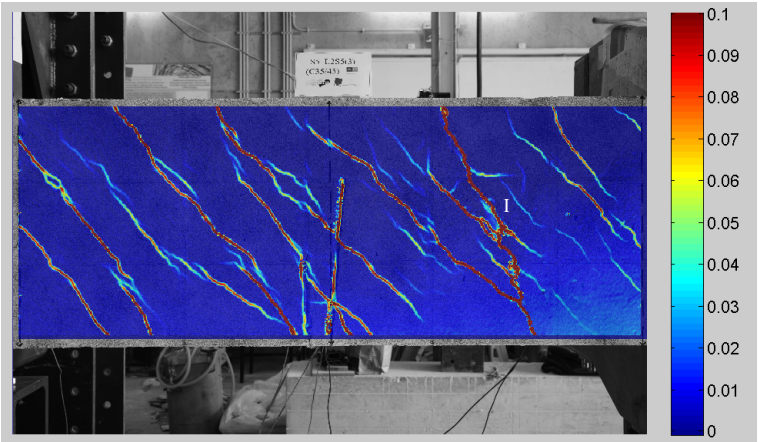

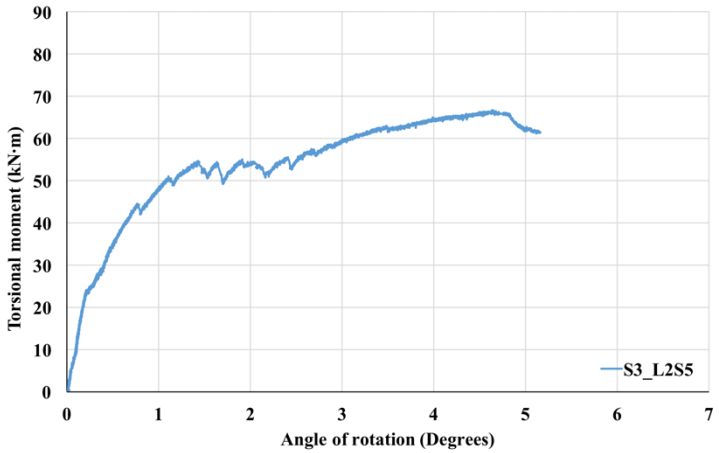

Peak
torsional
moment

5.815°/ 57.135 kN.m

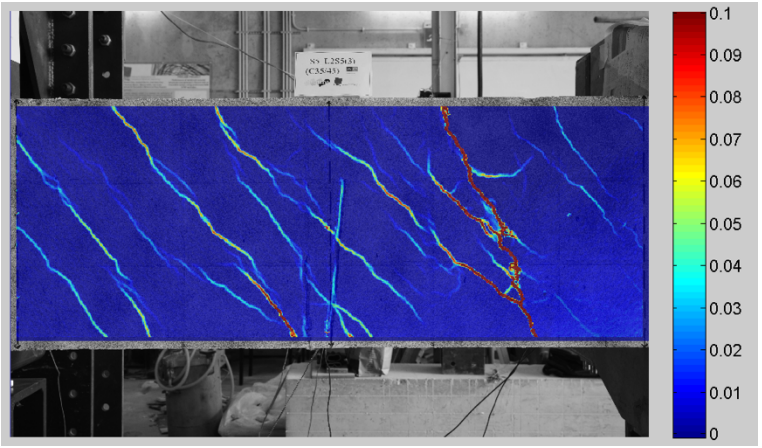

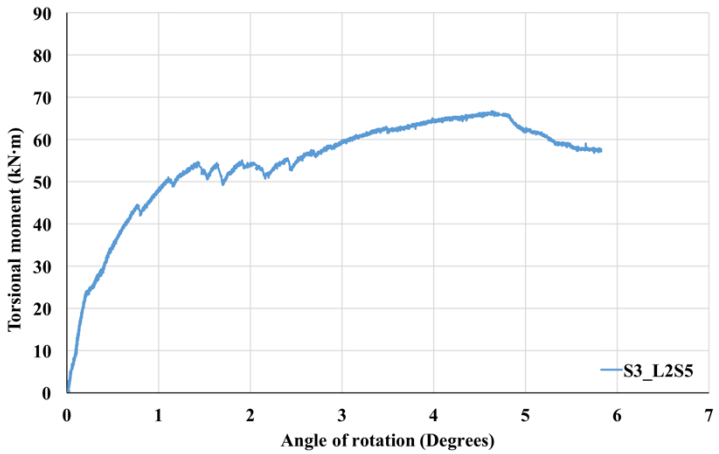

After failure

6. S3F_L4S10

Data	Images	Torsional moment *vs.* torsional angle of rotation	Remarks
0.682°/ 36.653 kN.m	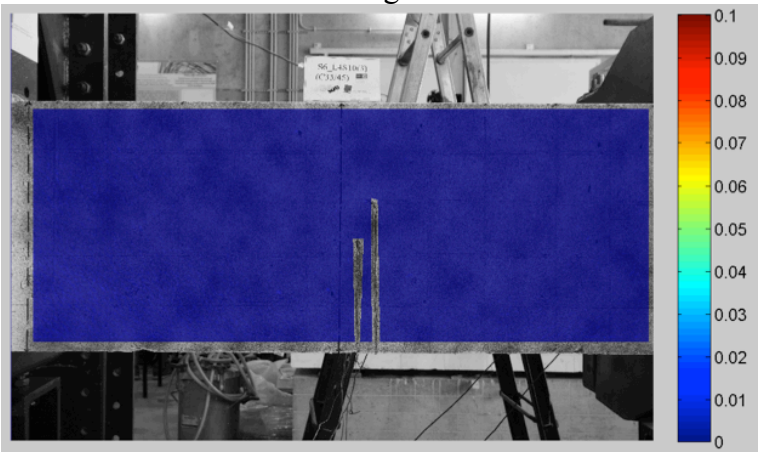	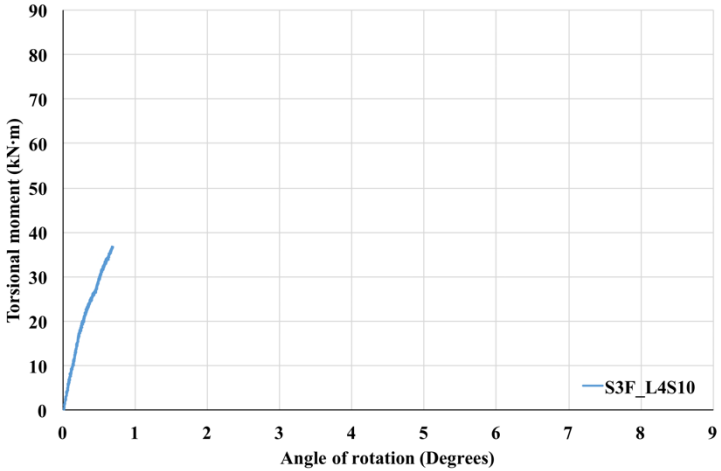	No cracks, linear section
0.912°/ 42.69 kN.m	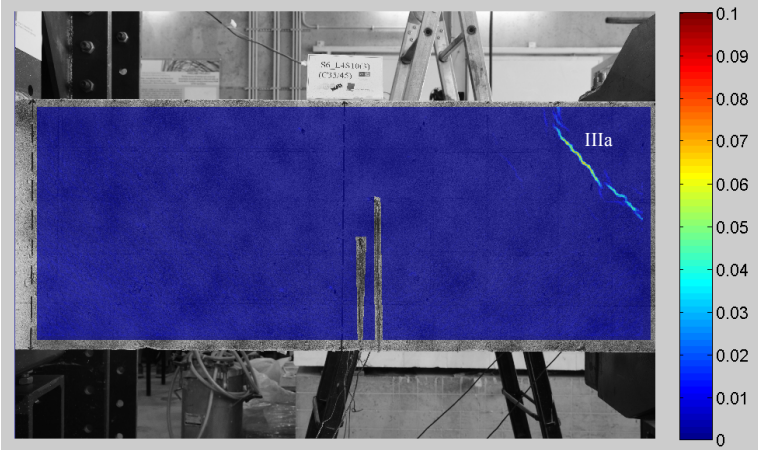	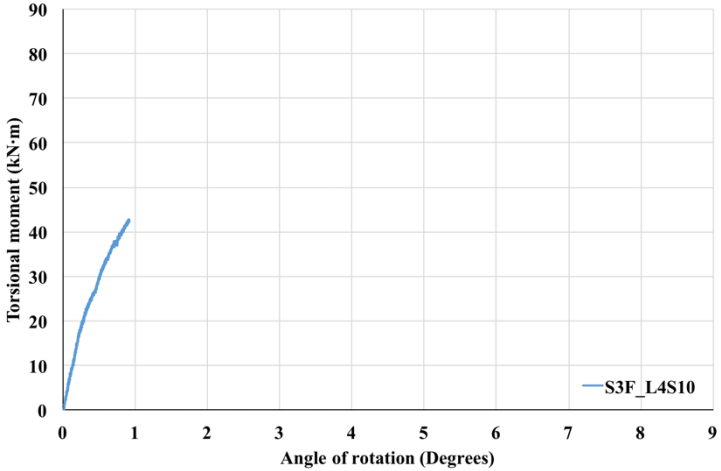	

1.491°/
51.263
kN.m

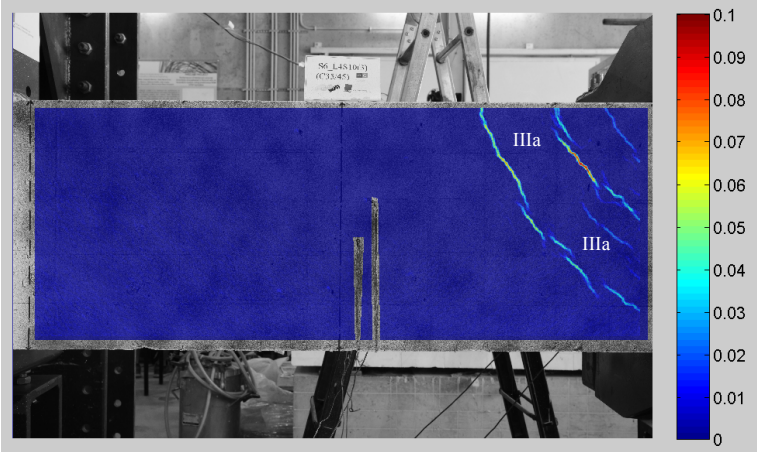

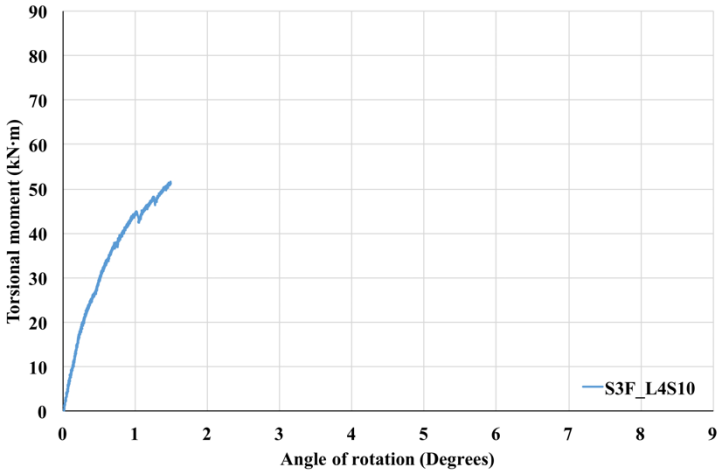

1.588°/
53.130
kN.m

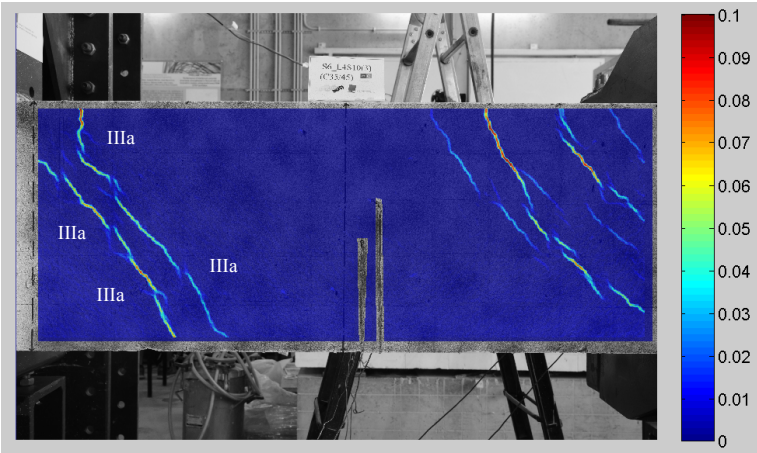

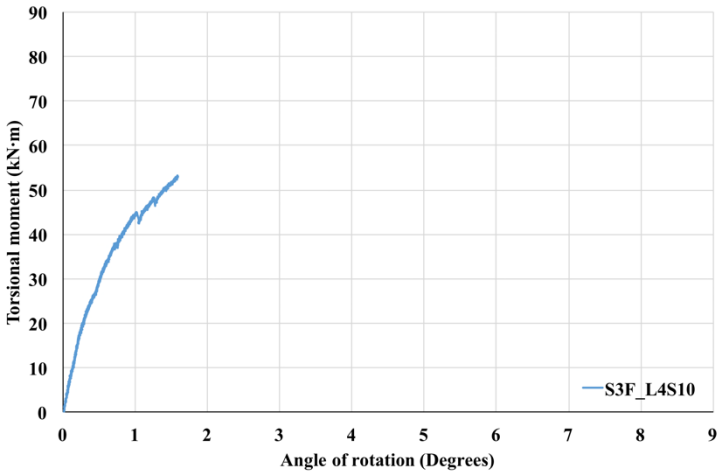

1.778°/
53.078
kN.m

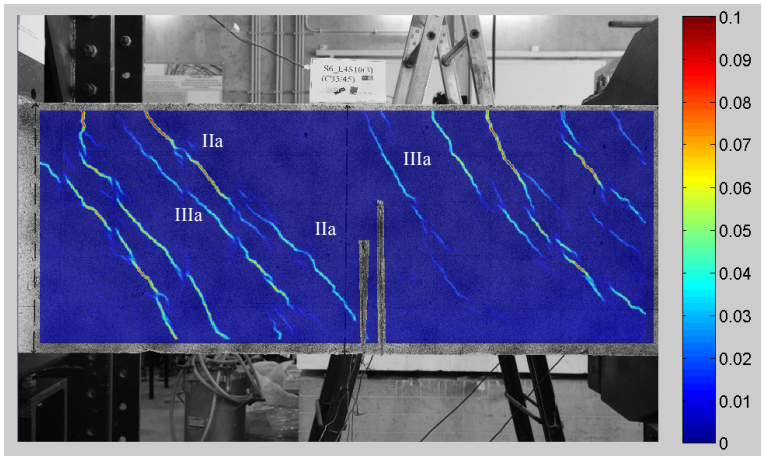

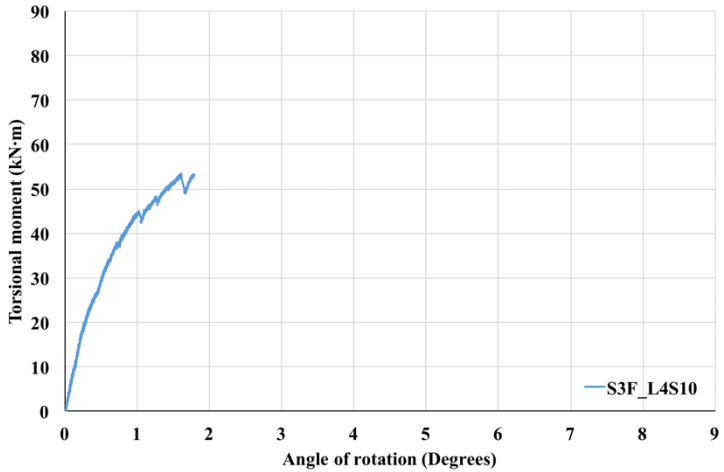

2.199°/
49.643
kN.m

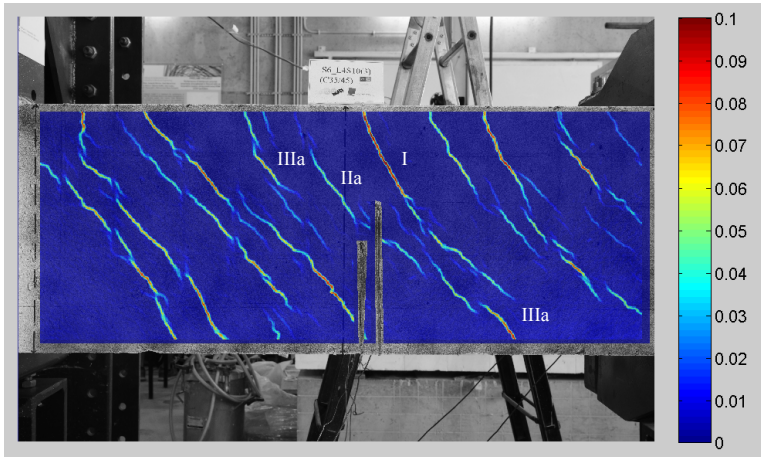

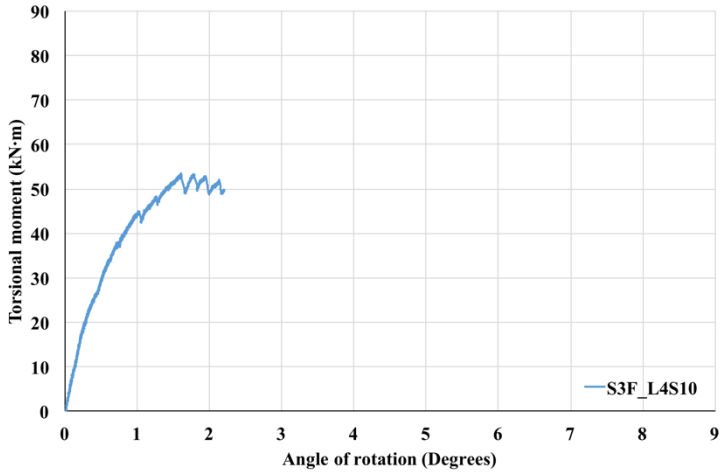

3.132°/
59.498
kN.m

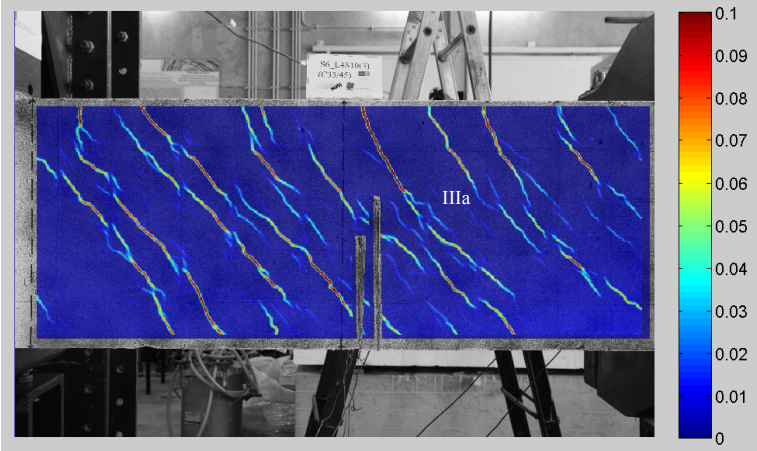

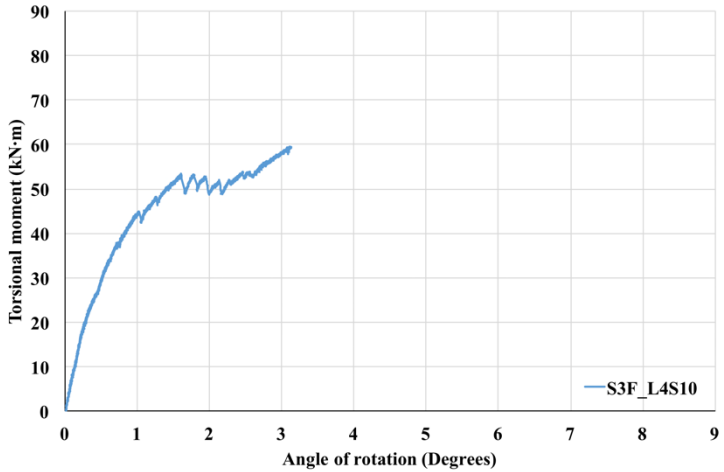

4.419°/
66.525
kN.m

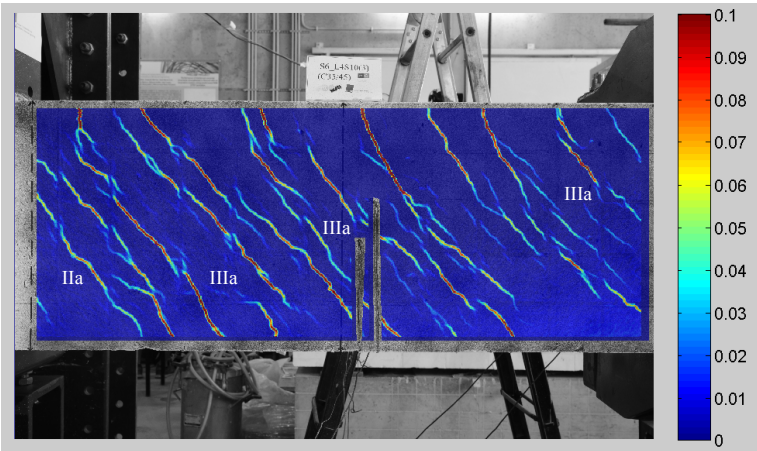

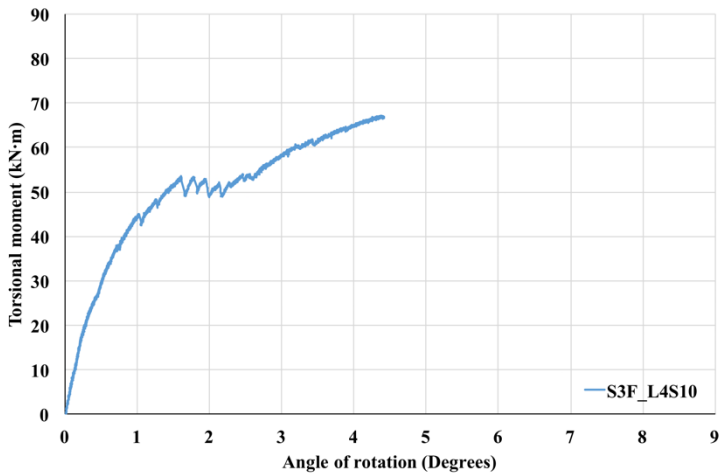

6.448°/
68.108
kN.m

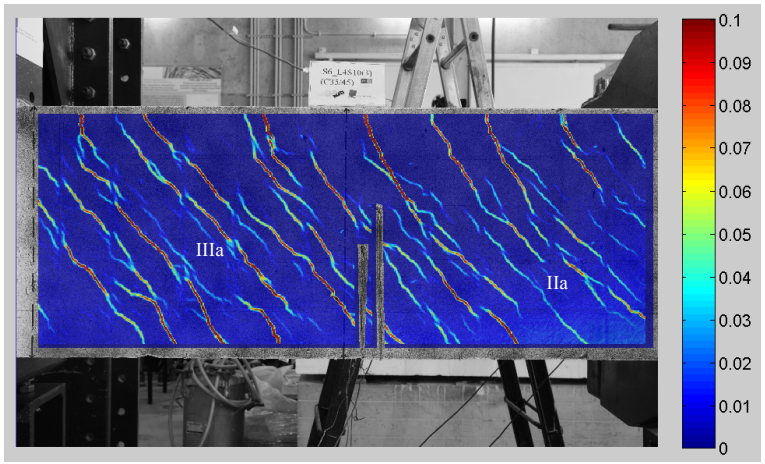

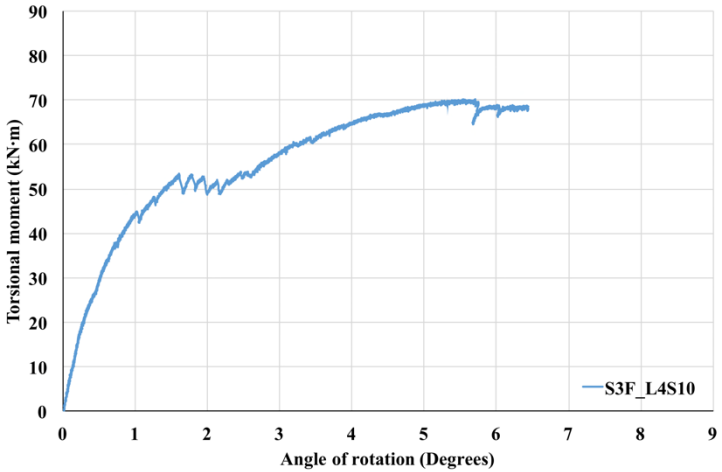

7.648°/
69.420
kN.m

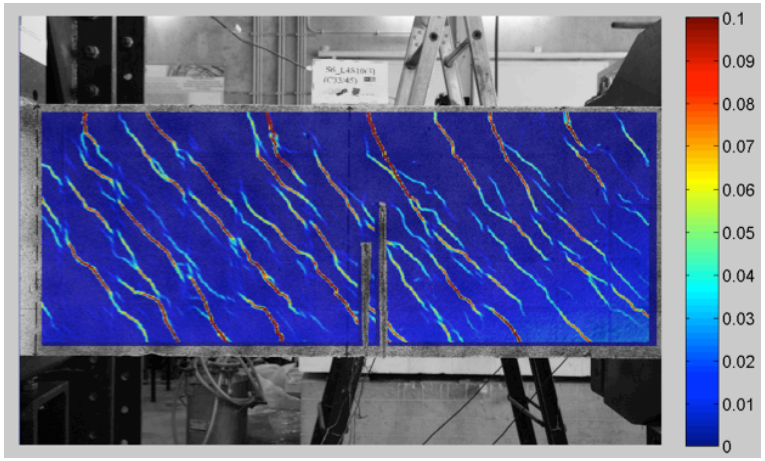

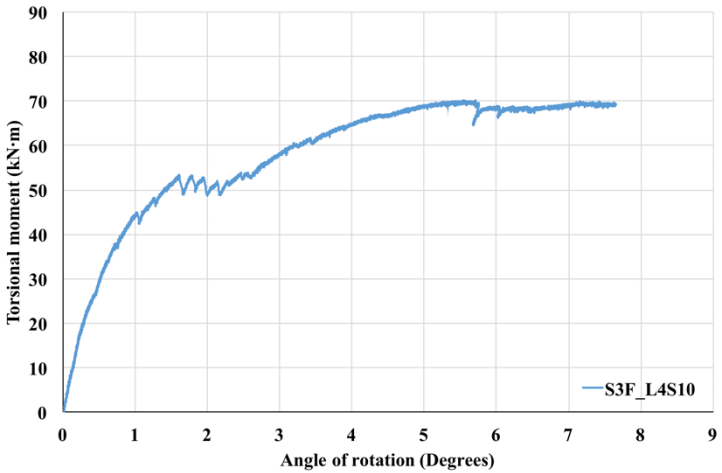

7.953°/ 67.703 kN.m	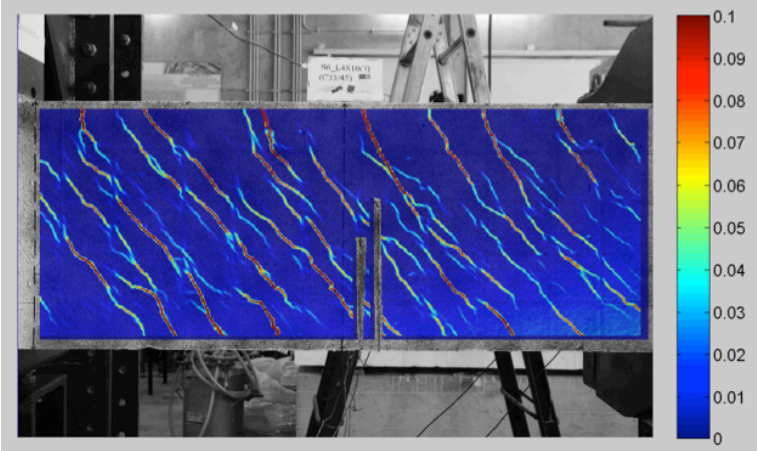	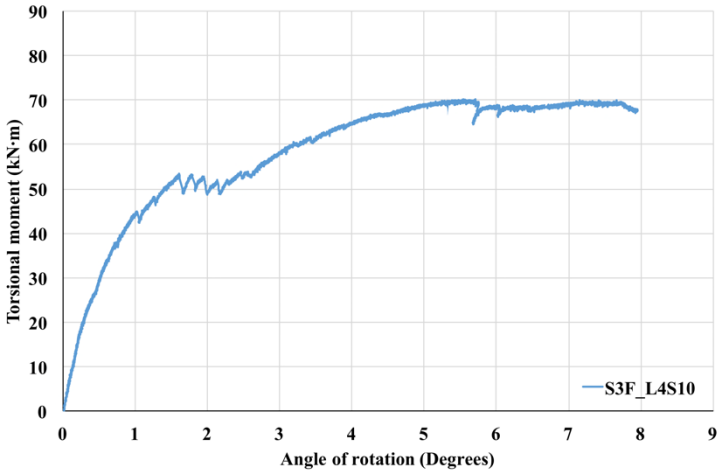	Premature failure